Electrochemical Studies at Modified Carbon Electrodes

By

LUYUN JIANG

Chemistry Department & St Catherine's College, Oxford

Supervisor: JOHN S FOORD

A thesis submitted for the degree of Doctor of Philosophy
to the Board of Physical Sciences at the University of Oxford

Trinity Term, 2014

Electrochemical Studies at Modified Carbon Electrodes

Luyun Jiang, St Catherine's College, Oxford

Doctor of Philosophy, Trinity Term 2014

Abstract

Electrochemistry finds widespread applications in the field of chemical analysis, so-called electroanalysis, as well as in electrosynthesis. The results obtained can be highly dependent on the chemical nature of the electrode used, and chemically modified electrodes are often employed to fine tune the electrochemistry to suit particular applications. This thesis is concerned with the investigation of the use of carbon materials, both as electrode substrates and electrode modifiers, primarily for electrochemical analysis. The work has been carried out using a range of electrochemical voltammetric techniques, as well as impedance measurements. A number of physical methods, including electron microscopy and X-ray photoelectron spectroscopy, have also been used to determine the physical and chemical structures of the materials employed.

The use of boron-doped diamond electrode (BDDE) for the electrochemical detection of H_2O_2 was explored. Although BDDE shows no useful electrochemical response to H_2O_2, a good electrochemical signal can be obtained if the electrode is modified with silver nanoparticles or haemoglobin. The best results are obtained using electrode interfaces fabricated by binding haemoglobin in an active form to silver nanoparticles prepared by electrodeposition on the BDDE in the presence of the surfactant $CH_3(CH_2)_{15}Br$, permitting state of the art performance with a limit of detection (LOD) <

0.5μM. The presence of haemoglobin at the BDDE surface is also capable of catalysing the electrochemical reduction from Ag^{+}(aq) to silver particles. However it reduces their adhesion to the electrode surface, hence they are lost to solution. This observation was used to demonstrate a viable process for the electrosynthesis of Ag nanoparticles, producing particles of about 10 nm diameter at a yield of approximately 50%.

The effects of modifying a glassy carbon electrode with various forms of nanocarbon material for the electrochemical detection of phenolic compounds including hydroquinone (HQ) and dihydroxybenzene (DHB) were studied. The nanocarbons considered included carbon black, graphene nanoplatelets and nanodiamond, for which the former two materials were found to show a large increase in the detection sensitivity. It was shown that the simultaneous detection of HQ and DHB was possible using these electrodes, and in 'real' samples such as river water and green tea. Additional modification of the electrodes with tyrosine also permitted detection of phenol and p-cresol. The nanodiamond and carbon black modified electrodes were also employed for the electrochemical detection of Bisphenol A (BPA), which can be severely hampered by electropolymerisation of the oxidation products of BPA, producing rapid electrode fouling. However because of the inert nature of diamond surfaces, it is shown that this fouling process can be minimised by modifying the glassy carbon electrode with nanodiamond. Alternatively, it was also observed that for the carbon black modified electrode, a strong electrochemical response could be seen associated with the quinone forms produced by BPA oxidation. The associated electrochemical signal is also found to be relatively insensitive to electrode fouling, opening up an alternative strategy for the detection of BPA. Finally the use of a carbon black modified glassy carbon electrode for the detection of dopamine in the presence of the interfering compounds, ascorbic and uric acids, was studied. The carbon black

modifier is shown to increase detection sensitivity, and help separate the electrochemical signals of the differing redox active species present in the solution.

Acknowledgements

If I can only thank one person for the support through the whole D. Phil process in the past 4 years, it has to be my supervisor *Prof.* John Foord. His endless patient, kindness and wisdom have guided me through all the tough situations. All his rigorous logic, cautious attitude and sharp insight make the results present in this thesis possible and have set up a good sample in my future career.

I would like to extend my gratitude to *Dr.* Jingping Hu who helped me to get my research started, solved a lot of technique problems in the lab and operate the Raman analysis for me. I also want to show the appreciation to other group members- Emina, Sirikarn, Patrick, Geoff, Inga, Celine, Chenbo, Christos, Johanna, Hugh and Isabel, and those who have left the group- Tony, Montree, Baixiang, Xiao Lu and Jia Gong, Dong Myung, Adam, Rowena, Vicky, Michael, Carl, Seb, Edward, for their kindness and enthusiasm that create the friendly environment in the office, and the discussions with them are always inspired and enjoyable.

I also want to say thank you to all my dear friends, Liang Kong, Yueyue, Liang Chen, Tingting, Zhuzi, Sirikarn, Patrick, Shuo Xu, Feng Xu, Chenbo and many others for all the happiness and sorrow that we shared. It is you that make my life in Oxford interesting and always full of fun and love. All the precious days spent with you have become one of the most cherished memories for me, and will never be forgotten.

I want to express my appreciation to the Chinese Scholarship Council for three-year financial support, without which it is impossible for me to study here, and St Catherine’s College for the generous overseas scholarship, decent high table dinner, and the opportunity of meeting many nice friends.

Acknowledgements

Finally, I would like to give my sincere thanks to my parents. Although they have divorced for 13 years, I can always feel the unconditional love and endless support from both of them, especially for my mom who has sacrificed a lot for me. And I feel deeply grieved and sorry that I was thousands of miles away when she needed me to stand by. It is their wrinkle and grey hairs that create me today, and I wish can make them proud.

Publications

1. **L. Jiang**, J, Hu, J. S. Foord. 'Determination of H_2O_2 at Boron Doped Diamond Electrode Modified by Ag NPs and Haemoglobin' *in preparation*

2. **L. Jiang**, and J. S. Foord. 'Electrochemical Synthesis of Silver Nanoparticles at Haemoglobin Modified Boron Doped Diamond Electrode in Aqueous Phase' *in preparation*

3. **L. Jiang**, and J. S. Foord. 'New Carbon Materials Sensors: Nano-diamond, Graphene and Carbon Black for Phenol Compounds Detection' *in preparation*

4. **L. Jiang**, and J. S. Foord. 'Determination of BPA at Carbon Black and Nano-diamond Modified Electrode' *in preparation*

5. **L. Jiang**, and J. S. Foord. 'A New Indirect Method to Determine Dopamine at Carbon Black Modified Electrode' *in preparation*

Contents

List of Abbreviations

AA	.....	Ascorbic acid
AFM	.....	Atomic force microscopy
ASF	.....	Atomic sensitivity factor
B.E.	.....	Binding energy
BDDE	.....	Boron-doped diamond electrode
BPA	.....	2,2-(4,4-dihydroxydiphenyl) propane
CB	.....	Carbon black
CE	.....	Counter electrode
CM	.....	Carbon materials
CNT	.....	Carbon nanotube
CTAB	.....	Cetyl hexadecylthmoniom bromide
CV	.....	Cyclic voltammagram
CVD	.....	Chemical vapour deposition
cyt.c	.....	Cytochrome c
DA	.....	Dopamine
DET	.....	Direct electron transfer
DHB	.....	1,2-dihydroxybenzenes
DHI	.....	5,6-dihydroxyindole
DPV	.....	Differential pulse voltammetry
DLS	.....	Dynamic light scattering
EIS	.....	Electrochemical impedance spectroscopy
ETR	.....	Electron transfer resistance
GC/MS	.....	Gas chromatography/mass spectrometry
GCE	.....	Glassy carbon electrode
GP	.....	Graphene
Hb	.....	Haemoglobin
HPLC	.....	High Performance-Liquid Chromatography
HQ	.....	Hydroquinone
HRP	.....	Horseradish peroxidise
IHP	.....	Inner Helmholtz plane

List of Abbreviations

IMFP	.....	Inelastic mean free path
LC/MS	.....	Liquid chromatography / mass spectrometry
LOD	.....	Limit of detection
Mb	.....	Myoglobin
MWCNT	.....	Multi-walled carbon nano-tube
ND	.....	Nano-diamond
NPs	.....	Nanoparticles
NPV	.....	Normal pulse voltammetry
OHP	.....	Outer Helmoltz plane
PVP	.....	Poly(N-vinylpyrrolidone)
R^2	.....	Coefficient of determination
RDE	.....	Rotating disk electrode
RE	.....	Reference electrode
rmp	.....	Rounds per min
RSD	.....	Relative standard deviation
SDS	.....	Sodium dodecyl sulphate
SEM	.....	Scanning electron microscopy
SEP	.....	Standard electrode potential
SWCNT	.....	Single-walled carbon nano-tube
UHV	.....	Ultra-high vacuum

List of Figures

List of Tables

List of Tables

Chapter 1 Introduction

1.1 Carbon materials

Carbon materials (CMs) have been attracting increasing interest in past decades due to its high surface area, chemical stability, high electrical conductivity, low cost and versatile forms such as powders, fibres, composites, monoliths and tubes.[1] They are well-known for their structural applications, which relate to aerospace structures, aircraft brakes, concrete structures and lubrication. They are also broadly used in thermal, environmental, biomedical and electrical applications.[2]

The great versatility of CMs arises from the strong dependence of the physical properties on the ratio of bonding configurations, sp^2 and sp^3, and generally falls into three categories based on the structure: graphite, diamond and amorphous carbon.[1,3] Graphite is the allotrope of carbon with mainly sp^2 bonding while diamond has sp^3 bonding. The unit cells of graphite and diamond are shown in **Figure 1.1**. Amorphous carbon contains both sp^2 and sp^3 bonding in varying ratios. **Table 1.1** gives the values of some key physical properties of the industrial standard products based on these materials, *i.e.* graphitic carbon (graphene as representative), diamond (single crystal diamond as representative) and amorphous carbon (carbon black as representative). These numbers may vary from different forms of each carbon material, highly depending on the morphology, particle size, sp^2 and sp^3 bonding and hydrogenated and oxygenated functional groups on the surface, and others.[4]

a b

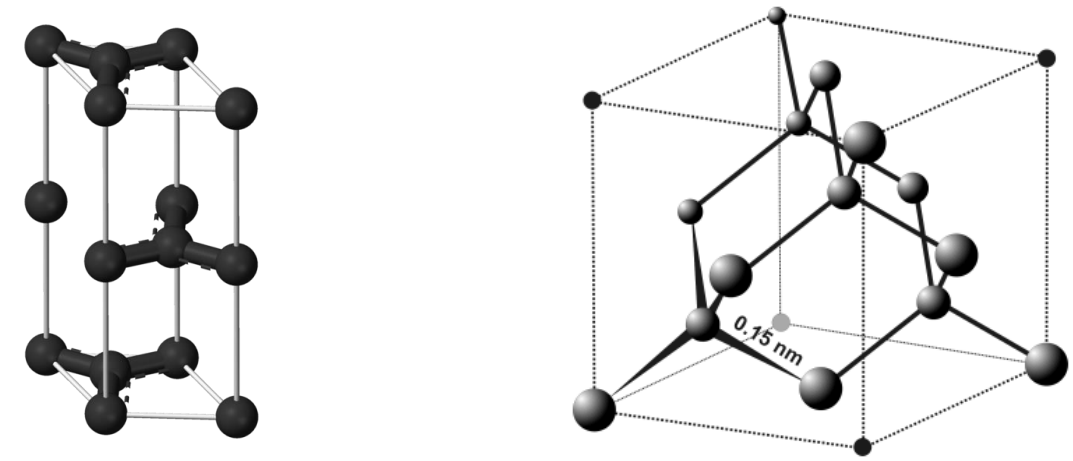

Figure 1.1 The unit cell of (a) graphite and (b) diamond[5]

Table 1.1 Key physical properties of graphite, diamond and amorphous carbon, data obtained from references[2,4-10]

	Graphite	Diamond	Amorphous carbon
Density (g cm^{-3})	2.267	3.515	1.4-1.8
Hardness (kg mm^{-2})	800-1200	10000	20-50
Optical gap (eV)	-0.04	5.5	1.5-4
Surface area (m^2 g^{-1})	275	270-280	806
Resistivity (Ω cm)	<0.05	>10	10-1000
Thermal conductivity (10^3 W m^{-1} K^{-1})	4.8-5.3	1-2	0.2-0.4

1.1.1 Graphitic carbon materials: graphene, carbon nano-tube

Graphite was named by Araham Gottlob Werner in 1789 from ancient Greek ‘to draw/write’, for its use in pencils, where it was commonly called lead. The sp^2 bonding structure of graphite leads to special properties and generates huge interest in the potential applications such as future generation of high-speed and radio frequency logic

devices, thermally and electrically conductive reinforced composites, sensors, and electrode for displays and solar cells.[11] Graphitic carbon materials include fullenrence, graphene (GP), carbon nanotube (CNT) and carbon fibre. Molecular structures of some graphitic materials are shown in **Figure 1.2**. Graphene, a single layer of graphite, was originally prepared by Geim and co-workers at Manchester University in 2004. [12,13] In general, suspensions of GP can contain up to five layers, in its reduced and oxidised forms of graphene and graphene oxide.[1] CNT is another class of graphitic material, which can be seen as a single GP sheet rolled on itself to form a tube.[1] It was reported that the performance of GP (mostly graphene oxide or multilayer graphene) was generally equal to, or substantially better than, the sensors made with single walled carbon nanotube, of which one explanation is that GP has better thermal conductivity and a higher concentration of edge and surface defects available for electrochemical reactions.[14,15] Meanwhile graphene also has some disadvantages because it is heterogeneous in nature and highly sensitive to the number of layers, the type of substrates and structure impurities.[15] Due to the difficulty of reliably producing high quality samples, especially in any scalable fashion, widespread implementation of GP has yet to occur, despite the intense interest and continuing experimental success. [15]

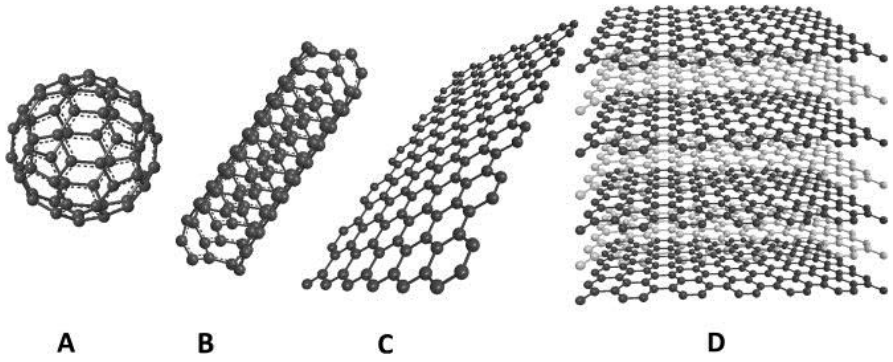

Figure 1.2 Forms of sp^2-bonded carbon: (a) Fullerence, (b) Single walled carbon nanotubes, (c) Graphene, (d) graphite[16]

1.1.2 Diamond-like carbon materials: boron-doped diamond and nano-diamond

Diamond is an allotrope of carbon with a cubic lattice connected by sp^3 bonds. Owing to its strong giant covalent bonding, diamond is the hardest naturally occurring materials known, deriving from the Greek *αδαμασ (*'unbreakable', 'unalterable'). It has been treasured as gemstone for almost 4000 years since being discovered in the river Penner, Krishna and Godavari. After large diamond deposits were discovered in South Africa in the 19th Century, diamond started to be used in engineering and electronic applications. In order to obtain high quality diamond, there have been abundant attempts to synthesise it artificially such as using high-pressure high temperature technique. [17] Since the 1980s, diamond has been successfully grown under low pressure by various methods of chemical vapour deposition (CVD), and soon became commercialised.[18,19] The success of diamond synthesis allows scientists to comprehensively exploit its outstanding physical and chemical properties such as extreme mechanical hardness, high room temperature thermal conductivity and electrochemical resistivity, high resistance to chemical corrosion, broad band transparency and high biological compatibility. This enables broad applications in abrasives, thermal management, electronic devices, optical devices, among others. [20]

Although diamond is an extremely efficient thermal conductor, most diamond materials are electrical insulators. In order to implement the applications in electrochemistry, boron is heavily doped in the CVD diamond to readily implant semi-metal electrical properties, combining the well-recognised properties of diamond such as mechanical stability, chemical inertness and optical features.[22] This boron-doped diamond (BDD) opens a new window for electrochemistry to work under extreme conditions such as

high anodic potential, chemically aggressive media, laser activation and fast mass transport. [21,22]

It was reported that diamond is far more chemically active in the form of nanoparticles, nano-diamond (ND), than it is in the bulk.[23,24] The detonation ND is formed from a detonation of an oxygen-deficient explosive mixture of TNT/RDX in a closed chamber. A schematic of the ND structure is shown in **Figure 1.3**. ND consists of an ordered diamond lattice core, surrounded by a shell of non-crystalline solid with a mixture of sp^2 and sp^3 bonding. Although the exact nature of the outer layer remains unclear, it is known that most surface carbon atoms are terminated with oxygen moieties, such as hydroxyl and carbonyl, as confirmed by Fourier transform infrared spectroscopy.[23,25] It should be noted that the dry powder of ND is a non-conductor. However, when a thin layer of ND was drop-coated onto a graphite electrode, a significant enhancement in redox response was observed.[23] Although the exact mechanism for the electron transfer remains to be elucidated, it can be attributed to electron injection into unoccupied surface states, as a consequence of unsaturated bonding in the surface layer of the ND. This was further demonstrated by the reports of the use of ND in both catalytic and electrochemical applications. [23,24]

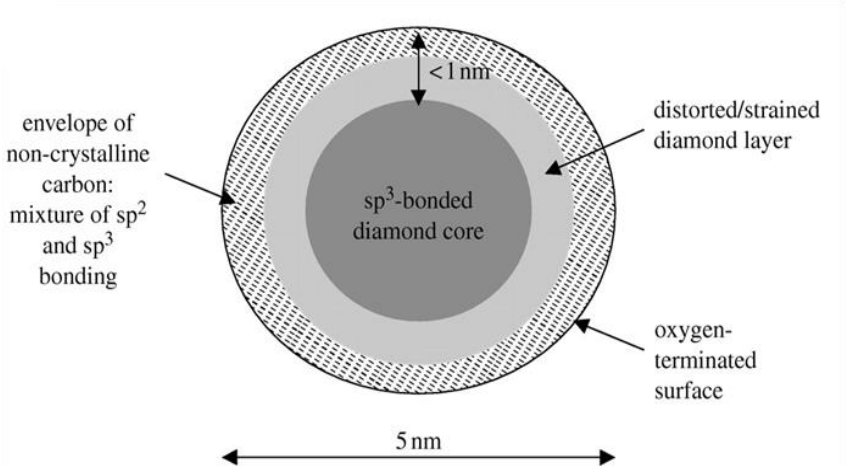

Figure 1.3 Schematic of a tentative model for a structure of 5 nm detonation ND.[23,25]

1.1.3 Amorphous carbon materials, carbon black

Amorphous carbon is a reactive form of carbon that has no crystalline structure, but is composed of mixed sp^3 and sp^2 bonding. [4,26,27] Conventional amorphous carbon such as activated carbon and carbon black (CB), is synthesised by pyrolysis and physical or chemical activation of organic precursors, such as coal, wood, fruit shell or polymers at elevated temperatures.[28,29] Due to properties including the large surface area, good electric conductivity, large thermal conductivity, high chemical stability and low density (40% to 60% of diamond density[27]), amorphous carbon materials are used extensively as electrode materials and additives for batteries, fuel cells and super-capacitors; as sorbents for separation processes and gas storage; and as supports for many important catalytic processes. [29] CB is one of the most important forms of amorphous carbon, of which TEM image is shown in **Figure 1.4**. [30] The surface properties of carbon blacks are influenced to a large extent by the foreign elements adsorbed on the surface, in particular by oxygenated groups.[4]

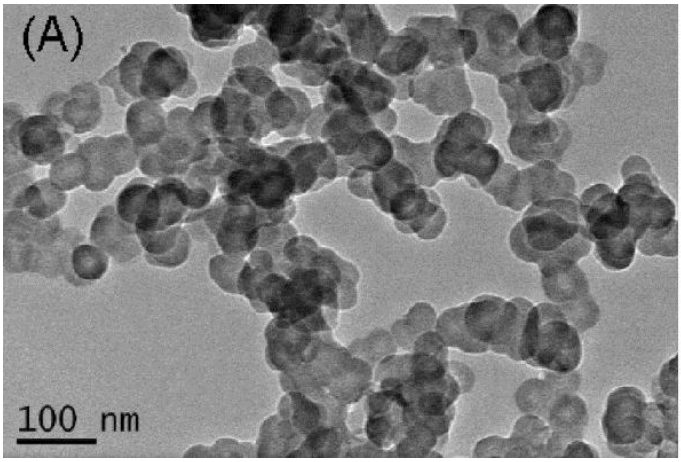

Figure 1.4 TEM image of carbon black nanoparticles[30]

1.2 Carbon materials in electrochemistry

CMs are widely used in electrochemistry because they combine unique properties: good electrical conductivity, remarkable corrosion resistance, high purity, low cost, high thermal conductivity, mechanical stability, light weight, diverse of physical structures and versatile in its surface chemistry.[31] In past decades, along with the abundant discoveries and rapid development of CMs, there have been increasing investigations to utilise CMs in the fields of electrical conduction, electromagnetic reflection, heating, thermal electricity, sensing, electrodes and so on.[2] Some important applications of CMs in electrochemistry are introduced as follows.

1.2.1 Electrically conductive additive

Due to the fact that some desired electrode materials are not adequately conductive, a conductive additive is required to form the functional electrode.[2, 32] Some CMs are capable to act as a conductive additive because of the chemical inertness and electrical conductivity. Graphene oxides, mesoporous carbon and CNT have all been exploited for this purpose, among which, carbon black is particularly common. One example is the

manganese dioxide (MnO_2) cathode where CB is added to improve the conductivity of the composite electrode, enhance the ability of the electrode to adsorb and hold electrolyte and provide compressibility and elasticity for the electrode. [33,34] This electrode is widely used in the Li/MnO_2 primary cell.[2,33] In lithium/sulfur batteries, since the elemental sulfur has inadequate electronic conductivity, the use of conductive carbons with high surface area and porosity is essential to achieve good utilisation of sulfur in positive electrodes. [35]

1.2.2 Current collectors

Current collectors are used in electrochemical cells (batteries and fuel cells), which require materials that are electrically conductive, and in some cases in electrochemical cells chemical resistance is also required. One problem for typical metal electrodes is that metals tend to have an oxide coating, and degrade gradually with time in air as the oxide often has relatively poor electrical conductivity.[2] CMs are superior to many metal conductors in terms of the fact that CMs have fewer oxides on it although they are not as conductive as metals. The current collector of the lithium/thionyl chloride (Li/$SOCl_2$) cell conventionally uses carbon black, which need a Teflon binder. [35] In electrical contacts, graphite flakes have been considered to be an ideal replacement for silver particles though the conductivity attained by graphite flakes is lower. In addition, the cost of CMs is normally much lower than the novel metal counterparts.

1.2.3 Electrodes

Carbon based electrode materials are well established and have been used in varied electrochemical technologies from electro-analysis to energy storage. Malakhova and Brainina summarised some attractive features of carbon electrode as follows. [36] First, depending on the type of carbon material, the conductivity of the electrode can change

from metal to semi-conductor. Second, the carbon surface can adsorb a variety of compounds by both physical and chemical sorption, yielding a functional coating and CMs can also form strong covalent bonds with some surface modifiers. The complexingg capacity of CMs is also higher than that of metals. Finally, a carbon surface is electrochemically inert over a wide interval of potentials. All these features predetermine the use of diverse CMs.

The traditional carbon electrodes are mainly based upon graphitic bonding schemes, among which the glassy carbon electrode (GCE) is the most popular one. GCE exhibits a low oxidation rate, suggesting a great inertness to chemical attack. The possible anodic potential range of GCE was reported to be wider than most other electrode materials, including most metals and semiconductors. [37,38] GCE was first reported by Yamada and Sato in 1962[39], and then introduced by Zittle and Miller in 1965 to the applications in electo-analytical chemistry. [40] Since then, GCE have been widely used commercially in voltammetry, stripping voltammetry, amperometry, coulometry, potensiometry, combining with vast modifiers including metal nanoparticles, carbon materials, enzymes, and polymers.[38,41-49] According to the statistics from 1990 to 2005, GCE was the first with respect to the number of papers published. [36]

Since first reported in 1987[50], the CVD boron doped diamond electrode (BDDE), has generated great interest in electrochemical applications and been comprehensively studied. In comparison to GCE, BDDE shows a low background current (an order of magnitude less), resistance to fouling and a wider potential window.[51-56] Unlike glassy carbon and other alike electrodes, diamond shows higher reproducibility without any essential regenerative treatment.[57] Moreover, diamond presents low adsorption of contaminating species and thereby appears more resistant against surface fouling. These

properties establish BDDE as a material of choice for electrochemical mineralisation in polluted water treatment, electro-analysis in the environment, food industry and pharmaceutical industry.[58] Among these, the applications in electro-analysis are of particular interest. There is an increase in publications of BDDE for the direct electrochemical detection of metal ions[59], chemical compounds[60] and biological compounds[60]. It also can be used as substrate to electro-deposit metallic NPs and metal oxide NPs, such as Pt, Ag, TiO_2, to exploit higher catalytic activity of such particles with smaller concentration compared to conventional bulk material.[61-67] In order to impart the catalytic activity and selectivity, various enzymes and catalysts are also bound to the BDD surface, such as tyrosinase[68], horseradish peroxidas[69] and cobalt phthalocyanine[70]. So far, the highly boron-doped diamond based electrode has been widely used for the detection of metal ions[46], inorganic compounds[71], organic compounds[72] and biochemical compounds.[60]

1.2.4 Electrode modifiers

To impart new functional chemistry and combine the benefits of different materials, such as transition metal complexes, metal nanoparticles and enzymes, electrode modification attracts endless enthusiasm. Hundreds of electrode modifiers have been reported to be immobilised on various electrodes by different methods including covalent binding, direct adsorption and physical coating with a matrix. The electrode modifiers include but are not limited to metal nanoparticles, polymer particles, bio/organic-compounds, non-metal nanoparticles and their combinations. Ideal modified electrode should possess most of the following characteristics[73]: strong mechanical and chemical stability; good short-term reproducibility and long-term stability of activity; a wide dynamic range (ideally linear) of response; low and stable background current;

good compatibility to the environment in use; conventional and reproducible fabrication; high selectivity; good catalytic activity if applicable. With the advantages as mentioned previously, CMs have become one of the most promising electrode modifiers. In this work GP, ND and CB were focused on, representing graphitic, diamond like, amorphous carbon respectively. These modifiers are all relatively new to sensing applications in comparison to other CM counterparts like CNTs. Therefore, more investigations are needed.

Most of the GP-based sensors reported so far employed graphene oxide (and its derivatives), or multilayer GP.[15] The high proportion of work with these forms of GP is likely to continue in the future because departures from 'ideal' GP obviously offer increased scope for tailoring properties when designing biosensors. [15] Pumera *et al.* highlighted important applications of GP in sensing and bio-sensing in three parts.[16] One was using graphene powder or graphene-composite as a transducer to modified electrodes for electrochemical sensing directly.[74] Another one is to incorporate bio-recognition compounds for biosensing.[75] The last is to deposit catalytic nanoparticles onto the conducting GP surface for consequent electrochemical sensing.[76] Some specific applications were also studied. Ohno *et al*.[77] investigated electrolyte-gated graphene field-effect transistors as high sensitive electrical sensors for detecting pH and biomolecule concentrations. An ionic liquid-functionalised graphene was used to detect nicotinamide adenine dinucleotide and ethanol.[78]

The detonation ND modified electrode was fabricated by Novoselova *et al.* in 2004[79], where the reduction and oxidation peaks of ferricyanide were observed. Since then, ND was applied in electro-analysis to detect various species, such as haemoglobin[43],

epinephrine[80] and glucose[81]. However, there are few investigations of using ND in electro-chemistry.

The most important interest in CB is its strong adsorption properties which are highly dependent on the surface chemical composition and morphology, together with other advantages such as good conductivity and low cost.[31] Although it is widely used in energy storage, fuel cell and construct sensors for analysing detection in gaseous phases[31], until 2011, few applications have been reported for using CB sensors in solution.[82] Very recently, there is increasing interest to investigate CB as electrode modifiers for electrochemical detection propose.[83-86] CB modified screen-printed electrodes were used as a H_2O_2 detector by Arduini *et al*.[82] Compton and co-workers reported the advantageous use of CB as a much cheaper alternative to multi-walled carbon nano-tubes for the determination of nicotine.[85] The response was improved with a CB modified electrode as a result of a significantly lower background current and a larger faradaic current. It was also reported that CB can be used to couple laccase to form a disposable BPA biosensor.[86] All the research shows that CB is a promising electrode modifier for highly sensitive and disposable sensors.

1.3 Aims and scope of the thesis

This thesis aims to investigate electrochemical applications of CMs as electrodes (GCE and BDDE) and electrode modifiers (GP, ND and CB) for electrochemical analysis (Chapter 3, 5, 6 and 7) and electro-synthesis (Chapter 4). This study distinguishes the different features of varying CMs. The combination of CM with enzymes was also explored to extend their use where certain conditions are required, such as milder detection potential and specific catalysis.

Chapter 1

Chapter 1 introduces the physical and electrochemical properties of three categories of carbon materials, *i.e.* graphite, diamond and amorphous carbon. The representative materials in each category are detailed including graphene and carbon nano-tube for graphitic carbon, boron-doped diamond and nano-diamond for diamond like carbon, and carbon black for amorphous carbon. The broad applications of CMs in electrochemistry are also introduced.

Chapter 2 introduces the experimental theories and techniques used in this work. It explains the fundamental principles and methodologies of electrochemistry. Characterisation techniques and instruments are briefly described, including XPS, SEM, DLS, UV-vis and XRD.

Chapter 3 aims to explore the combination of Hb molecule and silver nanoparticles on BDDE substrate for the H_2O_2 determination. This sensor provides a detection limit down to micro-molar level, a wide detection range up to 20 mM and a less negative potential of -0.2 V, which is highly competitive to other H_2O_2 sensors. It is also imparted with other advantages such as high stability, reproducibility and outstanding resistance to main interference.

Chapter 4 explores a new novel electrochemical synthesis of silver nanorparticles in aqueous phase approach by using Hb-BDDE as working electrode, $AgNO_3$ as silver resource and PVP as stabiliser. By this method, monodispersed Ag samples with a size around 10nm diameter are produced at a yield of around 50%.

Chapter 5 investigates the application of bare GCE, ND-GCE, GP-GCE and CB-GCE to determine phenol compounds, HQ and DHB, which are also determined simultaneously at GP-GCE and CB-GCE. After further modification by tyrosine, tyr/GP-GCE and tyr/CB-GCE are used to detect phenol and p-cresol. The main

conclusion is that state-of-the-art or beyond state-of-the-art performance can be obtained using the cheap and simple electrode modifier CB, compared to the expensive or complicated modifiers which are currently in use.

Chapter 6 develops an indirect determination of BPA for the first time at the disposable CB-GCE due to the strong adsorption properties and the high sensitivity of CB materials. In this method, the detection potential is about +0.4 V lower than at other sensors and the detection limit and sensitivity are both improved. ND-GCE is also used to detect BPA by direct oxidation, which can restrict the fouling from electropolymerised film of BPA. The noise and background current response at ND-GCE is small, leading to a large signal/noise ratio and low detection limit.

Chapter 7 extends the application of CB-GCE toward the determination of DA, both directly and indirectly. A high sensitivity and low detection limit down to 10^{-7} M are obtained.

References

(1) Zhai, Y.; Dou, Y.; Zhao, D.; Fulvio, P. F.; Mayes, R. T.; Dai, S. *Adv. Mater.* **2011**, *23*, 4828.

(2) Chung, D. D. L. *Journal of Materials Science* **2004**, *39*, 2645.

(3) Ferrari, A.; Robertson, J. *Physical review B* **2000**, *61*, 14095.

(4) Boehm, H. *Carbon* **1994**, *32*, 759.

(5) http://en.wikipedia.org/wiki/Graphite.

(6) Robertson, J. *Advances in Physics* **1986**, *35*, 317.

(7) Smith, W.; Thornhill, F.; Bray, R. *Industrial & Engineering Chemistry* **1941**, *33*, 1303.

(8) Chen, S.; Wu, Q.; Mishra, C.; Kang, J.; Zhang, H.; Cho, K.; Cai, W.; Balandin, A. A.; Ruoff, R. S. *Nature materials* **2012**, *11*, 203.

(9) Cheianov, V. V.; Fal'ko, V. I. *Physical Review Letters* **2006**, *97*, 226801.

(10) Murali, R.; Brenner, K.; Yang, Y.; Beck, T.; Meindl, J. D. *Electron Device Letters, IEEE* **2009**, *30*, 611.

(11) Allen, M. J.; Tung, V. C.; Kaner, R. B. *Chem. Rev.* **2009**, *110*, 132.

(12) Novoselov, K. S.; Geim, A. K.; Morozov, S.; Jiang, D.; Zhang, Y.; Dubonos, S.; Grigorieva, I.; Firsov, A. *Science* **2004**, *306*, 666.

(13) Novoselov, K.; Geim, A. K.; Morozov, S.; Jiang, D.; Katsnelson, M.; Grigorieva, I.; Dubonos, S.; Firsov, A. *nature* **2005**, *438*, 197.

(14) Shahil, K. M. F. *Nano Letters* **2012**, *12*, 861.

(15) Yang, W.; Ratinac, K. R.; Ringer, S. P.; Thordarson, P.; Gooding, J. J.; Braet, F. *Angew. Chem.-Int. Edit.* **2010**, *49*, 2114.

(16) Pumera, M.; Ambrosi, A.; Bonanni, A.; Chng, E. L. K.; Poh, H. L. *TrAC Trends in Analytical Chemistry* **2010**, *29*, 954.

(17) Yule, G. U. *Philosophical Transactions of the Royal Society of London. Series A, Containing Papers of a Mathematical or Physical Character* **1927**, *226*, 267.

(18) Matsumoto, S.; Sato, Y.; Tsutsumi, M.; Setaka, N. *Journal of Materials Science* **1982**, *17*, 3106.

(19) Kamo, M.; Sato, Y.; Matsumoto, S.; Setaka, N. *Journal of Crystal Growth* **1983**, *62*, 642.

(20) Field, J. E. *The properties of natural and synthetic diamond*; Academic Press London, 1992.

(21) Compton, R. G.; Foord, J. S.; Marken, F. *Electroanalysis* **2003**, *15*, 1349.

(22) Montilla, F.; Michaud, P.; Morallon, E.; Vazquez, J.; Comninellis, C. *Electrochimica Acta* **2002**, *47*, 3509.

(23) Holt, K. B. *Philosophical Transactions of the Royal Society A: Mathematical, Physical and Engineering Sciences* **2007**, *365*, 2845.

(24) Mochalin, V. N.; Shenderova, O.; Ho, D.; Gogotsi, Y. *Nature Nanotechnology* **2012**, *7*, 11.

(25) Palosz, B.; Pantea, C.; Grzanka, E.; Stelmakh, S.; Proffen, T.; Zerda, T.; Palosz, W. *Diamond and Related Materials* **2006**, *15*, 1813.

(26) Koelmans, A. A.; Jonker, M. T. O.; Cornelissen, G.; Bucheli, T. D.; Van Noort, P. C. M.; Gustafsson, O. *Chemosphere* **2006**, *63*, 365.

(27) Tersoff, J. *Physical Review Letters* **1988**, *61*, 2879.

(28) Yang, R. T. *Adsorbents: fundamentals and applications*; John Wiley & Sons, 2003.

(29) Liang, C.; Li, Z.; Dai, S. *Angewandte Chemie International Edition* **2008**, *47*, 3696.

(30) Guo, B.; Zebda, R.; Drake, S. J.; Sayes, C. M. *Particle and fibre toxicology* **2009**, *6*, 4.

(31) Donnet, J.-B. *Carbon black: science and technology*; CRC Press, 1993.

(32) Kohler, D.; Zabasajja, J.; Krishnagopalan, A.; Tatarchuk, B. *Journal of the Electrochemical Society* **1990**, *137*, 136.

(33) Frysz, C. A.; Shui, X.; Chung, D. *Journal of power sources* **1996**, *58*, 41.

(34) Sanchez-Gonzalez, J.; Macias-Garcia, A.; Alexandre-Franco, M.; Gomez-Serrano, V. *Carbon* **2005**, *43*, 741.

(35) Song, M.-K.; Cairns, E. J.; Zhang, Y. *Nanoscale* **2013**, *5*, 2186.

(36) Stozhko, N. Y.; Malakhova, N. A.; Fyodorov, M. V.; Brainina, K. Z. *Journal of Solid State Electrochemistry* **2008**, *12*, 1185.

(37) Alder, J.; Fleet, B.; Kane, P. *Journal of Electroanalytical Chemistry and Interfacial Electrochemistry* **1971**, *30*, 427.

(38) Van der Linden, W.; Dieker, J. W. *Analytica Chimica Acta* **1980**, *119*, 1.

(39) Yamada, S.; Sato, H. *Nature* **1962**, *193*, 261.

(40) Zittel, H.; Miller, F. *Analytical Chemistry* **1965**, *37*, 200.

(41) Wu, C.; Yu, S.; Lin, B.; Cheng, Q.; Wu, K. *Analytical Methods* **2012**, *4*, 2715.

(42) Ahammad, A. J. S.; Sarker, S.; Rahman, M. A.; Lee, J. J. *Electroanalysis* **2010**, *22*, 694.

(43) Zhu, J.-T.; Shi, C.-G.; Xu, J.-J.; Chen, H.-Y. *Bioelectrochemistry* **2007**, *71*, 243.

(44) Yao, H.; Sun, Y. Y.; Lin, X. H.; Tang, Y. H.; Huang, L. Y. *Electrochimica Acta* **2007**, *52*, 6165.

(45) Zhao, S.; Zhang, K.; Sun, Y. Y.; Sun, C. Q. *Bioelectrochemistry* **2006**, *69*, 10.

(46) McGaw, E. A.; Swain, G. M. *Analytica chimica acta* **2006**, *575*, 180.

(47) Jin, G. P.; Lin, X. Q.; Gong, J. M. *Journal of Electroanalytical Chemistry* **2004**, *569*, 135.

(48) Mathiyarasu, J.; Joseph, J.; Phani, K. L. N.; Yegnaraman, V. *Indian Journal of Chemical Technology* **2004**, *11*, 797.

(49) Zhao, H.; Zhang, Y. Z.; Yuan, Z. B. *Analytica Chimica Acta* **2001**, *441*, 117.

(50) Pelskov, Y. V.; Sakharova, A. Y.; Krotova, M.; Bouilov, L.; Spitsyn, B. *Journal of Electroanalytical Chemistry and Interfacial Electrochemistry* **1987**, *228*, 19.

(51) Nekrassova, O.; Lawrence, N. S.; Compton, R. G. *Analyst* **2004**, *129*, 804.

(52) Simm, A. O.; Banks, C. E.; Ward-Jones, S.; Davies, T. J.; Lawrence, N. S.; Jones, T. G. J.; Jiang, L.; Compton, R. G. *Analyst* **2005**, *130*, 1303.

(53) Tenne, R.; Patel, K.; Hashimoto, K.; Fujishima, A. *Journal of Electroanalytical Chemistry* **1993**, *347*, 409.

(54) Compton, R.; Goeting, C.; McKeown, R. J.; Foord, J. *Chem. Commun.* **1998**, 1961.

(55) Rao, T.; Fujishima, A. *Diamond and Related Materials* **2000**, *9*, 384.

(56) Fujishima, A. *Diamond electrochemistry*; Elsevier, 2005.

(57) Pleskov, Y. V. *Russian Journal of Electrochemistry* **2002**, *38*, 1275.

(58) Banks, C. E.; Hyde, M. E.; Tomčík, P.; Jacobs, R.; Compton, R. G. *Talanta* **2004**, *62*, 279.

(59) Iniesta, J.; Michaud, P. A.; Panizza, M.; Cerisola, G.; Aldaz, A.; Comninellis, C. *Electrochimica Acta* **2001**, *46*, 3573.

(60) Zhang, J. D.; Oyama, M. *Microchem J.* **2004**, *78*, 217.

(61) Wei, M.; Liu, Y.; Gu, Z.-Z.; Liu, Z.-D. *Journal of the Chinese Chemical Society* **2011**, *58*, 516.

(62) Gao, J.-S.; Arunagiri, T.; Chen, J.-J.; Goodwill, P.; Chyan, O.; Perez, J.; Golden, D. *Chemistry of materials* **2000**, *12*, 3495.

(63) McKenzie, K. J.; Asogan, D.; Marken, F. *Electrochemistry communications* **2002**, *4*, 820.

(64) McKenzie, K. J.; Marken, F. *Electrochemical and solid-state letters* **2002**, *5*, E47.

(65) Chatterjee, A.; Foord, J. *Diamond and related materials* **2006**, *15*, 664.

(66) Hyde, M.; Saterlay, A. J.; Wilkins, S. J.; Foord, J. S.; Compton, R. G.; Marken, F. *Journal of Solid State Electrochemistry* **2002**, *6*, 183.

(67) Attard, G. A.; Ahmadi, A.; Jenkins, D. J.; Hazzazi, O. A.; Wells, P. B.; Griffin, K. G.; Johnston, P.; Gillies, J. E. *ChemPhysChem* **2003**, *4*, 123.

(68) Notsu, H.; Tatsuma, T.; Fujishima, A. *Journal of Electroanalytical Chemistry* **2002**, *523*, 86.

(69) Wang, Q.; Kromka, A.; Houdkova, J.; Babchenko, O.; Rezek, B.; Li, M. S.; Boukherroub, R.; Szunerits, S. *Langmuir* **2012**, *28*, 587.

(70) Kondo, T.; Tamura, A.; Kawai, T. *Journal of the Electrochemical Society* **2009**, *156*, F145.

(71) Welch, C. M.; Hyde, M. E.; Banks, C. E.; Compton, R. G. *Analytical Sciences* **2005**, *21*, 1421.

(72) Weiss, E.; Groenen-Serrano, K.; Savall, A. *Journal of Applied Electrochemistry* **2008**, *38*, 329.

(73) Baldwin, R. P.; Thomsen, K. N. *Talanta* **1991**, *38*, 1.

(74) Kim, Y.-R.; Bong, S.; Kang, Y.-J.; Yang, Y.; Mahajan, R. K.; Kim, J. S.; Kim, H. *Biosensors and Bioelectronics* **2010**, *25*, 2366.

(75) Mao, S.; Lu, G.; Yu, K.; Bo, Z.; Chen, J. *Adv. Mater.* **2010**, *22*, 3521.

(76) Baby, T. T.; Aravind, S.; Arockiadoss, T.; Rakhi, R.; Ramaprabhu, S. *Sensors and Actuators B: Chemical* **2010**, *145*, 71.

(77) Ohno, Y.; Maehashi, K.; Yamashiro, Y.; Matsumoto, K. *Nano Letters* **2009**, *9*, 3318.

(78) Shan, C.; Yang, H.; Han, D.; Zhang, Q.; Ivaska, A.; Niu, L. *Biosensors and Bioelectronics* **2010**, *25*, 1504.

(79) Novoselova, I.; Fedoryshena, E.; Panov, E.; Bochechka, A.; Romanko, L. *Physics of the Solid State* **2004**, *46*, 748.

(80) Shahrokhian, S.; Khafaji, M. *Electrochimica Acta* **2010**, *55*, 9090.

(81) Zhao, W.; Xu, J.-J.; Qiu, Q.-Q.; Chen, H.-Y. *Biosensors and Bioelectronics* **2006**, *22*, 649.

(82) Arduini, F. *Electroanalysis* **2012**.

(83) Panchompoo, J.; Aldous, L.; Downing, C.; Crossley, A.; Compton, R. G. *Electroanalysis* **2011**, *23*, 1568.

(84) Lee, P.; Ward, K.; Tschulik, K.; Chapman, G.; Compton, R. *Electroanalysis* **2013**.

(85) Lo, T. W.; Aldous, L.; Compton, R. G. *Sensors and Actuators B: Chemical* **2012**, *162*, 361.

(86) Portaccio, M.; Di Tuoro, D.; Arduini, F.; Moscone, D.; Cammarota, M.; Mita, D.; Lepore, M. *Electrochimica Acta* **2013**, *109*, 340.

Chapter 2 Experimental Theories and Techniques

2.1 Electrochemistry and Electroanalysis

2.1.1 Introduction

Electrochemistry is a branch of chemistry that studies chemical reactions which take place at the interface of an electronic conductor (the electrode, a metal or a semiconductor) and an ionic conductor (the electrolyte), typically a solution phase. These reactions involve electron transfer between the electrode and the electrolyte resulting in reduction or oxidation of the species in solution. Electroanalysis can be defined as the application of electrochemistry to solve real-life analytical problems. Traditionally, electroanalysis is associated with the identification and measurement of amounts (concentrations) of chemical species, often using sophisticated instrumental methods. Electroanalysis offers a number of important potential benefits[1]: (a) high selectivity resulting from the choice of electrode material; (b) high sensitivity and low detection limit; (c) possibility of giving results in real time, or close to real time, particularly in flow systems for on-line monitoring; (d) application, as miniaturised sensors, in situations where other sensors may not be usable.

2.1.2 Equilibrium Electrochemistry

2.1.2.1 Electrochemical equilibrium

Electrochemistry is the study of phenomena associated with charge separation at electrode-electrolyte interfaces. The processes are thus heterogeneous in nature and can either be in equilibrium at the interface, or under partial or total kinetic control.[1] The

charge transfer processes can be represented in the simplest case of the oxidised species, O, and the reduced species, R, both soluble in solution, by

$$O + ne^- \rightleftharpoons R \qquad \text{Equation 2.1}$$

where O receives n electrons in order to be transformed into R.[1] One example is an electrochemical equilibrium established by dissolving both $K_4Fe(CN)_6$, and $K_3Fe(CN)_6$ in the solution with an immersed wire (an 'electrode') made of platinum or other inert metals, as shown in **Figure 2.1**. The electrochemical equilibrium is eventually established as follows,

$$Fe(CN)_6^{3-}(aq) + e^- \rightleftharpoons Fe(CN)_6^{4-}(aq) \qquad \text{Equation 2.2}$$

The equilibrium in Equation 2.2 involves the two dissolved anions and the electrons in the metal electrode. The establishment of equilibrium implies that the rate at which $Fe(CN)_6^{4-}$ gives electrons to the metal wire or 'electrode' is exactly balanced by the rate at which electrons are released by the wire to the $Fe(CN)_6^{3-}$ anions, which are said to be 'reduced'.[2] Correspondingly, the $Fe(CN)_6^{4-}$ ions losing electrons are said to be 'oxidised'. [2]

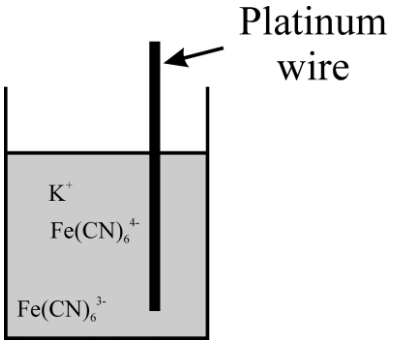

Figure 2.1 A platinum wire immersed into an aqueous solution containing both $K_4Fe(CN)_6$, and $K_3Fe(CN)_6$.[2]

The pertinent energy levels are shown in **Figure 2.2**.[2] The electronic structure of a metal involves electronic conduction 'bands' where the electrons are free to move throughout the solid, binding the (metal) cations rigidly together. The energy levels in

these bands form an effective continuum of levels which are filled up to an energy maximum known as the Fermi level. In contrast, the electronic energy levels associated with the solution phase $Fe(CN)_6^{3-}$ and $Fe(CN)_6^{4-}$ ions are discrete and relate to an unfilled molecular orbital in $Fe(CN)_6^{3-}$, which gains an electron to form $Fe(CN)_6^{4-}$. **Figure 2.2** shows that before electron transfer takes place between the electrode and the solution, the Fermi level is higher than the vacant orbital in the $Fe(CN)_6^{3-}$ ion. It is accordingly energetically favourable for electrons to leave the Fermi level and join the orbital in $Fe(CN)_6^{3-}$ species converting them to $Fe(CN)_6^{4-}$ ions. This energy difference is the driving force of the electron transfer. As this electron transfer proceeds, positive charge must build up on the electrode (metal) and the corresponding negative charge in the solution phase. Accordingly, the electronic energy in the metal must be lowered and so the Fermi level becomes progressively lower in the diagram, as shown in **Figure 2.2**. Correspondingly, the generation of negative charge in the solution must raise the electronic energy levels of the solution phase species. Ultimately, a status is reached when the Fermi level lies in between the energy levels of the two ions, so that the rate at which electrons leave the electrode and reduce $Fe(CN)_6^{3-}$ is exactly matched by the rate at which electrons join the metal from the $Fe(CN)_6^{4-}$ ions which become oxidised. This situation corresponds to dynamic equilibrium and once it is attained, no further net charge is possible. However, at the point of equilibrium, there is a charge separation between the electrode and the solution, and this is the origin of the electrode potential established on the metal.[2]

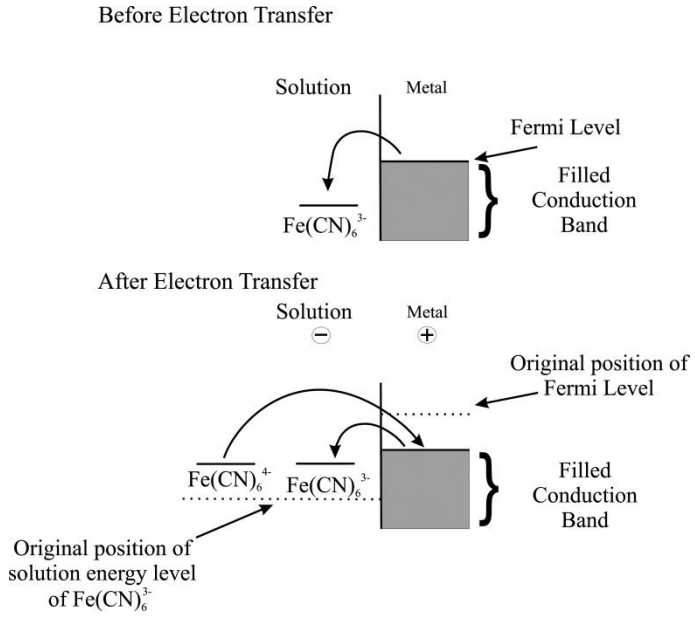

Figure 2.2 The energy of electrons in the ions in solution and in the metal wire[2]

2.1.2.2 *Nernst* equation and electrode potential

In order to predict whether a chemical reaction, as described above, is spontaneous, Josiah Willard Gibbs formulated a theory based on the free energy. The equation expresses the free energy change for a chemical reaction in the form[3]

$$\Delta G = \Delta G^0 + RT \ln \frac{\prod(\text{activities of reactants})}{\prod(\text{activities of products})} \qquad \text{Equation 2.3}$$

where ΔG is the change in *Gibbs* free energy, ΔG^0 is the change in standard *Gibbs* free energy, T is the Kelvin temperature and R is the gas constant, as 8.314 JK^{-1} mol^{-1}. Thus, for the electrode reaction shown in **Figure 2.1**, Equation 2.3 takes the form

$$\Delta G = \Delta G^0 + ln \frac{a_O}{a_R} \qquad \text{Equation 2.4}$$

Since the *Gibbs* free energy is the maximum amount of work that can be extracted from a system, the *Gibbs* free energy change of a reversible electrode reaction is related to the electrode potential[3]

$$\Delta G = -nEF \qquad \text{Equation 2.5}$$

Or, for the standard state

$$\Delta G^0 = -nE^0F \qquad \text{Equation 2.6}$$

where E is the potential, F is the *Faraday* constant, as 96485 C mol^{-1}, ΔG^0 is the standard *Gibbs* free energy change and E^0 is the standard electrode potential respectively. For a spontaneous electrochemical reaction, the change in *Gibbs* free energy should be less than zero.

Based on Gibb's work, Nernst extended the theory to include the contribution from electric potential on charged species. Substitution of Equation 2.5 and Equation 2.6 into Equation 2.4 gives the *Nernst* equation as[4]

$$E = E^0 + \frac{RT}{nF} ln \frac{a_O}{a_R} \qquad \text{Equation 2.7}$$

where E^0 is the standard electrode potential of the electrochemical reaction when all species have unit activity, R is the universal gas constant, F is the *Faraday* constant. In general the standard electrode potential (SEP) of any system ('couple' or 'half cell') is defined as the measured potential difference between the two electrodes of a cell in which all the chemical species contributing to the potential determining equilibrium at each electrode are represented at a concentration corresponding to unit activity in the case of a solution phase species, or to unit pressure in the case of a gas.[5]

In electroanalytical experiments, the most important quantity is usually the concentration of an electroactive species rather than its activity. Thus a form of *Nernst* equation in which concentration appears is often used as follows.[1]

$$E = E^{0'} + \frac{RT}{nF} ln \frac{c_O}{c_R} \qquad \text{Equation 2.8}$$

where $E^{0'}$ is called the *formal potential*. Recognising $\alpha = \gamma c$, where γ is the activity coefficient and c the concentration, it can be seen that the formal potential is defined from Equation 2.7 and 2.8 as

$$E^{0'} = E^{0} + \frac{RT}{nF} ln \frac{\gamma_O}{\gamma_R} \qquad \text{Equation 2.9}$$

2.1.2.3 Interfacial (double layer) phenomena

At the interface between any pair of conducting phases, a potential difference can generally exist whose magnitude is a function of both the composition and nature of the phases, *e.g.*, metal/electrolyte solution, metal/metal, electrolyte solution/ electrolyte solution.[3] The observed potential drop can be associated with the presence of an electrical double layer whose structure is responsible for many of the properties of a given system.[3] Electrode kinetics, to be considered in subsequent sections, are profoundly influenced by the structure of the double layer at an electrode/solution interface and it is with such systems that we shall be primarily concerned.

The model which gave rise to the term 'electrical double layer' was first put forward in the 1850's by Helmholtz, and a modern version is shown in **Figure 2.3**. Due to the chemical adsorption of charged species from solution, selective dissolution processes and the reaction of functional groups on the electrode surface, chemical forces can result in a charged layer at the solid surface in what is known as the *inner Helmholtz plane* (IHP)[1] which forms part of what is known as the *Stern layer*. Due to Coulombic interaction, solvated ions from the electrolyte can become bound to the surface in what is known as the *outer Helmoltz plane* (OHP). The net excess of charge in these planes must be equivalent to an equal and opposite charge in solution to preserve neutrality. This excess of charge is distributed over a diffuse region of the solution near the electrode surface known as the *Gouy-Chapman* layer.

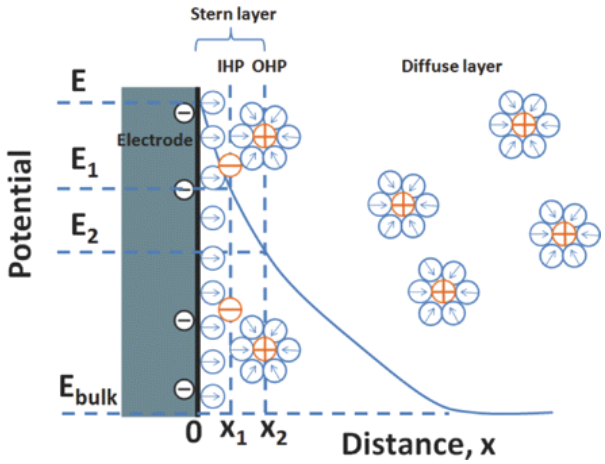

Figure 2.3 A schematic representation of the electrical double layer of a negatively charged interface[6]

The double layer acts as a capacitor so gives rise to a capacitive current if the capacitor is 'charged' for example by changing the applied potential between the solid electrode and the electrolyte.[1] As will be discussed in Chapter 5, 6 and 7, carbon black decorated electrodes usually exhibits a significantly higher background current (non-faradaic current) than other electrodes due to the high porosity and high density of electronic states. For electroanalytical measurements, the capacitive contribution is usually undesirable and various strategies are employed to reduce it, or at least reduce its influence on the measurement. [1]

2.1.2.4 Measurement of electrode potential: reference electrode

The difference in the inner potentials, of two phases (metal and solution) in contact, is a factor of primary importance to electrochemical processes at the interface between them because of its direct influence over the relative energies of charged species on either side of the interface.[4] However it is impossible to measure an absolute value for the potential drop at a single electrode/solution interface. Therefore, it is necessary to locate two electrodes in the cell. Obviously one of these will correspond to the system of interest under 'test', the so called 'working electrode'. The purpose of the second

electrode is to act as a 'reference electrode'. The cell is described by the shorthand notation:

Reference Electrode | Solution | Test electrode

where the vertical line (|) notates a boundary between two separate phases. The measured potential of the cell is given by[5]

$$\text{Measured potential} = (\phi_{test} - \phi_{solution}) - (\phi_{reference} - \phi_{solution})$$

The discussion above has introduced the idea of a reference electrode as a device which maintains a fixed value of its potential relative to the solution phase, $\phi_{reference} - \phi_{solution}$, and so facilitates potentiometric measurements of another electrode system relative to the reference electrode.[2] This requirement of a fixed value of reference electrode dictates that the reference electrode has certain special properties to ensure that this potential value does indeed stay fixed. In particular it should be very reproducible, establish equilibrium rapidly, easily set up and ideally not showing a large change of potential even a current passes through it.

The high stability of reference electrode potential is usually reached by employing a redox system with constant (buffered or saturated) concentrations of each participants of the redox reaction.[5] The common reference electrodes include (potential with respect to the standard hydrogen electrode) electrodes such as the standard hydrogen electrode (SHE, E=0.000V), saturated calomel electrode (SCE, E=+0.241 V), and silver/silver chloride electrode (Ag/AgCl, E=+0.197 V, saturated).

2.1.3 Dynamic electrochemistry

Although equilibrium electrochemistry is important, it is necessary to realise that electrochemical measurements are often of most interest when a current is being drawn through the electrochemical cell. Kinetic processes as well as equilibrium processes need to be taken into account in a general field which is often referred to as dynamic electrochemistry. The typical electrochemical process can be expressed as the scheme shown in **Figure 2.4**, which can be divided into three parts. One is the mass transfer from well-mixed bulk solution to the electrode surface where the electrochemical reaction occurs (step 1). It is mainly focused on the diffusion of electroactive species. The second part is about how the electrochemical reaction takes place, including rearrangement of the ionic atmosphere, reorientation of solvent dipoles and alterations in central ion-ligand distances (step 2-4). The last one is the electron transfer between electrode and species (step 5).

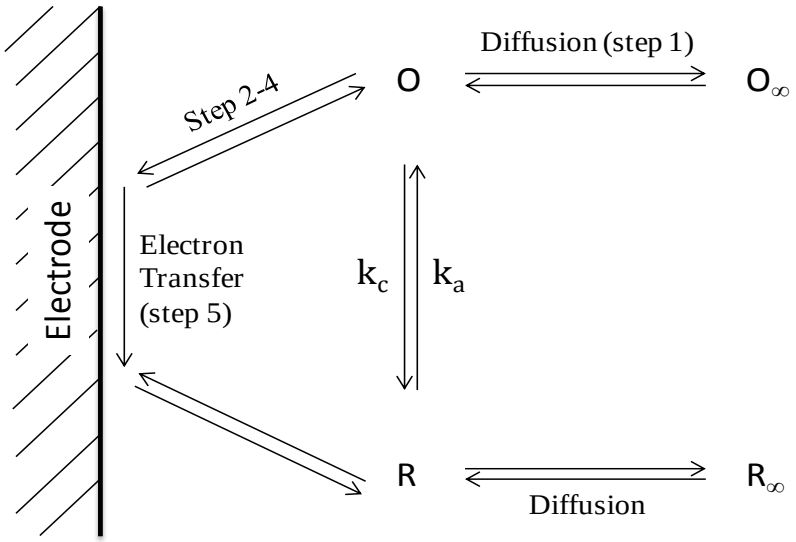

Figure 2.4 Scheme of electron transfer at an electrode. step 1: diffusion; step 2: rearrangement of the ionic atmosphere; step 3: reorientation of solvent dipoles; step 4: alterations in central ion-ligand distances; step 5: electron transfer.[1]

2.1.3.1 Mass transport

Mass transfer, that is, the movement of material from one location in solution to another, arises either from the differences in electrical or chemical potential at the two locations or from movement of solution. The types of mass transfer include migration, diffusion and convection.[4] In electrochemistry, migration and convection are often unwanted. Migration can be minimised by using a highly conductive electrolyte, to eliminate variations in the electric potential in the bulk solution. Convection can be prevented by the use of 'stagnant' solutions, unless it is especially wanted in which case it can be controlled using devices such as the rotating disk electrode (RDE). As a consequence, only the transport by diffusion is often involved in most dynamic electrochemical measurements.

2.1.3.1.1 Diffusion

Diffusion refers to the movement of species down the concentration gradient. The relationship between the speed of diffusion and the concentration gradient can be described by the *Fick's 1st Law* and *Fick's 2nd Law* in Equation 2.10 and 2.11 respectively.

$$j = -D\frac{dc}{dx} \qquad \text{Equation 2.10}$$

$$\frac{\partial c}{\partial t} = D\left(\frac{\partial^2 c}{\partial x^2} + \frac{\partial^2 c}{\partial y^2} + \frac{\partial^2 c}{\partial z^2}\right) \qquad \text{Equation 2.11}$$

where j is the flux (mol cm^{-2} s^{-1}) corresponding to the number of moles passing through unit area in unit time, D is known as the diffusion coefficient. It is strongly temperature sensitive, and provides a measurement of how far a molecule travels (diffuses) in a certain time.[2]

2.1.3.1.2 Current fluxes

In an electrode process, the concentration gradient is created by the consumption/generation of an electroactive species at the electrode surface.[1] As a result, the electroactive species diffuse between the bulk solution and electrode surface, which leads to the passage of an electrical current, I (amps, A) through the electrode as a result of electron transfer. If the kinetics at the surface are fast, then the current will be limited by the diffusion process. The diffusion flux of reactant undergoing electrolysis and the current is presented by the following equation

$$I = nFAj \qquad \text{Equation 2.12}$$

where n is the number of electrons transferred, F is the *Faraday* constant, A is the electrode area and j is the flux.

2.1.3.1.3 Cottrell equation

Consider the case of a step in the applied potential at an electrode and the variation of the electrochemical current with time in a field known as Chronoamperometry.[1] The potential is stepped at $t = 0$ from a value where no electro-active species react to a value where all the species that reach the electrode and react rapidly. For a planar electrode, which is uniformly accessible to species from the bulk solution, the resulting variation of current with time calculated from *Fick's second law* is given by the *Cottrell equation*

$$I = nFAj = \frac{nFAD^{1/2}C_{\infty}}{(\pi t)^{1/2}} \qquad \text{Equation 2.13}$$

where I is the current, n is the number of electrons transferred, F is the *Faraday* constant, A is the electrode area, j is the flux, D is the diffusion coefficient, C_{∞} is the

bulk concentration of electro-active species and t is the time.[1] The prediction from the Cottrell equation therefore is that the current will gradually decay with the square root of the time, eventually to zero. This behaviour is indeed seen at least over a restricted time range and provides a nice example of how mass transport can play a critical role in electrode processes.

2.1.3.1.4 Nernst diffusion layer

In the chronoamperometric experiment mentioned above, the predicted dependence of the current of the reciprocal of the square root of time is typically observed for up to a few seconds. At short periods there is a 'charging current' due to the double layer charging.[2] At long times, the experimentally measured current tends to be at an approximately steady value. A simplified model is displayed in **Figure 2.5** in which the bulk solution beyond a critical distance, δ, from the electrode is well mixed from various convection processes, so that the concentration of the electroactive species is maintained at a constant bulk value. Close to the solid electrode, the natural convection dies away due to the rigidity of the electrode and to the operation of frictional forces. This is the zone in **Figure 2.5** between 0 and δ, the so-called *Nernst diffusion layer*, a concept being helpful and insightful in developing voltammetric experiments which are going to be theoretically interpreted via diffusion-only models as follows.[2]

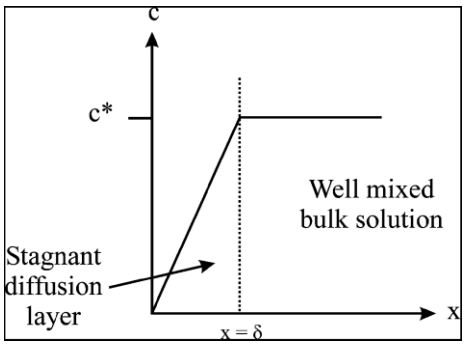

Figure 2.5 The *Nernst* diffusion layer model

2.1.3.2 Electrode Kinetics

While diffusion-only models can explain dynamic electrochemical behaviour at potentials far away from equilibrium, the kinetics of electron transfer have to be taken into account at lower applied potentials.

2.1.3.2.1 Bulter-Volmer model

The Butler-Volmer equation is one of the basic relationships in electrochemical kinetics and underpins various current interpretations of electrode kinetics. It describes how the electrical current at an electrode depends on the electrode potential, considering that both cathodic and anodic reactions can occur at the same electrode. We consider the reduction of $Fe(CN)_6^{3-}$ and oxidation of $Fe(CN)_6^{4-}$. The rate constants of reduction and oxidation can be described by k_c and k_a respectively. It follows from above that the following rate law can be written for the net process

$$j = k_c[Fe(CN)_6^{3-}]_0 - k_a[Fe(CN)_6^{4-}]_0 \qquad \text{Equation 2.14}$$

where $[Fe(CN)_6^{4-}]_0$ and $[Fe(CN)_6^{3-}]_0$ is the concentration for each species at electrode surface. The rate constants k_c and k_a is potential dependant. The precise interplay emerges below. **Figure 2.6** shows a reaction profile for the process of interest. Since $Fe(CN)_6^{4-}$, $Fe(CN)_6^{3-}$ and e^- are all charged species it follows that the profile shown must be a function of both potential of solution, ϕ_s, and potential of metal ϕ_m.[2] By altering ϕ_s and/or ϕ_m, the reactant profile is changed so that either the reduction of $Fe(CN)_6^{3-}$ the oxidation of $Fe(CN)_6^{4-}$ is the downhill, thermodynamically driven reaction as shown in **Figure 2.7**.[2]

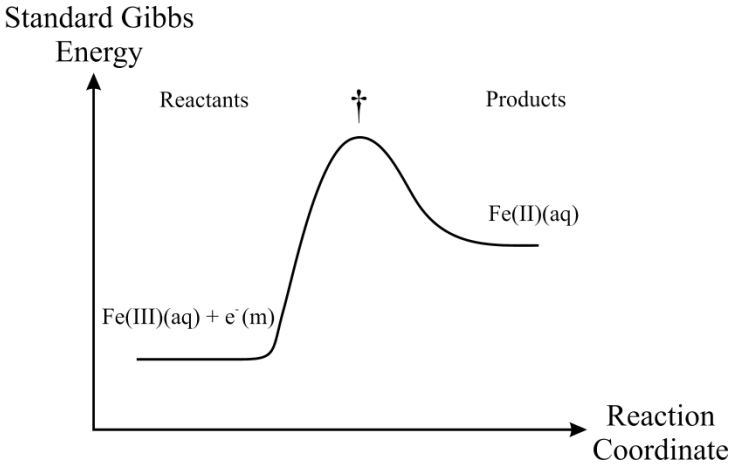

Figure 2.6 A reaction profile for the $[Fe(CN)_6]^{3-/4-}$ electrode process. Note that both ϕ_s and ϕ_m are fixed.[2]

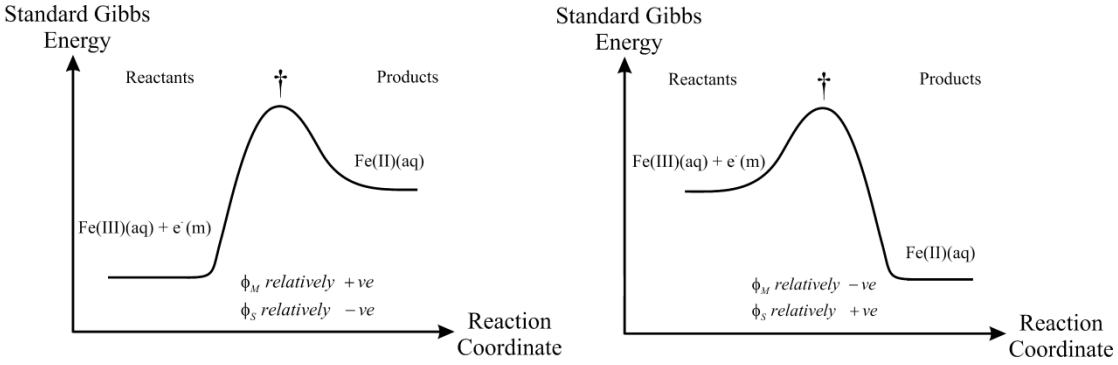

Figure 2.7 Changing ϕ_m and ϕ_s alters the energy profile for an electrode process.[2]

Arrhenius equation relates the rate constants k_c and k_a to the *Gibbs* energies of activation, as follows[2]

$$k_c = A_c e^{\frac{-\Delta G_c^*}{RT}} \qquad \text{Equation 2.15}$$

$$k_a = A_a e^{\frac{-\Delta G_a^*}{RT}} \qquad \text{Equation 2.16}$$

After evaluating the *Gibbs* energies of activation and hence the electrochemical rate constant via Equation 2.15 and Equation 2.16, the result is that

$$k_c \propto \exp\left[\frac{-\alpha F(\phi_m - \phi_s)}{RT}\right] \qquad \text{Equation 2.17}$$

$$k_a \propto \exp\left[\frac{\beta F(\phi_m - \phi_s)}{RT}\right] \qquad \text{Equation 2.18}$$

where β, known as a transfer coefficient, is such that $0 < \beta < 1$, and α equals to $1 - \beta$. Equation 2.17 and Equation 2.18 tell us that the electrochemical rate constants for the oxidation of $Fe(CN)_6^{4-}$ (k_a) and for the reduction of $Fe(CN)_6^{3-}$ (k_c) depend exponentially on the electrode potential.[2] It is indicated that the transfer coefficient β (and hence also α) lay in the range zero to unity. Often, but not always, $\alpha \sim \beta \sim 0.5$, implying that the transition state lies intermediate in its electrical behaviour between the reactants and products.[2] Then the full Butler-Volmer equation can be expressed as

$$I = nFA\left[C_O {k_c}^o \exp\left[\frac{-\alpha F(E - E^{o\prime})}{RT}\right] - C_R {k_a}^o \exp\left[\frac{\beta F(E - E^{o\prime})}{RT}\right]\right] \qquad \text{Equation 2.19}$$

This equation thus predicts how the current flowing at the electrode depends on the applied overpotential and reactant concentrations at the electrode surface. It works well for qualitative analysis. However, due to the simplifications made in derivation, the agreement with experimental data can be poor. Therefore other more detailed theories have been built up to model electrochemical reactions such as *Marcus* theory and *Marcus-Hush-Chidsey* formalisms which offer real chemical insights as to the huge variation in electrode reaction kinetics.

2.1.3.2.2 Marcus Theory

Marcus theory was first reported by Marcus in 1963 and have been widely adopted to explain the rates of electron transfer reactions between the oxidised species, O, and the

reduced species, R, as shown in Equation 2.1.[7] It was originally formulated to address the rates of outer sphere and inner sphere electron transfer reactions. The electron transfer is governed by quantum mechanical tunnelling which takes place on a time scale of 10^{-15} to 10^{-16} s, much faster than nuclear motions (vibrations) which occur on a significantly longer time scale of 10^{-13}s. The main concept is about the reorganisation energy to distort O and R forms to a similar geometry where electron transfer can occur. This energy is small if O and R have similar geometry, whereas it can be large if the two forms have very different bonding lengths and angles. Similar rules apply to electron transfer at an electrode.[7] As a consequence fast electrode processes will be observed when both species, O and R, in the redox process have comparable shapes and salvation, whereas slow transfer occurs if the shapes are very different.

2.1.4 Cyclic voltammetry

A common way to probe the dynamic electrochemical process is to provide a programmed voltage or current and to measure the consequent current response or voltage. Of the various techniques, cyclic voltammetry is probably one of the most useful with regard to the study carried out in this thesis.

Cyclic voltammetry is based on a potential sweep method which consists of scanning a chosen region of potential and measuring the current response arising from the electron transfer and associated reactions that occur. The basic cyclic voltammetry scheme is shown in **Figure 2.8**. The fundamental theory behind this is that the complete electrochemical behaviour of a system can be obtained through a series of steps to different potentials with recording of the current-time curves, to yield a three-dimensional *i*-*t*-*E* surface.[4] To avoid the tedious data and gain more information in a single experiment, sweeping the potential with time and recording the *i*-*E* curve (**Figure**

2.8b) directly is customary, which is obviously equivalent to recording current versus time. [4] The *i*-*E* curve is also known as cyclic voltammogram (CV).

Usually, the potential is varied linearly with time, as shown in **Figure 2.8**a from time t_0 to t_1. If the scan is began at a potential well negative of the electroactive region of a species which involves oxidation (say E_0) no current will flow. But as the potential becomes more positive, an oxidation current will be observed as recorded in **Figure 2.8**b. As the potential continues to grow more positively, the surface concentration of the active species being consumed will drop because of diffusion limitations. Hence the current will drop. If we reverse the potential scan, suddenly the potential is sweeping in a negative direction (see **Figure 2.8**a) and in the electrode's vicinity there is a large concentration of the reducible form of the electroactive species. Thus a reduction current will be seen.[4]

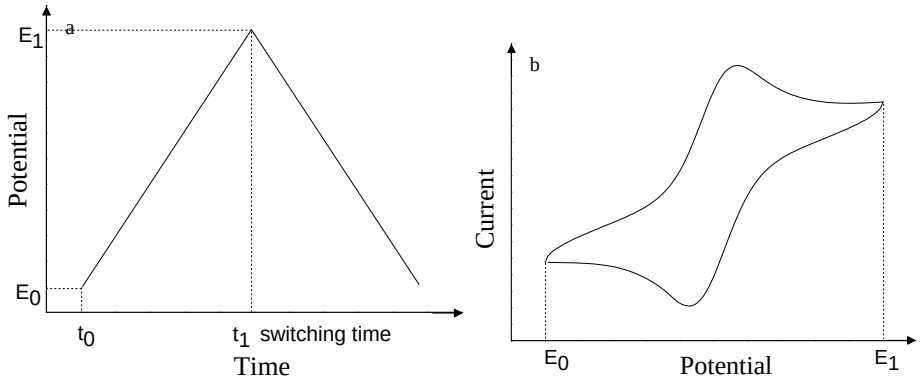

Figure 2.8 (a) Cyclic potential sweep waveform; (b) resulting cyclic voltammogram

The total current obtained is a sum of a contribution from a faradaic reaction and a contribution from capacitive (non-faradaic) according to

$$I = I_c + I_F = \upsilon C_d + I_F \qquad \text{Equation 2.20}$$

where I_c is the non-faradaic current proportional to the scan rate υ, I_F is the faradaic current, C_d is the capacitance of electrode.

Cyclic voltammetry provides a useful survey of the electrochemical reactions which can occur in the system. It also provides mechanistic details and kinetic parameters. The typical CVs are shown in **Figure 2.9** in reversible, quasi-reversible and irreversible systems resulting from differing rates of electron transfer.

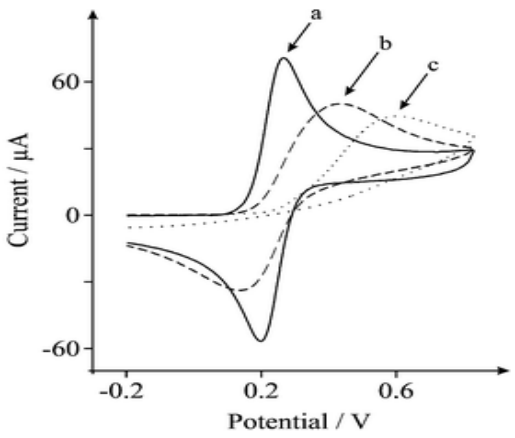

Figure 2.9 Voltammograms of (a) reversible, (b) quasi-reversible and (c) irreversible electron transfer at graphene electrode[4]

For fast electron transfer kinetics, a so-called Nernstian (reversible) system, the peak current, i_p, can be given by the *Randles-Sevčik* equation[4]

$$i_p = (2.69 \times 10^5) n^{3/2} A D^{1/2} C v^{1/2} \qquad \text{Equation 2.21}$$

where n is the transferred electron number, A is the electrode surface, D is the diffusion coefficient, C is the concentration in bulk solution, v is the scan rate. This applies to a simple system which is controlled by the diffusion between the bulk solution and the electrode. Therefore in such a system, the peaks increase linearly with the square root of the scan rate. And for the fast electron transfer kinetics, the peak separation is given by[4]

$$|E_c - E_a| \cong \frac{57\ mV}{n} \qquad \text{Equation 2.22}$$

where E_c is the reduction potential, E_a is the oxidation potential and n is the transferred electron number. And the peak-peak separation is independent of the scan rate. When the electron transfer kinetics is slow, the peak separations seen increases and becomes a function of the scan rate. Various methods exist which can fit such data to obtain good estimates of the electron transfer rate constants.

Adsorbed species lead to changes in the shape of the CV, since the species do not have to diffuse to the electrode surface. In particular, if only adsorbed species are oxidised or reduced, in the case of fast kinetics the cyclic voltammogram is symmetrical, with oxidation and reduction peak potentials coincident. The peak current is proportional to v (not $v^{1/2}$), which therefore represents a diagnostic of the electrode reaction of adsorbed species in a reversible process

$$i_p = \frac{n^2F^2\nu A\Gamma}{4RT} \qquad \text{Equation 2.23}$$

where Γ is the surface excess of species before the sweep. The relationship between peak current and scan rate can be therefore used to distinguish between an adsorption controlled process and a diffusion controlled reaction.

Fundamentally cyclic voltammetry seeks to measure the current flowing at the electrode of interest (working electrode WE) as a function of the potential drop at the electrode-electrolyte interface. This is normally carried out with a computer controlled potentiostat in this thesis, using a three electrode system in high concentrations of background electrolyte.[1] Under these conditions, the potentiostat defines a potential between the WE and a reference electrode (RE) and adjusts the potential on a third

electrode (counter electrode, CE) such that no current flows through the RE.; the current flowing though the WE is then determined, yielding the current-potential relationship, which is then repeated at differing potentials between WE and RE to determine the full CV plot.

2.1.5 Other electrochemical techniques

2.1.5.1 Square wave voltammetry (SWV)

Square wave voltammetry is one of the voltage pulse techniques and has been widely used in electroanalysis. The square wave voltammetric waveform applied to the WE consists of a square wave superimposed on a staircase, as demonstrated in **Figure 2.10**. The currents at the end of the forward and reverse pulses are both registered as a function of staircase potential. The difference between them, the net current, is larger than either of its two component parts in the region of the peak which is centred on the half-wave potential. The current is given, for a reversible system, by a modified form of the *Cottrell equation* as shown in Equation 2.13, in which $I \propto t^{-1/2}$. This means that the charge $Q \propto t^{-1/2}$ can also be used for analysis. Experimental data are obtained in the form of a series current for given values of potential which are then plotted and joined together.

Note that the capacitive contributions of current can be effectively discriminated against before they die away, since over a small potential range between forward and reverse pulses, the capacitance is constant and is thus annulled by subtraction. In this way the pulses can be shorter than in differential pulse voltammetry (DPV) or normal pulse voltammetry (NPV) which normally sampled after the capacitive current has died away.

Apart from the advantages of enhancing the signal and increasing the speed of the experiment, in many electroanalytical applications in the negative potential region, oxygen does not have to be excluded from solution when using SWV unless it interferes directly with the electrode reaction under study.[1] At rather negative potentials in the limiting current region for oxygen reduction, the forward and reverse currents are equal, leading to a zero net current, for a scan in the positive direction from negative potentials, the fast effective scan rate means that no electroactive species have time to diffuse to the electrode surface from bulk solution in a significant way. Thus, the bubbling nitrogen or argon prior to the experiment is avoided, decreasing experimental time and simplifying the procedure.

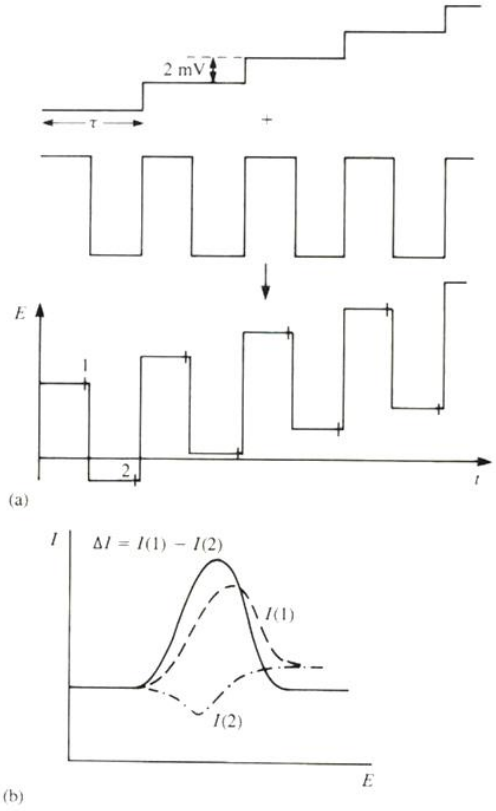

Figure 2.10 Square wave voltammetry (a) schematic waveform (sum of staircase and a square wave). (b) schematic voltammetric profiles of staircase potential.[1]

2.1.5.2 Electrochemical impedance spectroscopy (EIS)

Faradaic impedance measurement is normally performed in a cell which contains a solution with both forms of a redox couple at a potential where the species are electrochemically active. For example, one might use 1 mM $Fe(CN)_6^{3-}$ and $Fe(CN)_6^{4-}$ in 1M KCl. The electrical impedance is measured as a function of the frequency of an ac modulation source. The technique where the cell or electrode impedance is plotted *vs.* frequency is called *electrochemical impedance spectroscopy*. In a general sense, an electrochemical cell can be considered as an equivalent electrical circuit of resistors and capacitors that pass current with the same amplitude and phase angle. A frequently used circuit called the *Randles equivalent circuit* is shown in **Figure 2.11**. The parallel elements are introduced because the total current through the working interface is the sum of distinct contributions from the faradaic process, i_f, and double-layer charging, i_c. The double-layer capacity is nearly a pure capacity; hence it is represented in the equivalent circuit by the element C_d. The faradaic process cannot be represented by simple linear circuit elements whose values are independent of frequency. It must be considered as general impedance, Z_f. Of course, all the current must pass through the solution resistance; therefore R is inserted as a series element to represent this effect in the equivalent circuit.

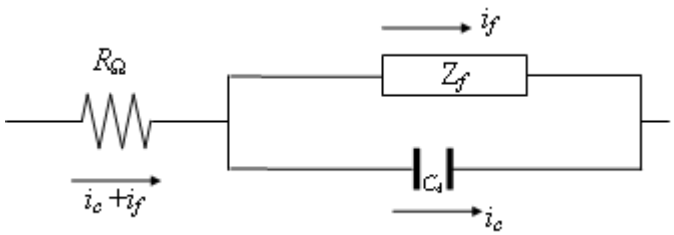

Figure 2.11 Randle Equivalent circuit of an electrochemical cell.[4]

The variation of the impedance with frequency is often of interest and can be displayed in different ways. A *Nyquist* plot is shown in **Figure 2.12**, which displays the real ($Z^{'}$) *vs.* imaginary ($-Z^{''}$) parts of the impedance. The approach provides a powerful way of determining important quantitative properties of an electrochemical cell. Unfortunately a drawback is that the exact equivalent circuit is not always known.

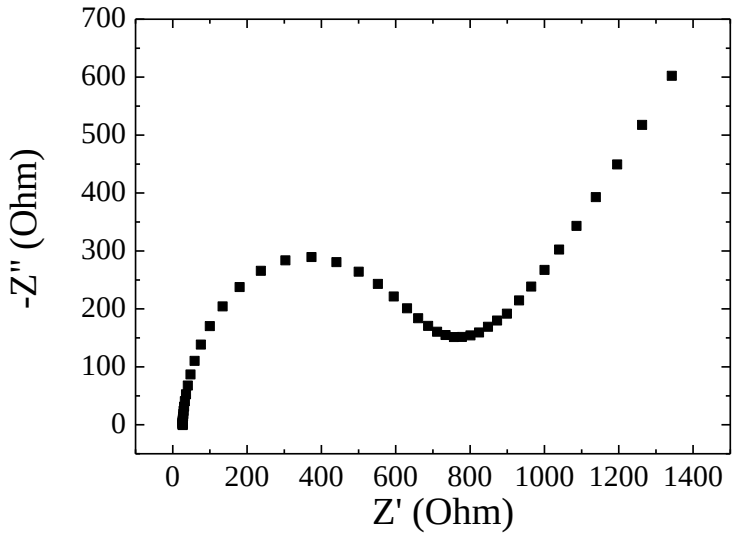

Figure 2.12 A sample of Nypquist plot in a solution containing 0.1 M KCl, 1 mM $[Fe(CN)_6]^{3-/4-}$ at BDDE

2.1.6 Instrumentation

In this thesis, the electrochemical measurements are performed using a μ-AUTOLAB III potentiostat (PGSTAT128N, Eco-Chemie, Netherlands), running GPES software (Version 4.9). The three-electrode system in use consists of a working electrode of interest, Pt wire auxiliary electrode as counter electrode and Ag/AgCl as reference electrode. The typical scan rate for CV and SWV is of 50 mV s^{-1}. The EIS was run on the same equipment with the FRA software. Other specifically alerting experimental conditions will be stated.

Chapter 2

2.2 Other techniques

2.2.1 X-ray photoelectron spectroscopy (XPS)

X-ray Photoelectron Spectroscopy (XPS), also known as Electron Spectroscopy for Chemical Analysis (ESCA), was developed in the middle 1960s by K. Siegbahn (1981 Nobel Prize winner) and his research group.[9,10] It works by irradiating a sample material with monoenergetic soft X-rays causing electrons to be ejected. The kinetic energies of these ejected photoelectrons can be used directly for the identification of elements in the sample. And the relative concentrations of elements can be determined from the photoelectron intensities. With the rapid development in vacuum technology, XPS is now applied commercially and broadly.

2.2.1.1.1 Basic principle

The operation of XPS involves irradiating the sample in ultra-high vacuum (UHV) with monochromatic X-rays, and analysing the energy of photoelectrons. Ejection of photoelectrons is a very direct way of obtaining characteristic information of atoms. The process of photoelectron emission is schematically illustrated in **Figure 2.13**a along with the Einstein equation which relates the energy of the process. These photons can penetrate up to 1 μM into the sample and create photoelectrons in this region. Most of the photoelectrons cannot escape the surface due to inelastic scattering and the consequent loss in kinetic energy. Only electrons from the top several layers (< 1nm)[11] can leave the surface and be detected as an XPS peak, so XPS is very surface sensitive. The XPS spectrum is obtained by plotting the number of electrons per energy interval versus their kinetic energy or the corresponding binding energy. Because the core levels of each element have a unique binding energies, the XPS spectrum can be used to

identify the element and determine the relative concentration of each element. Small changes in binding energy known as chemical shifts also reflects the chemical state of the material.[12]

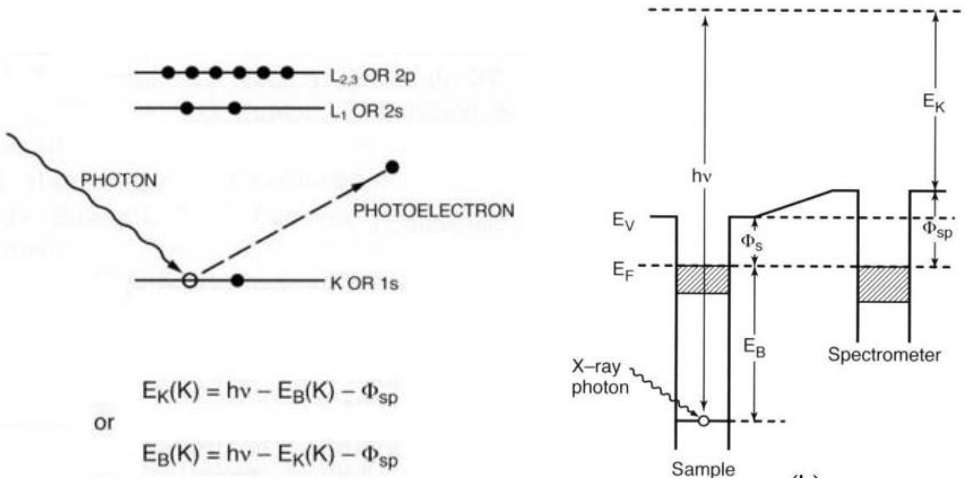

Figure 2.13 (a) the photoelectron emission process in XPS (b) the different energy levels in XPS[12]

2.2.1.1.2 Quantification analysis of XPS spectrum

The intensity (I) of a photoelectron peak can be determined by

$$I = j\rho\sigma K\lambda \qquad \text{Equation 2.24}$$

where j is the flux of photon, ρ is the concentration of atoms, σ is the photonionisation cross-section for photoelectron emission, K refers to instrumental parameters and λ is the electron attenuation length. Quantitative data of XPS can be routinely obtained by determining the area (intensity, I_i) under the peaks after background substraction (*e.g.* step, linear, Shirley background subtraction), and applying the atomic sensitivity factor (ASF, S_i). Hereby the relative elemental proportion N_i is given by

$$N_i = \frac{I_i/S_i}{\sum(I_i/S_i)} \qquad \text{Equation 2.25}$$

The equation assumes the uniform sample composition is within the XPS sample depth as determined by the inelastic mean free path (IMFP) of the escaping electron. The IMFP is an index of how far an electron can travel through a solid before losing energy, which depends on the electron kinetic energy. The IMFP values are plotted as a function of kinetic energy in **Figure 2.14**.

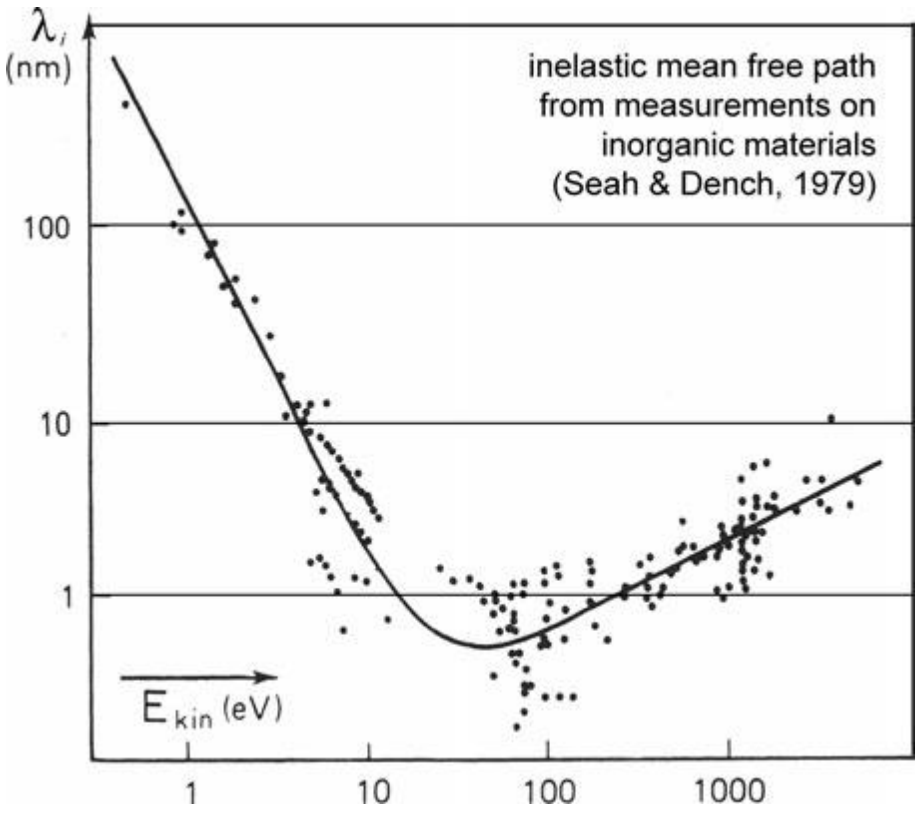

Figure 2.14 The variation of inelastic mean free path with electron kinetic energy ('universal curve')[13,14]

2.2.1.1.3 Instrumentation

An XPS apparatus contains a source of X-rays within an ultrahigh vacuum (10^{-8} to 10^{-10} mbar) stainless steel chamber with UHV pumps, an electron collection lens, a electron energy analyser, and an electron detector system, as shown in **Figure 2.15**. Provided the

exciting energy is high enough, core level spectra can be obtained for all elements of the periodic table except H and He (since both have no core level) and the determined binding energies of these core levels are sufficiently unique for their unambiguous assignment. Mg Kα (1253.6 eV) and Al Kα (1486.6 eV) X-rays satisfy this requirement and therefore are commonly used as excitation sources.

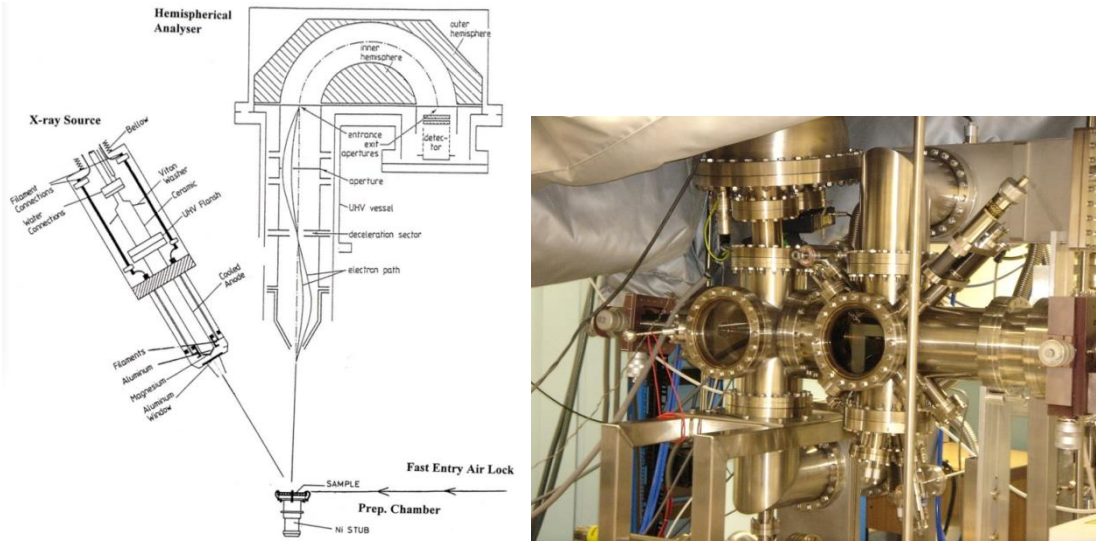

Figure 2.15 (a) Schematic diagram of XPS comprising X-ray source and hemispherical analyser[15]; (b) photo of XPS instrument in J. Foord Group

2.2.2 Scanning electron microscopy (SEM)

Scanning electron microscopy is one of the most widely used techniques in materials sciences because it combines the simplicity and ease of specimen preparation of the optical microscope, with some of the performance capability and flexibility of the more expensive and complex transmission electron microscope. SEM was originally devised in Germany in 1930's by Knoll and Von Ardenne and can be considered as having had its origins in the early electrical facsimile machines.[16,17] The first commercial SEM, the Cambridge 'Stereoscan' was produced by Cambridge Instruments in the UK in 1965.[18]

The principle of SEM is shown in **Figure 2.16**a. An electron beam strikes the specimen to be examined and is rastered over it.[18] As a result of the impact of the incident beam on the specimen, a variety of electron and photon emissions are produced. The SEM image is formed by detecting scattered electrons to yield a signal which is amplified and used to modulate the brightness of a display. Thus a magnified map or image of the specimen is produced without the need for any imaging lenses. The resolution is typically around 10 nm, set by how tightly focussed the electron beam is as it impinges on the sample. The image formed from secondary electrons produced in the scattering process typically reflects the morphology of the sample, rather like an optical image, but of course the resolution is much higher. This method of imaging offers several important advantages[18]:

- Magnification is achieved in a purely geometric manner and can be varied by simply changing the dimensions of the area scanned on the specimen.
- Any emission which can be stimulated from the specimen under the impact of the incident electron beam, *e.g.* electrons, X-rays, visible photons, heat, or sound, can be collected, detected and used to form an image. For example an X-ray image can be used for element mapping.
- Several different types of image can be produced and displayed simultaneously from the same area of the sample so enabling different types of information to be correlated.
- Because the image on the screen is derived from an electrical signal which varies with position of the beam and the image can be electronically processed to control or enhance contrast, reduce noise, identify features *etc*.

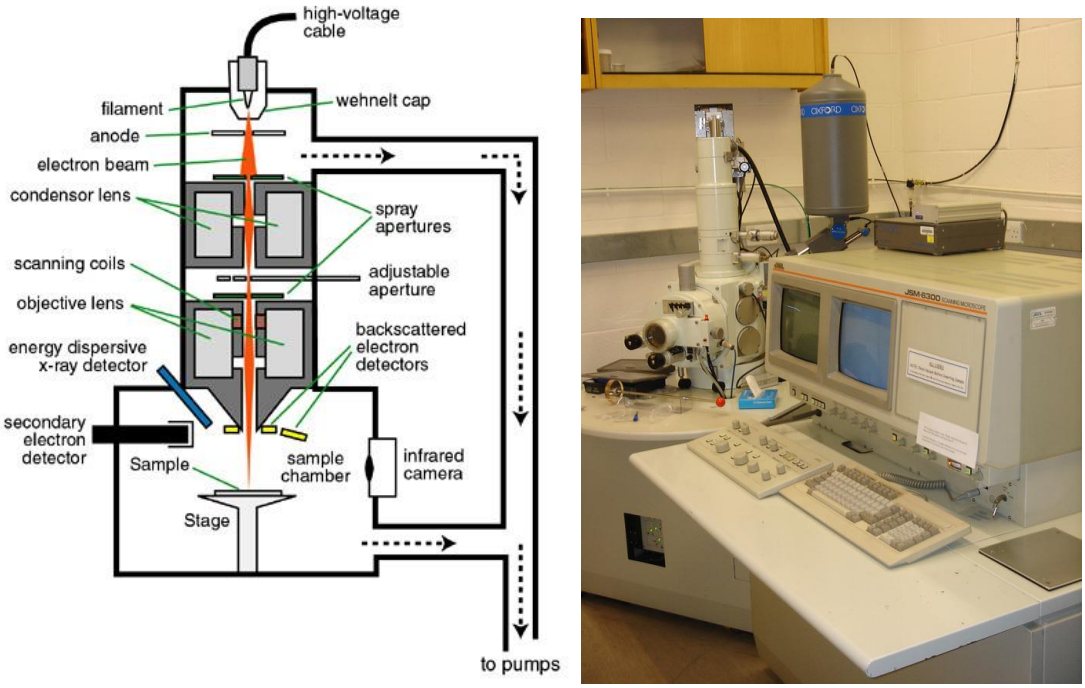

Figure 2.16 (a) Schematic diagram of SEM; (b) photo of Scanning Electron Microscopy/Energy Dispersive X-ray Detector (SEM6300 in Materials Department of Oxford)

2.2.3 Dynamic light scattering (DLS)

Dynamic light scattering, sometimes referred to as Quasi-Elastic Light Scattering, is a non-invasive, well-established technique for measuring the size and size distribution of molecules and particles typically in the submicron region.[19] In this method, a laser light hits the particles and *Rayleigh scattering* can be observed in all directions. This scattering can be detected as a time-dependent fluctuation based on the *Brownian motion* of the small particles. In this way, the velocity of Brownian motion can be characterised; enabling the translational diffusion coefficient to be obtained. The size of particles can then be calculated by the *Stokes-Einstein* equation as follows[20,21]

$$d = \frac{kT}{3\pi\eta D}$$ Equation 2.26

where d is the hydrodynamic diameter, k is the *Boltzmann's constant*, T is the absolute temperature, η is the viscosity, D is the translational diffusion coefficient. Normally DLS is concerned with the measurement of particles suspended within a liquid. An accurately known temperature is necessary for the DLS measurement since the viscosity of a liquid is related to its temperature. The temperature also needs to be stable, otherwise convection currents in the sample will cause non-random movements that will disturb the correct interpretation of size.[22] The DLS experiment process can be seen is a simple schematic diagram in **Figure 2.17**. The instrument used in this thesis is Protein Solution particle size detector model 801 used with the software Omnisize 300, in Bio-chemistry Department of Oxford University.

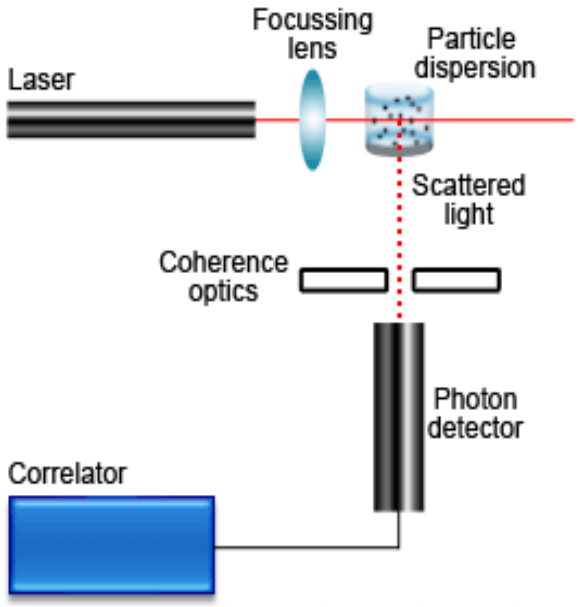

Figure 2.17 Schematic diagram of a conventional, 90° dynamic light scattering instrument[22]

2.2.4 Ultraviolet–visible spectroscopy

Ultraviolet–visible spectroscopy or ultraviolet-visible spectrophotometry is a routinely applied method in analytical chemistry by using the light in the visible and adjacent

(near-UV and near-infrared) range to promote electronic excitation in the species of interest. Measurements may be performed in absorption or reflection mode. This technique is complementary to fluorescence spectroscopy, in that fluorescence deals with transitions from the excited state to the ground state, while absorption measures transitions from the ground state to the excited state.[23] UV-visible adsorption can be used in both qualitative and quantitative ways based on *Beer-Lambert* law[24]

$$A = log_{10}\left(\frac{I_0}{I}\right) = \varepsilon \times c \times L \qquad \text{Equation 2.27}$$

where A is the measured absorbance, I_0 is the intensity of the light at a given wavelength, I is the transmitted intensity, ε is the extinction coefficient constant, L is the path length through the sample (internal widths of the cuvette), and c is the concentration of the species of interest. Because ε and L are constant for given compounds, the concentration can be considered to be proportional to the measured absorbance, which can be read directly from the UV-visible spectrum. The UV-visible instrument used in this thesis is the Lambda 750s UV-visible spectrometer located in Inorganic Chemistry Research building of Oxford University.

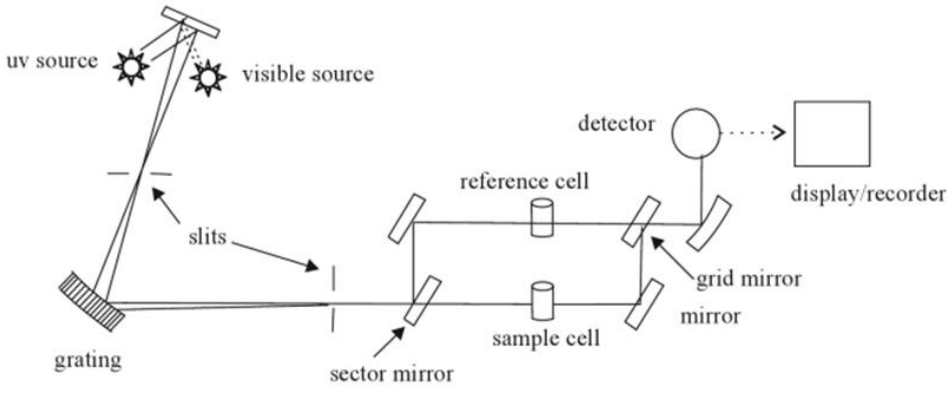

Figure 2.18 Schematic diagram of UV-visible spectrometer[25]

2.2.5 X-ray diffraction (XRD)

X-ray crystallography is a method used for determining the atomic and molecular structure of a crystal, in which the crystal atoms cause a beam of X-rays to diffract into many specific directions. By measuring the angles and intensities of these diffracted beams, a crystallographer can produce a picture of the density of electrons within the crystal. From this electron density map, the mean positions of the atoms in the crystal can be determined, as well as the chemical bonds, disorder and various other information.[23]

X-rays primarily interact with the electrons in atoms. When X-ray photons collide with electrons, some photons from the incident beam will be deflected away from the direction where they originally travel. If the wavelength of these scattered X-rays does not change (meaning that X-ray photons do not lose any energy), the process is called elastic scattering (*Thompson* Scattering) in that only momentum has been transferred in the scattering process.[18] A regular array of scattering centres produces a regular array of spherical waves. Although these waves cancel one another out in most directions through destructive interference, they add constructively in a few specific directions, determined by *Bragg's law*

$$2\mathrm{d}\sin\theta = \mathrm{n}\lambda \qquad \text{Equation 2.28}$$

where θ is the incident angle, d is the distance between the two planes, and λ is the wavelength of incident X-rays. Thus scattered peaks appear at angles which enable the distance between the scattering planes to be calculated. This underlies the method of powder XRD used in this thesis, whereby the scattered peak positions can be compared

to published data to confirm the chemical composition of crystalline regions of the sample.

The diffracted beams from large perfect crystals are very sharp. However P. Scherrer showed in 1918 that the diffracted beam is broadened when the particle size is small and proposed an equation to calculate the particle size given by[26-28]

$$D_{hkl} = \frac{\kappa\lambda}{B_{hkl}\cos\theta} \qquad \text{Equation 2.29}$$

where D_{hkl} is the crystallite size in the direction perpendicular to the lattice planes, hkl are the Miller indices of the planes being analysed, κ is a numerical factor frequently referred to as the crystallite-shape factor, λ is the wavelength of the X-rays, B_{hkl} is the width (full-width at half-maximum) of the X-ray diffraction peak in radians and θ is the Bragg angle. This equation can be used to estimate particle size in the absence of other contributions to line broadening. The instrumental broadening is neglected in this work.

Powder diffraction data can be collected using either transmission or reflection geometry, as shown in **Figure 2.19**. Because the particles in the powder sample are randomly oriented, these two methods will yield the same data. In the MRL X-ray facility, powder diffraction data are measured using the Philips XPERT MPD Diffractometer, which measures data in reflection mode and is used mostly with solid samples.

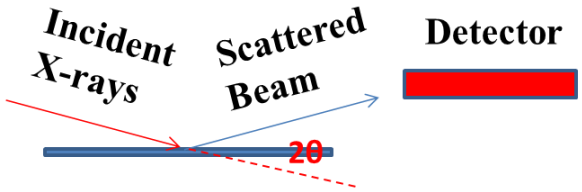

Figure 2.19 Schematic diagram of XRD of powder sample

In this thesis a Philips Analytical X'pert Pro powder diffractometer is used to characterise silver particle samples in Chapter 4. The scans for each sample were taken over a range of 2θ from 20° to 80°, in steps of 4×10^{-3}. X'Pert Highscore software was employed for data analysis and phase assessment.

References

(1) M.A.Brett, C.; Brett, A. M. O. *Electroanalysis*; Oxford University Press: Oxford, **1998**.

(2) Compton, R. G.; Banks, C. E. *Understanding voltammetry*; World Scientific, **2007**.

(3) D.R.Crow *Principles and Applications of Electrochemistry*; Chapman and Hall: New York, **1974**.

(4) Bard, A. J.; Faulkner, L. R. *Electrochemical methods: fundamentals and applications*; Wiley New York, **1980**.

(5) Compton, R.; Sanders, G. *Electrode potentials*; Oxford University Press, **1996**.

(6) Wu, J.; Risalvato, F. G.; Ke, F.-S.; Pellechia, P.; Zhou, X.-D. *Journal of the Electrochemical Society* **2012**, *159*, F353.

(7) A.C.Fisher *Electrode Dynamics*; Oxford University Press, **1996**.

(8) Marcus, R. *Annual Review of Physical Chemistry* **1964**, *15*, 155.

(9) Siegbahn, K.; Nordling, C.; Johansson, G.; Hedman, J.; Heden, P.; Hamrin, K.; Gelius, U.; Bergmark, T.; Werme, L.; Manne, R. *ESCA applied to free molecules*; North-Holland publishing company, **1970**.

(10) Siegbahn, K.; Nordling, C.; Fahlman, A. *Nov. Act. Uppsaliensis* **1967**, *20*.

(11) Crist, B. V. *Handbooks of Monochromatic XPS Spectra*; XPS International LLC, **2004**.

(12) Hüfner, S. *Photoelectron spectroscopy: principles and applications*; Springer: Berlin, **2003**.

(13) Egerton, R. F. *Electron energy-loss spectroscopy in the electron microscope*; Springer, **1996**; Vol. 233.

(14) Seah, M.; Dench, W. *Surface and interface analysis* **1979**, *1*, 2.

(15) Fuchs, E.; Oppolzer, H.; Rehme, H. *Particle beam microanalysis: fundamentals, methods and applications*; VCH, **1990**.

(16) Von Ardenne, M. *GB patent* **1937**, *511204*.

(17) Knoll, M. *Zeitschrift für technische Physik* **1935**, *16*, 467.

(18) R.W.Cahn; P.Haasen; E.J.Kramer *Materials Science and Technology: a comprehensive treatment*; VCH, **1992**; Vol. 2A.

(19) Berne, B. J. *Dynamic light scattering: with applications to chemistry, biology and physics*; DoverPublications, **1976**.

(20) Einstein, A. *Annalen der physik* **1905**, *322*, 549.

(21) Von Smoluchowski, M. *Annalen der physik* **1906**, *326*, 756.

(22) *http://www.malvern.com/en/default.aspx;* Malvern official website.

(23) Skoog, D. A. *Principles of instrumental analysis*; Thomson Brooks/Cole, **2007**.

(24) Beer, A. *Ann. Phys. Chem* **1852**, *86*, 78.

(25) Sivasankar, B. *Engineering Chemistry*; Tata McGraw-Hill Publishing Company Limited: New Delhi, **2008**.

(26) Holzwarth, U.; Gibson, N. *Nature Nanotechnology* **2011**, *6*, 534.

(27) Patterson, A. *Physical Review* **1939**, *56*, 978.

(28) Scherrer, P. *Nachrichten von der Gesellschaft der Wissenschaften zu Göttingen, mathematisch-physikalische Klasse* **1918**, *1918*, 98.

Chapter 3 Determination of H_2O_2 by Boron Doped Diamond Electrode Modified by Ag NPs and Haemoglobin

3.1 Introduction

Hydrogen peroxide (H_2O_2) has widespread and diverse chemical applications. As a mild, 'green' and efficient oxidising agent, hydrogen peroxide is commonly used in chemical synthesis and environmental treatments, including destruction of phenols and other aromatic compounds.[1] It is also involved in various industries, *e.g.* food processing, textiles, paper bleaching, beverage packaging and minerals processing. To provide examples, in fuel cells, it is critical to control the H_2O_2 concentration since the hydroxyl radicals generated from H_2O_2 lead to degradation of fuel cell membranes.[2] H_2O_2 is the product of biochemical reactions, so it plays an important role in living systems.[3-5] Therefore there is significant interest in the detection and monitoring of this compound.

Numerous investigations have been carried out to determine H_2O_2 based on such methods as titrimetry, spectrophotometry and chemiluminescence. For example spectrophotometry has been used to determine the concentration of H_2O_2 in aqueous solvent systems, with a detection limit as low as 50 nM.[6] However the equipment for these methods are usually relatively expensive and restricted in the mode of application. Since the first H_2O_2 sensor was reported in 1954[7], electrochemical method became an alternative approach to detect trace species in a mature, flexible, low-cost and effective way to analyse trace species.[8,9] Although classic metal electrodes like platinum have

been well-studied for H_2O_2 detection, increasing interest has been focussed on carbon based modified sensors in order to achieve higher sensitivity and a lower detection limit. A promising carbon based electrode is boron doped diamond because of its stability and inertness, low levels of background noise and wide potential operating window.[10] Boron doped diamond electrodes have been demonstrated in many chemical sensing applications, as mentioned in chapter 1.[10-14] However, the bare diamond electrode shows a poor electrochemical response to H_2O_2. In this regard, diamond behaves in a way similar to many other carbon based electrodes.

One common approach to overcome this problem is by depositing metal particles onto the electrode surface, for example Ag, Au, Pt, Pd, Ir, Rh, Ag/Au, Pt/Ag, Pt/Pd.[15,16] Modification of the electrode with metal nanoparticles improves the electrochemical signal and leads to lower detection limits because of this large surface-to-volume ratio and enhanced mass transport in comparison to their bulk counterparts. Among these metal particles, silver works well due to the favourable catalytic properties, surface enhanced optical phenomena and highest thermal and electrical conductivity.[17] **Table 3.1** summarises work on H_2O_2 sensors based on silver particles with their detection limit and detection range. Simm and Compton *et al* reported a BDD microelectrode array with diverse metals (Ag, Au, Cu) deposited via electro-deposition, with preliminary experiments on the cathodic detection of H_2O_2.[18] A variety of Ag modified carbon electrodes, including glassy carbon, graphene and carbon nanotubes have been used for the cathodic detection of H_2O_2 which minimises the interferences from other chemical species.[19-23] The detection limits are around 0.5 to 2.8 μm. Other non-metallic electrode modification approaches have also been reported. Karyakin *et al*. achieved a detection limit of 10^{-7} mol L^{-1} with a Prussian blue modified electrode[24]. Zhou *et al*. provided a new probe of a nonfluorescent derivative of resorufin with a 5 pmol detection limit.[25]

Kondo *et al* developed a cobalt phthalocyanine-BDD electrode for H_2O_2 detection, of which the LOD was reported to be 4.9 nM. However, only an anodic peak at +0.78 V can be observed and the interference from AA and DA were consequently very significant at such positive potentials.[26]

Another approach to the detection of H_2O_2 is to modify the carbon electrode with various protein motifs, often using nanoparticles to bind the protein to the surface and promote electron transfer. These sensors exhibit outstanding advantages in accuracy, precision and selectivity, and have undergone significant development in the past decade. Electrodes modified with haeme proteins, including horseradish peroxidise (HRP), haemoglobin (Hb), myoglobin (Mb), cytochrome c (cyt.c) and catalase, have all proved to be capable of H_2O_2 detection.[27,28] A list of some enzyme based chemical H_2O_2 sensors is given in **Table 3.2**. Detection limits are generally of the order of 1 μM. Cytochrome c, covalently attached to BDDE has been briefly discussed recently for H_2O_2 detection, again with a similar detection limit.[29]

Notwithstanding the work noted above, there has been little detailed work done on diamond electrodes modified with Ag nanoparticles and haemoglobin, perhaps the most common approach used in other electrode systems, to fully assess the capability of this electroanalytical approach for the detection of H_2O_2. The present chapter is therefore focussed on carrying out this assessment. Ag NPs were deposited onto BDDE by both wet chemical drop-coating and electrochemical deposition. The resulting Ag NPs modified BDDE were then used as supporting materials to immobilise Hb to form Hb/Ag NPs-BDDE. Detailed studies concerning the preparation of these modified electrode structures, their chemical properties and electrochemical performance are reported.

Table 3.1 Detection limit (μM) and detection range (μM) of H_2O_2 at sensors based on silver particles

Sensors	Detection limit	Detection range	Reference
Hb/Ag NPs-BDDE	0.42	0.5 μM-20 mM	ours
Ag-BDDE	295	-	Simm, A[18]
Ag-GCE	2	5-40 μM	Welch, C[30]
Ag-SWCNT	2.76	16 μM-18 mM	Bui, M[19]
Ag/DNA-GCE	0.6	2.0 μM-2.5 mM	Wu, S[20]
Ag NPs/graphene	0.5	0.1-100 mM	Liu, S[21]
Ag NPs/ATP-GCE	2.4	10 μM-21 mM	Chen, H[22]
Ag microspheres-GCE	1.2	-	Zhao, B[23]

Table 3.2 Detection limit (μM) and detection range (μM) of H_2O_2 at sensors based on enzymes

Sensors	Detection limit	Detection range	Reference
Hb microbelt (GCE)	0.61	10-230	Ding, Y[31]
HRP/DNA-Ag (GCE)	2.0	7.0-7.8	Ma, L[32]
CAT/NiO NPs(GCE)	0.6	1-1000	Salimi,A [33,34]
Cyt c/Ag NPs(GCE)	9.8	8.5-130	Feng, J[35]
Mb(Hb, HRP)/ SWCNT-CTAB(GCE)	8.07	24.2-1670	Wang,S[36]
Hb/undoped nanocrystalline	0.4	5-25	Zhu, J[37]

diamond(GCE)			
Hb/PAN-co-PAA (GCE)	4.5	-	Shan, D[38]
Hb/chitosan and nano$CaCO_3$ (GCE)	8.3	-	Shan, D[39]
Hb/nano-Gold (ITO)	4.5	10-700	Zhang, J[40]
Hb/nano-Ag sol-gel (GCE)	0.1	1-250	Xu, Y[41]
Hb/ nano-Ag-chitosan (GCE)	0.5	0.75-216	Yu, C[42]

3.2 Experimental

3.2.1 Reagents

The as-grown polycrystalline BDDEs ([B]>10^{20} cm^{-3}) used in this work were obtained from Element Six. Reagents including silver nitrate ($AgNO_3$, ≥ 99.0%), sodium acetate (CH_3COONa), acetic acid (CH_3COOH), potassium ferricyanide ($K_3Fe(CN)_6$, 99.99+%), L-ascorbic acid ($C_6H_8C_6$, ≥ 99%), dopamine hydrochloride ($C_8H_{11}NO_2{\cdot}HCl$, ≥ 99%), cetyl hexadecylthmoniom bromide (CTAB, $CH_3(CH_2)_{15}Br$, ≥ 97%), sodium dodecyl sulphate (SDS, $CH_3(CH_2)_{11}OSO_3Na$, ≥ 98.5%),), hydrogen peroxide (50 wt.%) and sodium phosphate (Na_2HPO_4, ≥ 99.0%), Monosodium phosphate (NaH_2PO_4, ≥ 99.0%) and phosphoric acid (H_3PO_4, 85 wt.%) were obtained from Sigma-Aldrich and are of A.C.S. reagent grade. Electrochemical experiments were routinely carried out in 0.1 M phosphate buffer solution (phosphate buffer, pH 7.4). All solutions and subsequent dilutions were prepared with Milli-Q water (>18 MΩ cm). The solutions were deoxygenated by bubbling N_2 gas for 20 minutes prior to use.

3.2.2 Electrode modification

The BDDEs were cleaned before use by polishing with alumina powder which was removed by ultrasonicating in water. Then the electrodes were scanned for 15 voltammetric cycles in 0.1 M HNO_3 solution from -1.4 to +2.5 V.

Citrate-stabilised Ag NPs were synthesised according to method proposed by Doty and Lee.[43] First, 0.5 ml of 10 mM ice-cold $NaBH_4$ was rapidly injected into an aqueous solution containing 0.5 ml of 0.01 M $AgNO_3$ and 20 ml of 1 mM sodium citrate under continuous stirring for 15 min, resulting in a yellow colloidal solution. After aging in the open air for 12 hours, the solution colour changed to green, This colour change was reported to be correspond to the aggregation and growth of the Ag NPs, from about 40 nm for the yellow colour to larger than 200 nm for the green colour.[44,45] 10 µL of the both fresh and aged Ag NPs suspensions were drop-coated onto BDDEs and dried to form the silver modified boron doped diamond electrode denoted as Ag NPs-BDDE.

The Ag NPs-BDDE was also fabricated by an electrochemical deposition method as follows procedure. A fixed potential of -0.1 V was applied for 100 s in aqueous solution containing 10 mM $AgNO_3$ and 0.2 M acetic buffer at room temperature. To disperse the nanoparticles and make the deposition more homogeneous, 1 mM cetyl hexadecylthmoniom bromide (CTAB) and sodium dodecyl sulphate (SDS) were explored as surfactants. These three Ag NPs-BDDEs, *i.e.* without surfactant, with CTAB and with SDS, will be compared and discussed in the results and discussion section.

The optimised Ag NPs-BDDE, which is the one fabricated by electrochemical deposition with CTAB as a surfactant, was subsequently coated with haemoglobin by

dipping into 4 mg L^{-1} Hb solution at -4℃ for 2 hours, forming the Hb/Ag NPs-BDDE. The electrode was rinsed with Milli-Q water before use. The equipment used in this work including the Auto-Lab, SEM, XPS and DLS, are discussed in the experimental section.

3.3 Results and discussion

3.3.1 Ag NPs-BDD fabrication

3.3.1.1 Ag NPs-BDDE fabricated by wet chemical method

Metal NP decorated electrodes are usually fabricated either by coating with existing metal particles from solution or by electro-deposition on the surface in question. Both methods were studied and compared in this work to identify the optimum approach for production of Ag NPs for the H_2O_2 detection. The first approach used a wet chemical method to produce Ag NPs which were subsequently drop-coated onto BDDE. Two Ag suspensions were prepared and compared. One Ag suspension is labelled "fresh" and was of the initial yellow colour. It was stored in a sealed bottle after preparation to isolate the air. The other one is called "aged". it was stored in an open bottle for 12 hours until the colour changed to green. **Figure 3.1** shows SEM images of both samples. For the fresh sample (**Figure 3.1**a) regular nanocubes of Ag NPs with about 100 nm sides can be observed. The particles are well dispersed over the surface as expected from a good dispersion in the drop coating solution. A similar structure for Ag NPs prepared by wet chemical methods has been also reported in the literature.[45-47] The surface morphology of the sample prepared from the aged Ag NPs sample is shown in **Figure 3.1**b. The Ag NPs observed in the aged sample are of larger size, and are less regular and more spherical than those in the fresh sample. It implies that the silver

particles may continue to grow in solution and partly aggregate to clusters. This aggregation and shape change is associated with the colour change of Ag NPs, from yellow to green, compatible with changes reported elsewhere in the literature.[44,46,48] It is reported that different geometrical shapes of Ag NPs give distinct optical wavelengths, changing from 670nm (red) to 450 nm (blue) with the shape changes from a triangle to a sphere.[49]

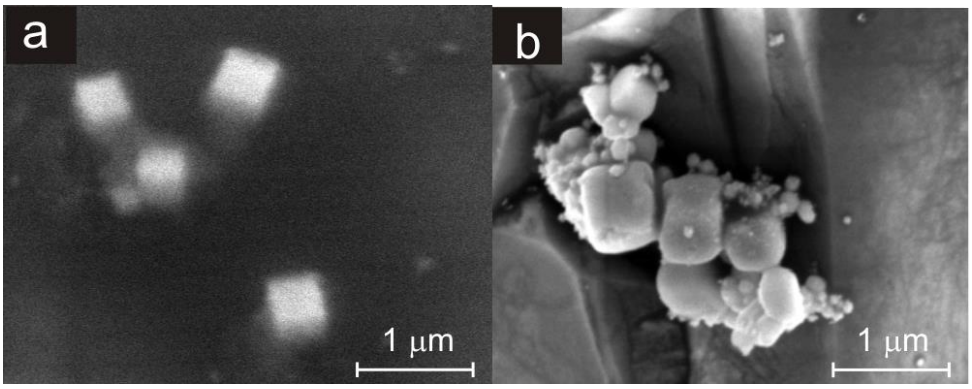

Figure 3.1 SEM images of (a) fresh sample and (b) aged sample of Ag NPs-BDDEs. The Ag NPs were prepared by wet chemical method and drop-coated onto BDDE surface.

3.3.1.2 Ag NPs-BDDE fabricated by electrochemical deposition

3.3.1.2.1 Influence of deposition time

The electrochemical deposition is another approach widely used to modify electrodes with silver particles. Experimental variables including deposition time and the concentration of $AgNO_3$ were optimised as below. The deposition was conducted for 30, 60, 100, 150 and 200 s respectively, by applying a potential of -0.1 V at BDDE in a solution containing 10 mM $AgNO_3$ and 0.1 M acetic buffer. Then the resulting Ag NPs-BDDEs were scanned in 0.1 M acetic buffer from -0.2 to +1 V where the redox stripping of Ag/Ag^+ normally occurs (SEP of +0.8 V).[51,52] The CVs are depicted in **Figure 3.2**, where redox pairs are observed in all the profiles around +0.6/+0.3 V,

corresponding to the oxidation and subsequent reduction of silver particles at BDDE surface in agreement with the literature.[53] The stripping peak current rises as expected with increase in deposition time, indicating that more Ag NPs were deposited on the surface at longer deposition times. It also shows that by changing the deposition length, the surface coverage can be easily controlled.[54] However, because of the diffusion limitation, the amount of Ag NPs deposited rapidly saturates as the deposition time increases, as suggested from the peak currents from 100, 150 and 200 s.

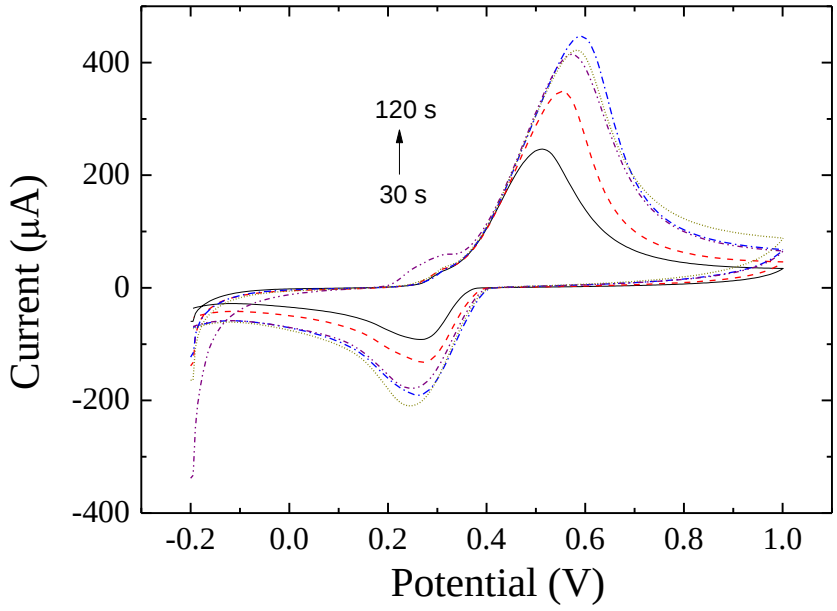

Figure 3.2 Cyclic voltammograms in 0.1 M Ac buffer at Ag NPs-BDDEs which were modified by electrochemical deposition time of 30, 60, 100, 150 and 200 s respectively

3.3.1.2.2 Influence of silver source concentration

The concentration of $AgNO_3$ was also studied and optimised. The electro-deposition was conducted in solutions with various $AgNO_3$ concentrations from 0.1 to 10 mM. Then the cyclic voltammetry was performed at the resulting Ag NPs-BDDEs in 0.1 M Ac buffer, as displayed in **Figure 3.3**. Again as expected the stripping peak current, associated with the amount of Ag NPs on the BDD surface, grows with higher concentration of $AgNO_3$. It means that more Ag NPs were deposited. However, there is

no significant increase in peak current between 0.5 mM $AgNO_3$ and 0.1 mM $AgNO_3$, in contrast to the enhancement observed from 0.5 to 1 mM. To sum up, Ag advantageously modifies the electrochemical properties of the diamond electrode, although a significant coverage is needed to observe significant effects. Although this coverage can be controlled by deposition time or concentration as seen above, it was found that good results could be obtained using 10 mM $AgNO_3$ with deposition times of 100 s so this was used as an optimal condition for electro-deposition in all the subsequently relevant experiments.

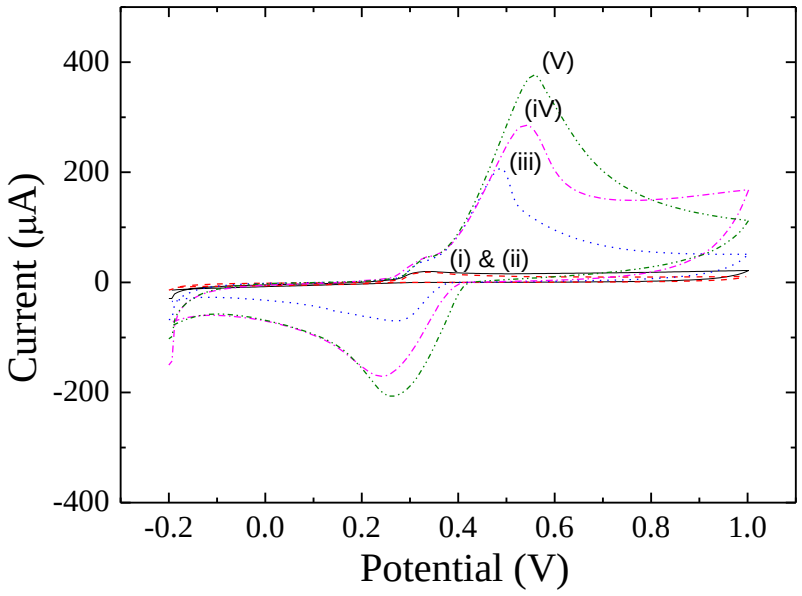

Figure 3.3 Cyclic voltammograms in 0.1 M Ac buffer at Ag NPs-BDDEs which were modified by electrochemical deposition through applying -0.1 V for 100 s in $AgNO_3$ of (i) 0.1 mM, (ii) 0.5 mM, (iii) 1 mM, (iv) 5 mM and (v) 10 mM

3.3.1.2.3 Influence of surfactants

Surfactants are commonly used to stabilise the silver particles.[45,55] In this work, both anionic surfactant SDS and anionic surfactant CTAB were therefore added into the deposition solution. These surfactants affect the morphology of Ag NPs deposited on BDDE which was investigated by SEM. The images for Ag NPs-BDDE without

surfactant, with CTAB and with SDS are shown in **Figure 3.4**. **Figure 3.4**a is taken on the Ag NPs-BDDE without surfactant, where the particles shape and size are quite variable and a dendritic morphology develops. Some particles are as small as 30-100 nm and some bulks are larger than 2 μM. **Figure 3.4**b is the SEM image of the Ag NPs-BDDE surface using CTAB as surfactant and the one shown in **Figure 3.4**c was prepared with SDS as surfactant. Again quite varied structures are seen. With CTAB the dendritic agglomerations seen in the absence of surfactant tended to disappear, whereas with SDS although some large agglomerations were observed, a high concentration of fine sized particles was seen compared to the absence of surfactant. The results therefore suggest that the presence of surfactant could be used to regulate the properties of the deposited silver. In general, with the addition of surfactant, the shape and size of silver particles are more uniform. And the anionic surfactant, CTAB, can help to provide silver particles with smaller size and better dispersion than the anionic surfactant SDS. The difference arose from the different charge of their active part, that is SDS ($CH_3(CH_2)_{11}OSO_3Na$) is an anionic surfactant and CTAB ($((C_{16}H_{33})N(CH_3)_3Br$) is cationic surfactant. It suggested that the cationic surfactant might benefit the silver particle dispersion.

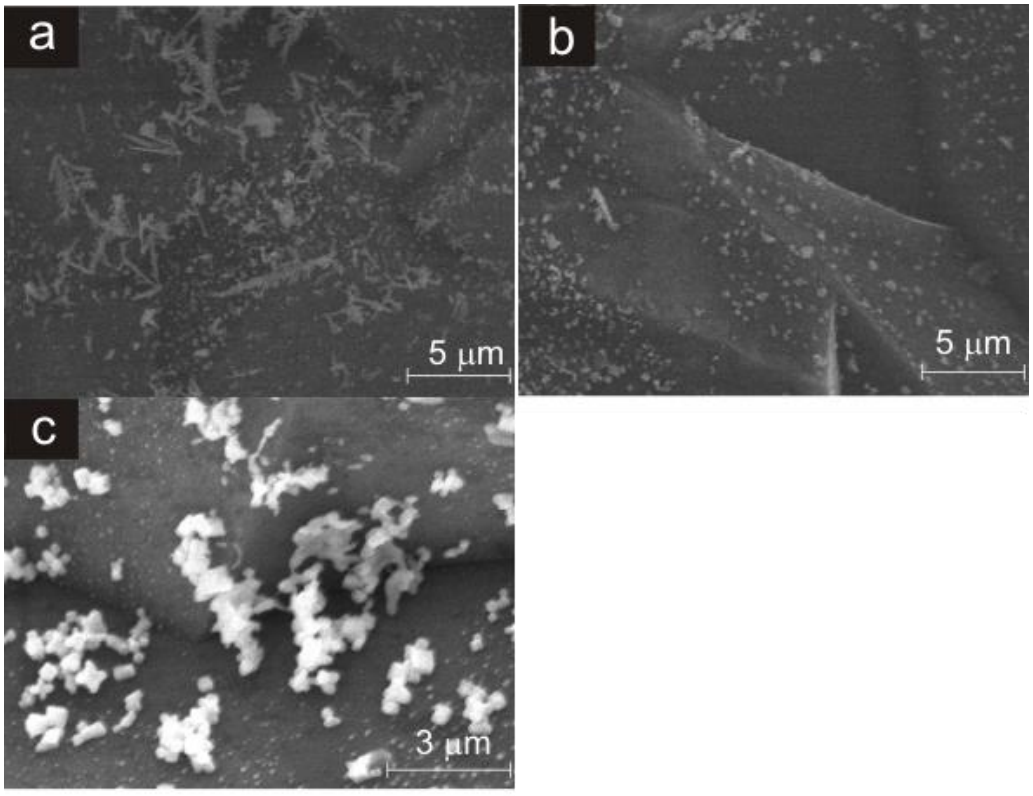

Figure 3.4 SEM images for Ag NPs-BDDEs made from electro-chemical deposition in a solution containing 0.1 M Ac buffer and 10 mM Ag NO_3 at -0.1 V for 100 s, (a) without surfactant; with the addition of 1 mM (b) CTAB and (c) SDS as surfactant respectively.

3.3.1.3 Comparison of both methods

In order to compare the Ag NPs-BDDEs made from both wet chemical and electro-deposition approaches, the total amount of silver particle on BDDE surface needs to be comparable. In electro-deposition, the loading can be calculated from coulometry. Approximately 4×10^{-6} g Ag NPs was deposited on all electrode surfaces equivalent to 0.0034 Coulomb using the stated deposition conditions. A similar surface concentration of pre-synthesised nanoparticles was thus deposited on the surface by drop-coated using the silver nanoparticle solutions by controlling the total volume of the added drops of known concentration. The SEM images in **Figure 3.1** and **Figure 3.4** show the different

morphologies for both Ag NPs-BDDEs. The Ag NPs from the wet chemical method had more regular shape but larger size.

XPS analysis was conducted at all types of Ag NPs-BDDEs. The spectra were similar in each case, as representatively shown in **Figure 3.5**. The typical peaks of metallic silver at 368 eV for Ag $3d_{5/2}$ and 374 eV for Ag $3d_{3/2}$ are observed, along with expected C 1s (285 eV) and O 1s (532 eV) peaks associated with exposed oxygen functionalities bonded to diamond. Appropriate XPS sensitivity factors were used to convert peak areas to atomic concentrations.[44] Elemental compositions were typically around 16 % oxygen, 78% carbon and 5% silver for electrochemical deposition, whereas the wet chemical approach yielded smaller Ag coverage around 3.5%. Given the particles are significantly bigger than the XPS sampling depth, these concentrations essentially correspond to the fraction of the surface covered with Ag. Since the SEM data in **Figure 3.1** and **Figure 3.4** shows the drop-coated Ag particles tend to be larger than the electrodeposited counterparts, a lower calculated concentration in XPS is actually qualitatively consistent with the same total silver loading. In view of this result, these preparation methods of Ag NPs-BDDEs using wet chemical and electro-deposition methods were used for H_2O_2 detection, to enable a fair comparison to identify the more optimal approach.

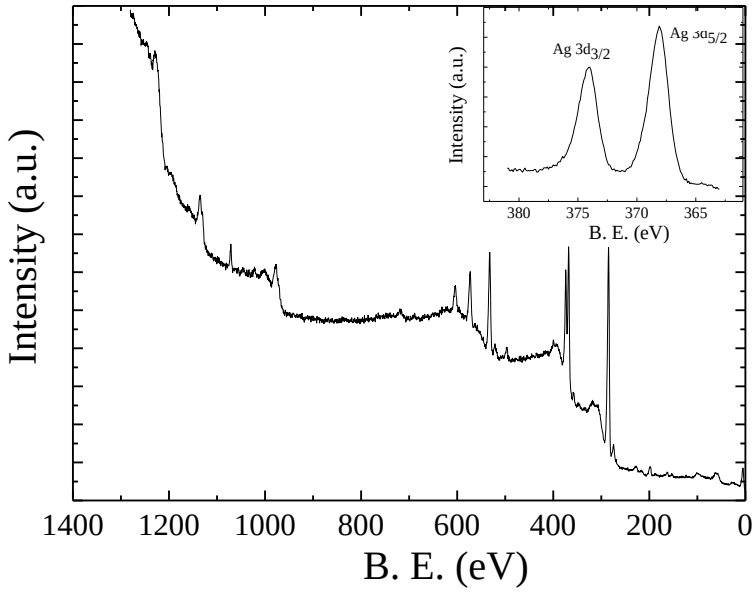

Figure 3.5 X-ray photoelectron spectroscopy spectrum of Ag NPs-BDDE

3.3.2 Ag NPs-BDDE for H_2O_2 detection

3.3.2.1 Initial electrochemical studies

The Ag NPs-BDDEs by both wet chemical and electro-deposition method are compared for H_2O_2 determination in this section. Because the oxidation of H_2O_2 has inherent interference problems in many analytical situations, the detection based on the reduction of H_2O_2 is of particular interest. The mechanism for hydrogen peroxide reduction on silver surface has been studied for decades. Since reported by Masataka Honda[56,57] and developed by many scientists later such as Georg Flatgen[58], the reduction of H_2O_2 at silver surfaces is proposed as the equations below:

$$H_2O_2 + e^- \rightleftharpoons OH_{(ads)} + OH^- \qquad \text{Equation 3.1}$$

$$OH_{(ads)} + e^- \rightleftharpoons OH^- \qquad \text{Equation 3.2}$$

$$2OH^- + 2H^+ \rightleftharpoons 2H_2O_2 \qquad \text{Equation 3.3}$$

However differing features such as an autocatalytic mechanism can feature under different conditions so the mechanism above should be treated as an oversimplification.[59] Typical cyclic voltammetry results are shown in **Figure 3.6**a for H_2O_2 reduction at Ag NPs-BDDE in a solution containing 0.1 M phosphate buffer and 0.1 mM H_2O_2 at progressively by increasing scan rate of 0.15, 0.2, 0.25 and 0.3 V s^{-1}. The electrode was fabricated by electro-chemical deposition without surfactant. At the scan rate of 0.15 V s^{-1}, a reduction peak at about -0.6 V is observed with the current approximate to 7×10^{-4} A. At the scan rate of 0.2 V s^{-1}, the peak potential shifts toward to more negative values about -0.7 V and the current increases to 9×10^{-4} A. Similar shift and increase are also observed at scan rate of 0.25 and 0.3 V s^{-1}. The resulting peaks current are plotted against scan rate in **Figure 3.6 b**, yielding a linear response between them. Simplistically, the proportional relationship of peak current to scan rate represents a diagnostic of electrode reaction of adsorbed species. However in view of the complicated reaction mechanisms for peroxide reduction, it is probably safer to view this result as being an indicator that simple diffusion electrochemistry is not observed in this system.

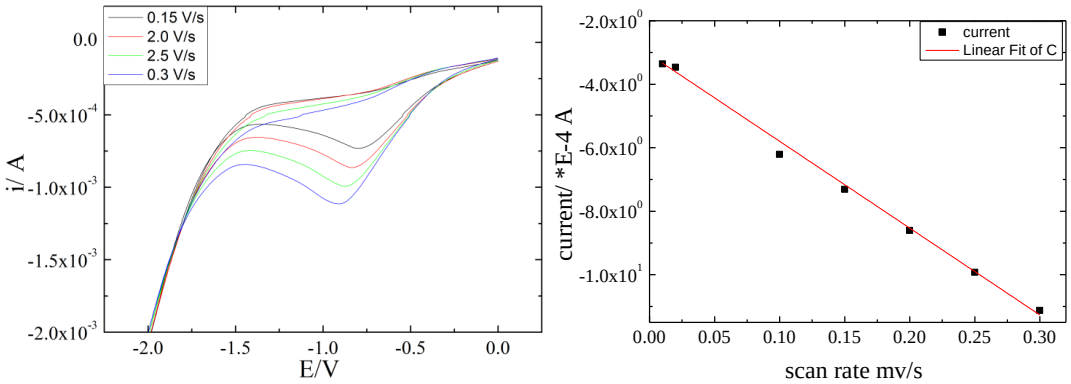

Figure 3.6 (a) cyclic voltammograms in a solution containing 0.1 M phosphate buffer buffer and 0.1 mM H_2O_2 at Ag NPs-BDDE with scan rate of 0.15, 0.2, 0.25 and 0.3 V s^{-1}; (b) plot of peak current *vs.* the scan rate

The voltammetry of H_2O_2 was performed in various electrolytes, including dilute nitric acid (pH 0.97), Ac buffer (pH 4.63), phosphate buffer (pH 7.26) and NaOH (pH 13). The corresponding typical CVs are displayed in **Figure 3.7**, at the Ag NPs-BDDE fabricated by electro-chemical deposition without surfactant. Shown together is the voltammogram at bare BDDE in 0.1 M phosphate buffer as reference to compare (line i), which is featureless in the potential window studied. In NaOH solution which has the highest pH value, a weak and broad wave for H_2O_2 reduction appears round -0.6 V with a maximum current of 12 µA. In the phosphate buffer, a clear peak-shape curve is observed at about -0.5 V and with a larger peak current of 25 µA. The reduction current of H_2O_2 maintains this value in the Ac buffer and HNO_3 solution. However, although the acidic solution can provide more hydrogen ions which favour H_2O_2 reduction, these reduction peaks are broad and ill-defined. Also considering that the phosphate buffer is more close to a system in vivo, 0.1 M phosphate buffer was routinely used for electrochemical H_2O_2 detection in the subsequent work.

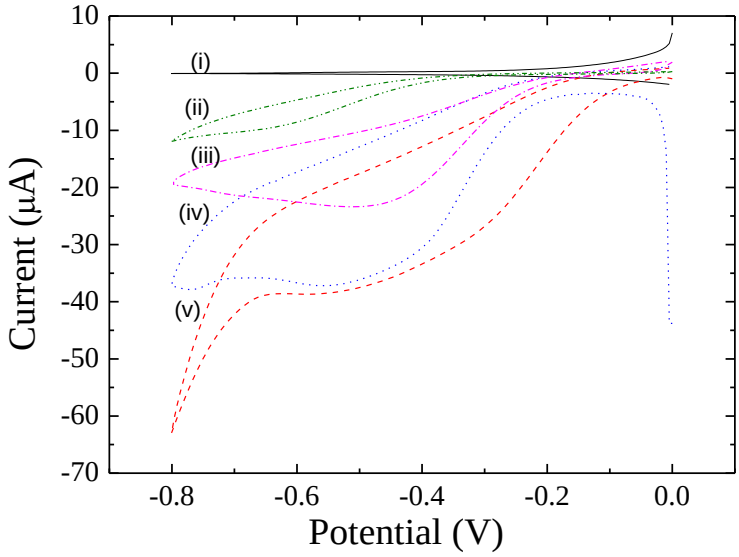

Figure 3.7 Cyclic voltammograms of 10 mM H_2O_2 at (i) bare BDDE; Ag NPs-BDDE in (ii) 0.1 mM NaOH (pH 13), (iii) 0.1 mM phosphate buffer (pH 7.26), (iv) 0.1 mM Ac buffer (pH 4.63), and (v) 0.1 mM HNO_3 (pH 0.97)

3.3.2.2 Ag NPs-BDDE for H_2O_2 Detection

Ag NPs-BDDEs fabricated by both wet chemical method and electro-chemical deposition were compared for the detection of H_2O_2 reduction by cyclic voltammetry performed in 0.1 M phosphate buffer (pH 7.4) as a fuction of H_2O_2 concentration. The potential range is from 0 to -0.8 V, which is the normal range that peroxide sensors based on cathodic reduction operate.[8,9,23,24,30,58,60-62] The CVs are shown in **Figure 3.8**. The CV (**Figure 3.8a**) at bare BDDE is also displayed for comparison. The current curve is featureless and no reduction wave appears in the potential range studied. It shows that H_2O_2 is not reduced at the clean diamond electrode. Data from an electrode prepared by casting the fresh sample Ag NPs solution are displayed in **Figure 3.8b** and the corresponding data from an aged sample are shown in **Figure 3.8c.** The wave corresponding to the reduction of H_2O_2 is observed at about -0.5 to -0.6 V in all profiles and the current increases with H_2O_2 concentration. To compare the two electrodes, the reduction peak of H_2O_2 at the aged sample is better resolved and well-defined than the fresh sample since the over-potential is slightly smaller and the current is higher. This is somewhat unexpected since the fresh sample shows the better Ag dispersion. It suggests the reaction is sensitive to the structure of the Ag NPs such that the aged sample performs better. **Figure 3.8d** and e are the CVs at the electrodeposited Ag NPs-BDDEs with SDS and CTAB as surfactants respectively. Well resolved reduction peaks of H_2O_2 are observed at about -0.4 to -0.5 V, which is lower than those at the wet cast electrodes, indicating the good activity of these electrodes towards the H_2O_2 reaction. The peak current at the Ag NPs-BDDE fabricated by electro-deposition with CTAB is not only stronger than the one with SDS, but also three times stronger than those at Ag NPs-BDDEs by the wet chemical method. In all cases the current is significantly less than the diffusion limit for a planar electrode, showing that access of analyte to the Ag NPs

followed by reaction, rather than diffusion from the bulk solution, is limiting the response at these loading of Ag NPs.

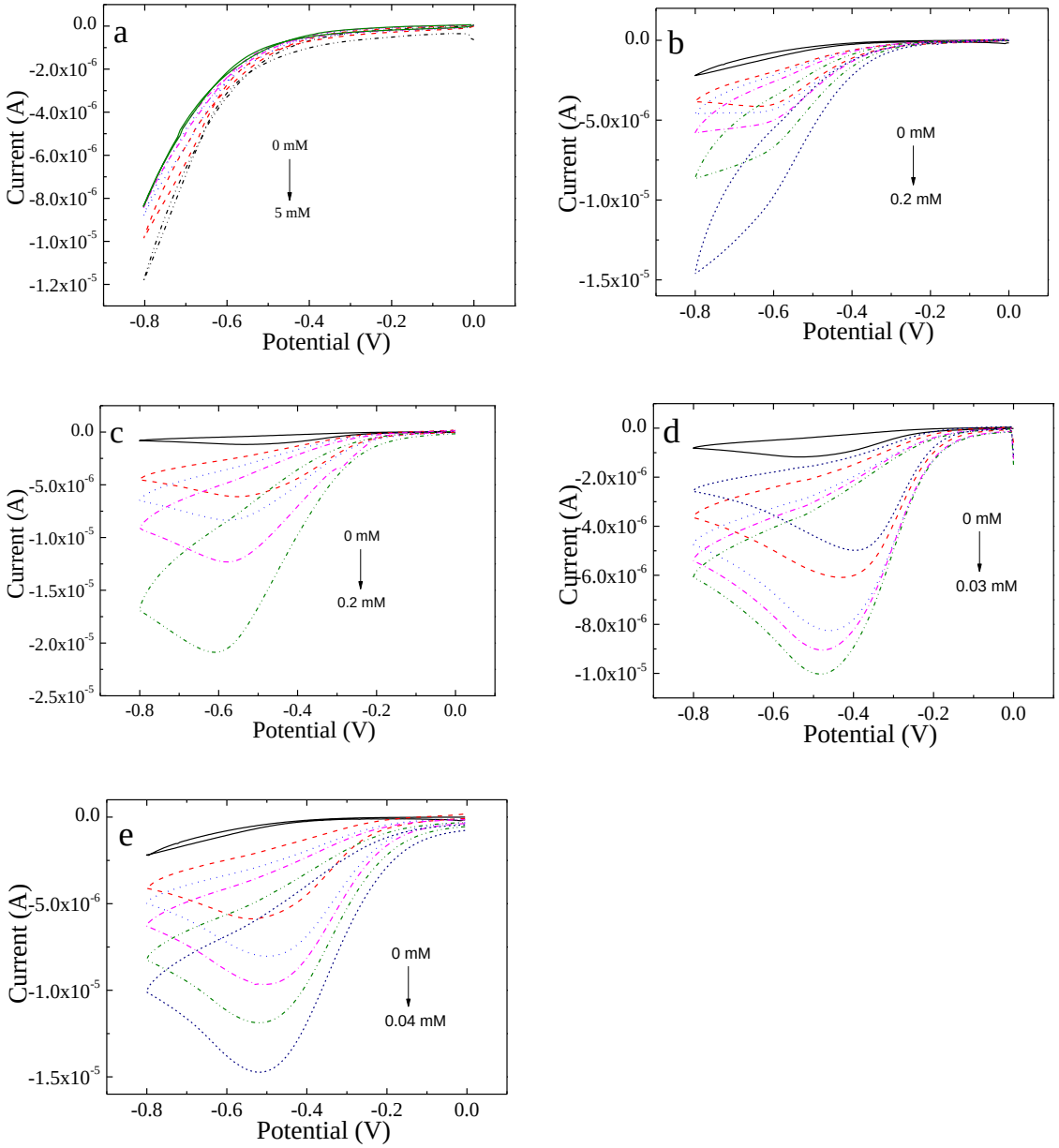

Figure 3.8 Cyclic voltammograms of continuous addition of H_2O_2 in 0.1 M phosphate buffer at (a) bare BDDE; Ag NPs-BDDE by wet chemical method of (b) fresh sample and (c) aged sample, and Ag NPs-BDDE by electrochemical deposition using (d) SDS and (e) CTAB as surfactant

The limit of detection (LOD) was calculated from cyclic voltammetry data by dividing three times the background noise by the gradient of the response versus concentration plot (S/N=3). Due to the variations in sensitivity, the LOD obtained from the aged Ag

NPs fabricated by the wet chemical method and the electrode with SDS surfactant prepared by electrochemical deposition was inferior to the CTAB electro-deposition approach (1.54 μM). This result is similar to those obtained at a Ag NPs modified glassy carbon electrode, where a LOD of 2 μM was reported by Compton *et al* [30] and other data for Ag-modified electrodes shown in **Table 3.1**. It is also found that the Ag NPs-BDDE fabricated by electro-deposition with CTAB as surfactant showed the best reproducibility with less than 2% variation in sensitivity observed between differing electrodes prepared under the same conditions, and it appeared that the Ag NPs deposited by wet casting showed inferior adhesion Therefore, considering the sensitivity, detection limit, reproducibility and stability of attachment to the surface, Ag NPs-BDDEs fabricated by electrochemical deposition with CTAB as surfactant were preferred, compared to the other approaches noted above, and all subsequent work involving Ag modified electrodes used this preparation method.

3.3.2.3 Electrode inactivation and reactivation

Ag NPs-BDDEs are easily inactivated, if, for example, kept in the air for 48 hours or after several consequent cyclic voltammetric scans. The reason may be that the silver surface can be oxidised in the air or poisoned by $OH_{(ads)}$ gradually. Similar deactivation was reported by many other researchers, such as Flatgen.[58] So it is a general phenomenon rather than being limited to the use of diamond substrates. Flatgen also proposed a reactivation process by sweeping the electrode at an anodic potential. In this way, the inactive silver surface was stripped off and a fresh surface was exposed. However, at the same time the silver material was also lost and might pollute the sample.

Here, the stripping method and other possible treatments to reactivate the Ag NPs-BDDE were investigated. The inactive electrode was obtained by leaving the Ag NPs-

BDDE in the open air for 48 hours. Cyclic voltammetry was conducted at this inactivated electrode in a solution containing 0.1 M phosphate buffer and 4 mM H_2O_2, as displayed in **Figure 3.9** line i. The curve is featureless through the whole potential window studied, which means the reduction of H_2O_2 cannot occur at the electrode. The stripping treatment was performed at this inactive electrode by sweeping from +1 to -1 V in 0.1 M phosphate buffer for two scans. Then the cyclic voltammetry was conducted again under the analogous conditions to above and the CV is shown in **Figure 3.9** line ii. A clear peak of H_2O_2 reduction is observed at *ca.* -0.6 V, which means the Ag NPs-BDDE has been reactivated. The inactive electrodes were also treated by potentiostatic coulometry through applying a fixed potential of +1 and -1 V for 100 s in 0.1 M phosphate buffer respectively. The CVs at these resulting electrodes are also shown in **Figure 3.9**, line iii and line iv. The H_2O_2 reduction peak is seen in both curves. It proves that the Ag NPs-BDDE also can be reactivated by both cathodic and anodic potentiostatic coulometry treatments. The mechanism for anodic potentiostatic coulometry is similar to that for sweep stripping, but that for cathodic treatment is still unknown. It may be that the negative potential reduces any adsorbed species on the surface thus exposing electro-active sites. As can be seen from **Figure 3.9**, the peak current for H_2O_2 reduction at a stripping reactivated electrode is stronger than after treatment by anodic and cathodic potentiostatic coulometry, suggesting that the stripping approach is more proficient. However, despite the lower peak current, cathodic potentiostatic coulometry is still an efficient approach to reactive Ag NPs-BDDE, which is of great interest because it can avoid the consumption of Ag NPs.

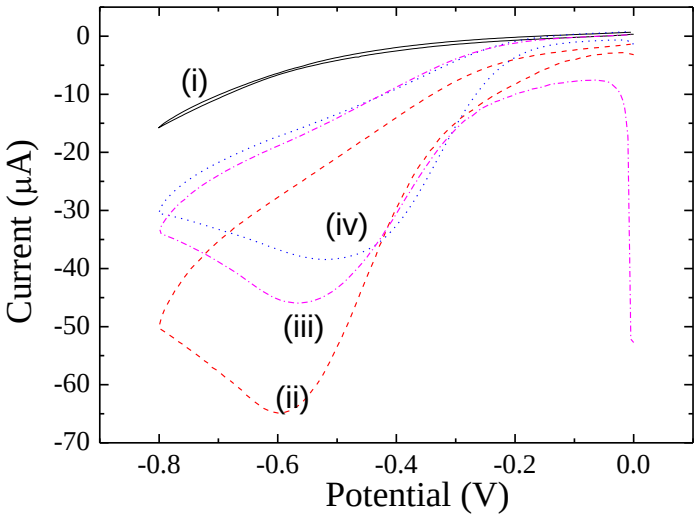

Figure 3.9 Cyclic voltammograms in a solution containing 0.1 M phosphate buffer and 4 mM H_2O_2 for (i) inactivated Ag NPs-BDDE, (ii) re-activated by sweeping from -1 to +1 V, (iii) re-activated by applying +1 V potential for 60 s and (iv) re-activated by -1 V for 60 s

Two comparable experiments were thus designed to investigate the influence of the reactivation treatment on electrode stability. The Ag NPs-BDDE was kept in 0.1 M phosphate buffer, and after periods of 1, 6, 12, 24, 48 and 168 hours respectively, the electrode was taken out and tested by cyclic voltammetry in the solution containing 0.1 M phosphate buffer and 4 mM H_2O_2. The points of peak current of H_2O_2 reduction against each storing time length are plotted in **Figure 3.10** as the red square (line ii). Another parallel experiment was carried out through the same process, but before each cyclic voltammetry, a fixed potential of -1 V was applied at the Ag NPs-BDDE for 100 s to re-activate the electrode. The resulting plot of reduction current *vs.* storing timeis also shown in **Figure 3.10** as the black circles (line i). For the electrode without the pre-treatment of cathodic potentiostatic coulometry, the current drops from the initial value of 90 μM to about 60 μM at 10 hours. After 48 hours, the reduction peak of H_2O_2 was hardly seen and the current at -0.5 V was 28 μA, only a third of the initial value. On the other one, the current at the electrode that was reactivated every time also starts from

about 90 µA, but only dropped to 74 µA at 10 hours. The peak current is stable around 65 µM after 20 hours, about 70% of the initial value. After 7 days, the reduction peak still can be observed. This experiment demonstrated that the electro-response and using life of Ag NPs-BDDE can be significantly enhanced by the cathodic potentiostatic coulometry treatment.

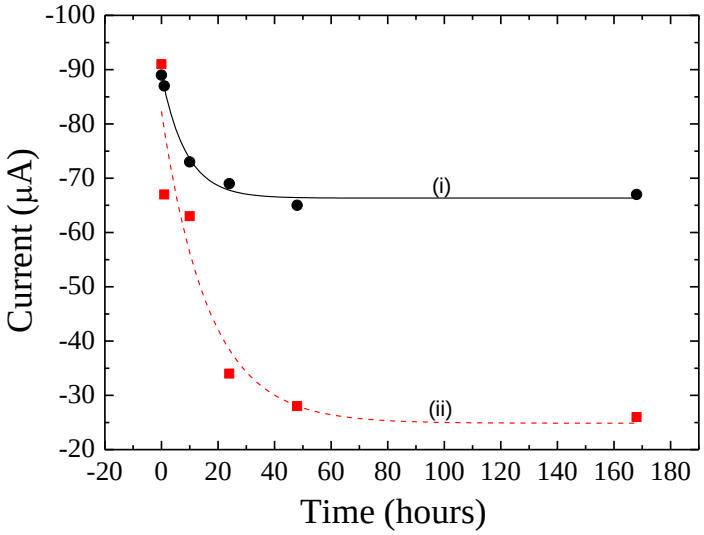

Figure 3.10 Plot of peak current of H_2O_2 reduction *vs.* storing time, obtained from cyclic voltammetry in a solution containing 0.1 M phosphate buffer and 4 mM H_2O_2 at Ag NPs-BDDE stored in 0.1 M phosphate for 1, 16, 12, 24, 48 and 168 hours respectively (i) with and (ii) without applying -1 V for 100 s before the cyclic voltammetry each time

An ultrasonic method was also investigated to reactivate the Ag NPs-BDDE.[63,64] To start the experiment, two subsequent cyclic voltammetry scans were conducted at a Ag NPs-BDDE in a solution containing 0.1 M phosphate buffer and 10 mM H_2O_2, as shown in **Figure 3.11**. Although the reduction peak of H_2O_2 are clearly observed at both first (line i) and second scans (line ii), the peak current drops from 500 µA in the first scan to about 300 µA in the second scan. Then the electrode was placed in an ultrasonic bath for 30 s in Milli-Q water, after which cyclic voltammetry was performed again under the analogous condition respectively. The CV displays as line iii in **Figure 3.11**,

where is seen that the peak current recovers to 320 µA. Similarly, after another 3 min ultrasonic was carried out at the Ag NPs-BDDE, the peak current enhanced to 430 µA, which can be seen in line iv. This experiment result proves that the ultrasonic treatment also can be used to reactivate the electrode. The mechanism is unclear but can be understood as that the physical adsorbed molecule on the Ag NPs-BDDE surface, even some chemical adsorbed species, can be stripped off by ultrasonic treatment.

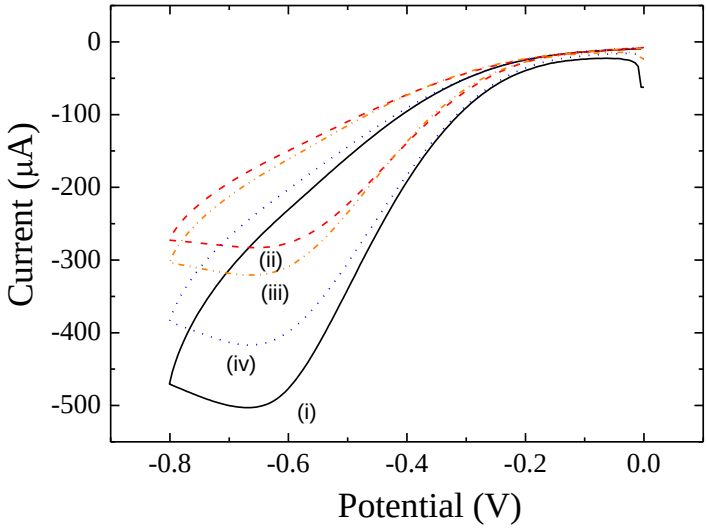

Figure 3.11 Cyclic voltammograms of two consecutive scans at Ag NPs-BDDE (i) first and (ii) second, then ultrasonic for (iii) 30 s and (iv) 30 min respectively, in a solution containing 0.1 M phosphate buffer and 10 mM H_2O_2

3.3.3 Characterisation of Hb/Ag NPs-BDDE

3.3.3.1 Surface properties of Hb/Ag NPs-BDDE

The Hb/Ag NPs-BDDE was fabricated by immersing Ag NPs-BDDE, made by electro-deposition with CTAB as surfactant, into 4 mg L^{-1} haemoglobin for 2 hours, and then rinsed by de-ionized water before use. After drying, an XPS spectrum of the Hb/Ag NPs-BDDE was recorded, as shown in **Figure 3.12**. Peaks for N 1s at 398 eV, Ag $3d_{5/2}$ at 368 eV and Ag $3d_{3/2}$ at 374 eV are clearly observed. The nitrogen peak is associated with the Hb molecule[42] and it thus indicates that the haemoglobin molecules were

successfully attached on the Ag NPs-BDDE surface. As will discussed below, Hb significantly improves the relevant electrochemical performance of diamond in the presence of Ag NPs, but not in their absence, indicating the Ag NPs are responsible for this binding of Hb in an active form to the electrode surface. Thus the Ag NPs are used to promote the electrochemical detection of H_2O_2.

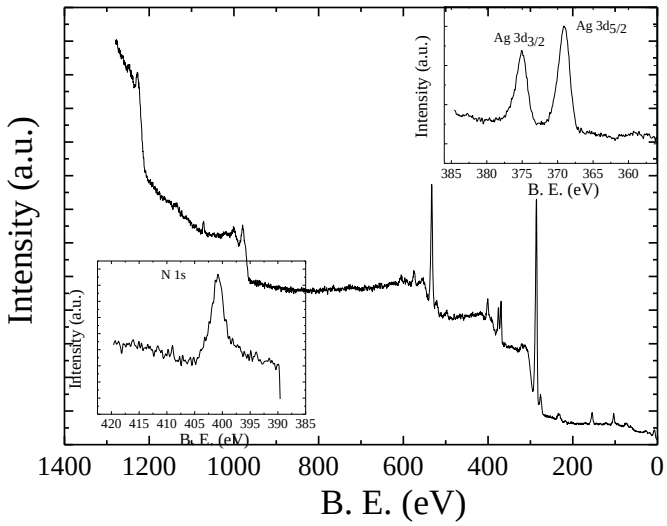

Figure 3.12 X-ray photoelectron spectroscopy spectrum of Hb/Ag NPs-BDDE

3.3.3.2 Kinetics of Hb/Ag NPs-BDDE in $[Fe(CN)_6]^{3-/4-}$ probes

Cyclic voltammetry was performed to electrochemically characterise the Hb/Ag NPs-BDDE. Electrodes were prepared by immersing in 4 mg L^{-1} Hb solution for different length of time, 0, 0.5, 30 and 120 min respectively, leading to differing extents of accumulation of Hb on the interface. **Figure 3.13** shows the CVs at these Hb/Ag NPs-BDDEs in a solution containing 0.1 M KCl as supporting electrolyte and 10mM potassium ferricyanide ($[Fe\ (CN)_6]^{3-/4-}$) as redox probe. The cyclic voltammogram obtained at Ag NPs-BDDE is also shown (line i) where the peak-peak separation is about 80 mV, showing a typical quasi-reversible electron transfer character, as normally observed for this couple at various types of diamond electrodes. At the electrode that

was dipped into haemoglobin solution for 0.5 min (line ii), some decrease in the peak currents and increase in the peak-to-peak separation are observed, showing less reactive sites of Ag NPs, as a result of the adsorption of Hb molecule onto the electrode surface.

The efficient heterogeneous rate constants for the electron transfer of potassium ferrocyanide redox at each electrode can be calculated to by *Nicholson* method [65,66]

$$k^0 = \psi[D_0 \pi \nu \left(\frac{nF}{RT}\right)^{\frac{1}{2}}](\frac{D_R}{D_o})^{\alpha/2} \qquad \text{Equation 3.4}$$

where the ψ refers to a kinetic parameter, D_0 is diffusion coefficient for the potassium ferricyanide (7.6×10^{-6} cm^2 s^{-1}), D_R is diffusion coefficient for potassium ferrocyanide (6.3×10^{-6} cm^2 s^{-1}), α is transfer coefficient (assuming 0.5) and ν is scan rate (50 mV s^{-1}).[68,69] From the measured peak-to-peak separation, and the reported diffusion coefficients for potassium ferricyanide/ferrocyaninde (7.6×10^{-6} / 6.3×10^{-6} cm^2 s^{-1})[52], the k^0 for the electron transfer at Ag NPs-BDDE was calculated as 2.4×10^{-3} cm s^{-1} which is fairly typical of analogous electrode systems.[68] Then the reaction rate constant reduced to be 4.8×10^{-4} cm^2 s^{-1} at the Hb/Ag NPs-BDDE that was immersed for 0.5 min, due to the Hb adsorption. For longer immersion time, 30 and 120 min as line iii and line iv shown in **Figure 3.13**, the peak-peak separation further increases and the peaks become more attenuated. Therefore, the reaction rate constant cannot be calculated. It indicates that more Hb molecules were adsorbed onto the surface. The results indicate that the binding of Hb is on a fairly slow time scale and long contact times with the Hb solution are needed.

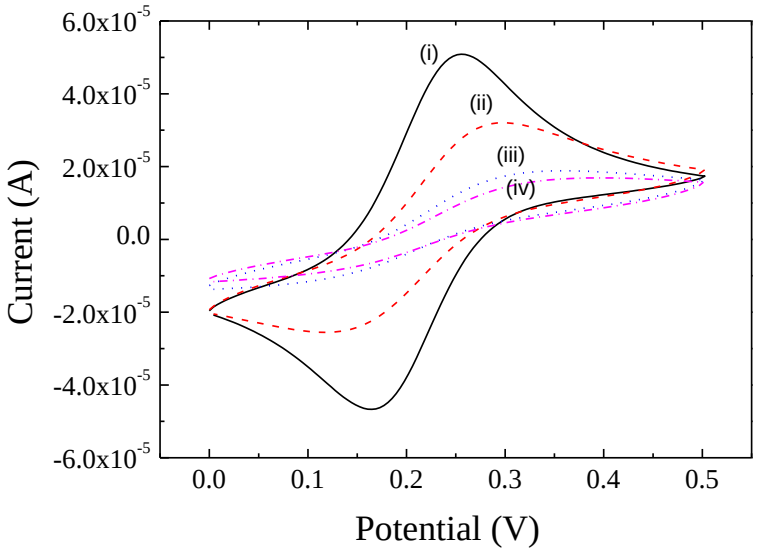

Figure 3.13 Cyclic voltammograms in 10 mM $[Fe(CN)_6]^{3-/4-}$ and 0.1 M KCl at Hb/Ag NPs-BDDEs which were dipped into 4 mg L^{-1} Hb solution for (i) 0 min, (ii) 0.5 min, (iii) 30 min and (iv) 120 min respectively

This deactivation of the electrode due to the Hb adsorption, is also shown clearly in the impedance measurement using the $[Fe(CN)_6]^{3-/4-}$ probe. These electrodes were fabricated by immersing the Ag NPs-BDDEs into Hb solution for 0, 0.5 and 2 min respectively. An open circuit potential was applied. The curves in the *Nyquist*'s diagram, shown in **Figure 3.14**, were fitted by FRA software using the normal simple equivalent circuit, comprising a faradaic charge transfer resistance and series Warburg impedance, in parallel with a double layer capacitance, all in series with a circuit resistance. It can be seen that the electron transfer resistance (ETR) increases from 1.2 to 2.3 and 5.6 kΩ, corresponding to 0, 0.5 and 2 min dipping time respectively. It indicated the drop in the heterogeneous rate constant with more Hb adsorbed onto the surface. The reaction rate constant also can be estimated in these measurements, to be 1.56×10^{-3} and 6.7×10^{-4} cm^2 s^{-1} for 0 and 0.5 min respectively, similar to the value calculated from the CV approach noted above. The charge transfer resistance continues to increase by small amounts up to immersion times of about 100 minutes, so a 2 hour

immersion time was employed in subsequent work to ensure that the adsorption of Hb on the electrode surface is saturated.

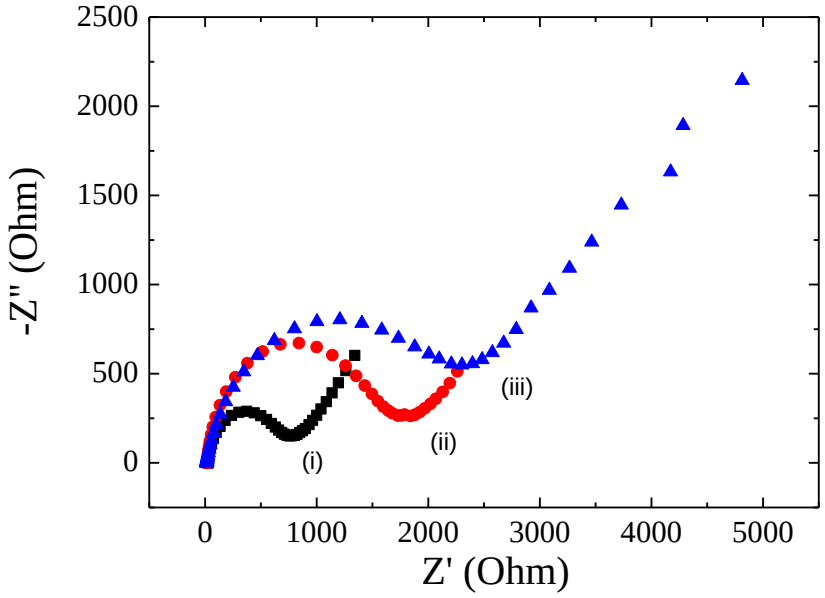

Figure 3.14 *Nyquist* impedance plots in the presence of 10 mM $[Fe(CN)_6]^{3-/4-}$ in 0.1 M KCl from 100 mHz to 0.01 Hz, at open circuit potential at Hb/Ag NPs-BDDEs which were dipped into 4 mg L^{-1} Hb solution for (i) 0, (ii) 0.5 and (iii) 2 min.

Further EIS were conducted with $[Fe(CN)_6]^{3-/4-}$ as a probe at bare-BDDE, Ag NPs-BDDE, Hb-BDDE and Hb/Ag NPs-BDDEs, as shown in **Figure 3.15**. Calculated charge transfer resistances are shown in **Table 3.3**. The charge transfer resistances at both the bare diamond electrode (line iii) and the silver modified ones (line iv) are lower than those obtained from the Hb based electrode (line i and ii) as expected, as a result of the resistance from the Hb on the electrode surface. It is interesting to note that the charge transfer resistance at the bare electrode is also significantly greater after exposing to Hb solution. This shows that it is not just the Ag treated electrode which adsorbs Hb; the bare diamond electrode must also do so. However we observe below that the Hb and Ag modified electrode perform much better for H_2O_2 detection than in the absence of Ag. So it seems that the critical role of Ag is not just to promote the binding of Hb; rather it is to promote the binding in an active form.

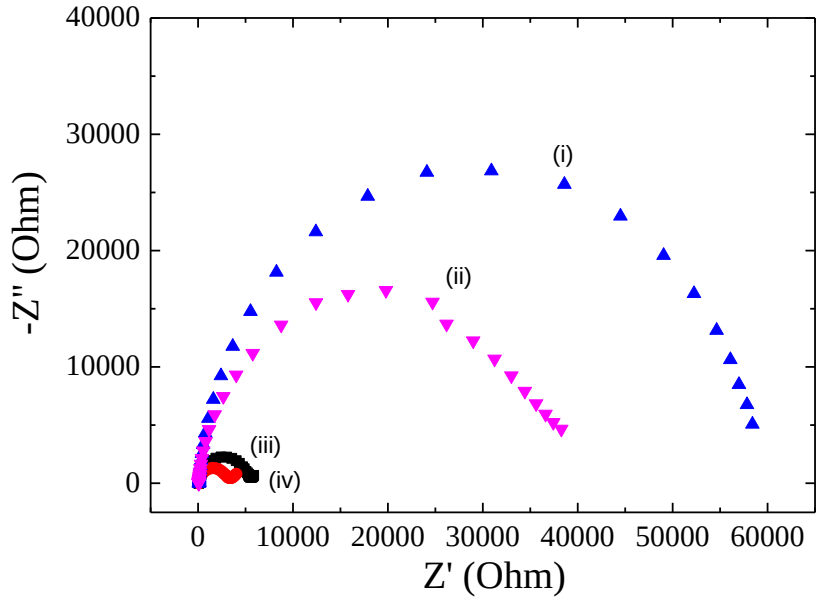

Figure 3.15 *Nyquist* impedance plots in the presence of 10 mM $[Fe(CN)_6]^{3-/4-}$ in 0.1 M KCl from 100 mHz to 0.01 Hz, at open circuit potential, at (i) Hb-BDDE and (ii) Hb/Ag NPs-BDDE, (iii) bare BDDE and (iv) Ag NPs-BDDE respectively.

3.3.3.3 Kinetics at Hb/Ag NPs-BDDE with H_2O_2 as a redox probe

Hydrogen peroxide was also used as redox probe to investigate the electrochemical activity on these electrodes and to gain some further qualitative insights. ESI were performed in a solution containing 0.1 M KCl and 10 mM H_2O_2 at bare-BDDE, Ag NPs-BDDE, Hb-BDDE and Hb/Ag NPs-BDDEs respectively. The *Nyquist's* plots are shown in **Figure 3.16**, and the electron transfer resistances are also listed in **Table 3.3**. The ETR at bare BDD is 205.5 kΩ with H_2O_2 as a probe, significantly larger than the value $[Fe(CN)_6]^{3-/4-}$ in $[Fe(CN)_6]^{3-/4-}$. However, it is down to 2.4 kΩ at Ag NPs-BDDE, close to the value obtained in $[Fe(CN)_6]^{3-/4-}$, showing that the silver particles can enhance the transfer rate from the H_2O_2 probe. The improvement of electrode transfer rate by Ag NPs also can be seen from that fact that the resistance is reduced from 44.4 kΩ at Hb-BDDE to 1.8 kΩ at Hb/Ag NPs-BDD.

On the other hand, unlike the increased resistance effect seen in $[Fe(CN)_6]^{3-/4-}$, the Hb molecule mediated catalytic activity to the H_2O_2. The ETR is decreased from 205.5 kΩ at a bare BDDE to 44.4 kΩ at a Hb-BDDE, and from 2.4 kΩ at Ag NPs-BDDE to 1.8 kΩ at the Hb/Ag NPs-BDDE, showing a promotion of Hb toward electron transfer for the H_2O_2 reaction. Note that in the presence of Ag NPs, the resistance is more than ten times lower at the Hb modified electrodes. It indicates that silver particles can boost the electron transfer between Hb and the BDDE, therefore proving the best catalysic capability towards the H_2O_2 reaction among all the diamond electrodes studied. The *Nyquist*'s plots curves for the Ag-BDDE and Hb/Ag NPs-BDDE can be seen in details from the inset in **Figure 3.16**.

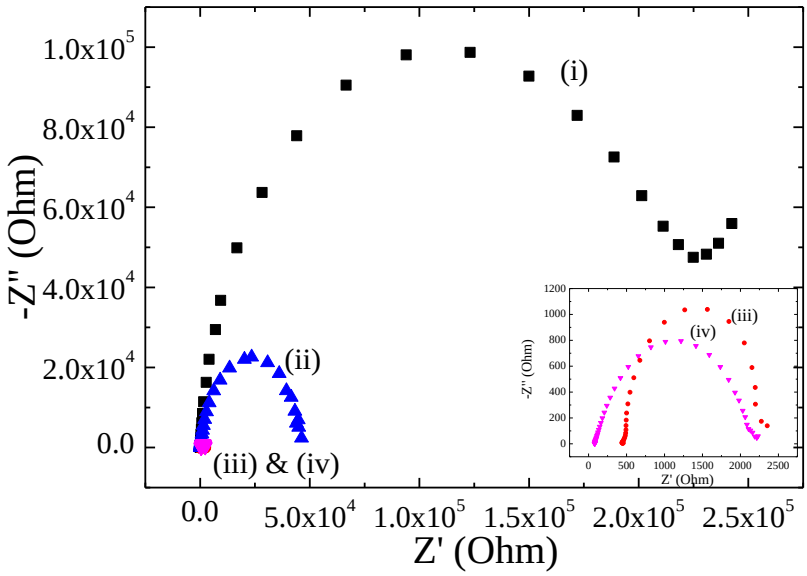

Figure 3.16 *Nyquist* impedance plots in the presence of 10 mM H_2O_2 in 0.1 M KCl from 100 mHz to 0.01 Hz, at open circuit potential, at (i) bare BDDE, (ii) Hb-BDDE, (iii) Ag NPs-BDDE and (iv) Hb/Ag NPs-BDDE respectively. Inset: zoomed in plots of (iii) and (iv)

Table 3.3 Transfer resistance using $[Fe(CN)_6]^{3-/4-}$ and H_2O_2 as redox probe at bare BDD, Ag NPs-BDD, Hb-BDD and Hb/Ag NPs-BDDEs (kΩ)

	Bare BDD	Ag NPs-BDD	Hb-BDD	Hb/Ag NPs-BDD
$[Fe(CN)_6]^{3-/4-}$	5.12	2.95	58.8	35.3
H_2O_2	205.5	2.4	44.4	1.8

3.3.4 Hb/Ag NPs-BDD for H_2O_2 detection

3.3.4.1 Determination of H_2O_2

3.3.4.1.1 Cyclic voltammetry

The detection of H_2O_2 at Hg/Ag NPs-BDDE was investigated by cyclic voltammetry first, which was carried out in 0.1 M phosphate buffer with H_2O_2 increasing from 0 to 0.1 mM, as shown in Figure **3.17**. In the absence of H_2O_2, no significant cathodic peak appears, indicating that no redox reaction occurs in this potential range. In the presence of H_2O_2, is the current increases although there is no peak maximum seen in the useful over-potential range up to +0.6 V; significant reduction currents are noted due to the reduction of H_2O_2, which are much larger (up to x 20 higher) than in the absence of Hb (**Figure 3.8**). The CV data thus confirm a very significant rise in electrode activity using the combination of Hb and Ag NPs. Since the active site of Hb is deeply buried in the protective protein matrix, direct electron exchange with an electrode is usually very difficult, such as bare diamond electrode.[70] In our case silver nanoparticles seem to provide a favourable surface to promote direct electron transfer between Hb and diamond substrate.

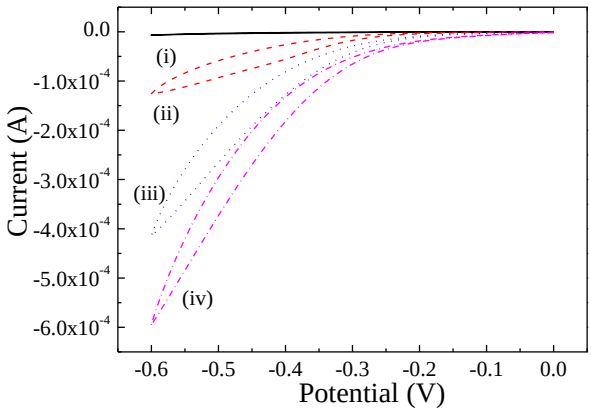

Figure 3.17 Cyclic voltammograms at Hb/Ag NPs-BDDE in solutions containing 0.1 M phosphate buffer and H_2O_2 of (i) 0 mM, (ii) 0.01 mM, (iii) 0.05 mM and (iv) 0.1 mM H_2O_2

3.3.4.1.2 Steady-state amperometry

Amperometry was performed to determine H_2O_2 and compare the analytical performance of the differing modified electrodes. Experiments were conducted with a fixed potential of -0.2 V in 0.1 M phosphate buffer at the modified BDDEs in a rotating disk electrode (RDE) configuration at 1200 revolutions per minute (rpm). After initial current stabilisation, H_2O_2 solution was successive added into the solution, which resulted in an increasing concentration. The steady state current responses are measured as a function of the H_2O_2 concentration. **Figure 3.18** shows the current response for the differing electrodes. The bare electrode (line i) and Hb diamond electrode (line ii) show no useful response at low concentrations of H_2O_2. Although the Ag modified electrode does show measurable current changes with the increase in concentration of H_2O_2, it can be seen that the Hb and Ag NPs modified electrode shows the most sensitive behaviour, with a current response which is 6× times higher. As shown in the inset good detection linearity is seen up to 8 mM and beyond. The LOD (S/N=3) of H_2O_2 at Ag NPs-BDDE was calculated to be 2.5 µM. This LOD was close to the result of CV, 1.54 µM and many Ag modified electrodes were reported around 2 µM, as shown in **Table 3.1**. At Hb/Ag NPs-BDDE, the LOD (S/N=3) can be calculated to be 0.42 µM. The noise, sensitivity and detection limit at Ag NPs-BDDE and Hb/Ag NPs-BDDE are listed in **Table 3.4**. To sum up, both Ag NPs-BDDE and Hb/Ag NPs-BDDE are capable ofH_2O_2 detection. However, because of the higher sensitivity and lower detection limit, the Hb/Ag NPs-BDDE is obviously a better choice. It is course rather difficult to compare measurements in differing laboratories to say which is the ‘best’ modified electrode, but the result seems competitive with main body of published data.

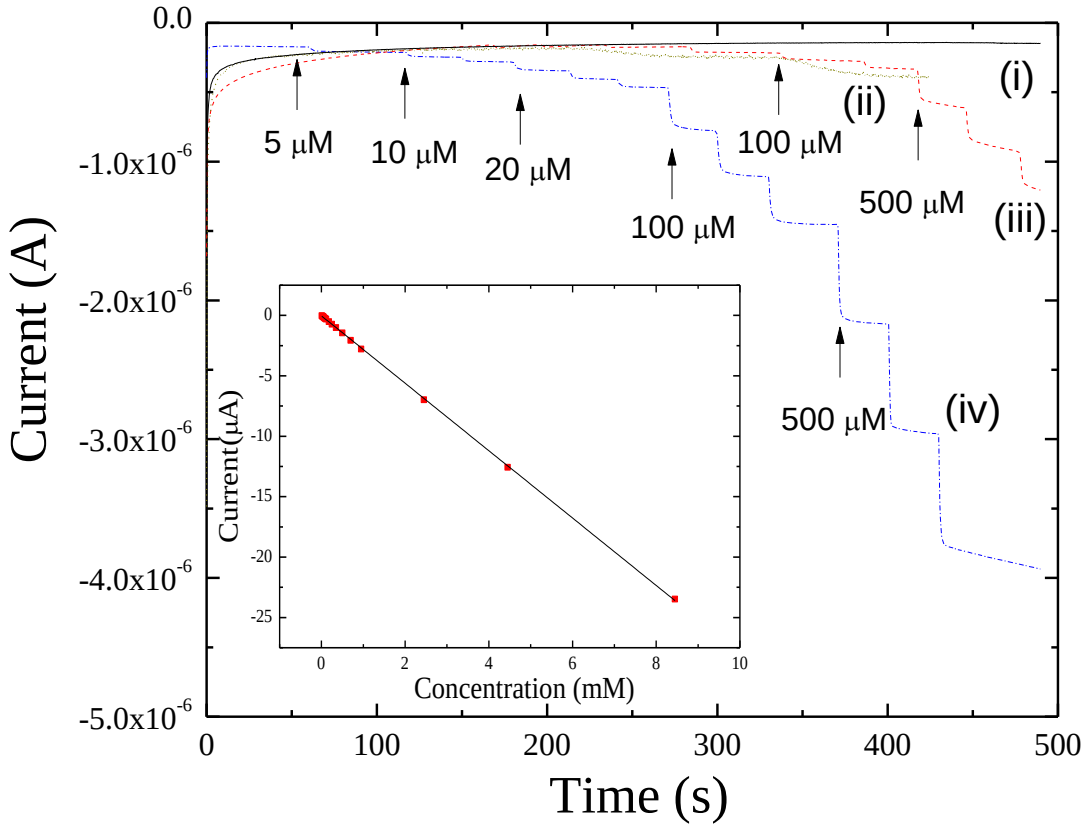

Figure 3.18 Amperometric graph at fixed potential of -0.2 V in 0.1 M phosphate buffer at (i) bare BDDE, (ii) Hb-BDDE, (iii)Ag NPs-BDDE and (iv) Hb/Ag NPs-BDDE with successive addition of H_2O_2. Inset: plot of current *vs.* H_2O_2 concentration at the Hb/Ag NPs-BDDE

3.3.4.2 Influence of different applied potential

The applied potential of 0, -0.2 and -0.4 V were all investigated for the amperometric experiments. The data at Ag NPs-BDDE and Hb/Ag NPs-BDDE are shown in **Table 3.4** for the differing potentials. Two competitive factors need to be considered, *i.e.* sensitivity and level of noise, since the detection limit is dependent on the signal-to-noise ratio. At low applied potential, the noise is significantly lower at both sensors, which benefits the detection limit. However obviously the sensitivity is reduced at the same time as the potential shifts to more positive value and the reduction process becomes reaction limited. The best results seem to be observed at around -0.2 V. At more positive potential the sensitivity drops rapidly whereas the noise from the

competing faradiac process seems to rise at more negative potentials. Overall, the optimised potential that can give a best detection limit is -0.2 V at Hb/Ag NPs-BDDE (0.42 μM) with a linear range higher than 20 mM. This result meets most of the requirements in H_2O_2 determination. For example several beverages commonly drunk by humans can contain H_2O_2 above 100 μM.[71] In human blood plasma, the level of H_2O_2 can be about 35 μM, sometimes exceeding 100 μM in urine.[71]

Table 3.4 Detection limit (μM), sensitivity (μA mM^{-1}) and noise (nA) of H_2O_2 detection at Hb/Ag NPs-BDDE and Ag NPs-BDDE (in parentheses) in applied potential of 0, -0.2 and -0.4 V

Potential	Sensitivity	noise	LOD (S/N=3)
0	0.266 (-)	0.1 (-)	1.13×10^{-6}(-)
-0.2	2.83 (0.7)	0.4 (1.0)	0.42 (4.3)
-0.4	12.48 (8.2)	20 (80)	4.81 (29)

3.3.4.3 Stability and interference

The stability and reproducibility of the Hb/Ag NPs-BDDE were studied by comparing the performance of cyclic voltammetry. After 10 days storage in 0.1 M phosphate buffer under -4℃, the response current retained about 90% of its original value. The relative standard deviation (RSD) was 0.7% for 10 measurements at the same Hb/Ag NPs-BDDE and 4.7% for 3 different electrodes prepared using the same nominal procedure.

The main interference species for hydrogen peroxide in human blood plasma include uric acid, ascorbic acid and dopamine.[41] It is reported that the concentrations of H_2O_2 in blood plasma is about 35 μM, and UA, AA and DA are typically 0.5, 0.1, and 0.5 mM respectively.[24] These species were added into an electrochemical cell with Hb/Ag NPs-

BDDE as working electrode and under the applied potentials of -0.2 V. The amperometic graph is shown in **Figure 3.19**. The current reveals the response of sensor to those species. There is hardly any current change for UA whiles a small increase for the AA and decrease for DA. However, in comparison to the signal change for H_2O_2, the contributed current changes are negligible, showing that the Hb/Ag NPs-BDDE is relatively free from the interference of these species.

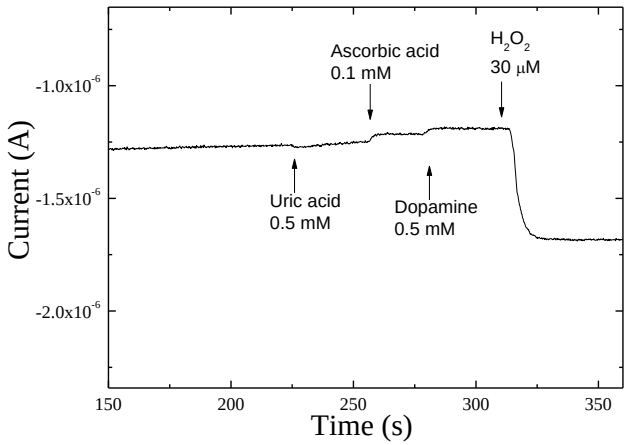

Figure 3.19 Amperometric graph at a fixed potential of -0.2 V at Hb/Ag NPs-BDDE in 0.1 M phosphate buffer with successive addition of 0.5 mM uric acid, 0.1 mM ascorbic acid, 0.5 mM dopamine and 30 μM H_2O_2

3.4 Conclusion

The present work has reported detailed studies of the fabrication of a diamond electrochemical hydrogen peroxide sensor based on the cathodic reduction of H_2O_2. Notable points to emerge from the work are as follows.

- Diamond electrodes themselves show no useful electrocatalytic response for the detection of H_2O_2.
- Methods of functionalising the electrode with Ag NPs were studied to compare differing treatments at similar silver loadings. With regard to the wet casting method of Ag NPs, the particles showed a much improved electro-response to H_2O_2 if the Ag colloidal solution was aged, leading to larger particle size and more sphere-like shape, suggesting the response depended sensitively on the particle size and shape.
- With regard to electrochemical deposition of Ag, again a dependence on Ag morphology was observed, with the one deposited in the presence of CTAB performing best.
- These electrodeposited Ag electrodes also were found to perform better than those electrodes fabricated by wet chemical deposition, with regard to adhesion and stability of the metal particles, reproducibility, LOD and sensitivity. Using the CTAB stabilised Ag NPs modified electrodes, performance similar to other modified carbon electrodes were achieved.
- The effects of introducing Hb to the electrode surface were also investigated. Hb was found to adsorb on the bare diamond electrode on a long time scale (> 100 min) improving the electrochemical response to H_2O_2, which however remained quite insensitive.

- If Hb was added in the presence of Ag NPs then a synergic effect was observed. It is proposed that Ag helps bind the Hb in an active form at the electrode surface, which in turn promotes the electrochemical reduction of H_2O_2.
- Steady-state amperometry method was used to detect the reduction of H_2O_2 by applying fixed potential and measuring the current flowing. The result showed that Hb/Ag NPs-BDD is much more sensitive than Ag NPs-BDD for the detection of H_2O_2 with consequent reduction in LOD. At an applied potential of -0.2 V a state-of-the-art LOD < 0.5 μM with a linear range to 20 mM is observed.
- The sensor was shown to show good stability and reproducibility The Hb/Ag NPs-BDDEs was also proved to be free from major interference of H_2O_2 including Glucose, Uric acid, Ascorbic acid, Dopamine.

To sum up, a new modified H_2O_2 biosensor has been investigated in this work, based on the combination of the Hb molecule and Ag NPs on the BDDE substrate. This sensor provides a detection limit down to micro-molar level and a wide detection range up to 20 mM, which is very competitive to other H_2O_2 sensors, together with other advantages of high stability, reproducibility and freedom from major interference.

References

(1) Jones, C. W. *Application of Hydrogen Peroxide and Derivatives*; The royal society of chemistry: Cambridge, 1999.

(2) Gubler, L.; Koppenol, W. H. *Journal of the Electrochemical Society* **2012**, *159*, B211.

(3) Niethammer, P.; Grabher, C.; Look, A. T.; Mitchison, T. J. *Nature* **2009**, *459*, 996.

(4) D'Autreaux, B.; Toledano, M. B. *Nat. Rev. Mol. Cell Biol.* **2007**, *8*, 813.

(5) Rhee, S. G. *Science* **2006**, *312*, 1882.

(6) Rhee, S. G.; Chang, T. S.; Jeong, W.; Kang, D. *Mol. Cells* **2010**, *29*, 539.

(7) Hurdis, E. C.; Romeyn, H. *Analytical Chemistry* **1954**, *26*, 320.

(8) Chen, W.; Cai, S.; Ren, Q. Q.; Wen, W.; Zhao, Y. D. *Analyst* **2012**, *137*, 49.

(9) Chen, S. H.; Yuan, R.; Chai, Y. Q.; Hu, F. X. *Microchimica Acta* **2013**, *180*, 15.

(10) Luong, J. H. T.; Male, K. B.; Glennon, J. D. *Analyst* **2009**, *134*, 1965.

(11) Nekrassova, O.; Lawrence, N. S.; Compton, R. G. *Analyst* **2004**, *129*, 804.

(12) Chailapakul, O.; Siangproh, W.; Tryk, D. A. *Sensor Letters* **2006**, *4*, 99.

(13) Panizza, M.; Cerisola, G. *Electrochimica Acta* **2005**, *51*, 191.

(14) Welch, C. M.; Hyde, M. E.; Banks, C. E.; Compton, R. G. *Analytical Sciences* **2005**, *21*, 1421.

(15) Zhang, Y.; Wilson, G. S. *Journal of Electroanalytical Chemistry* **1993**, *345*, 253.

(16) Lee, K. S.; El-Sayed, M. A. *Journal of Physical Chemistry B* **2006**, *110*, 19220.

(17) Lin, L.; Qiu, P. H.; Cao, X. N.; Jin, L. T. *Electrochimica Acta* **2008**, *53*, 5368.

(18) Simm, A. O.; Banks, C. E.; Ward-Jones, S.; Davies, T. J.; Lawrence, N. S.; Jones, T. G. J.; Jiang, L.; Compton, R. G. *Analyst* **2005**, *130*, 1303.

(19) Bui, M. P. N.; Pham, X. H.; Nan, K. N.; Li, C. A.; Kim, Y. S.; Seong, G. H. *Sensors and Actuators B-Chemical* **2010**, *150*, 436.

(20) Wu, S.; Zhao, H.; Ju, H.; Shi, C.; Zhao, J. *Electrochemistry Communications* **2006**, *8*, 1197.

(21) Liu, S.; Tian, J. Q.; Wang, L.; Sun, X. P. *Journal of Nanoparticle Research* **2011**, *13*, 4539.

(22) Chen, H.; Zhang, Z.; Cai, D.; Zhang, S.; Zhang, B.; Tang, J.; Wu, Z. *Talanta* **2011**, *86*, 266.

(23) Zhao, B.; Liu, Z. R.; Liu, Z. L.; Liu, G. X.; Li, Z.; Wang, J. X.; Dong, X. T. *Electrochemistry Communications* **2009**, *11*, 1707.

(24) Karyakin, A. A.; Karyakina, E. E. *Sensors and Actuators B-Chemical* **1999**, *57*, 268.

(25) Zhou, M. J.; Diwu, Z. J.; PanchukVoloshina, N.; Haugland, R. P. *Anal. Biochem.* **1997**, *2*, 162.

(26) Kondo, T.; Tamura, A.; Kawai, T. *Journal of the Electrochemical Society* **2009**, *156*, F145.

(27) Wang, Q.; Kromka, A.; Houdkova, J.; Babchenko, O.; Rezek, B.; Li, M. S.; Boukherroub, R.; Szunerits, S. *Langmuir* **2012**, *28*, 587.

(28) Mueller, S.; Millonig, G.; Waite, G. N. *Adv. Med. Sci.* **2009**, *54*, 121.

(29) Liu, M. C.; Zhao, G. H.; Qi, Y. *International Journal of Environmental Analytical Chemistry* **2012**, *92*, 534.

(30) Welch, C. M.; Banks, C. E.; Simm, A. O.; Compton, R. G. *Anal. Bioanal. Chem.* **2005**, *382*, 12.

(31) Ding, Y.; Wang, Y.; Li, B. K.; Lei, Y. *Biosensors & Bioelectronics* **2010**, *25*, 2009.

(32) Ma, L. P.; Yuan, R.; Chai, Y. Q.; Chen, S. H. *Journal of Molecular Catalysis B-Enzymatic* **2009**, *56*, 215.

(33) Salimi, A.; Noorbakhsh, A.; Mamkhezri, H.; Ghavami, R. *Electroanalysis* **2007**, *19*, 1100.

(34) Salimi, A.; Hallaj, R.; Soltanian, S.; Mamkhezri, H. *Analytica Chimica Acta* **2007**, *594*, 24.

(35) Feng, J. J.; Zhao, G.; Xu, J. J.; Chen, H. Y. *Analytical Biochemistry* **2005**, *342*, 280.

(36) Wang, S.; Xie, F.; Liu, G. *Talanta* **2009**, *77*, 1343.

(37) Zhu, J. T.; Shi, C. G.; Xu, J. J.; Chen, H. Y. *Bioelectrochemistry* **2007**, *71*, 243.

(38) Shan, D.; Cheng, G.; Zhu, D.; Xue, H.; Cosnier, S.; Ding, S. *Sensors and Actuators B: Chemical* **2009**, *137*, 259.

(39) Shan, D.; Wang, S.; Xue, H.; Cosnier, S. *Electrochemistry Communications* **2007**, *9*, 529.

(40) Zhang, J. D.; Oyama, M. *Electrochimica Acta* **2004**, *50*, 85.

(41) Xu, Y. X.; Hu, C. G.; Hu, S. S. *Sensors and Actuators B-Chemical* **2008**, *130*, 816.

(42) Yu, C. M.; Zhou, X. H.; Gu, H. Y. *Electrochimica Acta* **2010**, *55*, 8738.

(43) Doty, R. C.; Tshikhudo, T. R.; Brust, M.; Fernig, D. G. *Chemistry of Materials* **2005**, *17*, 4630.

(44) Pastoriza-Santos, I.; Liz-Marzán, L. M. *J. Mater. Chem.* **2008**, *18*, 1724.

(45) Pastoriza-Santos, I.; Liz-Marzán, L. M. *Nano Letters* **2002**, *2*, 903.

(46) Alvarez-Puebla, R. A.; Aroca, R. F. *Analytical Chemistry* **2009**, *81*, 2280.

(47) Gentry, S. T.; Fredericks, S. J.; Krchnavek, R. *Langmuir* **2009**, *25*, 2613.

(48) Futamata, M.; Maruyama, Y.; Ishikawa, M. *Vibrational Spectroscopy* **2002**, *30*, 17.

(49) Mock, J.; Barbic, M.; Smith, D.; Schultz, D.; Schultz, S. *The Journal of Chemical Physics* **2002**, *116*, 6755.

(50) Maruyama, Y.; Ishikawa, M.; Futamata, M. *Chem. Lett.* **2001**, 834.

(51) R.W.Cahn; P.Haasen; E.J.Kramer *Materials Science and Technology: a comprehensive treatment*; VCH, 1992; Vol. 2A.

(52) Granger, M. C.; Swain, G. M. *Journal of the Electrochemical Society* **1999**, *146*, 4551.

(53) Gregg, B. A.; Heller, A. *The Journal of Physical Chemistry* **1991**, *95*, 5970.

(54) Campbell, F. W.; Belding, S. R.; Baron, R.; Xiao, L.; Compton, R. G. *Journal Of Physical Chemistry C* **2009**, *113*, 9053.

(55) Sun, Y. G.; Xia, Y. N. *Science* **2002**, *298*, 2176.

(56) Honda, M.; Kodera, T.; Kita, H. *Electrochimica Acta* **1983**, *28*, 727.

(57) Honda, M.; Kodera, T.; Kita, H. *Electrochimica Acta* **1986**, *31*, 377.

(58) Flatgen, G.; Wasle, S.; Lubke, M.; Eickes, C.; Radhakrishnan, G.; Doblhofer, K.; Ertl, G. *Electrochimica Acta* **1999**, *44*, 4499.

(59) Westbroek, P.; Temmerman, E.; Kiekens, P. *Analytica Chimica Acta* **1999**, *385*, 423.

(60) Galus, Z. *Fundamentals of Electrochemical Analysis*; Ellis Horwood: New York, 1994.

(61) Kondo, T.; Einaga, Y.; Sarada, B. V.; Rao, T. N.; Tryk, D. A.; Fujishima, A. *Journal of the Electrochemical Society* **2002**, *149*, E179.

(62) Liu, H. G.; Wen, M.; Zhang, F.; Liu, D.; Tian, Y. *Analytical Methods* **2010**, *2*, 143.

(63) Suslick, K. S. *Kirk-Othmer Encyclopedia of Chemical Technology* **1998**.

(64) Mason, T.; Paniwnyk, L.; Lorimer, J. *Ultrasonics sonochemistry* **1996**, *3*, S253.

(65) Nicholso.Rs *Analytical Chemistry* **1965**, *37*, 1351.

(66) Bard;, A. J.; Faulkner, L. R. *Electrochemical methods-Fundamentals and application* Danvers, 2001.

(67) Kadara, R. O.; Jenkinson, N.; Banks, C. E. *Sensors and Actuators B-Chemical* **2009**, *138*, 556.

(68) Adams, R. N. *Electrochemistry at solid electrodes*; Marcel Dekker, INC; New York and Basel, 1969.

(69) Sawyer, D.; Roberts, J. L. *Experimental Electrochemistry for Chemists*; John Wiley and Sons, 1974.

(70) Zhao, Y. D.; Bi, Y. H.; Zhang, W. D.; Luo, Q. M. *Talanta* **2005**, *65*, 489.

(71) Halliwell, B.; Clement, M. V.; Long, L. H. *Febs Letters* **2000**, *486*, 10.

Chapter 4 Electrochemical Synthesis of Ag NPs at Hb-BDDE with Protection of PVP in Aqueous Phase

4.1 Introduction

Metallic nanopowders are of great importance as modern materials because of their unique optical, thermal, chemical and physical properties, correlating to the large surface-bulk ratio and nano-scale effects.[1,2] Among various metal nanoparticles, silver nanoparticles (Ag NPs) are especially attractive due to the highest electrical conductivity and thermal conductivity among all metals, characteristic of silver combined with unusual optical properties such as surface-enhanced Raman scattering, and effective biocidal ability whilst maintaining nontoxicity to human cells.[1,3-9] These properties are highly dependent on the size and shape of nanoparticles.[10,11] Therefore size and shape control are critical in nanomaterials manufacture. Small metal particles are usually prepared by chemical reduction of metal salts, and normally involve using powerful agents like $NaBH_4$ to reduce silver ions, then applying hard templates or softer directing agents to control the size and shape.[3,12,13] However, this method suffers from several drawbacks, including complicated multi-step procedures, toxic reagents and difficult purification. Since Reetz and co-workers reported the electrochemical synthesis of Pb-, Ni- and Pt/Pd colloids, this method became an alternative to yield nano-size transition metal particles.[13,14] Metal NPs synthesised by electrochemical methods are of high purity and the size and shape can be easily controlled by adjusting current density or applied over-potential.[15] At the same time, electrochemical synthesis also has some advantages in terms of cheap equipment, green agents, easy operation, and the potential to large quantity manufacture.

The electrochemical synthesis of silver nanoparticles was first reported by Sanchez, *et al.*[16] The experiment was carried out on a two-electrode system with silver sheet as the anode and platinum sheet as the cathode in the solution containing tetrabutylammoium bromide and acetonitrile. Controlled-current electrolysis was applied with a typical current of 1.25 mA and a typical potential around -2.75 V. The size of Ag NPs obtained was around 6 nm. Various factors were involved in this synthesis, including effects of the solvent, charge flow, current density, distance between electrodes, nature of the ammonium salt and temperature.[13] It is reported that silver particles can be obtained when using tetrabutylammonium bromide or acetate as the supporting electrolyte, but not in 0.1 M $NaClO_4$ solution.[16] It is also reported that platinum can be used as cathode, but aluminium always lead to electrochemical deposition on the surface due to the similarity between silver and aluminium in terms of lattice parameter and atomic radius.[16] The average size of nanoparticles was increased with higher polarity of medium and increasing experiment time (total charge flow), but decreased with higher current.

The most serious problem for electrochemical synthesis is the competition between particle formation and electrochemical deposition at the cathode surface.[16] Resolutions to solve the problem have been proposed including applying external excitation systems such as ultra-sonication or seeking new solution stabilizers. Yin *et al.* found the anionic stabiliser poly(N-vinylpyrrolidone) (PVP) can accelerate Ag NPs formation and lower silver deposition on the cathode, although the mechanism was still under debate.[17] It is proposed, as shown in **Figure 4.1** that with its polar groups, PVP can trap silver ions to form a Ag_m^{m+}-PVP complex which may obtain electrons more easily from the cathode than Ag ions in water. Thus the PVP played a role in promoting silver nucleation and inhibiting grain growth and particle aggregation. The ultrasonication system was also

introduced to enhance the movement of reduced particles, therefore improving the formation of Ag NPs in the aqueous phase. However silver electro-deposition still took place simultaneously, diminishing the effective surface for particle production.[11,16,17] On the other hand, the high negative applied potential, -2.75 V, also led to the interference of oxygen which is reduced at -1.5 V. Therefore, the solution must be oxygen free and under an inert atmosphere during the electrolysis. This is an inconvenience during electrochemical synthesis.

In recent years, carbon based electrodes, like the glassy carbon electrode and boron doped diamond electrode, have gradually replaced the metal electrode because of the advantages of a wide cathodic potential range, long-term stability, low background current and reproducibility. However no carbon based electrode has been used for electrochemical synthesis of metal nanoparticles so far. In this work, the electrochemical synthesis of Ag NPs was carried out at haemoglobin adsorbed boron doped diamond electrode (Hb-BDDE) in PVP and $AgNO_3$ solution. Diamond is of interest in part since it is known that many metal nanoparticles display poor adhesion on the electrode surface. This tendency was further enhanced through the use of the Hb molecule adsorbed on the BDDE surface which can accelerate the electron transfer and protect the surface from silver deposition. The reduced Ag_m^{m+}-PVP complex then can enter the solution and grow in aqueous phase gradually.

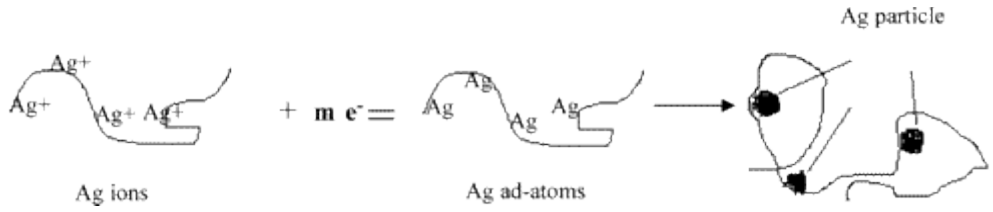

Figure 4.1 Schematic diagram showing formation of electrochemically produced PVP-stabilised silver clusters[17]

4.2 Experimental

4.2.1 Reagents

PVP, CTAB, SDS and sodium citrate were obtained from Sigma-Aldrich and were of A.C.S. reagent grade. Hb solution was prepared by dissolving 4 mg Hb into 1 mL water and was stored at 4 ºC. The Nafion solution (5 w.t.%, 0.874 g mL^{-1} at 25ºC) in lower aliphatic alcohols and water was purchased from Sigma-Aldrich and diluted by water to 4 mg mL^{-1}. Other chemicals and regular electrochemical methods have been described in previous chapters.

4.2.2 Electrochemical synthesis of Ag NPs and Apparatus

The electrochemical synthesis of Ag NPs was performed in the solution containing 0.1 M Ac buffer, 10 mM PVP and 10 mM $AgNO_3$ in a three-electrode system. Platinum was used as the counter electrode, and all potentials were measured against Ag/AgCl reference electrode through a salt bridge (0.1 M $NaNO_3$) to prevent reaction between chloride ions from Ag/AgCl and silver ions in solution. The working electrode was fabricated by immersing cleaned BDDE into 4 mg mL^{-1} Hb solution for 4 hours. A fixed voltage of -1 V was applied between Hb-BDDE and Pt electrode for 1000 s, at which potential silver ions were able to be reduced. The current was measured as shown in **Figure 4.2**; a typical current value was 0.7 mA. The solution was colourless initially and turned into pink during the electrochemical process, corresponding to the Ag NPs with a triangle shape and a size smaller than 10 nm according to the literature.[18] After synthesis, the colour changed to light yellow gradually, and then developed to dark yellow subsequently when the sediment started to form and the particles aggregated. This aggregation process could be accelerated by ultracentrifuge if desired. Note that

this Ag NPs suspension contained Ag NPs, PVP, Na^+, Ag^+, Ac^- and NO_3^-. The yield by this method will be calculated and discussed in subsequent work. SEM, XPS, UV-vis, XRD and DLS were applied to characterise the synthesised Ag NPs.

In order to discuss the factors that influenced the synthesis, some variations to the procedure were afforded, including using glassy carbon to replace BDDE; using Nafion to replace haemoglobin molecules; using SDS, CTAB, sodium citrate to replace the PVP. Details will be discussed in the discussion section, and the mechanism will be proposed.

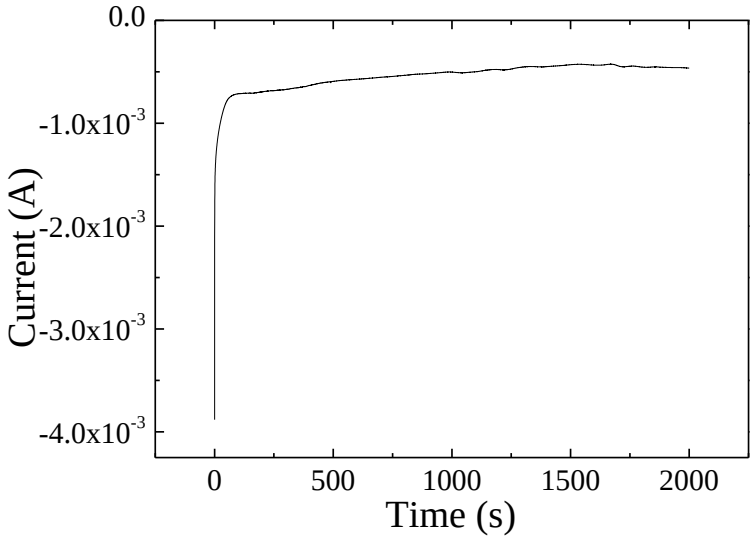

Figure 4.2 Amperometric graph at applied potential of -1 V at Hb-BDDE in a solution containing 0.1 M Ac buffer, 10 mM PVP and 10 mM $AgNO_3$

4.3 Results

4.3.1 Characterisation of Hb-BDDE

4.3.1.1 X-ray photoelectron spectroscopy

The surface composition and film thickness of Hb/BDDE was analysed by X-ray photoelectron spectroscopy after immersion of the electrode in the Hb solution for 120

minutes, followed by removal, rinsing and drying. The XPS spectrum shown in **Figure 4.3** was calibrated by the binding energy of C 1s at 284.6 eV according to the NIST X-ray Photoelectron Spectroscopy Database. Two other significant peaks are observed at 398.4 and 530.9 eV, corresponding to N 1s and O 1s. From Michigan State University data base[19], the XPS atomic sensitivity factors for oxygen, nitrogen and carbon are 0.66, 0.42 and 0.25 respectively. Then the molar ratio of carbon, nitrogen and oxygen on Hb-BDDE was calculated to be 51%, 22% and 27%. Although haemoglobin is a natural organic compound and does not have an exact molecule formula, it can be represented by the empirical formula. However, the formula varies in different databases. From Sigma Aldrich, Scifinder data base and RCSB Protein data bank, the ratio of C in Hb molecule can be in the range of 42-76%, N is about 15-46%, and O is about 8-20%. The ratio of C and N obtained from our XPS experiment are in this range but the ratio of O is relatively high. The high O ratio might be a result from the adsorption of oxygen on Hb molecule and BDD surface.

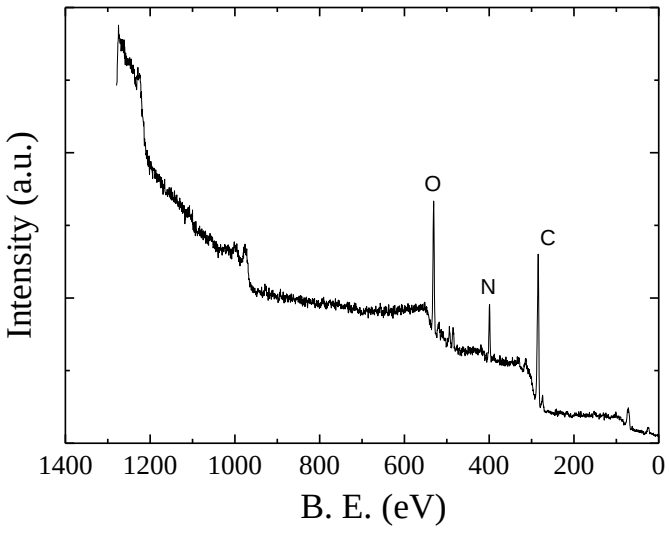

Figure 4.3 X-ray photoelectron spectrum of Hb-BDDE

Considering that the C:N obtained from Hb-BDDE is close to the theoretical value in Hb molecule, this carbon signal in XPS can be considered to be mostly attributed to the Hb molecule. The minimum layer thickness can be estimated by assuming that the probability of the photoelectron escaping from BDDE surface must be quite small, say less than 10%, otherwise a stronger C is signal would be seen in the spectrum. The depth of sample can be given by the equation as follows,

$$d = -\lambda \cos\theta \ln(\varphi) \qquad \text{Equation 4.1}$$

where λ is the electron inelastic mean free path (IMFP), θ is the photoelectron emission angle used and φ is the possibility of the photoelectron escaping from BDD surface without losing energy. The IMFP of carbon in diamond at kinetic energy of 1202 eV is about 19 Å, according to the database from National Institute for Materials Science.[20,21] Taking θ to be 90 degrees and φ to be 10%, the minimum depth of sample is calculated to be *ca.* 5.7 nm. Since the thickness of single molecule layer of haemoglobin was reported to be 3.8 nm by use of an optical method,[22] the sample depth at Hg-BDDE suggests that there must be at least one dense layer of Hb on BDD surface.

4.3.1.2 Cyclic voltammetry in $[Fe(CN)_6]^{3-/4-}$ and $FcOH^{0/+1}$ probes

The XPS measurement above suggests Hb adsorbs on the electrode surface even in the absence of Ag. However this is an ex-situ measurement method. Electrochemistry was used in addition therefore as an in situ probe. In *Chapter 3*, cyclic voltammetry of 10 mM potassium ferricyanide at Hb/Ag-BDDE have been represented in **Figure 3.13**. It is shown that the electrochemical response of $[Fe(CN)_6]^{3-/4-}$ redox decayed as the electrode was immersed into Hb solution for longer time, consistent with Hb adsorbed onto the Ag-BDDE surface thereby altering the surface chemical properties. The same

phenomenon is observed at Hb-BDDE as well. **Figure 4.4**a shows cyclic voltammograms in a solution containing 0.1 M KCl and 10 mM potassium ferricyanide at Hb-BDDEs which were immersed in Hb solution for different time lengths from 0 to 10 hours and washed by water before use. The initial curve is obtained at the bare BDDE, *i.e.* the black line of 0 min, where a typical reversible pair of redox peaks of $[Fe(CN)_6]^{3-/4-}$ can be observed at *ca.* +0.16/+0.27 V. With the increasing immersing time, the peak current of both oxidation and reduction declined gradually. And the peak-peak separation became wider. Taking the initial peak current at bare BDDE as 100%, then the peak current at Hb-BDDE can be represented by the percentage of the initial value. These percentages against immersing time are plotted in **Figure 4b**, where a sharp decay in the first 20 min can be observed. Then the response for $[Fe(CN)_6]^{3-/4-}$ dropped to 37% at Hb-BDDE after dipping into Hb solution for 35 min, and approached a limiting value of 27% after 120 min.

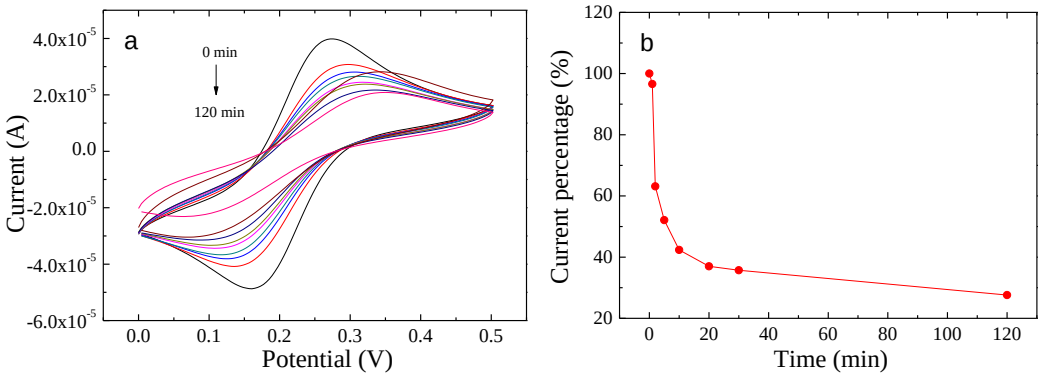

Figure 4.4 (a) Cyclic voltammograms in a solution containing 0.1 M KCl as supporting electrolyte and 10 mM $[Fe(CN)_6]^{3-/4-}$ at Hb-BDDEs which were fabricated by immersing BDDE into 4 mg mL^{-1} Hb solution from 0 to 10 hours (0, 0.5, 1, 2, 5, 10, 20, 30, and 120 min); (b) plot of the percentage of oxidation peak current *vs.* immersing time

The cyclic voltammetry was also carried out in 10 mM ferrocenemethanol at Hb-BDDE which was immersed in 4 mg mL^{-1} Hb solution from 0 to 5 hours, as shown in **Figure 4**a. The typical redox peak of $FcOH^{0/+1}$ appears at *ca.* +0.16/+0.25 V, which is clearly

observed at bare BDDE. As the electrode was dipped into Hb solution for longer time, the peak current decreases and the peak-peak separation is enlarged. Taking the peak current at bare electrode as the initial value, the plot of the percentage of each peak current against immersing time is displayed in **Figure 4b**. It is apparent that the current drops at the first 20 min to 70% and keeps decreasing gradually to about 55% at 120 min.

To sum up and compare, when BDDE was dipped into Hb solution for longer time, the response to $[Fe(CN)_6]^{3-/4-}$ and $FcOH^{0/+1}$ were both getting weaker, indicating that more Hb molecule was adsorbed on to the BDD surface and blocked active sites on the surface. However, the current decrease of $FcOH^{0/+1}$ is much more rapid because $[Fe(CN)_6]^{3-/4-}$ is a typical 'inner-sphere' probe and extremely sensitive to the surface chemistry and microstructure while $FcOH^{0/+1}$ is a 'outer-sphere' probe.

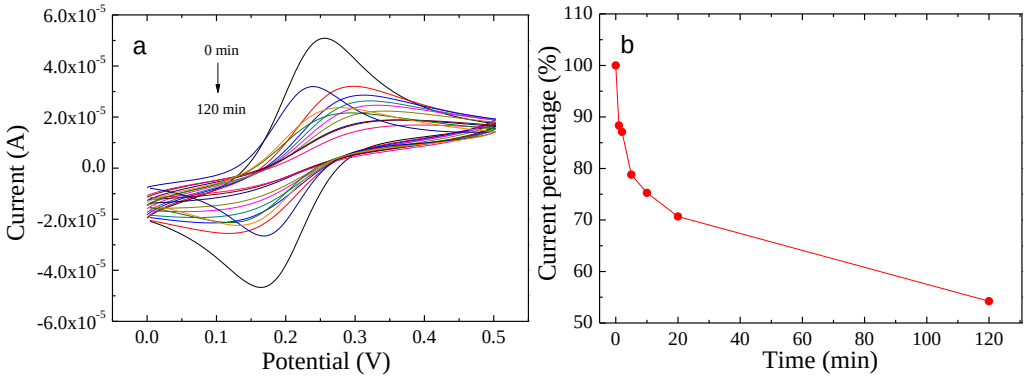

Figure 4.5 (a) Cyclic voltammograms in a solution containing 0.1 M KCl as supporting electrolyte and 10 mM $FcOH^{0/+1}$ at Hb-BDDEs which was fabricated by immersing BDDE into 4 mg mL^{-1} Hb solution for 0, 0.5, 1, 2, 5, 8, 10, 20, 60 and 120 min; (b) plot of the percentage of oxidation peak current *vs.* immersing time

4.3.2 Characterisation of Ag NPs

4.3.2.1 Scanning electron microscopy

The Hb-BDDE was used to manufacture Ag NPs by the procedure described in the experimental section. The morphology of the synthesised Ag NPs was investigated by SEM, with a focus on two types of Ag NPs suspension. One was the fresh Ag NPs which is light yellow colour for up to several hours after synthesis. The other was the aged Ag NPs that was kept in a bottle for 3 days until sediment appeared, with dark yellow colour. Both samples were prepared by dropping 100 μL Ag NPs suspension onto 0.64 cm^2 Si substrate and dried in the open air. The SEM images of both samples are exhibited in **Figure 4.6**. **Figure 4.6**a shows the morphology of fresh sample, and **Figure 4.6**b is the aged sample. It can be observed that the Ag NPs in initial solution are spherical in shape. The particles are well dispersed and uniform with approximately 50 nm in radius. However, the literature states that the size of Ag NPs with a light yellow colour should be about 10 nm. One reason for the larger size observed from SEM might be that the Ag NPs aggregated when drying in open air on the silicon substrate, because during drying the concentration of Ag NPs increases. Another reason may be that the Ag NPs of smaller sizes were hard to observe due to the interference from large Ag NPs and the limitation of maximum resolution of this equipment. **Figure 4.6**b shows SEM image for aged Ag NPs, where a thick polymer layer is displayed. This polymer layer is considered to be attributed to the cross linked PVP, which will be discussed in subsequent work. Also observed are some large size particles buried in the polymer. It suggests that silver NPs were captured and buried in the film after aging and drying on the silicon substrate. The size of aged Ag NPs is obviously much larger than the one in

fresh sample, and hard to measure because most of them were under the cover of PVP polymer.

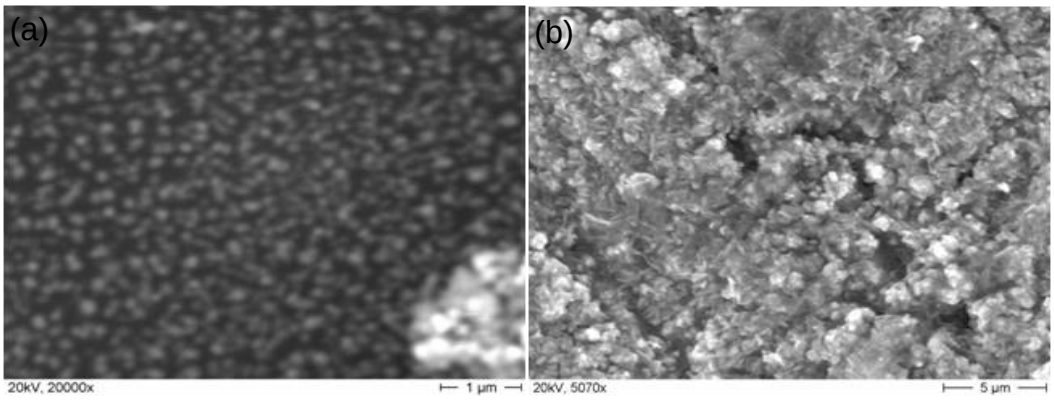

Figure 4.6 Scanning electron microscopy images of silver nano-particles that are (a) within 2 hours after preparation; (b) kept in a bottle open to air for 3 days on Si substrate.

4.3.2.2 X-ray photoelectron spectroscopy

XPS was performed to analyse the aged Ag NPs sample prepared by dropping 100 µL suspensions onto a BDD substrate then rinsing in water to eliminate the solute including Ag NO_3, Ac buffer and extra PVP. The narrow range spectrum is displayed in **Figure 4.7**, from 250 to 500 eV in banding energy, and the wide range spectrum can be seen in the inset. The profile was calibrated by the peak of C 1s of which the binding energy locates at 284.6 eV. The typical peaks of silver at 368.3 eV for Ag $3d_{5/2}$ and 374.2 eV for Ag $3d_{3/2}$ can be observed. Also observed is the peak at 398 eV for N 1s. Since the bonding energy of N 1s in $AgNO_3$ is 406.6 eV, this peak at 398 eV should be attributed to the N in PVP molecule. Taking the atomic sensitivity factors of N and Ag to be 0.42 and 5.2 respectively, the ratio of nitrogen to silver can be calculated to be 11:1. The molecule ratio of PVP *vs.* Ag NPs was also roughly calculated for the sediment precipitate. Since NO_3^- and extra PVP should have been washed out by water before

experiment, it can be assumed the N was mostly originated from PVP that trapped Ag NPs. The Ag particle size was analysed to be smaller than 10 nm by UV-vis, 8 nm by DLS and 4.4 nm by XRD. It is assumed Ag NPs are all of solid sphical shape, with an average size of Ag NPs of 7 nm and the *Van Der Waals radius* of one silver atom to be 172 pm[23], the atom number of each Ag NPs can be calculated to be 6.7×10^4. Since the linear formula of PVP is $(C_6H_9NO)_n$ and the average M_w of PVP is about 40000, the N atom number of each PVP chain can be roughly calculated to be 360. Because the N:Ag is 11:1, the ratio of PVP molecule: Ag NPs molecule is about 1200:1. Due to the limitation of the surface sensitivity of XPS, this is likely to be an overestimate. Nonetheless this ratio is much more concentrated than in the solution. This supports the assumption that PVP is implicitly involved in capturing Ag produced in the solution by this synthetic method.

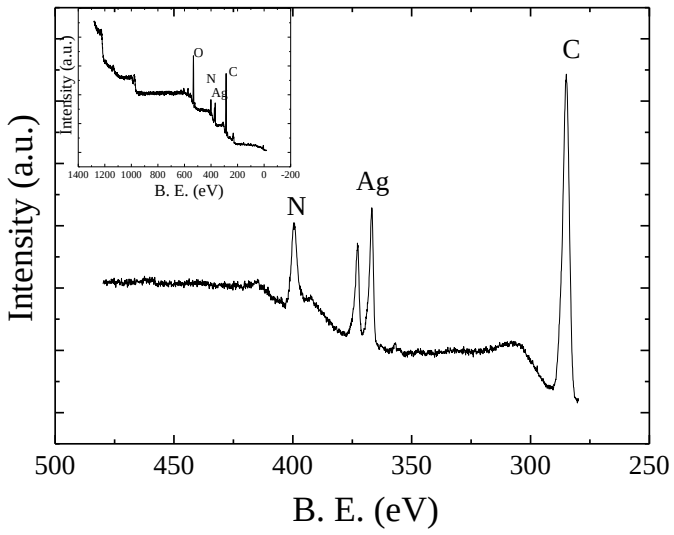

Figure 4.7 The X-ray photoelectron spectroscopy images of Ag NPs sample on BDD substrate from 250 to 500 eV in band energy. Inset: wide range spectrum from 0 to 1248 eV in band energy

For comparison, the XPS was also carried on the Ag NPs purchased from Sigma Aldrich. The Ag NPs solution was diluted to 50 mg L^{-1} which is close to the theoretical density of the Ag NPs suspension in this work (see below). Then the diluted solution

was drop-coated onto the BDD surface, rinsed by water and dried before doing the XPS. The XPS spectra in the binding energy window of 300 to 450 eV for both sample are compared and shown in **Figure 4.8**, where a is for Ag NPs from Sigma Aldrich and b is for Ag NPs obtained in this work. In both images, two peaks at 368 and 374 eV can be observed, which belong to Ag $3d_{5/2}$ and $3d_{3/2}$ respectively. However, the intensity for the sample from this work is lower than the sample from Sigma Aldrich. The data suggests the picture obtained above from the SEM that the aggregated precipitate does indeed contain silver but it also contains a significant amount of PVP, in contrast to the samples prepared from the suspended silver particles.

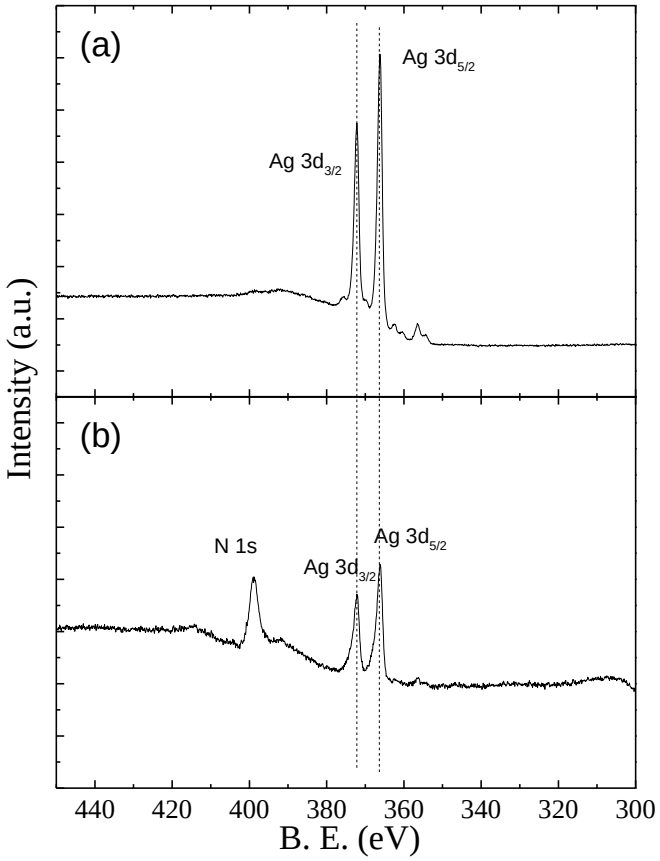

Figure 4.8 The X-ray photoelectron spectroscopy images of Ag NPs from (a) Sigma Aldrich and (b) this work.

4.3.2.3 UV-visible spectroscopy

UV-visible spectroscopy is a routinely applied method in analytical chemistry by using the light in the visible and adjacent range to excite electrons in the species of interest, to thereby record an absorption spectrum. It can be used in both qualitative and quantitative ways based on *Beer-Lambert* law. Here, absorption spectroscopy was applied to analyse the Ag NPs qualitatively, and later the quantitative determination of the Ag NPs concentration will be discussed. The spectroscopy was conducted of a transparent silica cuvette with internal widths of 1 cm and the light in the wavelength range from 300 to 800 nm. **Figure 4.9** shows a group of UV-vis absorption spectra in different aqueous samples, including water, 10 mM PVP & 10 mM Ag NO_3, Ag NPs suspension prepared at bare BDDE and Ag NPs suspension prepared at Hb-BDDE. Both Ag NPs suspensions were prepared by the same procedure mentioned in experimental section, but at different cathodes of bare-BDDE and Hb-BDDE respectively. In the spectra of both water and PVP& $AgNO_3$ sample, no obvious absorbance band is observed, as shown by black and red curves in **Figure 4.9**, which means none of these species can absorb the light in the range studied. For the Ag NPs suspension prepared at bare BDDE, a wide and weak peak appears in the range of 350 to 600 nm. On the contrary, the profile for the Ag NPs prepared at the Hb-BDDE exhibits a sharp band centred at 405 nm, which is a typical absorption band for silver nanoparticles as reported in the literature.[8,11,24,25] The low wavelength and high symmetry are associated with the small size and uniform size distribution. As suggested by the relationship between the Ag NPs size and the wavelength of spectra peak from Sigma-Aldrich in **Figure 4.10**, the peak centred at 405 nm indicated a particle size close to 10 nm.

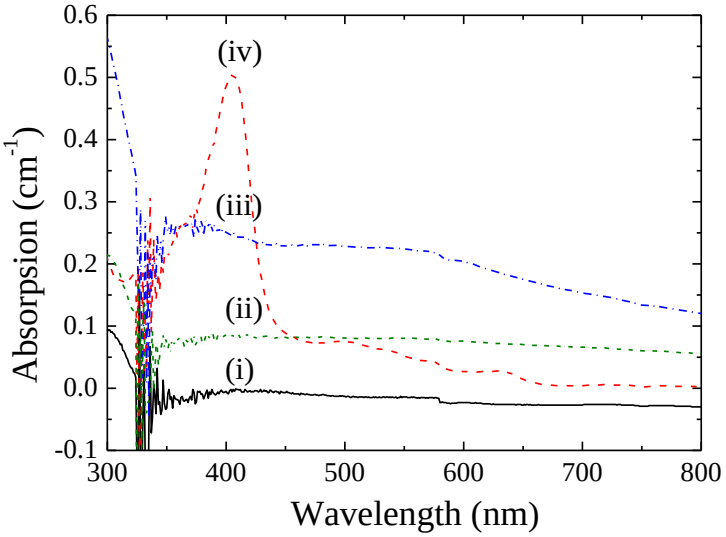

Figure 4.9 UV-vis spectra of (i) water, (ii) 10 mM PVP+10 mM Ag NO_3, (iii) Ag NPs obtained in this work at bare BDDE, and (iv) Hb-BDDE

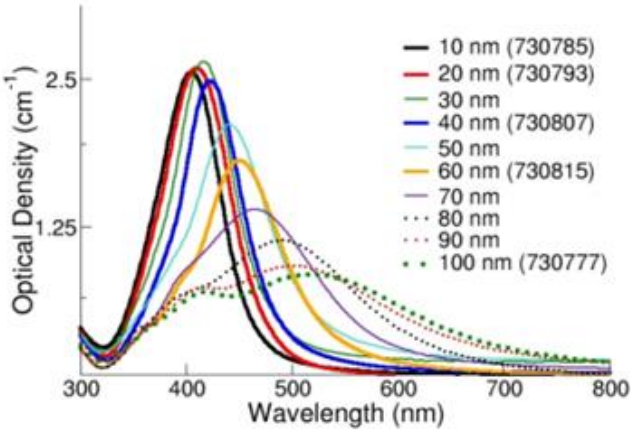

Figure 4.10 Extinction (scattering + absorption) spectra of silver nanoparticles with diameters ranging from 10-100 nm at mass concentrations of 0.02 mg mL^{-1}.[26]

4.3.2.4 Dynamic Light Scattering

DLS is an easy, quick and accurate technique to measure the Brownian motion and relates this to the size distribution of small particles in suspension. [27] In this method, a laser light hits the particles and *Rayleigh scattering* can be observed in all direction. These scattering can be detected as a time-dependent fluctuation based on the *Brownian*

motion of the small particles. In this way, the velocity of Brownian motion, and the translational diffusion coefficient can be obtained. The size of particles can be calculated by the *Stokes-Einstein* equation as mentioned in **Equation 2.26**. DLS was performed on the freshly prepared Ag NPs (within 2 hours) by diluting 30 µL Ag NPs solution into 250 µL in the cuvette made of silicon single crystal. The collection time was set up to 10 s for each cycle and each solution collected 10 cycles. The software, Omnisize 300, then automatically chose the reliable cycles to do the data analysis, including mass distribution, intensity distribution and number distribution. In our experiment, the number distribution was of the most concern.

The number distribution of fresh Ag NPs suspension is shown in **Figure 4.11**. Apparently, only one sharp peak can be observed, which means that the Ag NPs were highly uniform. The calculation carried out by Omnisize 300 indicates the particles were of the average size of 8.0 nm (relative standard deviation, %RSD < 6.8 %). Note that the diameter that is measured in DLS is a value that refers to a sphere that has the same translational diffusion coefficient (the velocity of the Brownian motion), *i.e.* the hydrodynamic diameter. Therefore, the real size should be smaller than this value.

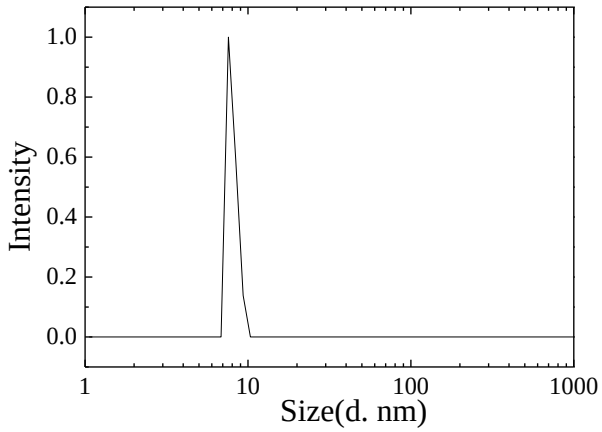

Figure 4.11 Number distribution of DLS of fresh Ag NPs suspension, prepared by applying -1 V for 1000 s in the solution contain 0.1 M Ac buffer, 10 mM PVP and 10 mM $AgNO_3$ at Hb-BDDE

4.3.2.5 X-ray diffraction

The size of the Ag NPs was also studied by XRD. The silver nanoparticles suspension was prepared by the procedure as mentioned above, and then 3×10 µL solution was successively dropped onto a clean silicon substrate where the XRD was performed. The XRD spectrum in the range of 30º to 80º (2θ) is shown in **Figure 4.12**. The peak around 38º, 46º, 66º and 76º are corresponding to the silver particle reflections (111), (200), (220) and (311) respectively, according to literature.[23,28,29] The Scherrer equation was used for calculation, as mentioned in Equation 2.29. (200) reflection was used here for calculation. For spherical silver nanoparticles, the value of κ equals to 0.95; λ is 0.15418 nm; B_{hkl} is measured to be 0.217 and the Bragg angle is 45.4 º. Therefore, the crystallite size can be calculated to be 4.4 nm. Note that this size is the mean size of the ordered domains, which may be smaller than the grain size, if any significant disorder is present in the crystallites

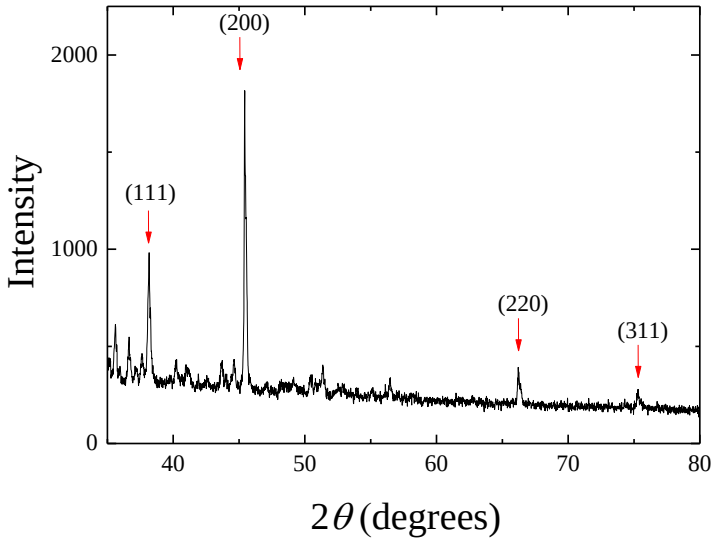

Figure 4.12 X-ray diffraction of Ag NPs which were prepared by applying -1 V for 1000 s at Hb-BDDE in the solution containing 0.1 M Ac buffer, 10 mM PVP and 10 mM $AgNO_3$

4.3.2.6 Yield

Overall the data recorded from UV-Vis, XRD and DLS are consistent with a conclusion that the synthetic method used results in the production of a fairly monodisperse suspension of silver nanoparticles with an effective diameter of the order of 10 nm or a little below. The next important parameter is to gauge the reaction yield. The theoretical yield of Ag NPs is defined as the amount of Ag NPs produced compared to the amount which would result if all the electrons passed through the system were totally channelled into Ag NPs production. The charge passed can be obtained from integration of the current in the interval of the synthesis period which is recorded in a current-time curve as shown in **Figure 4.2**. Then the mass of product can be calculated by *Faraday's law* as follows,

$$m = (\frac{Q}{F})(\frac{M}{z}) \qquad \text{Equation 4.2}$$

where m is the mass of silver in grams, Q is the total electric charge passed, F is the *Faraday* constant equal to 96485 C mol^{-1}, M is the molar mass of silver using 107.9 g mol^{-1}, z is the valency number which is 1 for silver reduction. For the sample shown in **Figure 4.2**, The Q calculated to be 1.04 C, the mass was 0.0012 g. Since the volume was 20 mL, the theoretical yield of Ag NPs was 58 mg L^{-1}.

The actual amount of Ag colloid produced was estimated by both square wave voltammetry method and UV-vis method. The standard addition method was used to measure the quantity of Ag NPs in SWV determination. Ag colloid of size 10 nm, which is close to the size of the Ag NPs in this work, was purchased from Sigma-Aldrich. Then this Ag suspension was diluted into different concentrations from 5 to

250 mg L^{-1} in the solution containing 0.1 mM Ac buffer, 10 mM Ag NO_3 and 10 mM PVP. In those solutions, SWV was performed in the potential range of +0.4 to +0.7 V, as shown in **Figure 4.13**a. Typical oxidation peaks of silver are obtained at about +0.5 V at all profiles, and peak current and peak potential both rise with the increasing concentration. The plot of peaks current against the concentration is displayed in **Figure 4.13**b, which shows that the peak current is proportional to the Ag NPs concentration. The plot was fitted by the software Origin8.0, and the fitted line is taken as the standard line. Then the SWV was carried out in the Ag NPs suspension obtained in this work, displayed as the black solid line in **Figure 4.13**a as well. The peak current measured is corresponding to a concentration of *ca.* 29 mg L^{-1} in the standard line, as shown in **Figure 4.13**b. The yield therefore can be calculated by the actual amount divided by the theoretical yield, about 51%. For 5 samples, the average yield was 55%.

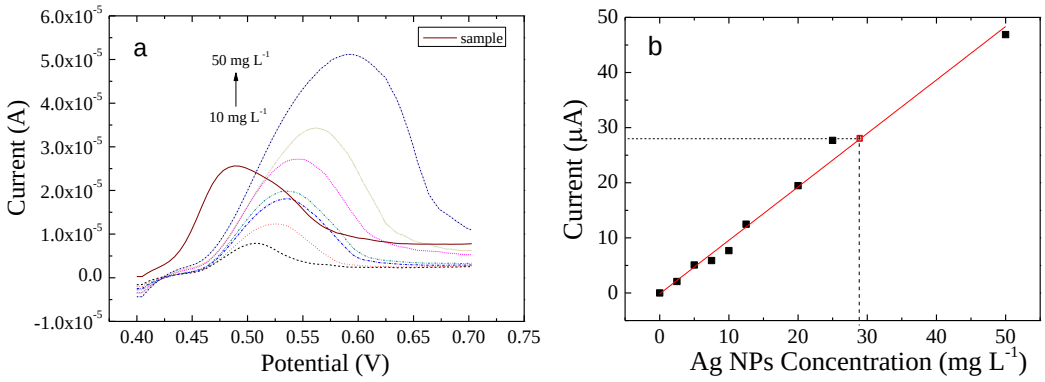

Figure 4.13 (a) Square wave voltammograms of 2.5, 5, 7.5, 10, 12.5, 20, 25 and 50 mg L^{-1} Ag NPs from Sigma Aldrich and the Ag NPs sample from this work; (b) plot of peak current *vs.* concentration of Ag NPs. The dash line represents the current obtained from the sample of this work, corresponding to a concentration of 29 mg L^{-1}.

As mentioned above, UV-visible spectroscopy method is commonly used to determine the concentration of adsorbing species in solution quantitatively, based on the Beer-Lambert law as shown in **Equation 2.27**. The standard addition method was also used to measure the quantity of Ag NPs. The 10 nm Ag colloid purchased from Sigma-

Aldrich was diluted into 5, 15, 25, 40 and 100 mg L^{-1}, in which solution UV-visible spectroscopy was performed. The spectra are displayed in **Figure 4.14**a. A typical absorption band centre at about 400 nm can be clearly observed in all the profiles, which is assigned to Ag NPs. The absorbance intensities for each solutions are plotted against the concentration as displayed in **Figure 4.14**b, where a linear line is obtained (%RSD<0.01%). This line is used as the standard line. Then the experiment was carried out in the Ag NPs obtained in this work, the spectrum also displayed in **Figure 4.14**a as the black solid line. The absorbance peak centred at *ca.* 405 nm. The absorbance intensity is about 0.5, corresponding to the concentration of 31 mg L^{-1} in the standard line as shown in **Figure 4.14**b. This concentration value is close to the result obtained by the SWV method, and the yield was calculated to be about 53%.

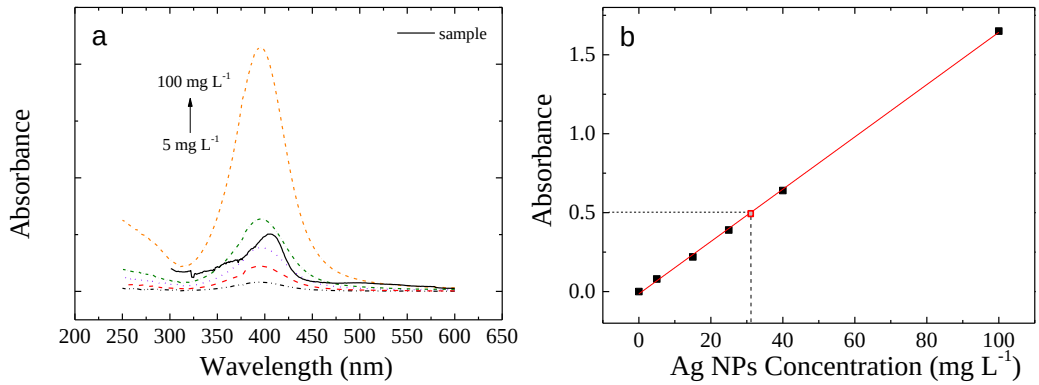

Figure 4.14 (a) UV-vis spectra of Ag NPs 5, 15, 25, 40 and 100 mg L^{-1} Ag NPs from Sigma Aldrich and the Ag NPs sample from this work; (b) resulting plot of the absorption peak of Ag NPs from Sigma Aldrich *vs.* the particle concentration. The dash line represents the absorbance obtained from the sample of this work, corresponding to a concentration of 31 mg L^{-1}.

4.3.3 Condition study

4.3.3.1 Comparison of BDDE and GCE

To investigate the role of BDDE, electrochemical synthesis experiment was also conducted on GCE, one of the common used carbon base electrodes, as an alternative

working electrode. The effect of different immersion times in Hb solution was studied by cyclic voltammetry in both [Fe $(CN)_6$]$^{3-/4-}$ and $FcOH^{0/+1}$ redox probes. The voltammograms of 0.1 M KCl and 10 mM [Fe $(CN)_6$]$^{3-/4-}$ at Hb-GCEs are shown in **Figure 4.15**a, which electrode was immersed into 4 mg L^{-1} Hb solution for 0 to 30 min. At the bare GCE a typical redox peak of [Fe $(CN)_6$]$^{3-/4-}$ is clearly seen. As the electrode was immersed into Hb for longer time and more Hb was adsorbed into the GCE surface, the peak current declined quickly and the peak became featureless. On the other hand, the cyclic voltammetry of 10 mM $FcOH^{0/+1}$ was also carried out at the Hb-GCEs with various immersing time. Although the peak current also decreased with the immersing time, the typical redox peaks of $FcOH^{0/+1}$ are still clearly observed at Hb-GC electrode after dipping into Hb solution for 2 hours. The difference between the CV of [Fe $(CN)_6$]$^{3-/4-}$ and $FcOH^{0/+1}$ is attributed to that the [Fe $(CN)_6$]$^{3-/4-}$ redox couple is much more sensitive to the electrode surface than $FcOH^{0/+1}$, as discussed above.

In comparison to Hb-BDDE, the results are similar at both Hb-GCE and Hb-BDDE. When the electrode was immersed into Hb solution, Hb molecules were adsorbed onto the surface and blocked some electrochemical active sites of electrode, leading to a decrease response in both [Fe $(CN)_6$]$^{3-/4-}$ and $FcOH^{0/+1}$ probes. Because [Fe $(CN)_6$]$^{3-/4-}$ is more sensitive to the surface change than $FcOH^{0/+1}$, the decrease in [Fe $(CN)_6$]$^{3-/4-}$ is more significant. However, it should be noted that the peak current at Hb-GCE (**Figure 4.15**a) declined much quicker than those at Hb-BDDE (**Figure 4.4**a), which is in line with the commonly held belief that adsorption at BDDE is relatively slow because of the inert nature of diamond.

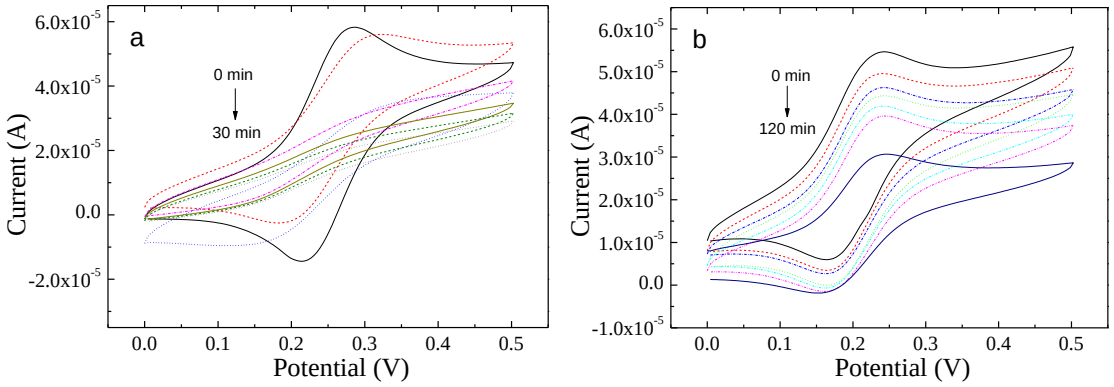

Figure 4.15 Cyclic voltammograms in 0.1 M KCl and (a) 10 mM $[Fe(CN)_6]^{3-/4-}$; (b) 10 mM $FcOH^{0/+1}$ at Hb-GCEs which were fabricated by immersing GC electrode into 4 mg L^{-1} Hb solution for (a) 0, 1, 2, 5, 10, 20 and 120 min; (b) 0, 1, 2, 5, 10, 20, 30 min

After being characterised, Hb-GCE was used to synthesise Ag NPs following the same procedure in the experimental section. However, after applying -1.0 V for 1000 s, the solution did not change colour while at Hb-BDDE the colour changed from colourless to light yellow. However some sediment was formed in the solution as observed by naked eye. Also observed was a thick silver film at Hb-GCE electrode surface, which is attributed to the electrochemical deposition of silver. After experiment, the solution was tested by DLS. Number distribution of DLS is shown in **Figure 4.16**. It can be seen that the particle size varies from 17 nm to 6591 nm with an average size of 375 nm. In comparison to this result, the sizes of Ag NPs prepared by Hb-BDDE are much smaller and uniform, most at 8 nm, which is suggested by the DLS result shown in **Figure 4.11**. The reason may be that BDDE surface is less polarized than the GCE surface and the van der Waals force between BDDE and silver is weaker. Therefore the kinetic rate of silver deposition is slower.

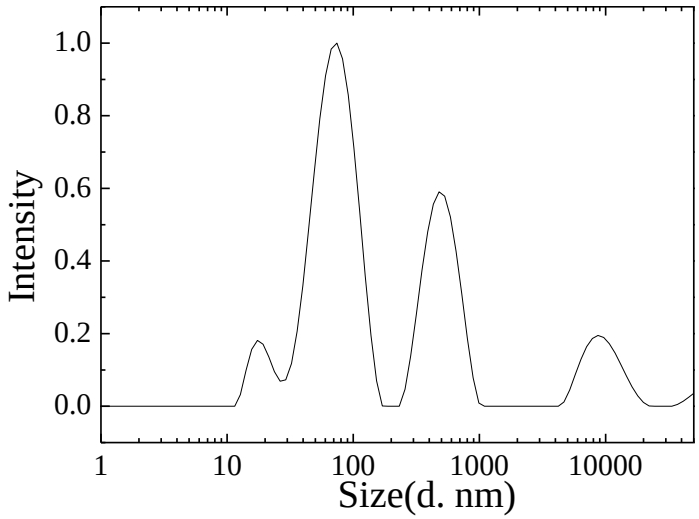

Figure 4.16 Number distribution of DLS of fresh Ag NPs suspension, prepared by applying -1 V for 1000 s in the solution contain 0.1 M Ac buffer, 10 mM PVP and 10 mM $AgNO_3$ at Hb-GCE

4.3.3.2 Comparison of the use of Hb molecule *vs.* Nafion as electrode modifier

The role of Hb molecule in synthesis experiment was further studied by using Nafion to modify BDDE instead of Hb. The reason to choose Nafion is because of its high conductivity to cations, resistance to chemical attack, and strong bonding with electrode surfaces (to cover and protect the electrode surface from electrode deposition). Also, the value of the isoelectric point of haemoglobin was reported to vary from pH 7.10 to 7.35, and the pK_a of Nafion was around pH 6.[30] Both of them should carry a net positive charge in the acetic acid buffer with pH 4.2. The Nafion was diluted into 4 mg mL^{-1} which is the same with Hb solution in use and this concentration is sufficient to cover the electrode surface according to literature.[31,32]

The same procedure in experimental section was applied to form Nafion-BDDE and synthesise Ag NPs electrochemically. The solution remained colourless throughout the process, and a thick silver film can be observed on the Nafion -BDDE. The resulting suspension was analysed by XRD and the diffraction pattern is shown in **Figure 4.15**.

Although some peaks can be seen, the intensities are extremely small compared to the XRD peaks on the sample prepared on Hb-BDDE (**Figure 4.12**). And apparently, no typical peak of Ag NPs can be observed. It indicates that Ag NPs failed to form in the solution; instead, most of the silver was deposited into the electrode surface.

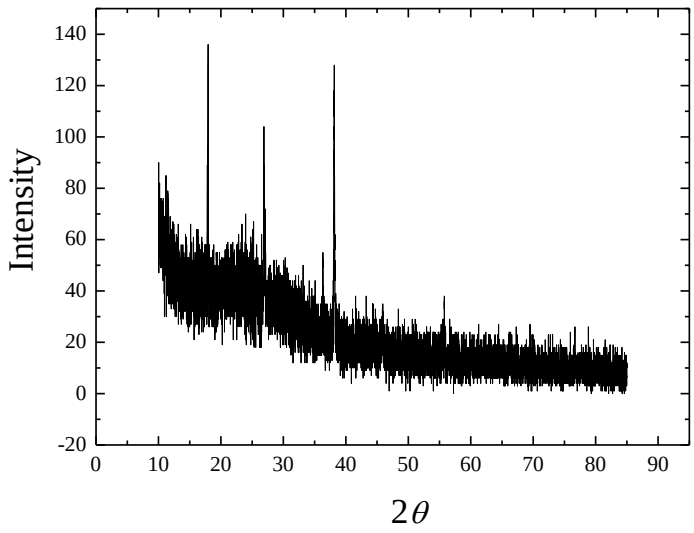

Figure 4.17 X-ray diffraction of Ag NPs which prepared by applying -1 V for 1000 s at Nafion-BDDE in the solution containing 0.1 M Ac buffer, 10 mM PVP and 10 mM $AgNO_3$

4.3.3.3 Comparison of SDS, CTAB, sodium citrate and PVP

Since the shape and size of nanoparticles are highly dependent on the stabiliser, especially in electrochemical synthesis,[16,17] more surfactants were examined here including CTAB, SDS and sodium citrate, together with PVP. Those stabilisers are commonly utilised to control the particle size and shape in wet chemical synthesis of silver nanoparticles.[12] The same procedure was applied when 10 mM PVP was replaced by 10 mM CTAB, SDS and sodium citrate respectively. When adding CTAB into the solution, large amount of grey sediments appeared after applying potential of -1 V. It is proved by XPS to be AgBr particles, which is likely to be generated by the reaction between the bromide ions from CTAB and silver ions from silver source $AgNO_3$. For

other stabilisers, Ag NPs can be obtained successfully. The particle size distribution of resulting samples which had been kept for 7 days were analysed by DLS. The number distributions of particle size of samples from PVP, SDS and sodium citrate are displayed in **Figure 4.18**. To increase accuracy, the particles of size larger than 10 µM were filtered. It can be seen that the average size of Ag NPs stabilised by PVP is around 10 nm, while the one stabilised by SDS is about 300 nm in a wide range from 100 nm to 1000 nm. The Ag NPs stabilised by sodium citrate have three size ranges with peaks centred at 20, 110 and 1100 nm respectively. As given by the particle size, PVP performed the best among these stabilisers. This result can be attributed to the different structures of these stabilisers, as shown in **Figure 4.19**. It is reported by Yin *et al.* that PVP can trap silver ions to form an Ag_m^{m+}-PVP complex which can reduce silver deposition and promoting silver nucleation. But sodium citrate is not a long chain molecule and the carbon and hydrogen in the long chain of SDS and CTAB cannot attract Ag^+ ion. Therefore, only PVP has polar groups in the long chain that can attract Ag^+ ion to form Ag_m^{m+}-PVP complex, which can reduce to be the Ag_m^{m-}-PVP and grow in aqueous phase.

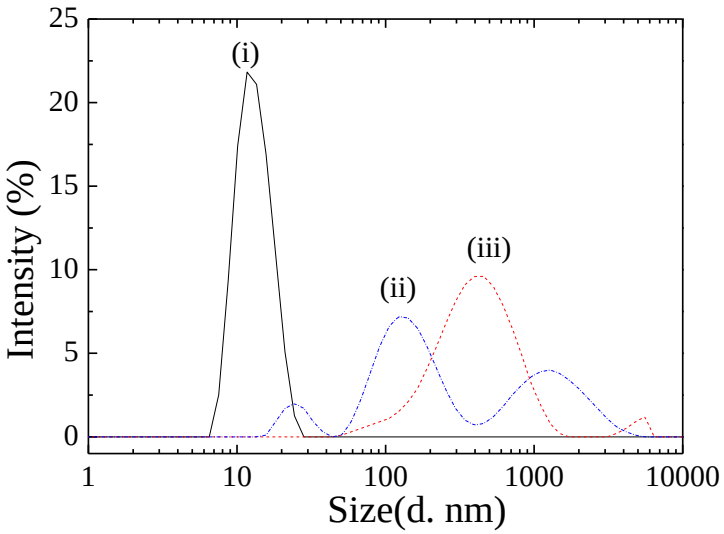

Figure 4.18 Number distribution of DLS of fresh Ag NPs suspension, prepared by applying -1 V for 1000 s at Hb-BDDE in the solution contain 0.1 M Ac buffer, 10 mM $AgNO_3$ and (i) 10 mM PVP, (ii) 10 mM sodium citrate and (iii) SDS respectively

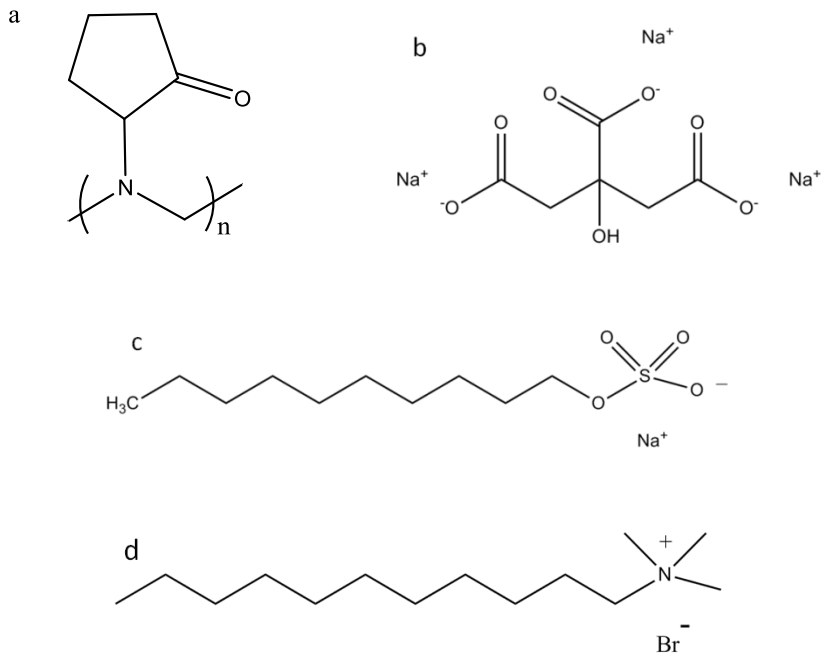

Figure 4.19 The molecular structure of (a) PVP, (b) sodium citrate, (c) sodium dodecyl sulphate (SDS) and (d) cetrimonium bromide (CTAB)

Based on the results above, a mechanism is proposed as follows. At first Ag^{+} ions are attached to the PVP to form an Ag_m^{m+}-PVP complex. Other stabilisers including CTAB, SDS and sodium citrate cannot form the long chain complex. This complex can diffuse to the Hb-BDDE surface to gain electrons and be reduced, and then diffuse back to the aqueous phase. In this process, competition between silver deposition and reduction is crucial. BDDE is inert and the Hb on the surface can also help to minimise the deposition. When using GCE as an alternative to BDDE and Nafion as an alternative to the Hb molecule, most Ag is deposited onto the surface and a low yield Ag NPs can form in the aqueous phase. In addition, PVP can reduce the rate of silver deposition. After that, the Ag NPs grows gradually in solution and the PVP acts as the electron provider and stabiliser to promote the nucleation of Ag NPs and prohibit aggregation as a result of its steric effect.[17,33] The reduced PVP cross-links to form the polymer.

4.4 Conclusions

A novel new electrochemical synthesis of silver nanorparticles in aqueous phase approach was developed by using Hb-BDDE as working electrode, $AgNO_3$ as silver resource and PVP as stabiliser.

- The XPS analysis of Hb-BDDE used for formation of the Ag NPs showed that most of the surface was covered by Hb and the ratio of C:N:O was about 51%, 22% and 27%. The minimum depth of sample is calculated to be about 5.7 nm, which suggests that there may be one dense layer of Hb on BDD surface.
- The Hb-BDDE was examined by cyclic voltammetry in $[Fe\ (CN)_6\ ]^{3-/4-}$ and $FcOH^{0/+1}$ probes. When BDDE is immersed into the Hb solution for longer time, more Hb molecules are adsorbed onto the electrode surface, blocking the electrochemical active site and reducing the response towards those probes.
- The synthesised Ag NPs were analysed by various techniques. The morphology of synthesised Ag NPs was observed by SEM. It was shown that the Ag NPs were well dispersed and uniform in approximate radius of 50 nm initially although it is believed this larger size results from particle aggregation in the preparation of the SEM sample. The UV-visible spectrum of Ag NPs obtained from this work shows a peak centred at 405 nm, which is associated with a particle size about 10 nm according to references. The size of Ag NPs was also investigated by DLS, showing an average size about 8 nm. The particle size of Ag NPs calculated from XRD line broadening was only 4.4 nm, with peaks corresponding to the silver particle reflections (111), (200), (220) and (311) being observed. So overall it is concluded that monodisperse samples with a size around 10nm diameter are produced by the method.

- The yield was calculated by both square wave voltammetry method and UV-vis method, given close results of 55% and 53% respectively.
- Other electrodes (Hb-GCE and Nafion-BDDE) and stabilisers (CTAB, SDS and sodium nitrate) were examined but were not successful.
- Based on the results therefore, BDDE, Hb and PVP all play quite specific and crucial roles in the success of the method.

References

(1) Caswell, K.; Bender, C. M.; Murphy, C. J. *Nano Letters* **2003**, *3*, 667.

(2) Schmid, G. *Chem. Rev.* **1992**, *92*, 1709.

(3) Lee, P. C.; Meisel, D. *Journal of Physical Chemistry* **1982**, *86*, 3391.

(4) Nie, S. M.; Emery, S. R. *Science* **1997**, *275*, 1102.

(5) Moskovits, M. *Reviews of Modern Physics* **1985**, *57*, 783.

(6) Maruyama, Y.; Ishikawa, M.; Futamata, M. *Chem. Lett.* **2001**, 834.

(7) Link, S.; El-Sayed, M. A. *Journal of Physical Chemistry B* **1999**, *103*, 8410.

(8) Kong, H.; Jang, J. *Langmuir* **2008**, *24*, 2051.

(9) Ma, J.; Zhang, J.; Xiong, Z.; Yong, Y.; Zhao, X. S. *J. Mater. Chem.* **2011**, *21*, 3350.

(10) Sun, Y. G.; Xia, Y. N. *Science* **2002**, *298*, 2176.

(11) Zhu, J. J.; Liu, S. W.; Palchik, O.; Koltypin, Y.; Gedanken, A. *Langmuir* **2000**, *16*, 6396.

(12) Jana, N. R.; Gearheart, L.; Murphy, C. J. *Chem. Commun.* **2001**, 617.

(13) Reetz, M. T.; Winter, M.; Breinbauer, R.; Thurn-Albrecht, T.; Vogel, W. *Chemistry-a European Journal* **2001**, *7*, 1084.

(14) Reetz, M. T.; Helbig, W.; Quaiser, S. A.; Stimming, U.; Breuer, N.; Vogel, R. *Science* **1995**, *267*, 367.

(15) Yu, Y. Y.; Chang, S. S.; Lee, C. L.; Wang, C. R. C. *Journal of Physical Chemistry B* **1997**, *101*, 6661.

(16) Rodriguez-Sanchez, L.; Blanco, M. C.; Lopez-Quintela, M. A. *Journal of Physical Chemistry B* **2000**, *104*, 9683.

(17) Yin, B. S.; Ma, H. Y.; Wang, S. Y.; Chen, S. H. *Journal of Physical Chemistry B* **2003**, *107*, 8898.

(18) Mock, J.; Barbic, M.; Smith, D.; Schultz, D.; Schultz, S. *The Journal of Chemical Physics* **2002**, *116*, 6755.

(19) Pastoriza-Santos, I.; Liz-Marzán, L. M. *J. Mater. Chem.* **2008**, *18*, 1724.

(20) Song, M.-K.; Cairns, E. J.; Zhang, Y. *Nanoscale* **2013**, *5*, 2186.

(21) Tanuma, S.; Powell, C. J.; Penn, D. R. *Surface and Interface Analysis* **2011**, *43*, 689.

(22) Fisk, A. A. *Proceedings of the National Academy of Sciences of the United States of America* **1950**, *36*, 518.

(23) http://www.periodictable.com/Properties/A/VanDerWaalsRadius.v.html.

(24) Jin, W. J.; Lee, H. K.; Jeong, E. H.; Park, W. H.; Youk, J. H. *Macromolecular Rapid Communications* **2005**, *26*, 1903.

(25) Cozzoli, P. D.; Comparelli, R.; Fanizza, E.; Curri, M. L.; Agostiano, A.; Laub, D. *Journal of the American Chemical Society* **2004**, *126*, 3868.

(26) http://www.sigmaaldrich.com/materials-science/nanomaterials/silver-nanoparticles.html.

(27) Berne, B. J. *Dynamic light scattering: with applications to chemistry, biology and physics*; DoverPublications. com, 1976.

(28) Zhao, B.; Liu, Z. R.; Liu, Z. L.; Liu, G. X.; Li, Z.; Wang, J. X.; Dong, X. T. *Electrochemistry Communications* **2009**, *11*, 1707.

(29) Chailapakul, O.; Siangproh, W.; Tryk, D. A. *Sensor Letters* **2006**, *4*, 99.

(30) Fanelli, A. R.; Antonini, E.; Caputo, A. *Biochimica et biophysica acta* **1958**, *30*, 608.

(31) Lee, S.-J.; Yu, T. L.; Lin, H.-L.; Liu, W.-H.; Lai, C.-L. *Polymer* **2004**, *45*, 2853.

(32) Hu, C.; Yuan, S.; Hu, S. *Electrochimica acta* **2006**, *51*, 3013.

Chapter 5 New Carbon Sensors: Nano-diamond, Graphene and Carbon Black for Phenols Detection

5.1 Introduction

Phenols are a class of chemical compounds which affect our daily life to a great extent.[1] Many phenolic compounds are widely used in chemical engineering processes, wood processing and plastics processing, and therefore exist in waste water, milk, fruit juice, canned food, cigarettes, tea and skin-lightening drugs to provide a few examples. They also can be found in organisms, for example aquatic biota, blood and liver. If a certain dose is exceeded, those phenolic compounds are toxic and harmful to humans and lead to various diseases like fatigue, tachycardia, mucous membrane damage, dermatitis, lung edema and liver, kidney and heart diseases.[2-4]

Chromatography, spectrophotometry, capillary electrophoresis and voltammetry methods are widely applied for the determination of phenolic compounds and detection limits in the micromolar region can be obtained.[5-8] Escarpa and Gonzales compared chromatographic and spectrophotometric methods for phenolic compounds and noted detection limits around 0.02 μg mL^{-1}.[7] The detection limit of catechol was reported to be 0.03-0.15 μg mL^{-1} by UV-vis method which, nevertheless, suffered from instability and low sensitivity.[9] Most of such methods require relatively expensive equipment, complicated pre-treatment of samples, long experimental time and well-trained technicians. Voltammetric determination is always considered as a valuable alternative because of its simple operation, high dynamic range, capability for real time monitoring and very low detection limit down to micromolar.

Voltammetry at modified electrodes has become a typical approach to determine phenolic compounds in the aqueous phase, and the mechanisms have been well investigated.[3,10,11] Biphenols, like hydroquinone (HQ) and 1,2-dihydroxybenzenes (DHB or catechol), can be directly oxidised at electrodes under low over-potential, as demonstrated in **Figure 5.1**a. Those biphenols can be detected by sensors such as Pt, Ti/IrO_2, Ti/SnO_2, BDD, GCE, CNT, Si sol-gel, montmorillonite, $Co(OH)_2$, TiO_2/Au, nano-grass.[12,13] For mono-phenols detection, enzymes are usually applied to oxidise mono-phenol to o-biphenols which are subsequently oxidised to *o*-quinones, as demonstrated in **Figure 5.1**b.[14] The widely used enzymes include tyrosinase (tyr), lactase and polyphenol oxidase. To support these enzymes and maintain their capability of catalysis and electroactivity, the working electrode normally needs to be decorated by conductive materials in advance. The materials that have been investigated include polymers (phosphate-doped polypyrrole film; aminophenyl), nanoparticles (Au, ZnO, Al sol-gel, $MgFe_2O_4$-SiO_4, titania, $CaCO_3$, Si, nano-grass); carbon materials (graphite, SWCNT, MWCNT) and a combination of the above mentioned (Au+graphite).[14-16] **Table 5.1** shows the detection limit, detection range and sensitivity of some phenolic sensors from literature. The typical detect limit is down to the order of 10^{-7} M in a range of 10^{-7} to 10^{-4} M.

(a) (b)

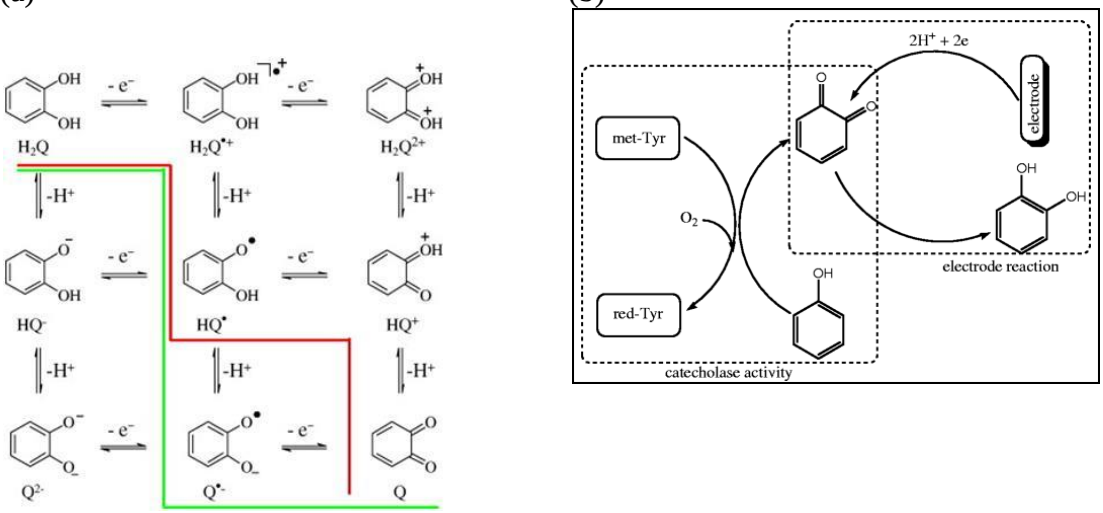

Figure 5.1 (a) The oxidisation and reduction process of hydroquinone[10]; (b) is the scheme for tyrosine modified electrode for phenol detection.[11]

Table 5.1 Detection limit (μM) and detection range (μM) of phenol compounds at various sensors

Sensors	Tackle	LOD	Detection range	Ref.
Tyr/MWCNTs	phenol	0.2	0.4-10	Ren, J[17]
	HQ	0.2	0.2-60	Ren, J[17]
	DHB	0.2	0.2-10	Ren, J[17]
Tyr/MWCNTs	phenol	1.1	1.5-25	Hashemnia, S[11]
	DHB	0.9	2.0-15.0	Hashemnia, S [11]
	p-cresol	2	2.0-15.0	Hashemnia, S [11]
Tyr/Ti	DHB	0.09	0.22-13	Kochana, J[14]
	Phenol	0.13	0.44-11	Kochana, J[14]
	p-cresol	0.14	0.22-7.7	Kochana, J[14]
Tyr/Ap-BDD	Phenol	0.1	1-200	Zhou, Y[18]

	p-cersol	0.2	1-200	Zhou, Y [18]
Tyr/$CaCO_3$	DHB	0.0044	0.06-2	Shan, D[3]
	p-cresol	0.0054	0.06-2	Shan, D [3]
	Phenol	0.0062	0.1-1	Shan, D [3]
Tyr/polymer	Phenol	1.0	1-175	Zhou, Y[15]
	p-cresol	0.5	1-200	Zhou, Y [15]
GCE	HQ	3.9	3.9-1360	Ziyatdinova, G[19]
	DHB	7.33	14.7-688	[19]
SPE	phenol	-	0.5-6	Capannesi, C[20]
	DHB	-	0.5-5	Capannesi, C [20]
HRP-GC	phenol	4.4	50-100	Dai Z[21]
montmorillonite	HQ	0.57	5-2000	Kong, Y[12]
$Co(OH)_2$	HQ	0.5	5-125	Fan, L[13]
graphene-polyoxometalate	HQ	0.09		Cao, L[22]
graphene-polyoxometalate	DHB	0.05		Cao, L[22]
Al-doped Si	DHB	0.1	0.5-50	Lin, H[23]
Graphene-chitosan-GCE	HQ	0.75	1-300	Yin, H[24]
PDDA-G/GCE	HQ	0.25	1-500	Wang, L[25]

Among these supporting materials, carbon materials exhibit promising potential and have raised increasing interest in the last decade due to the advantages of consistently high sensitivities[11,17], prevention from passivating and fouling[19] and superior biocompatibility to enzyme modification. CNT and graphite have been successfully used in phenolics detection[26-28], although with noted limitations.[11] In addition, due to the complicated preparation procedure for electrode modification, electrode performance can be quite variable and depends greatly on experimental conditions.[17] Therefore, other carbon materials are worthy of investigation. In this work, nano-diamond, graphene and carbon black are investigated because of their specific characteristics as introduced in Chapter 1.[29-31] ND is unique for its sp^3 carbon electronic structure and other characteristics which can enhance the sensitivity for phenolic detection.[30,32] Also, the diamond particle is more inert to fouling. GP is found to have better thermal conductivity than SWCNT[33] and a high concentration of edge and surface defects where electrochemical reaction can take place. Performances of GP are reported generally equal to, or substantially better than, the sensors made with SWCNTs.[34] CB exhibits the best conductivity among all the carbon materials[35], with a smaller particle size[35] and a larger surface area than graphite. [30]

In this work, ND, GP and CB modified GCEs were first investigated to detect the biphenols, HQ and DHB, by square wave voltammetry and amperometry approaches. The fabrication procedures of these sensors are simple, quick and do not require great expertise. High sensitivity and low detection limit of down to nanomolar are achievable with high stability and reproducibility. Real samples of tap water, Thames river water, and green tea were tested by CB-GCE. GP-GCE and CB-GCE were further modified by tyrosine. The tyr/GP-GCE and tyr/CB-GCE were employed to detect monophenols, including phenol and p-cresol. Phenol and p-cresol can be converted by tyrosine and

consequently oxidised to quinone and *p*-quinones respectively which can be detected at a low potential.

The simultaneous determination of HQ and DHB was another focus in this work. HQ and DHB are isomers that often coexist in the environment, and both are considered as pollutants with high toxicity by the US Environmental Protection Agency (EPA) and the European Union (EU).[2] Therefore, the simultaneous determination of HQ and DHB is of great importance for real time monitoring. However, one big problem is their highly overlapped voltammetric peaks. Carvalho *et al.* started to apply a multivariate calibration method to simulate and analyse the full voltammogram aimed at separating each peak.[36] Some modified sensors also proved able to simultaneously detect HQ and DHB, such as poly(thionine)-GCE[37] and Zn/Al-GCE[38]. Due to the rapid development of carbon materials, direct peak separation was observed and reported at MWCNTs[39,40], PASA/MWCNTs[41], graphitized mesoporous[42] and polymer/graphene[25]. However, these established methods require extra steps of chemical or physical pre-treatment and separation. Also, the competition between both isomers at sensor surfaces still leads to non-linear dependence of current for each concentration in mixture.[36,43,44] Therefore, the simultaneous determination of HQ and DHB suffers from low sensitivity and poor accuracy. In this work, two distinct peaks of HQ and DHB can be observed at GP-GCE and CB-GCE without pre-treatment. The magnitude of the current is directly proportional to each concentration, with a low detection limit down to 10^{-8} μM. Therefore, it is possible to enable GP-GCE and CB-GCE for the real monitoring of HQ and DHB simultaneously.

5.2 Experimental

Tyrosine, phenol, p-cresol, hydroquinone and di-hydrobenzene were obtained from Sigma-Aldrich and are of A.C.S. reagent grade. The commercial Monarch 430 carbon black (Cabot Corporation, CB M 430, diameter 27 ±10 nm) was kindly donated by Prof. Richard Compton who obtained it from James M Brown Ltd (Staffordshire, UK). Graphene nano-platelets of 3 μm diameter and less than 10 nm thickness was obtained from Angstrom materials; the nanodiamond powder (ND-105/G4) was purchased from Yorkshire Bioscience Ltd. Other chemicals and regular electrochemical methods have been described in previous chapters. All the glassy carbon electrodes were cleaned before use by polishing with alumina powder which was removed by ultrasonication in water for 3 min. And electrochemical experiments were routinely carried out in 0.1 M phosphate buffer solution (phosphate buffer, pH 7.4) at room temperature. All solutions and subsequent dilutions were prepared with Milli-Q water (>18 MΩ cm).

Graphite, graphene and carbon black suspensions were prepared by adding 1 mg powder into 1 mL milli-Q water, and ultrasonicing for 1 hour before use. For the nano-diamond suspension, the following procedure was applied. 5 g milling beads were mixed with 1 mg nano-diamond powder and 5 mL milli-Q water. The mixture was sonicated for 15 hours, and then centrifuged (3×5 minutes, 10,000 rounds per min (rpm)). 10 μL carbon materials suspensions were drop-coated onto glassy carbon electrode with surface area of 0.0707 cm^2, and dried in the fume hood to form the electrode denoted as graphite-glassy carbon electrode (graphite-GCE), graphene-glassy carbon electrode (GP-GCE), carbon black-glassy carbon electrode (CB-GCE) and nanodiamond- glassy carbon electrode (ND-GCE) respectively. The amount of the carbon materials on the surface is about 0.01 mg. These carbon modified electrodes

were then used to detect bi-phenols (HQ and DHB). Tyrosine modified electrodes were fabricated by dropping 10 μL 1 mg mL^{-1} tyrosine solution (5.5×10^{-7} mol) onto the GP-GCE and CB-GCE surface and dried in the air for 1 hour, forming Tyr/GP-GCE and Tyr/CB-GCE. These biosensors were studied to determine phenol and cresol.

Dynamic light scattering was used to analyse the sizes of graphite, nano-diamond, graphene and carbon black powder. The average size of graphite is 56.4 nm and about 80 nm for graphene particles. The initial size of ND was about 50 nm, and after 12 hours ultra-sonication, reduced to 4-5 nm. Carbon black is easy to suspend in water with size 5-8 nm. However, the suspension became inhomogeneous and large clusters emerged generally after one week. It is assumed that all the dropping materials stick into the GCE surface uniformly. The densities of graphite, graphene, nano-diamond and carbon black are similar at around 1.7-2.23 g cm^{-3}.[45] Given the amount of carbon material on the surface is 0.01 mg, the thickness of these modifiers is about 630 nm.

5.3 Results and discussion

5.3.1 Biphenol detection

5.3.1.1 Determination of HQ

5.3.1.1.1 Cyclic voltammetry

In order to compare the performance of carbon material modified electrodes, the total amount of carbon on the GCE surfaces needs to be comparable. A similar surface concentration of NP suspension was drop-coated on the surface by controlling the total volume of the added drops of known concentration. Approximately 0.01 mg carbon materials were deposited on all electrode surfaces, with a thickness of about 630 nm, as mentioned above. The electrochemical redox process of hydroquinone - quinone is

shown in **Figure 5.3**, which involves a two electron transfer - two hydrogen ion transfer.

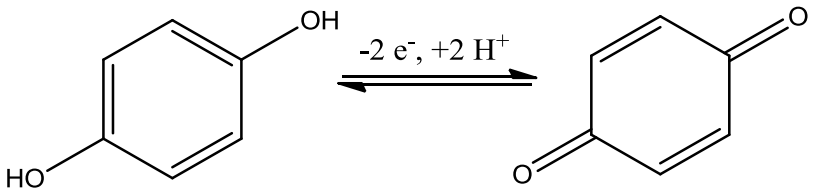

Figure 5.2 Electrochemical oxidation and reduction of hydroquinone-quinone

These electrodes, *i.e.* ND-GCE, GP-GCE and CB-GCE, were used to detect HQ by conducting cyclic voltammetry in a solution containing 0.1 M phosphate buffer and 0.2 mM hydroquinone in the potential window from -0.4 to +0.4 V where the HQ oxidation and reduction normally occur.[38,46-49] All the profiles are shown in **Figure 5.3**a, where the CV at bare GCE and graphite-GCE are also displayed for comparison. The redox peaks of HQ can be observed in all profiles at slightly different peak potentials and with varying peak current. Voltammograms at bare GCE, graphite-GCE, ND-GCE and GP-GCE can be observed more clearly in **Figure 5.3**b. The black solid curve is obtained at bare GCE (line i), where a pair of peaks can be observed at -0.06/+0.32 V. This peak-peak separation is wider than the value of +0.01/+0.20 V at graphite-GCE (line ii), ND-GCE (line iii) and GP-GCE (line iv). Also, the peak current at bare GCE is lower than for the modified electrodes, showing that the sensitivity toward HQ reduction and oxidation is improved by the modification. Taking the diffusion coefficient of HQ to be 2×10^{-9} cm^2 s^{-1},[50] the diffusion limit current of the oxidation peak for 0.2 mM HQ at a scan rate of 0.05 V s^{-1} can be calculated to be 1.43×10^{-5} A (using the equation 2.21), close to the value of 1.36×10^{-5} A at GP-GCE. The anodic peak current at GP-GCE is higher than the value at ND-GCE (1.02×10^{-5} A), graphite-GCE (9.7×10^{-6} A) and bare GCE (4.5×10^{-6} A). It shows that GP-GCE exhibits the fastest kinetic among these

electrodes. However, the value at CB-GCE (1.24×10^{-4} A, line v) is significantly higher than the diffusion limit current, suggesting this reaction is not limited by diffusion, but under adsorption control as suggested by the result of cyclic voltammetry conducted at various scan rates, which will be discussed subsequently. Also, the peak-peak separation at CB-GCE is much narrower than the others and more symmetrical, showing the characteristics of an adsorption process.

It should be noted that the background current (non-faradaic current) and the noise (current fluctuations of non- faradaic current) at CB-GCE are higher than those at other electrodes. In addition, a shoulder peak at -0.2 V is observed at CB-GCE, which was also reported at Zn/Al layered double hydroxide film modified glassy carbon electrode in the presence of 0.1 mM DHB.[38] One of the explanation is that some by-products were generated from the oxidation or electrochemical degradation of HQ, then oxidised/reduced at the electrode surface.[51] This peak also may be attributed to the reaction of the some oxygen moieties on the carbon black surface.[52,53]

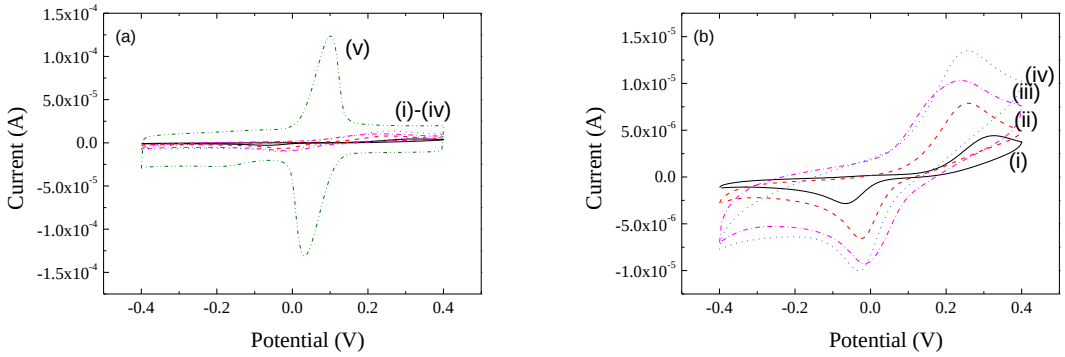

Figure 5.3 Cyclic voltammograms in a solution containing 0.1 M phosphate buffer and 0.2 mM hydroquinone at (i) bare GCE, (ii) graphite-GCE, (iii) ND-GCE, (iv) GP-GCE and (v) CB-GCE respectively

The surface processes of HQ at bare-GCE, GP-GCE, ND-GCE and CB-GCE were studied by cyclic voltammetry with increasing scan rate at these electrodes in 0.2 mM HQ and 0.1 M phosphate buffer. It is apparent that the peak currents at all electrodes are

increased with higher scan rate, which are plotted in **Figure 5.4**. At bare-GCE, GP-GCE and ND-GCE (**Figure 5.4** a-c), the current shows a linear increase with the square root of scan rates, . It indicates a diffusion controlled process. Note that the peak-peak separation increases with higher scan rate, showing the irreversibly character of the electron transfer kinetics. This diffusion controlled process is widely observed for most phenolic sensors, such as carbon nano-tube modified electrodes.[19,40,41,46,47] In contrast, the peak current of HQ is linear to the scan rate at CB-GCE (**Figure 5.4** d). It suggests that the reaction is under adsorption control on the carbon black modified surface.[54,55] The heterogeneous electron transfer rate constant for the electron transfer processes can be calculated by using the *Laviron equation*[54,56]

$$\log k = \alpha \log(1-\alpha) + (1-\alpha)\log\alpha - \log\left(\frac{RT}{nFv}\right) - \alpha(1-\alpha)\frac{nF\Delta E_p}{2.3RT} \qquad \text{Equation 5.1}$$

where k is the heterogeneous rate constant, α is the transfer coefficient, v is the scan rate, ΔE_p is the difference between the peak potential of the anodic and cathodic peaks and n, F, R, T have their usual significance. If the value of $\Delta E_p/n$ is larger than 200 mV, a graph of $E_p = f(\log v)$ yields two straight lines with a slope equal to $-2.3\frac{RT}{n\alpha F}$ for the cathodic peak, and $2.3\frac{RT}{(1-\alpha)nF}$ for the anodic peak. Therefore, α and n of HQ at CB-GCE were calculated to be 0.46 and 1.7, similar to literature (α=0.51/0.55/0.33; n=2).[24,49,57,58] And the rate constant k is 2.06 $cm^2\ s^{-1}$, which is significantly higher than the value at graphene/chitosan-GCE (0.0147 $cm^2\ s^{-1}$)[24], CILE (0.0629 $cm^2\ s^{-1}$)[57] and carbon fibers (0.0219 $cm^2\ s^{-1}$ in water and 0.167 $cm^2\ s^{-1}$ in 1M H_2SO_4)[59].

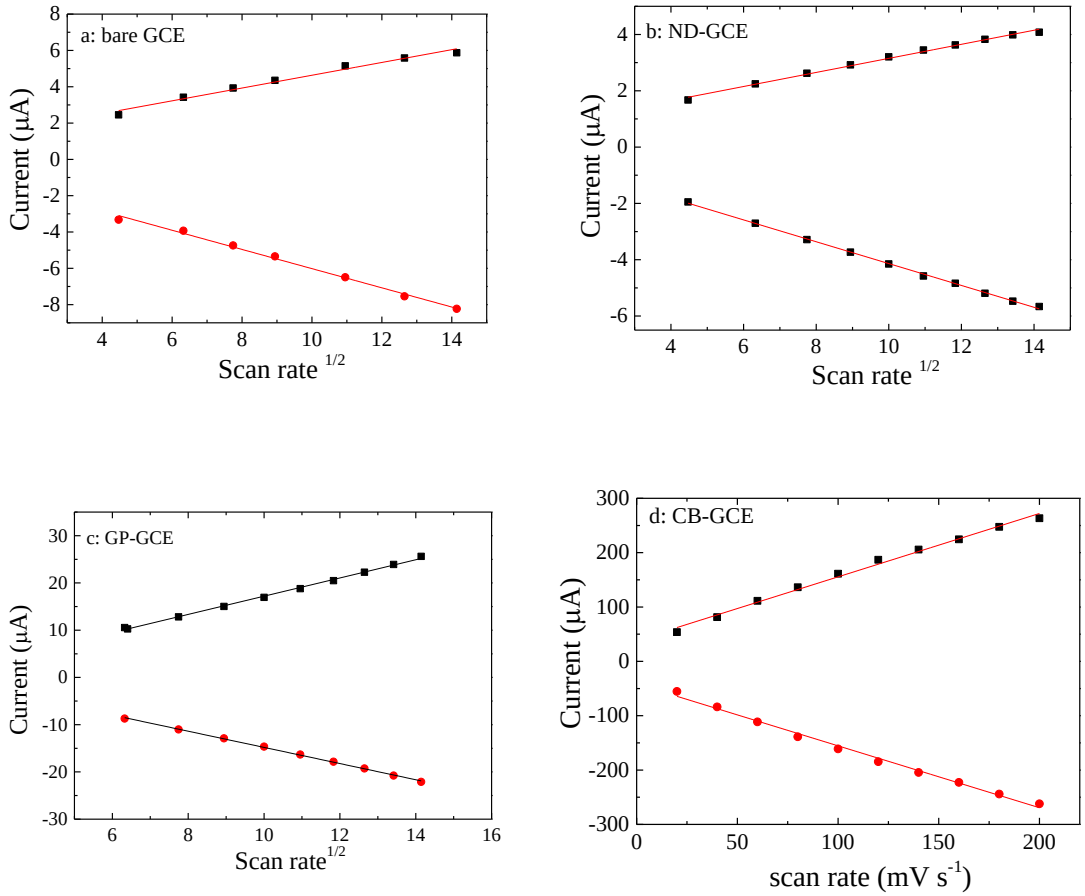

figure 5.4 Plots of peak current against scan rate obtaining from cyclic voltammograms in the solution containing 0.2 mM HQ and 0.1 M phosphate buffer at scan rate from 20 to 200 mV s^{-1} in steps of of 20 mV s^{-1} at (a) bare GC, (b) ND-GC, (c) GP-GC and (d) CB-GC

In order to further investigate the adsorption of HQ on all the electrodes studied, cyclic voltammetry was also performed in 0.1 M phosphate buffer which had been pre-treated by being immersed in 0.2 mM HQ for different lengths of time and carefully rinsed. This pre-treatment allowed differing extents of accumulation of HQ at the interface. **Figure 5.5** shows the resulting CVs at pre-treated bare GCE, ND-GCE, GP-GCE and CB-GCE. Also shown are the CVs in the presence of 0.2 mM HQ to be compared with. At bare GCE (see **Figure 5.5**a) there is no significant peak in the potential range studied, as well as at ND-GCE (**Figure 5.5**b) and GP-GCE (**Figure 5.5**c), in comparison to the curves in the presence of 0.2 mM HQ. The absence of HQ redox

peaks indicated that little HQ was adsorbed onto the electrode surface or the adsorption was so weak that HQ on the surface was easy to be washed off by water. As seen from **Figure 5.5**d, redox peaks of HQ are observed at the pre-treated CB-GCE in 0.1 M phosphate buffer. Also, the peak current rises gradually with an increase in dipping time from 10 to 300 s, suggesting increasing amount of HQ adsorbed on the surface. The inset shows the plot of peak current against time length. It can be seen that the current increases sharply at the beginning and reaches the plateau around 5 min. Seen from the CVs, this current is about one third of the value in the solution in the presence of 0.2 mM HQ, showing a strong adsorption of HQ at CB-GCE surface.

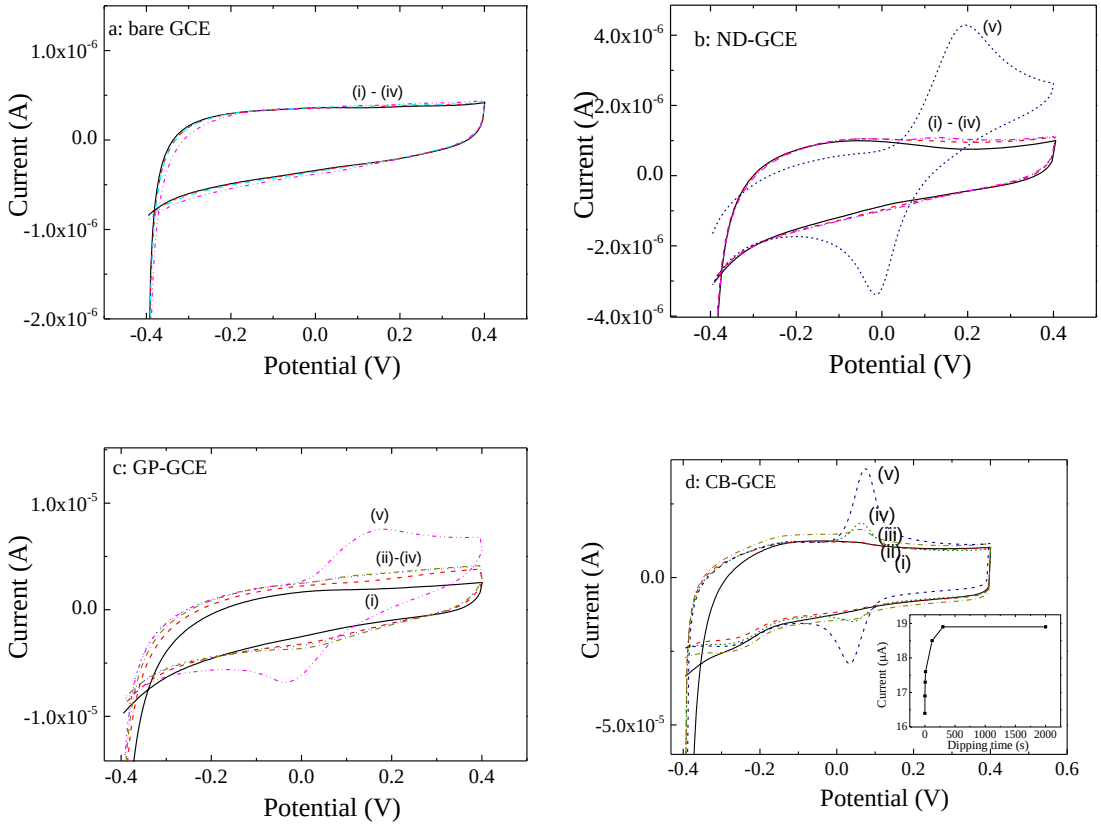

Figure 5.5 Cyclic voltammograms at (a) bare GC, (b) ND-GC, (c) GP-GC and (d) CB-GC electrodes, which electrodes were dipped into 0.2 mM HQ solution for (i) 0, (ii) 1, (iii) 10 and (iv) 300 s respectively and then rinsed before scan in 0.1 M phosphate buffer in the absence of HQ, and (v) in the presence of 0.2 mM HQ; Inset: plot of peak current *vs.* dipping time

The adsorption experiment was also carried out at a CB-GCE electrode pre-treated in more concentrated 2 mM HQ solution from 0 to 120 s. The CVs in 0.1 M phosphate buffer at pre-treated CB-GCE are displayed in **Figure 5.6**. The inset plots the peak current against the dipping time. The peak currents are greater the higher the concentration of the solution of HQ, showing that the CB layer is not chemically saturated with HQ in the concentration range even after long immersion time. It is not clear why the peak current drops after long immersion time; possibly some electrode fouling is occurring.

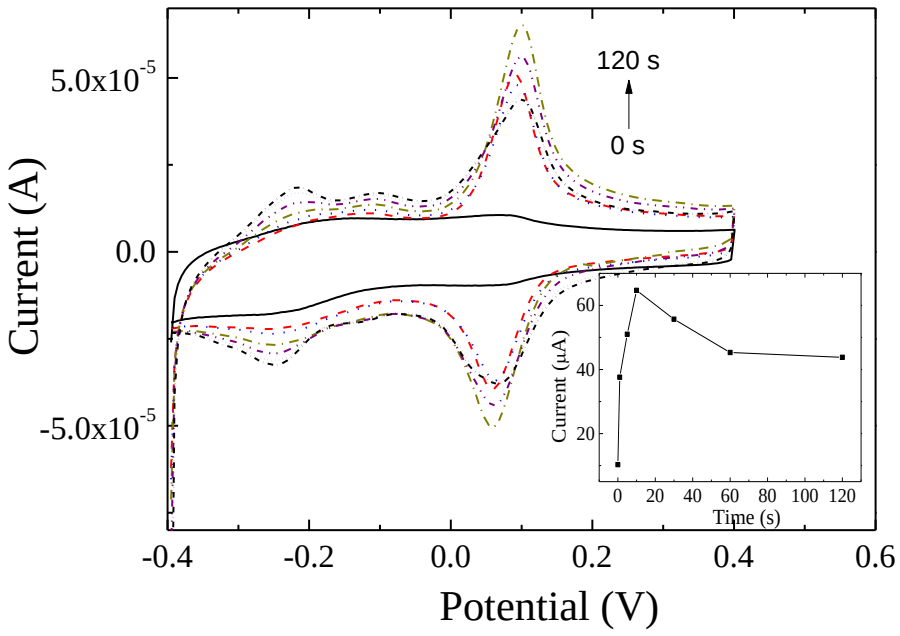

Figure 5.6 Cyclic voltammograms in the solution containing 0.1 M phosphate buffer at scan rate of 50 mV s^{-1} at CB-GCE. The electrode was dipped into 2 mM HQ solution for 0, 1, 10, 60, 120 s respectively; Inset: plot of peak current *vs.* the dipping time

Cyclic voltammograms with increasing HQ concentration in 0.1 M phosphate buffer, at bare GCE, ND-GCE, GP-GCE and CB-GCE are shown in **Figure 5.7**. The concentration of HQ increased from 0 to 200 μM. Correspondingly, a pair of redox peaks of HQ appears and grows gradually at all the electrodes. It is apparent that peaks

at modified electrodes are all better resolved and well-defined than at bare GCE over a wide potential range and the currents are higher, consistent with **Figure 5.3**. As expected, CB-GCE exhibits strongest sensitivity among all the electrodes. Due to the extremely high sensitivity, the LOD (S/N=3) obtained at CB-GCE (0.11 μM) is better than the value at GP-GCE (0.54 μM), ND-GCE (1.67 μM) and bare-GCE (2.35 μM), as shown in **Table 5.2**. This result is relatively similar or better than other glassy carbon electrodes. More comparison will be discussed in subsequent work.

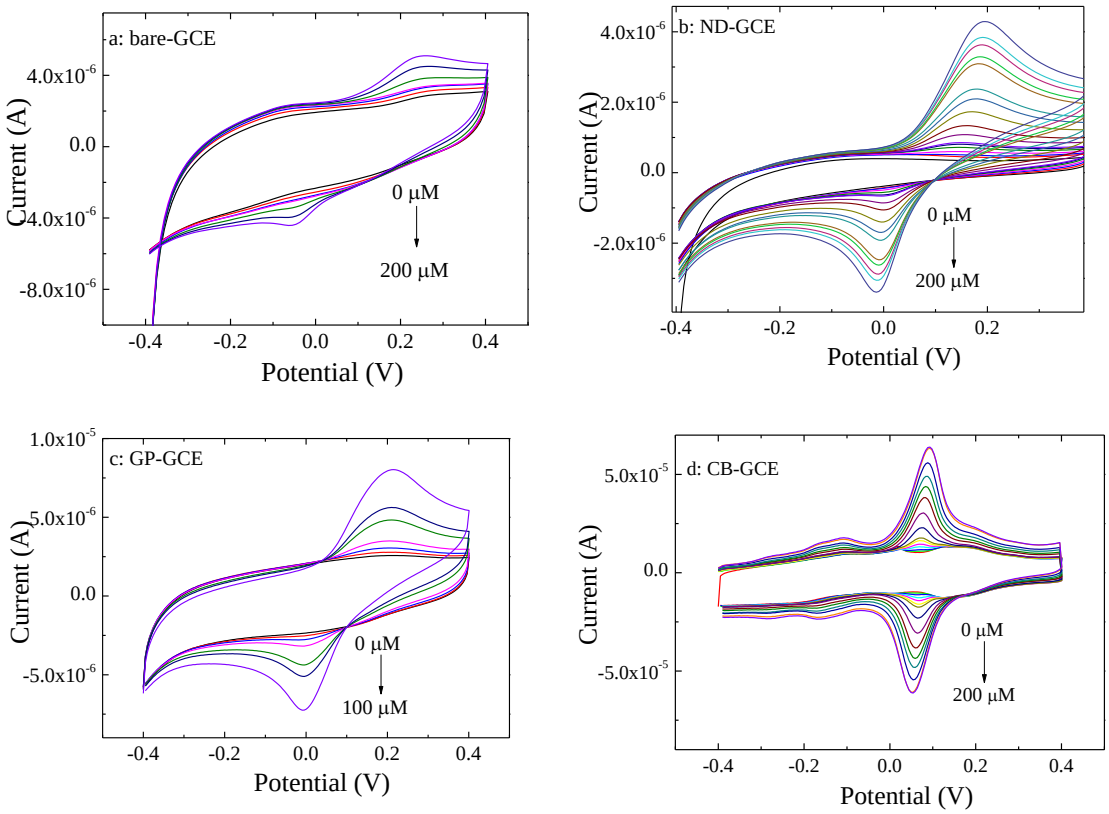

Figure 5.7 Cyclic voltammograms in a solution containing 0.1 M phosphate buffer and hydroquinone from 0 to 200 μM at (a) bare GCE (step of 40 μM), (b) ND-GCE (step of 20 μM), (c) GP-GCE (0, 10, 20, 40, 50, 100 μM) and (d) CB-GCE respectively (step of 20 μM).

5.3.1.1.2 Square wave voltammetry

As one of the most widely used techniques in electroanalysis, SWV has advantages in discriminating the signal against broad background contributions to the measured

current.[60] As a result, low detection limit can be achieved. Therefore, SWV was conducted to determine hydroquinone. **Figure 5.8**a, c, e and g display the voltammograms at bare GCE, ND-GCE, GP-GCE and CB-GCE respectively, scanning from 0 to +0.4 V in a solution of 0.1 M phosphate buffer and differing concentrations of HQ. Parameters were optimised, with frequency of 10 Hz, sensitivity of 1 mV and amplitude of 10 mV, which are used in all the subsequent work in this thesis. Also depicted aside are the corresponding plots of peak current against the concentration of HQ (**Figure 5.8** b, d, f and h). In the absence of HQ, the voltammograms are featureless and no Faradaic curve can be observed at any of the electrodes. When HQ is present, an anodic peak corresponding to the HQ oxidation appears at bare GCE (+0.25 V, starting to be observed when HQ>50 μM), ND-GCE (+0.1 V, HQ>5 μM), GP-GCE (+0.07 V, HQ>1 μM) and CB-GCE (+0.05 V, HQ>1 μM) in all profiles and the current increases with increasing HQ concentration.

The linearity dependence of the peak current to concentration of HQ gives quantitive information to calculate the LOD (S/N=3). The LOD for bare GCE, ND-GCE, GP-GCE and CB-GCE are calculated to be 5.01, 0.55, 0.28 and 0.094 μM respectively, as displayed in **Table 5.2**. CB-GCE provides the lowest LOD due to the highest sensitivity. In comparison to the value obtained from CVs, the LOD from SWV at CB-GCE are improved significantly (0.094 vs. 0.11 μM), which might be due to the compensation of the capacitance contribution at CB-GCE surfaces. In addition, the correlation coefficient of the linearity at ND-GCE (coefficient of determination R^2=0.995), GP-GCE (R^2=0.998) and CB-GCE (R^2=0.999) are all better than the value at bare GCE (R^2=0.925).

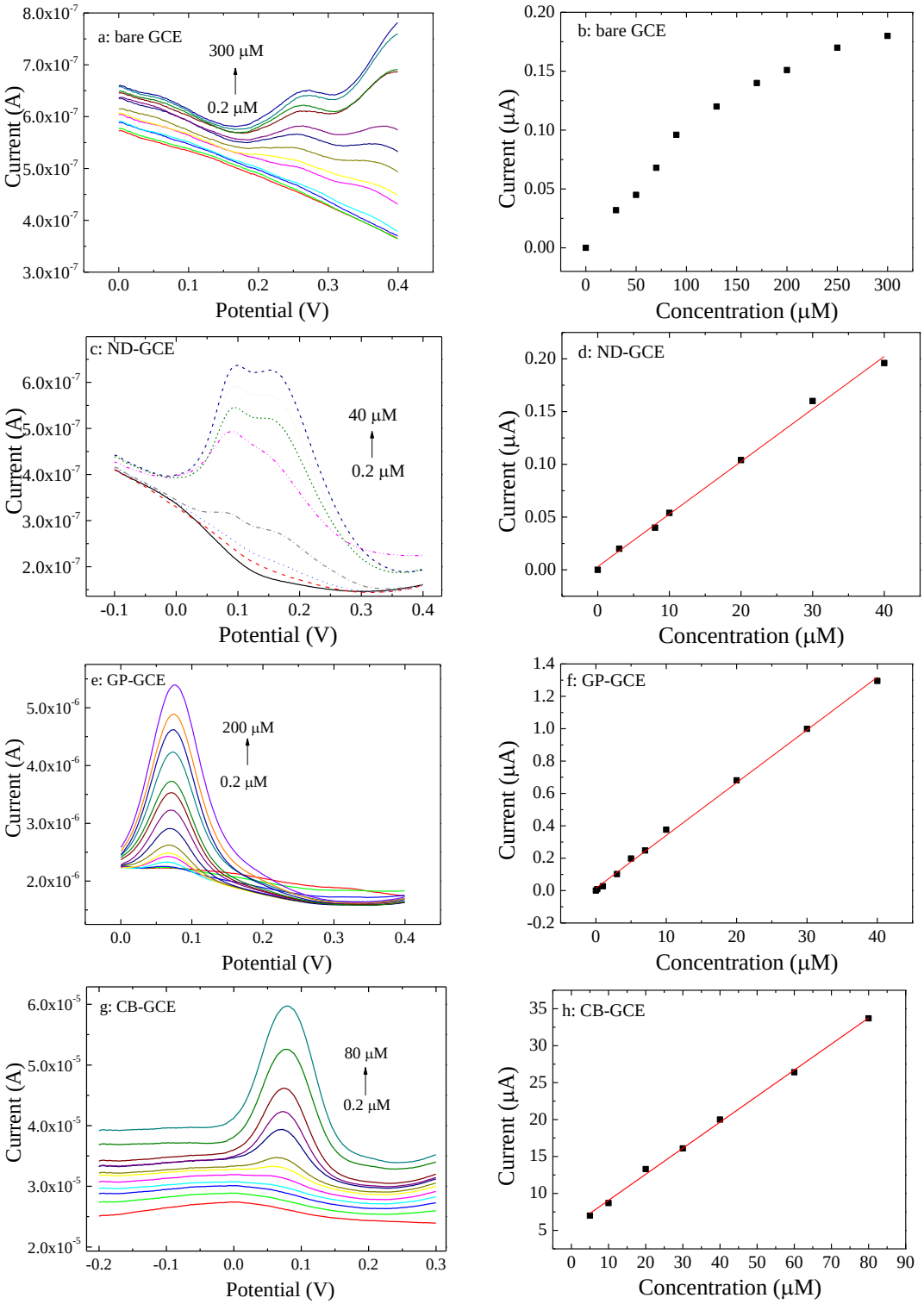

Figure 5.8 Square wave voltammograms in a solution containing 0.1 M phosphate buffer and increasing concentration of HQ at (a) bare GCE, (c) ND-GCE, (e) GP-GCE and (g) CB-GCE. And the corresponding plot of peak current *vs.* the concentration at (b) bare GCE, (d) ND-GCE, (f) GP-GCE and (h) CB-GCE

5.3.1.1.3 Amperometric Current-time curve

Amperometry is a widely performed electroanalytical approach for determination of phenolic compound.[11] In this method, a fixed potential is applied between modified GCEs and Pt counter electrode, which causes the injected HQ to be oxidised at the electrode surface and a current to flow. This potential should be chosen so that the magnitude of the current is directly proportional to concentration. Seen from the CVs shown in **Figure 5.3**, the oxidation peak appears around +0.3 V at bare GCE, and around +0.15 V at ND-GCE, GP-GCE and CB-GCE. In order to keep consistency, a potential of +0.3 V was chosen for the amperometric experiments at all the electrodes. A rotating disk electrode was used to stir the solution at speed of 1200 rpm, by which equilibrium at electrode-solution interface can be achieved more quickly.

The current-time curves are shown in **Figure 5.9**. After initial current stabilisation, HQ was injected into solution and the steady state current response was measured as a function of concentration. Seen from **Figure 5.9**a, the current at bare GCE does not respond significantly to 0.1, 1 and 2 μM HQ significantly, showing that these concentrations are too low to be detected. When 10 and 20 μM HQ was added, a significant current rise appears. Similarly, the current at ND-GCE (**Figure 5.9**c) also hardly responds to concentrations lower than 10 μM. However, the successive addition of 0.02, 0.05 and 0.1 μM HQ gives rise to a current at GP-GCE (**Figure 5.9**e) although the increase is barely in comparison to the noise. CB-GCE also responds to the addition of 0.2 μM HQ (**Figure 5.9**g), and the current increase is one magnitude stronger than the value at GP-GCE. The response to 1 and 10 μM HQ at GP-GCE and CB-GCE can be found in the insets. However, the noise, fluctuation of current in the absence of HQ, is of the order of 10^{-8} A at CB-GCE, which is also notably larger than the value at GP-

GCE (about 10^{-9} A). The resulting current increases against injected HQ concentration are plotted in **Figure 5.9**b, d, f and h, corresponding to bare GCE, ND-GCE, GP-GCE and CB-GCE respectively. Linear lines are fitted to obtain the sensitivity, *i.e.* the slope. The correlation coefficients of the linearity at GP-GCE (R^2=0.999) and CB-GCE (R^2=0.998) are better than bare GCE (R^2=0.992) and ND-GCE (R^2=0.995). The detection limits (S/N=3) are shown in **Table 5.2**. The value at bare GCE, ND-GCE, GP-GCE and CB-GCE are 1.75, 0.43, 0.17 and 0.012μM, which are all better than the results obtained by CV and SWV.

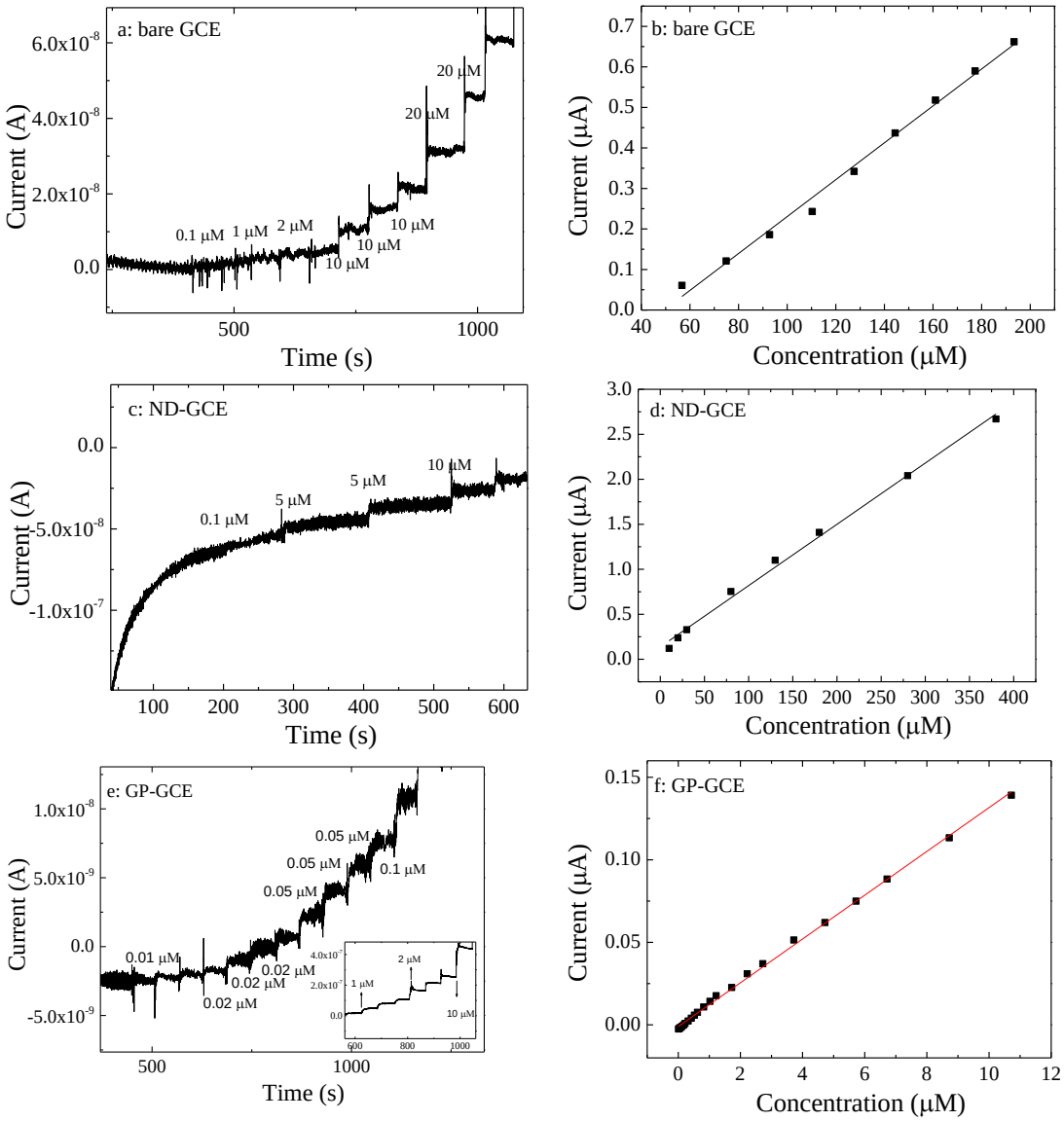

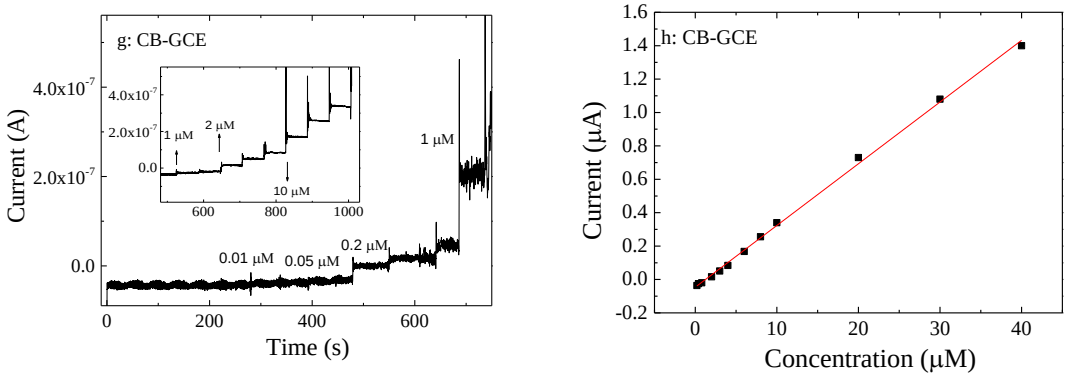

Figure 5.9 Amperometric graph at potential of +0.3 V in 0.1 M phosphate buffer with successive addition of HQ at (a) bare GCE, (c) ND-GCE, (e) GP-GCE and (g) CB-GCE; And the corresponding plot of peak current *vs.* the concentration at (b) bare GCE, (d) ND-GCE, (f) GP-GCE and (h) CB-GCE. Inset: amperometric graph in a wider range

5.3.1.1.4 Summary and comparison

The LOD of HQ sensors found in this work and electrodes in the literature are listed in **Table 5.2**. The LOD of HQ was reported to be 3.9 μM at GCE recently[19], similar to our result of 2.68 μM at GCE. Some modifiers such as montmorillonite[12] and $Co(OH)_2$[13] improved the LOD to about 0.5 μM. The result at ND-GCE of 0.55 μM is close to those sensors. Other carbon materials, such as multi-walled carbon nanotude [17], graphene-polyoxometalate [22]and graphene-chitosan[24], were also reported, most of which the LODs were down to the order of 10^{-7} M. The LOD at GP-GCE in this work also can achieve this level by both SWV and amperometry methods. Compared with all the electrodes mentioned above, CB-GCE can provide an even lower LOD of 0.012 μM. The reason can be that due to the strong adsorption, the concentration of HQ is higher at carbon black surface, resulting in higher sensitivity than other electrodes. However, the noise at CB-GCE is also larger so the ultimate detection limit is a balance between these two factors. Of the modifiers studied, the conclusion is that graphene produces a useful improvement in signal performance in comparison to the other modifiers seen in the table, whereas CB seems to produce an improvement better than has been observed previously due to the higher sensitivity.

Table 5.2 Detection limit (μM) of HQ at various sensors from this work and literature by cyclic voltammetry, square wave voltammetry and amperometry methods respectively

Sensors	CV	SWV	Amperometric
bare GCE	2.35	5.01	1.75
ND-GCE	1.67	0.55	0.43
GP-GCE	0.54	0.28	0.17
CB-GCE	0.11	0.094	0.012
GCE	3.9[19]		
Tyr/MWCNTs			0.2[17]
graphene-polyoxometalate		0.09[22]	
$Co(OH)_2$		0.5[13]	
montmorillonite		0.57[12]	
PDDA-G/GCE		0.25 (DPV)[25]	
Graphene-chitosan		0.75 (DPV)[24]	

5.3.1.2 Determination of DHB

5.3.1.2.1 Cyclic voltammetry

DHB, the isomer of HQ, is another important phenolic compound that is problematic as a water pollutant. Similar to the HQ determination above, DHB was also detected in this work at bare GCE, GP-GCE, ND-GCE and CB-GCE by cyclic voltammetry, square

wave voltammetry and amperometry methods respectively. The electrochemical process of DHB is demonstrated in **Figure 5.10**.

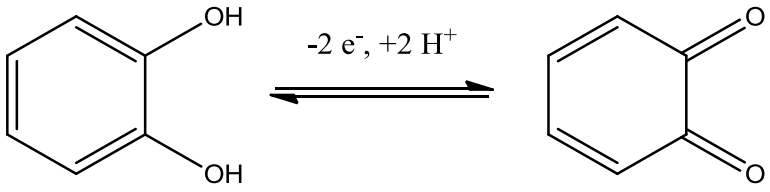

Figure 5.10 Electrochemical oxidation and reduction of DHB

The cyclic voltammetry was performed at bare GCE, GP-GCE, ND-GCE and CB-GCE in a solution containing 0.1 M phosphate buffer and 0.2 mM DHB. **Figure 5.11**a exhibits the CVs at all electrodes and the **Figure 5.11**b without CB-GCE. Similar to the voltammograms of HQ, the CB-GCE shows the strongest peak current and narrowest redox peak-peak separation at +0.15/+0.2 V. This potential was about 0.05 volt higher than HQ redox peaks at CB-GCE. At other electrodes (see **Figure 5.11**b), the anodic peak potential of DHB are in the range of +0.15 to 0.3 V, which is also more positive than the result of HQ redox.[61] Also the peak current at bare GCE is the lowest, followed by ND-GCE and GP-GCE, consistent with the result of HQ as shown above. The diffusion coefficients of HQ and DHB were reported to be similar in aqueous solution.[62] Taken the value of 1.6×10^{-9} cm^2 s^{-1},[62] the current limit for 0.2 mM DHB at scan rate of 0.05 V s^{-1} can be calculated to be 1.28×10^{-5} A. The peak current at bare GCE, ND-GCE and GP-GCE are 0.63, 0.79 and 1.21×10^{-5} A respectively, which is close to this value. However, the peak current at CB-GCE is much higher (5.4×10^{-5} A), showing a non-diffusion control character as observed in HQ reaction at CB-GCE.

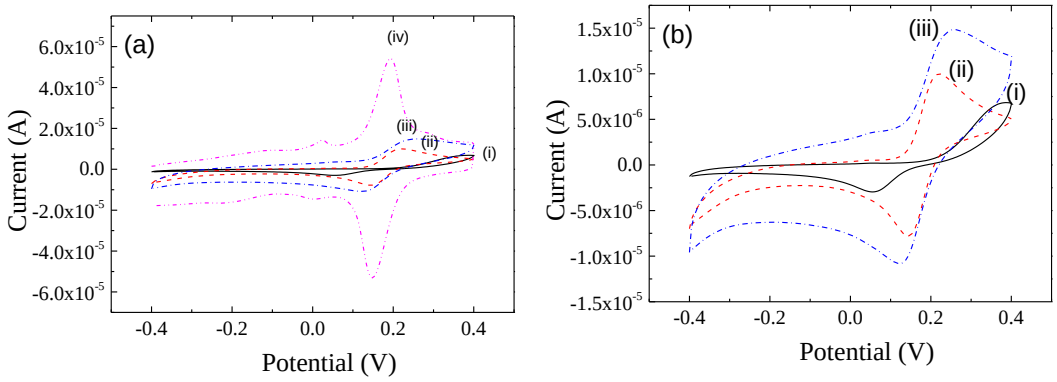

Figure 5.11 Cyclic voltammograms in a solution containing 0.1 M phosphate buffer and 0.2 mM DHB at (i) bare GCE, (ii) ND-GCE, (iii) GP-GCE, and (iv) CB-GCE respectively

Cyclic voltammetry with increasing scan rates was conducted at these electrodes to characterise the electrode surface process. **Figure 5.12** shows CVs of 0.2 mM DHB in 0.1 M phosphate buffer at bare GCE, ND-GCE and CB-GCE with scan rate from 20 to 1000 mV s^{-1}. The insets plot the resulting peak current of both oxidisation and reduction against scan rate. Apparently, the peak current at bare GCE, ND-GCE and GP-GCE shows a linear increase with the square root of scan rate, suggesting the surface process at these electrodes are under diffusion control. However, the proportional relationship of peak current to scan rate at CB-GCE represents a diagnostic of an electrode reaction of adsorbed species. It is in agreement with the results obtained from HQ solution. Considering the similarity of HQ and DHB, the kinetics of DHB redox reaction are not discussed further here.

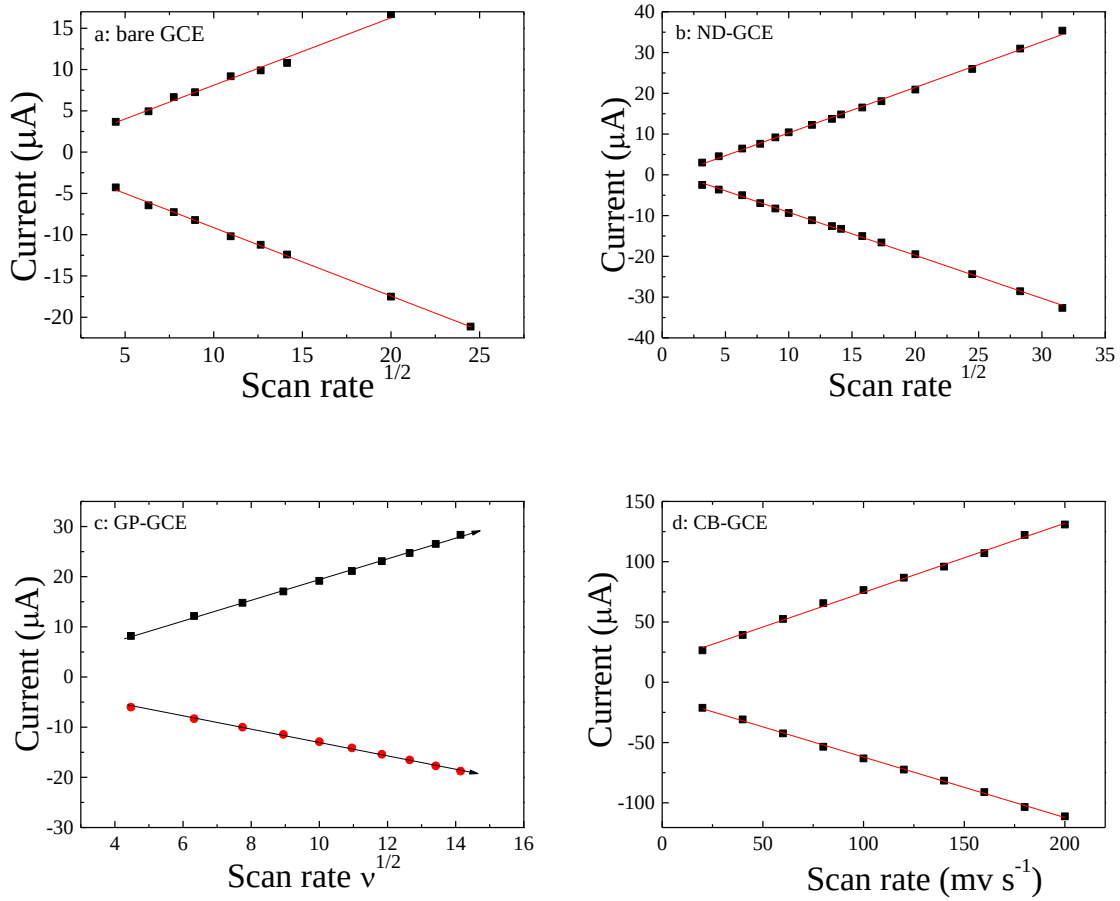

Figure 5.12 Cyclic voltammograms in the solution containing 0.2 mM DHB and 0.1 M phosphate buffer at scan rate from 20 to 1000 mV s^{-1} in steps of 100 mV s^{-1}, at (a) bare GCE and (b) ND-GCE; and scan rate from 20 to 200 mV s^{-1} in steps of 20 mV s^{-1} (c) GP-GCE and (d) CB-GCE; Insets: plots of peak current *vs.* scan rate (a, b and c); or square root of scan rate (d)

In order to study the adsorption of DHB, bare GCE, ND-GCE, GP-GCE and CB-GCE were immersed into 0.2 mM DHB solution for 0, 1, 10 and 300 s respectively, then rinsed by water and put into 0.1 M phosphate buffer for cyclic voltammetric scan from -0.4 to 0.4 V. The resulting CV profiles are shown in **Figure 5.13**. Also shown is the CV at each electrode in a solution of 0.1 M phosphate buffer and 0.2 mM DHB. Similar to the results of HQ, peaks are hardly observed at bare GCE (**Figure 5.13**a), ND-GCE (**Figure 5.13**b) or GP-GCE (**Figure 5.13**c), although the current increases slightly at the potential where DHB redox reaction occurs. It indicates that the adsorption of DHB at these electrodes is weak. However, at CB-GCE a pair of well resolved peaks of DHB

can be observed around +0.15 V. The peak current against dipping time is shown in **Figure 5.13**d. After dipping into the DHB solution for longer time, the peak current increases, suggesting more DHB was adsorbed at the CB-GCE surface. Then the peak current reaches a plateau at about 50 s, quicker than the 300 s in HQ solution. In addition, the peak current at 30 min is two thirds as strong as the value in 0.2 mM DHB solution. In comparison to the result of the same experiment in HQ solution, where the current had only one fifth the value in 0.2 mM solution. This is an indication that the adsorption of DHB at CB-GCE is stronger than HQ.

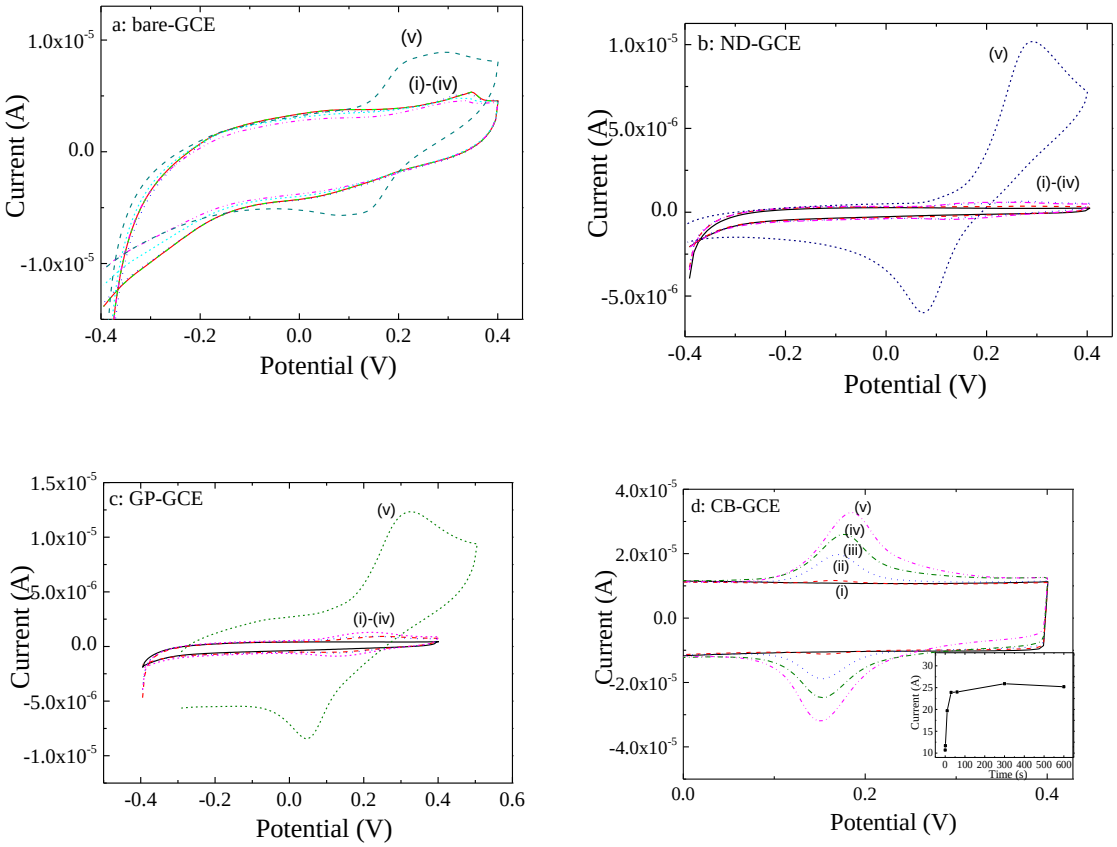

Figure 5.13 Cyclic voltammograms at (a) bare GC, (b) ND-GC, (c) GP-GC and (d) CB-GC electrodes, which were dipped into 0.2 mM HQ solution for (i) 0, (ii) 1, (iii) 10 and (iv) 300 s respectively and then rinsed before scanning in 0.1 M phosphate buffer in the absence of HQ, and (v) in the presence of 0.2 mM HQ; Inset: the plot of peak current *vs.* dipping time

Cyclic voltammetry was also used to determine DHB quantitatively. The CVs in **Figure 5.14** were conducted in 0.1 M phosphate buffer with the continuous addition of DHB with resulting concentration from 0 to 200 μM at bare GCE, GP-GCE, ND-GCE and CB-GCE respectively. At these electrodes, a pair of peaks can be observed in the presence of DHB, and the peak current is enhanced as the concentration of DHB increases. Due to the adsorption effect, the peak-peak separation at CB-GCE is much narrower than these at bare GCE, ND-GCE, GP-GCE and CB-GCE, *ca.* +0.015 V in the presence of 10 μM DHB, which is getting larger with the increasing concentration of DHB. Also, the sensitivity at CB-GCE is the highest. The LOD (S/N=3) can be calculatedas 3 time noise divided by the sensitivity, as shown in **Table 5.3**. The values are 1.64, 0.6, 0.25 and 0.13 μM at bare GCE, ND-GCE and GP-GCE and CB-GCE respectively.

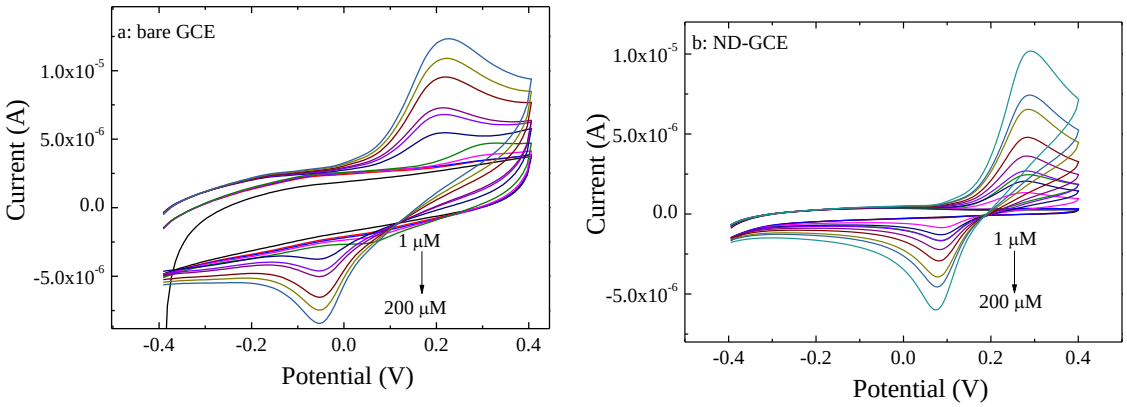

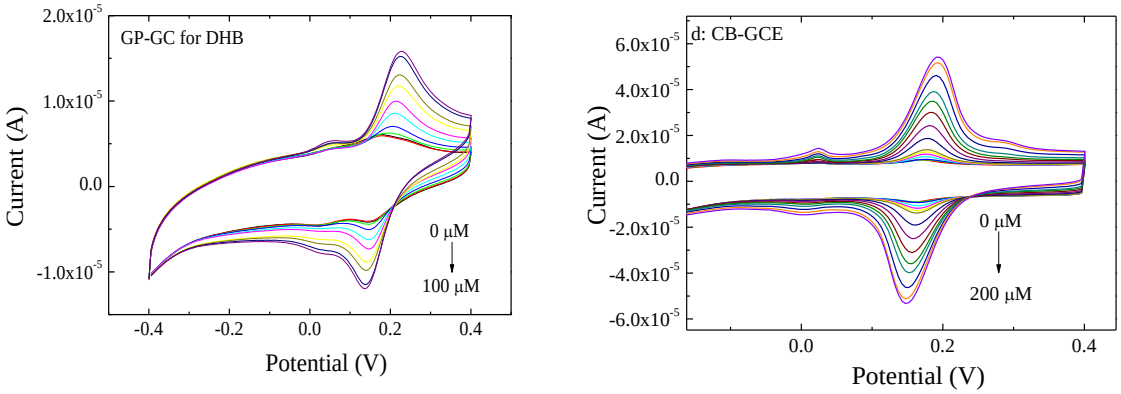

Figure 5.14 Cyclic voltammograms in a solution containing 0.1 M phosphate buffer and continuous addition of DHB from 0 to 200 μM in steps of 20 μM at (a) bare GCE, (b) ND-GCE, (c) GP-GCE and (d) CB-GCE respectively

5.3.1.2.2 Square wave voltammetry

DHB was also determined by SWV in a solution of 0.1 M phosphate buffer at bare GCE, ND-GCE, GP-GCE and CB-GCE. **Figure 5.15** shows the voltammograms at each sensor with increasing DHB concentration. Also shown are the plots of peak current against DHB concentration. The oxidation peak of DHB can be observed at a potential *ca.* +0.18 V in the presence of DHB. However, bare GCE only responds to the concentration higher than 10 μM while a lower concentration can be detected by ND-GCE, GP-GCE and CB-GCE. The peak current shows a linear increase with DHB from a low to high concentration at bare GCE (**Figure 5.15**b), ND-GCE (**Figure 5.15**d), GP-GCE (**Figure 5.15**f) and CB-GCE (**Figure 5.15**h), with the correlation coefficient of 0.988, 0.991, 0.999 and 0.997 respectively. The LOD (S/N=3) can be calculated to be 1.2, 0.12, 0.10 and 0.023 μM for bare GCE, ND-GCE, GP-GCE respectively, as shown in **Table 5.3**. These values are significantly lower than those obtained by cyclic voltammetric methods, especially at CB-GCE. The extremely low LOD at CB-GCE is attributed to the adsorption process and the minimised capacitance contribution at CB-GCE by SWV.

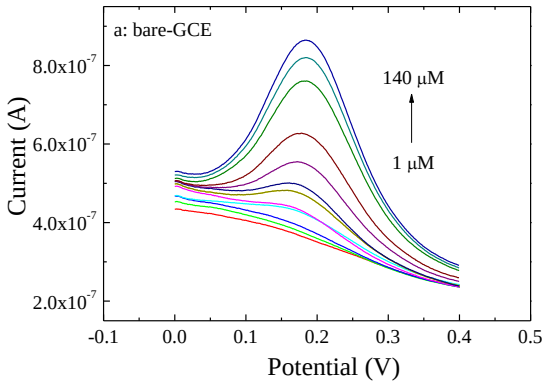
a: bare-GCE
140 μM
1 μM
Current (A)
Potential (V)

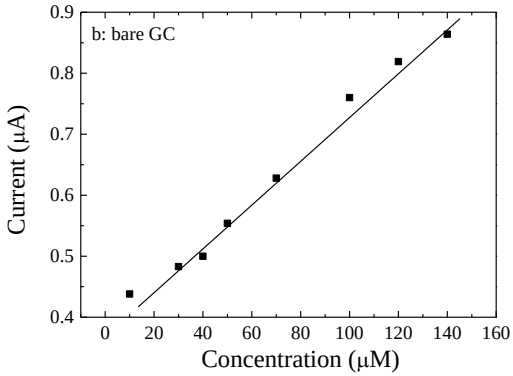
b: bare GC
Current (μA)
Concentration (μM)

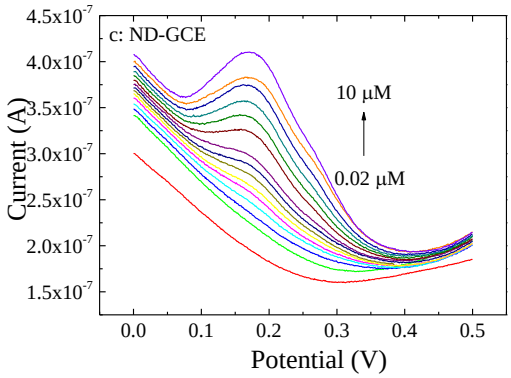
c: ND-GCE
10 μM
0.02 μM
Current (A)
Potential (V)

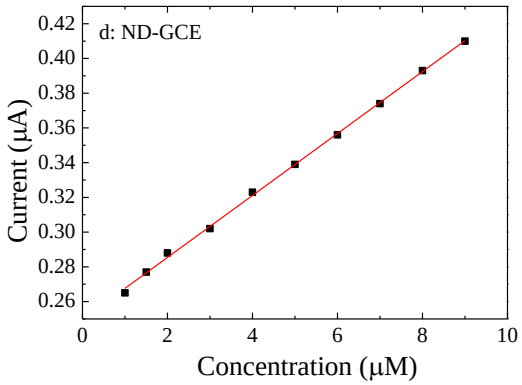
d: ND-GCE
Current (μA)
Concentration (μM)

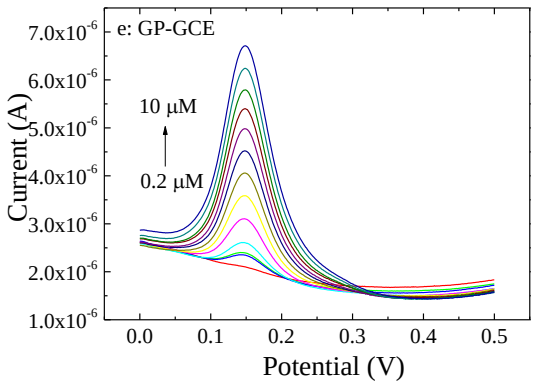
e: GP-GCE
10 μM
0.2 μM
Current (A)
Potential (V)

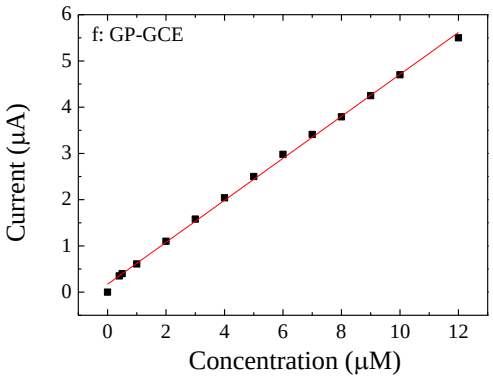
f: GP-GCE
Current (μA)
Concentration (μM)

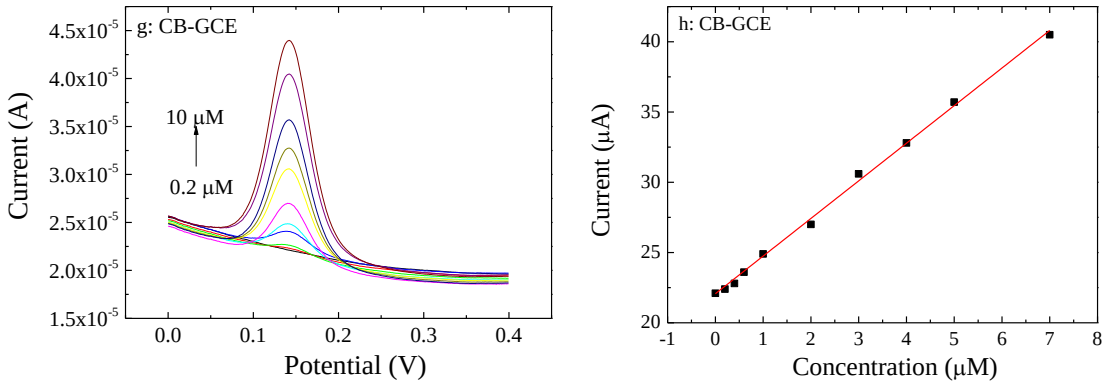

Figure 5.15 The square wave voltammograms in a solution containing 0.1 M phosphate buffer and continuous addtion of DHB at (a) bare GCE (step of 20 µM), (c) ND-GCE (step of 1 µM), (e) GP-GCE (step of 1 µM) and (g) CB-GCE (step of 1 µM). And the corresponding plots of peak current *vs.* the concentration at (b) bare GCE, (d) ND-GCE, (f) GP-GCE and (h) CB-GCE

5.3.1.2.3 Amperometric Current-time curve

DHB was also determined by the amperometry method at bare GCE, ND-GCE, GP-GCE and CB-GCE. The applied potential was chosen to be +0.2 V at all the electrodes, for the same reason as mentioned for HQ determination by amperometric method. At this potential, the oxidation of DHB occurs at all these electrodes. The solution was stirred by a RDE during the detection process. After the current reached a steady state, DHB was injected and the current increase was recorded. The current-time curves at bare GCE, ND-GCE, GP-GCE and CB-GCE are shown in **Figure 5.16**a, c, e and g. The insets are the curves at larger time scale. Although the current increases slightly at low concentration at bare GCE, only at 10 µM is a significant rise is observed. And seen from **Figure 5.16**b, the current does not increase linearly with DHB concentration. Therefore the detection limit cannot be readily evaluated using the standard method. The current-time curve for ND-GCE is shown in **Figure 5.16**c. An increase can be observed when 1 µM DHB was injected. At GP-GCE and CB-GCE (**Figure 5.16**e and g), an even lower concentration of 0.1 µM can be detected. The resulting plots of

current increase at ND-GCE, GP-GCE and CB-GCE against the injection of DHB are displayed in **Figure 5.16**d, f and h, yielding a linear line where the slope gives the sensitivity. Then the LOD (S/N=3) can be calculated to be 0.97, 0.086 and 0.017 μM respectively, as listed in **Table 5.3**.

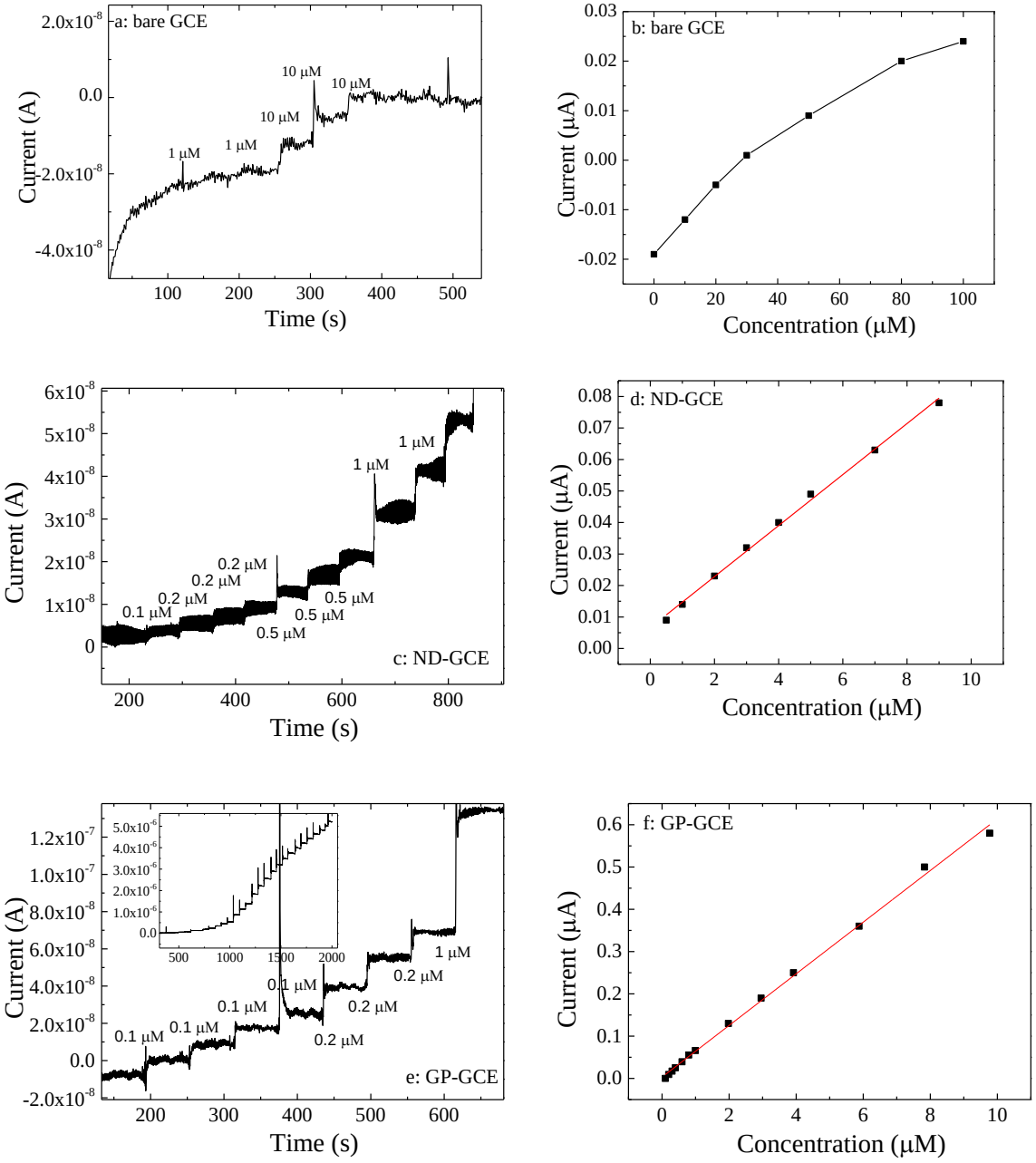

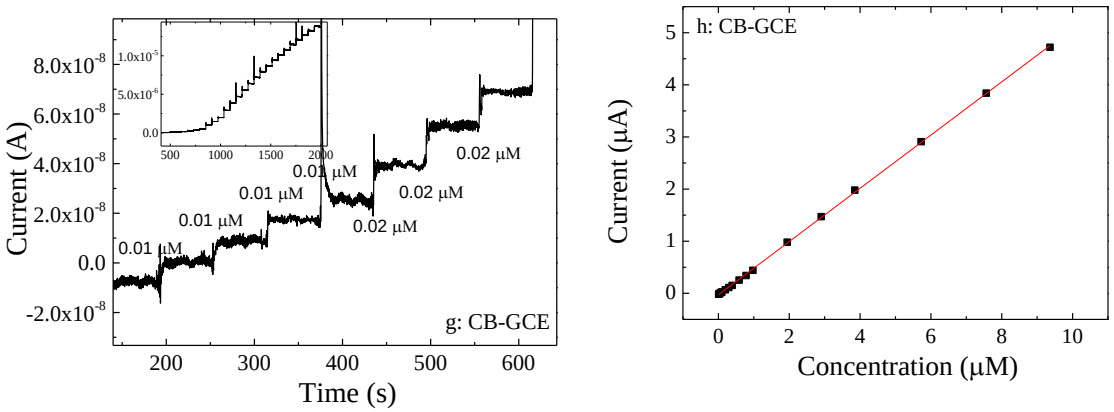

Figure 5.16 Amperometric graph in a solution of 0.1 M phosphate buffer and successive addition of DHB at (a) bare GCE, (c) ND-GCE, (e) GP-GCE and (g) CB-GCE; and the corresponding plots of current *vs.* concentration of DHB. The applied potential was +0.2 V. Insets: amperometric graph in a wider range

5.3.1.2.4 Summary and Comparison

The LOD of DHB sensors from this work and other literature are listed in **Table 5.3**. Many sensors have been developed for DHB detection, including non-carbon materials (Al/SiO_2 with LOD of 0.1 µM[23]), carbon materials sensors (GCE of 7.33 µM[19], SPE of 0.5 µM [20], graphene-polyoxometalate of 0.05 µM[22]), biosensors (tyr/MWCNTs of 0.2 µM [11,17], tyr/Ti of 0.09 µM[14]). In this work, the detection limits of DHB were found to be 1.2 µM at bare GCE, 0.12 µM at ND-GCE, 0.086 µM at GP-GCE and 0.017 µM at CB-GCE, which are better than most of the DHB sensors. Given the cheapness of CB, and the complexity or cost of many other electrode modifiers, the effectiveness of CB is quite striking.

Table 5.3 Detection limit (μM) of DHB at various sensors from this work and literature by cyclic voltammetry, square wave voltammetry and amperometry methods respectively

Sensors	CV	SWV	Amperometric
bare GCE	1.64	1.2	-
ND-GCE	0.60	0.12	0.97
GP-GCE	0.25	0.10	0.086
CB-GCE	0.13	0.023	0.017
Al/SiO_2[23]		0.1	
GCE[19]		7.33	
SPE[20]		0.5	
graphene-polyoxometalate[22]		0.05	
tyr/MWCNTs[11,17]			0.2

5.3.1.3 Simultaneous determination of HQ and DHB

Since HQ and DHB often co-exsit in the same solution and being oxidise at similar potentials, it is of interest to explore if there is a methodology to detect them simultaneously. This is explored in this section. SWV were conducted in the solution containing 0.1 M phosphate buffer, 10 μM HQ and 10 μM DHB at bare GCE, ND-GCE, GP-GCE and CB-GCE, from -0.2 to +0.8 V. The profiles are shown in **Figure 5.17**. At bare GCE (**Figure 5.17**a), although a weak and broad curve appears in the range of 0.1 to 0.3 V, no well-resolved peak can be observed in the potential window studied. At ND-GCE (**Figure 5.17**b), one wide peak centred at +0.11 V appears,

showing that the oxidation peaks of HQ and DHB are overlapped with each other and cannot be identified at ND-GCE. However, two distinct peaks at -0.01 and +0.01 V can be observed at both GP-GCE (**Figure 5.17**c) and CB-GCE (**Figure 5.17**d), corresponding to the oxidation of HQ and DHB respectively. Note that the peak heights at CB-GCE are 6 times higher than the one at GP-GCE. These two distinct peaks of HQ and DHB indicate that both GP-GCE and CB-GCE are capable of being used to simultaneous determine HQ and DHB. Therefore both electrodes were investigated.

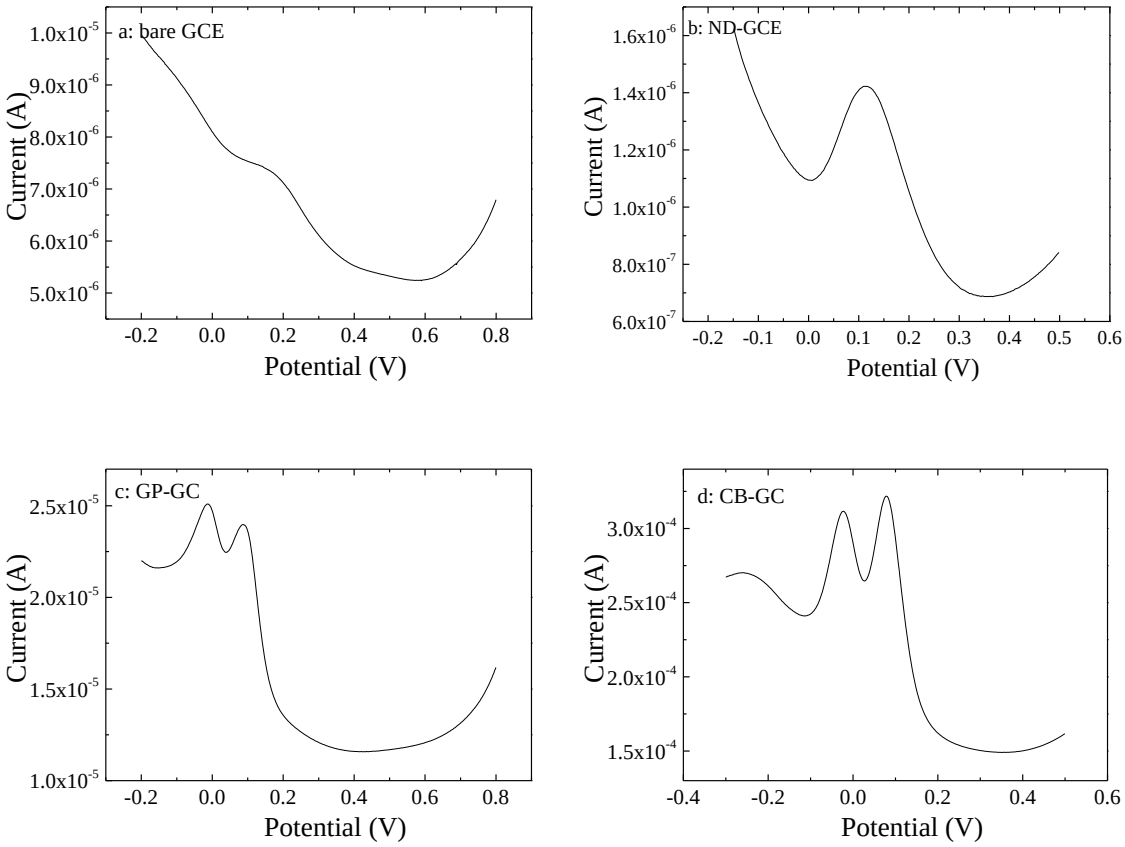

Figure 5.17 Square wave voltammograms in a solution containing 0.1 M phosphate buffer and 10 µM HQ and DHB at (a) bare GCE, (b) ND-GCE, (c) GP-GCE and (d) CB-GCE

The simultaneous determination of HQ and DHB was conducted in a solution containing 0.1 M phosphate buffer and increasing HQ and DHB at GP-GCE, scanning from -0.2 to +0.8 V where the oxidation of HQ and DHB occurs. First HQ and DHB

solution of the same concentration were added into solution simultaneously, from 2 to 10 µM. The resulting voltammograms are displayed in **Figure 5.18**a. Two distinct peaks appear and rise gradually with the increasing concentration, corresponding to the oxidation of HQ and DHB. Then the concentration of HQ was fixed at 10 µM, and DHB was added, increasing from 12 to 20 µM, as shown in **Figure 5.18**b. Apparently, the peak for HQ oxidation is hardly changed, showing that the oxidation of HQ is independent of DHB concentration. On the other hand, the other peak for DHB oxidation grows significantly. After that, the concentration of DHB was fixed at 20 µM, and HQ started to be added, as shown in **Figure 5.18**c. Seen from the figure, the injection of HQ increases the peak current of HQ alone while it does not change the peak of DHB at GP-GCE. A conclusion can be reached that the oxidation peaks of HQ and DHB are only dependent on each concentration.

The detection independence of HQ and DHB can be seen clearly by the plot of peak current against concentration as shown in **Figure 5.18**d. The upper square points are for DHB oxidation peaks, and the lower dots are for HQ, showing a higher response of DHB than HQ at GP-GCE. However, the slopes of each line are similar, indicating a similar sensitivity. It can be seen that the peak current shows a linear increase with HQ and DHB by both simultaneous and separate injections. It supports the idea that the peak response at GP-GCE to HQ and DHB are independent and did not interfere with each other, and that simultaneous detection of HQ and DHB at GP-GCE is reliable. The LOD (S/N=3) can be calculated to be 0.061 µM for HQ and similarly 0.063 µM for DHB.

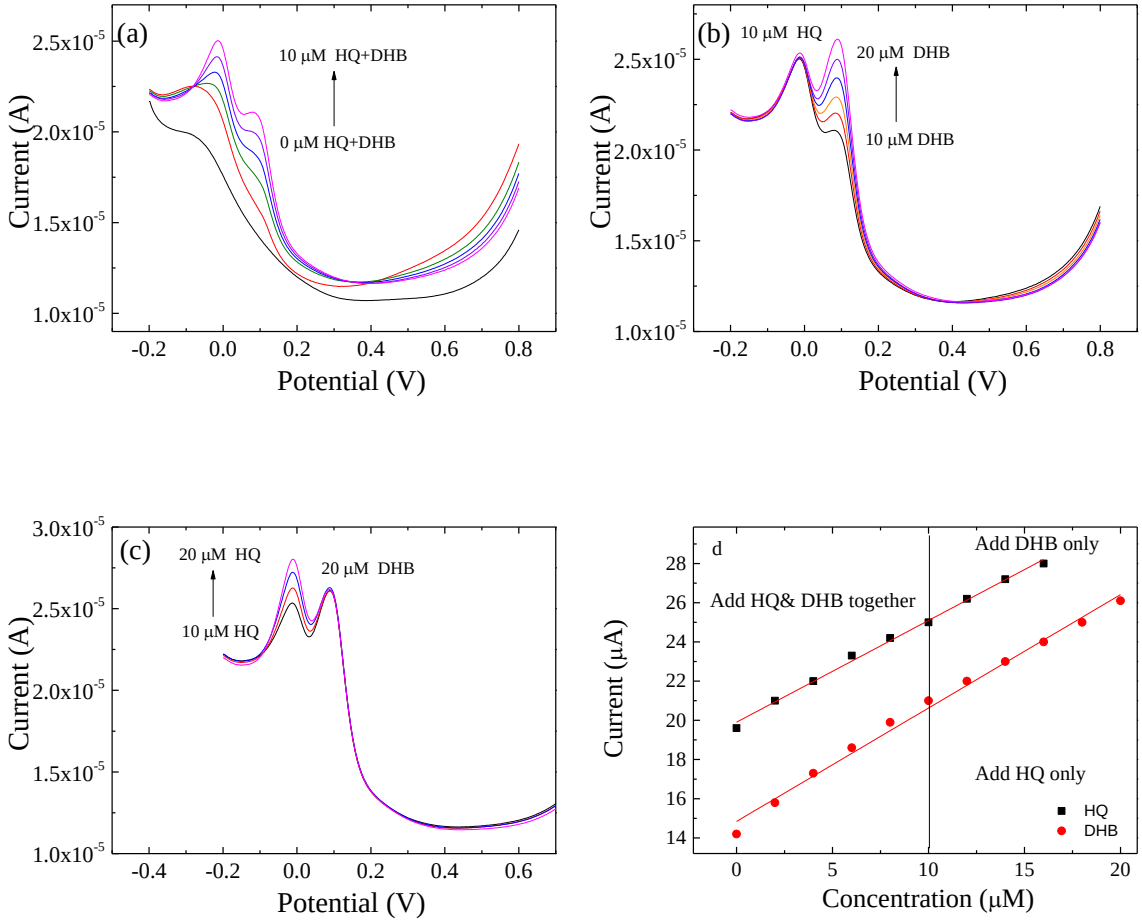

Figure 5.18 Square wave voltammograms at CB-GCE in 0.1 M phosphate buffer and (a) continuous addition of HQ and DHB from 0 to 10 µM; (b) 10 µM DHB and increasing HQ from 10 to 20 µM and (c) 20 µM HQ and increasing DHB from 10 to 16 µM; And (d) the corresponding plot of peak current *vs.* the concentration. All the concentration steps are 2 µM

Square wave voltammetry was also performed at CB-GCE to detect HQ and DHB simultaneously following the similar procedure at GP-GCE. **Figure 5.19**a shows the voltammograms when increasing the concentration of HQ and DHB together from 0 to 8 µM. **Figure 5.19**b is the voltammograms in HQ which increases from 8 to 13 µM when DHB is of 8 µM while **Figure 5.19**c is for adding DHB from 8 to 13 µM with a fixed HQ of 13 µM. In the presence of HQ and DHB, two distinct peaks can be observed around 0 and 0.1 V, corresponding to the oxidation of HQ and DHB respectively. These peaks are both enhanced as HQ and DHB were injected together, as

shown in **Figure 5.19**a. When increasing the concentration of HQ only, the peak of HQ rises correspondingly while DHB does not change significantly (**Figure 5.19**b). And when HQ was fixed, only the peak for DHB grows gradually in the presence of more DHB (**Figure 5.19**c). The plot of current *vs.* concentration can be found in **Figure 5.19**d, which data are obtained from **Figure 5.19**a, b and c. Alike the results from GP-GCE, the peak current of DHB at CB-GCE is relatively higher than the one of HQ. Apparently, the peak currents of both HQ and DHB are linear to the concentration of HQ and DHB respectively. And the slope of DHB is higher than the one of HQ, showing a higher sensitivity. The detection limit at CB-GCE for HQ and DHB determination are calculated to be 0.018 and 0.015 µM respectively.

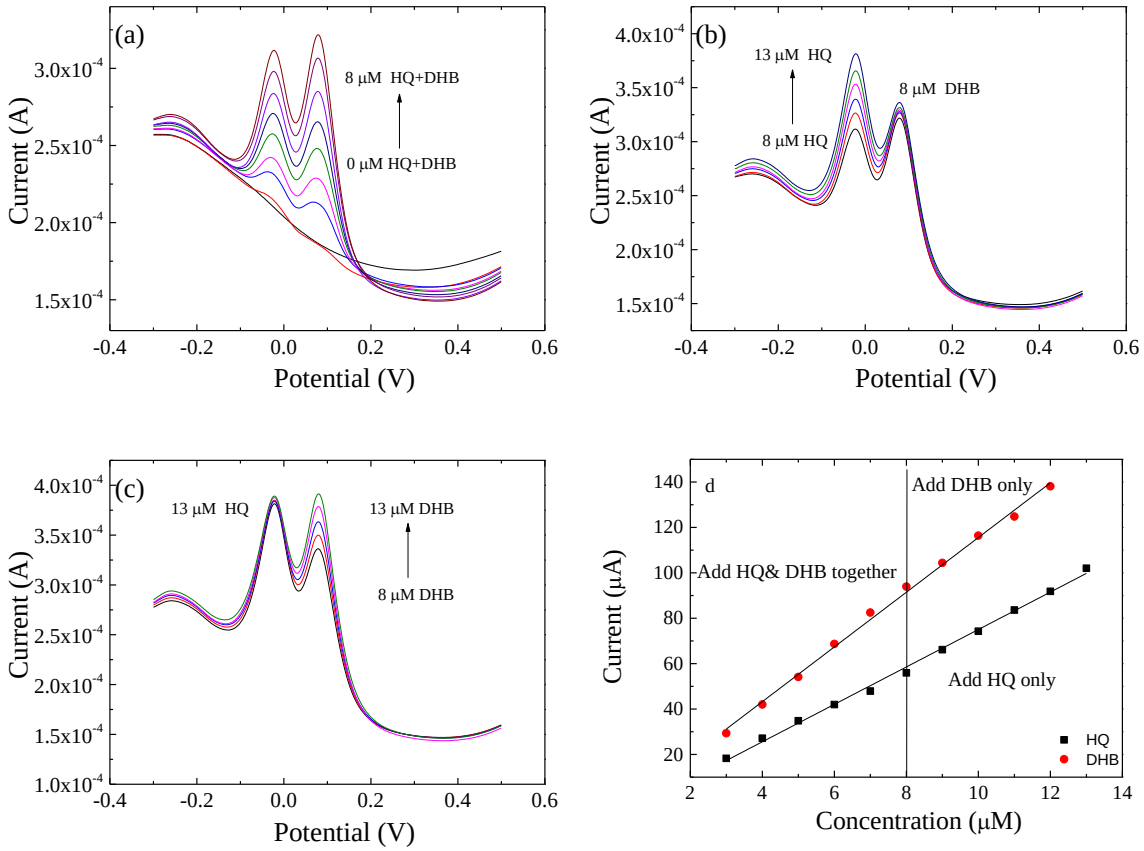

Figure 5.19 Square wave voltammograms at CB-GCE in 0.1 M phosphate buffer and (a) continuous addition of HQ and DHB from 0 to 8 µM; (b) 8 µM DHB and increasing HQ from 8 to 13 µM and (c) 13 µM HQ and increasing DHB from 8 to 13 µM; And (d)

the corresponding plot of peak current *vs.* the concentration; All the concentration steps are 1 μM

The detection limits of simultaneous determination of HQ and DHB at GP-GCE and CB-GCE in this work are shown in **Table 5.4**, together with the results from reported literature. The LOD obtained at CB-GCE is only one third of the one at GP-GCE, which is one magnitude lower than other sensors.

Table 5.4 Detection limit (μM) of simultaneous determination of catechol and hydroquinone at various electrodes

sensors	Detection limit HQ/DHB	Reference
GP-GCE	0.061/0.063	This work
CB-GCE	0.018/0.015	This work
Poly+graphene	0.2/0.25	Wang, L[25]
Graphitized mesoporous	0.91/1.31	Thangaraj, R[42]
Graphene+cobalt hexacyanoferrate	0.2/0.21	Huang, K[63]
MWNTs/Co(II)TPP/GCE	0.8/0.5	Deng, K[64]
electrospun carbon nanofiber	0.2/0.4	Guo, Q[65]
Au+carbon fibers	0.36/0.86	Huo, Z[66]
graphene-chitosan composite film	0.75	Yin, H[24]
PASA/MWNTs	1.0	Zhao, D[41]
Zn/Al-GCE	1.2/9.0	Li, M[38]
MWNTs	0.75	Qi, H[39]
MWNTs	0.6	Ding, Y[40]
Activated GCE	0.16/0.11	Ahammad, A[2]
Nano-Au	0.5/0.65	Han, L[47]

5.3.1.4 Real sample analysis

CB-GCE and GP-GCE were used as sensors to detect phenol compounds in samples of tap water, green tea and Thames river water by spike and recovery method. In this

method, HQ/DHB with a known concentration (called *added concentration*) is added into one real sample, in which solution the SWV is conducted and a concentration is measured by standard addition method (called *found concentration*). The value of found concentration divided by the added concentration is the *recovery* which reveals the amount of phenol compounds in such real sample.

First is to establish the standard current-concentration line. SWV was carried out in the solution containing 0.1 M phosphate buffer and increasing HQ from 1 to 10 µM at CB-GCE from -0.2 to 0.4 V, as shown in **Figure 5.20**a. The peak current corresponding to each HQ concentration was plotted, and a line of peak current against HQ concentration can be obtained. This line is used as the standard current-concentration line. The same experiments were carried out in the solution of DHB at CB-GCE, and the graph can be found in **Figure 5.20**b. The standard current-concentration lines at GP-GCE were also obtained but were not shown here.

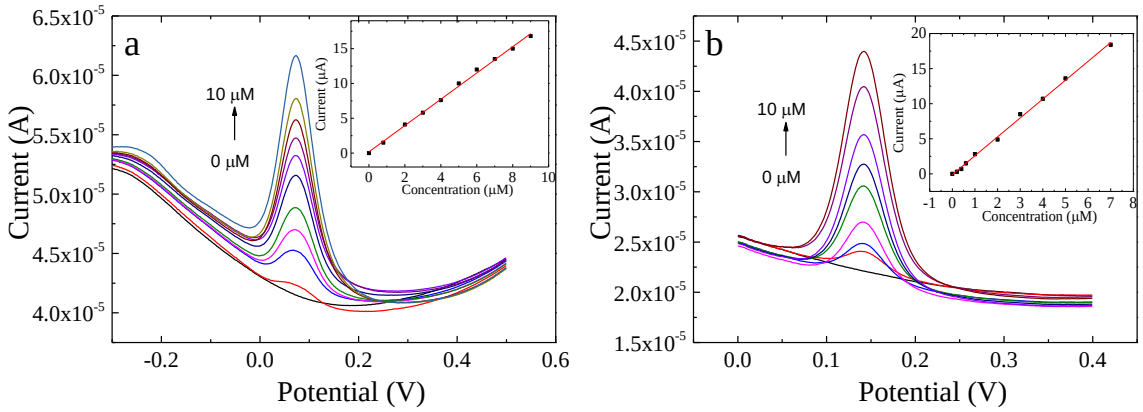

Figure 5.20 Square wave voltammograms at CB-GCE in 0.1 M phosphate buffer and continuous addition of (a) HQ from 0 to 10 µM, and (b) increasing DHB from 0 to 10 µM in steps of 1 µM; Insets: plot of peak current against concentration

Then the solution was made up in tap water, containing 0.1 M phosphate buffer. SWV was conducted under the same condition as above, and known concentrations of HQ

was added (2.0, 4.0 and 6.0 μM), of which the peak current is related to a concentration in the standard current-concentration line (**Figure 5.20**a). Then the peak current response to a concentration can be measured and the recovery concentration can be obtained (2.05, 4.2 and 6.04 μM). The found concentration divided by added concentration can give the value of recovery (102.5%, 105% and 100.7%). The average recovery is about 102 %.

The same procedure was carried out to detect DHB at CB-GCE and HQ and DHB at GP-GCE. All the data can be found in **Table 5.5**. The recovery of DHB was found to be 100.7-102.5 % at CB-GCE and 96.7-109% at GP-GCE. And the recovery of HQ was 97.8-104.3% at CB-GCE and 94.7-115% at GP-GCE. Apparently, reproducibility at CB-GCE is better than the one at GP-GCE since the recovery range is narrower. On the other hand, the recovery range of HQ is wider than DHB at both electrodes, indicating a higher concentration of HQ present in the tap water. Thames river water was also analysed by the same method at CB-GCE. The average recoveries in river water are 107% for HQ and 105% for DHB. These values are much higher than the one at tap water, suggesting the presence of other easily oxidisable species in the sample.

Table 5.5 Recovery of HQ and DHB in Thames river water detected by SWV method at CB-GCE and GP-GCE

		Added (μM)	Found (μM)	recovery
CB-GCE	HQ (average 102%)	2.0	2.05	102.5%
		4.0	4.2	105%
		6.0	6.04	100.7%
	DHB(average 101%)	2.0	2.1	104.3 %
		3.0	3.02	100.7%
		4.0	3.91	97.8%
GP-GCE	HQ(average 103%)	2.0	2.18	109%
		4.0	4.18	104.5%
		6.0	5.8	96.7%
	DHB(average 104%)	2.0	2.1	105%
		4.0	4.6	115%
		6.0	5.68	94.7%

Green tea is known to contain low concentrations of HQ and DHB so the sensors were explored in this application.[23] A green tea bag was boiled in 50 mL 0.1 M phosphate buffer at 80˚C for 5 min to obtain the sample. Then 10 μM DHB and HQ was added. SWV was conducted in both solutions, as shown in **Figure 5.21**. The voltammogram in 0.1 M phosphate buffer (made by Milli-Q water) is also displayed to compare. Using the current-concentration line, the recoveries of HQ and DHB in tea water are calculated to be 137% and 141%. The concentration of HQ and DHB in tea sample was calculated

to be 13.71 and 18.3 μM, corresponding to 48 and 64 μM g^{-1} in the tea, which is of the same magnitude as reported in the literature.[23,42]

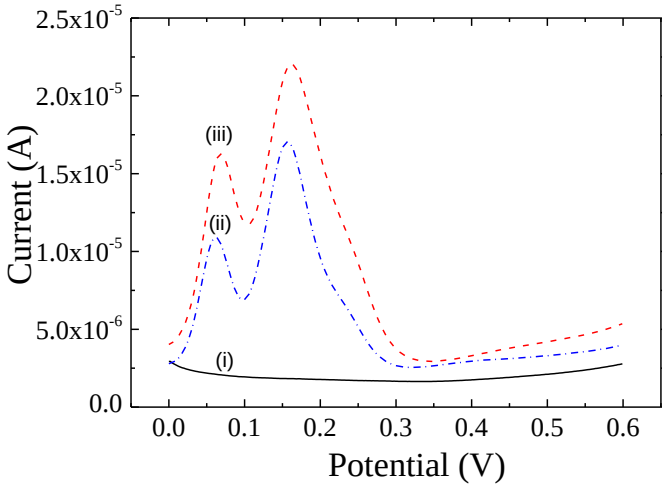

Figure 5.21 Square wave voltammograms at CB-GCE in (i) 0.1 M phosphate buffer, (ii) green tea sample and (iii) green tea sample with 10 μM HQ and DHB

5.3.2 Monophenol detection

5.3.2.1 Biosensors for phenol and p-cresol

Both phenol and p-cresol can be oxidised directly at electrodes. However, it normally requires a high overpotential (>1.2 V) so large scale interference from oxidisable species in solution is always observed.[57] To solve this problem, tyrosine can be used to catalyse the oxidation of phenol and p-cresol into DHB and HQ which then can be detected at low potential. The mechanism was shown in **Figure 5.1**.[67-69] The determination of bi-phenol compounds (HQ and DHB) at carbon materials decorated electrodes has been discussed above. GP-GCE and CB-GCE exhibited better sensitivity and detection limit than bare GCE and ND-GCE. Therefore the mono-phenol compounds (phenol and p-cresol) were studied at these two electrodes. In this work, tyrosine was applied to modify GP-GCE and CB-GCE (formed tyr/GP-GCE and

tyr/CB-GCE), aiming for the determination of both phenol and p-cresol. The modification procedure can be found in experimental section.

Cyclic voltammetry of phenol and p-cresol are conducted in 0.1 M phosphate buffer at electrodes in the presence and absence of tyrosine respectively. **Figure 5.22** shows the CVs of 0.1 mM phenol and p-cresol at CB-GCE, GP-GCE, tyr/CB-GCE and tyr-GCE, in the potential range from -0.4 to +0.4 V with scan rate of 50 mV s^{-1}. **Figure 5.22**a is for phenol at GP-GCE and tyr/GP-GCE while **Figure 5.22**b is at CB-GCE and tyr/CB-GCE. It can be seen that no significant peak can be observed at GP-GCE and CB-GCE, showing that phenol was not oxidised at these electrodes in this potential range. However, after modification with tyrosine, a pair of redox peaks appears at both tyr/GP-GCE and tyr/CB-GCE in the potential around +0.1 V. It indicates that the reaction of phenol and p-cresol can be catalysed by tyrosine. Similarly, the CVs of p-cresol can be found in **Figure 5.22**c (at GP-GCE and tyr/GP-GCE) and **Figure 5.22**d (CB-GCE and tyr/CB-GCE). The significant Faradaic peaks can only be observed at tyr/GP-GCE and tyr/CB-GCE at about 0 V, showing that tyrosine is necessary for the redox reaction of DHB in this potential range. Note that the non-Faradaic current at CB-GCE is much higher than the one at GP-GCE (5×10^{-6} *vs.* 1×10^{-6} A) and the Faradaic current at tyr/CB-GCE is about 5 times higher than the one at tyr/GP-GCE, consistent with the previous observation in determination of HQ and DHB.

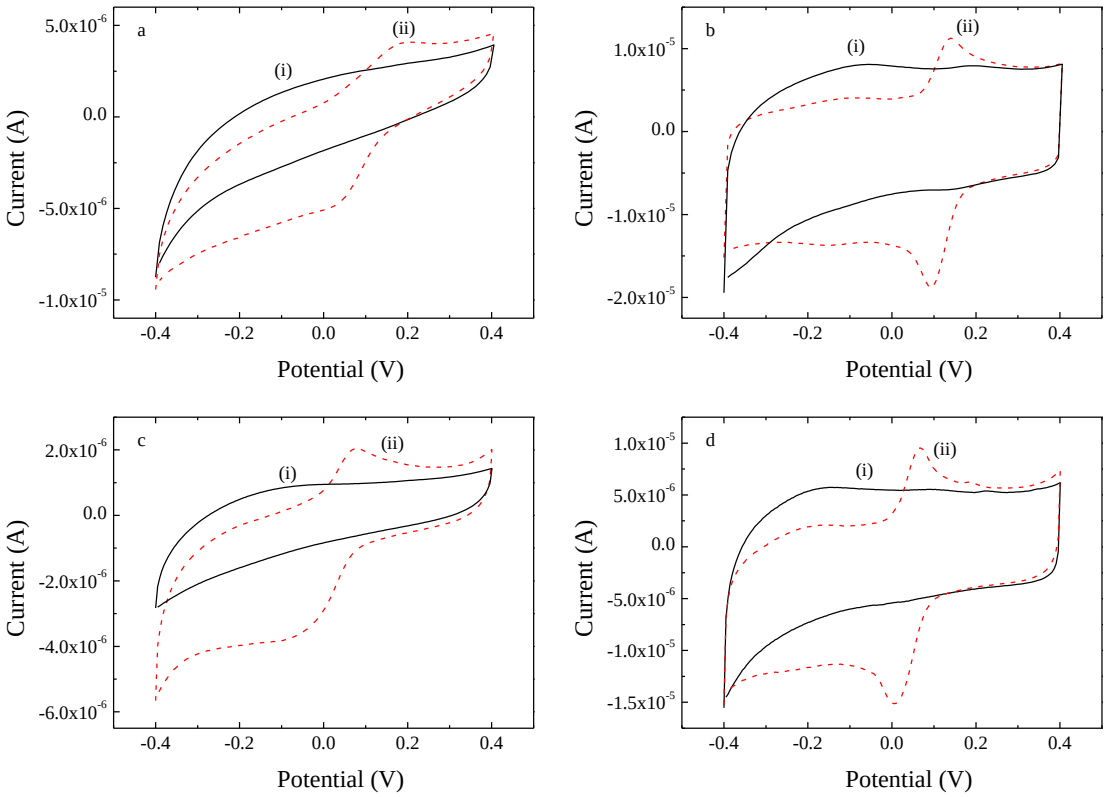

Figure 5.22 Cyclic voltammograms in a solution containing 0.1 M phosphate buffer and 0.1 mM (a and b) phenol and (c and d) p-cresol at (a and c) (i) GP-GCE and (ii) tyr/GP-GCE, (b and d) (i) CB-GCE and (ii) tyr/CB-GCE respectively

The current responses to phenol and p-cresol at these electrodes depend on the amount of modifiers. This influence was studied by conducting cyclic voltammetry in a solution containing 0.1 M phosphate buffer and 0.1 mM p-cresol at tyr/GP-GCE and tyr/CB-GCE. The carbon materials and tyrosine were deposited on the surface by drop-coating using the carbon materials suspensions and controlling the total volume of the added drops of known concentration. “One portion” refers to 5 µL solution with concentration of 1 mg mL^{-1} for all the materials. **Figure 5.23**a shows the CVs of 0.1 mM p-cresol at tyr/GP-GCE with 5 µL of GP and 5, 10, 15 and 20 µL of tyrosine. The CV in the absence of p-cresol is also shown for comparison. In the presence of p-cresol, a reduction peak is clearly observed in all profiles, which is attributed to the reduction of quinone that is generated from p-cresol by the catalytic reaction with oxygen mediated by tyrosinase. This peak current increases significantly with more tyrosine on the

electrode surface, showing a clear dependence of the electrode kinetic on the amount of catalyst, although poisoning is seen if too much tyrosine is added. However, the oxidation peaks are all relatively weak and ill-resolved. The same experiments were also carried out at tyr/CB-GCE with 5, 10, 15 and 20 µL of tyrosine, with results displayed in **Figure 5.23**b. Compared with the featureless curves in 0.1 M phosphate buffer, a pair of peaks appears when p-cresol is present at all the electrodes with different amount of tyrosine. However, although tyrosine is necessary to obtain the signal of p-cresol at this potential window (see **Figure 5.22**), there is no increase in current above a critical addition amount of tyrosine.

Figure 5.23c displays the CVs at tyr/GP-GCE with 0, 5, 10, 15 and 20 µL graphene and 5 µL of tyr. A pair of redox peaks is observed and both peak currents increase with more graphene on the electrode surface at fixed tyrosine loading. The voltammograms at tyr/CB-GCE with increasing carbon black materials are shown in **Figure 5.23**d. Both oxidation and reduction peaks can be observed. Also observed is the peak current increase gradually when more carbon black is loaded at fixed tyrosine. It appears overall that general increase occur in signal strength as the carbon loading is increased, but this monotonic increase is not observed in the tyrosine loading; at high loadings the signal can become independent of the amount of tyrosine or can indeed decrease.

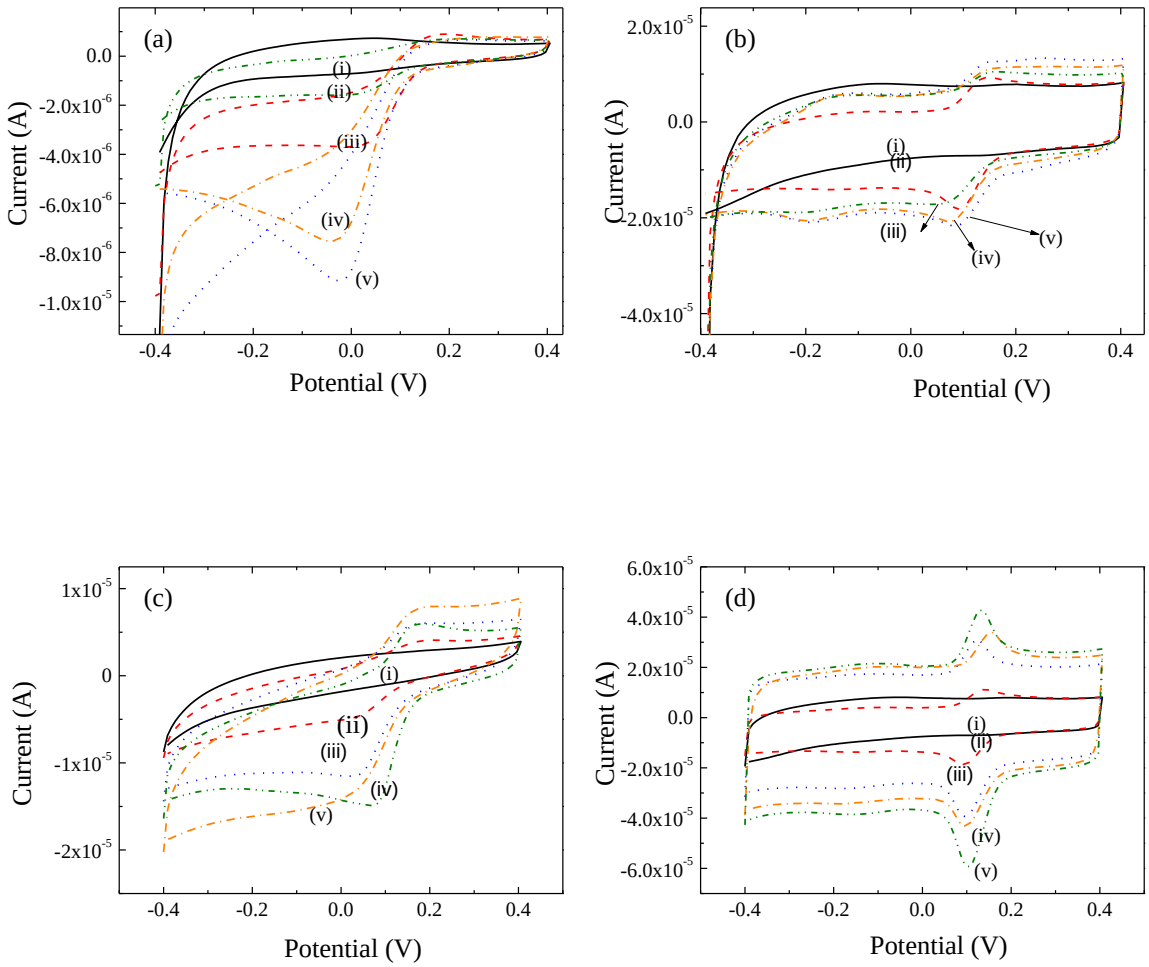

Figure 5.23 Cyclic voltammograms in a solution containing 0.1 M phosphate buffer and 0.1 mM p-cresol at (a) tyr/GP-GCE and (b) tyr/CB-GCE with 5 µL carbon suspension and (i) 0, (ii) 5, (iii) 10, (iv) 15 and (v) 20 µL tyrosine; (c) tyr/GP-GCE and (d) tyr/CB-GCE with 5 µL tyrosine and (i) 0, (ii) 5, (iii) 10, (iv) 15 and (v) 20 µL carbon suspension. All the suspensions were of concentration of 1 mg L^{-1}.

5.3.2.2 Detection of phenol and p-cresol

In the literature, the potential where the reduction of phenol compounds occurs is typically used, especially at enzyme modified sensors, which is normally in the range of 0 to -0.15 V.[11,15,17,18,70] Therefore, a cathodic potential was applied to detect phenol and p-cresol at tyr/GP-GCE and tyr/CB-GCE. Amperometry was conducted in 0.1 M phosphate buffer at a fixed potential of -0.1 V. **Figure 5.24** shows the current-time

curve with successive additions of phenol. From **Figure 5.24**a can be seen that the tyr/GP-GCE can respond to phenol from 0.025 µM and can reach the equilibrium within 5 s. The plot of current against concentration is shown in **Figure 5.24**b. The sensitivity was calculated to be 2.14 µA μM^{-1}, and the detection limit was 0.014 µM. The current-time curve at tyr/CB-GCE is shown in **Figure 5.24**c and the plot of current increase corresponding to phenol concentration were in **Figure 5.24**d. Note that tyr/CB-GCE can respond to a phenol of concentration of 2.5 nM, ten times lower than tyr/GP-GCE. The sensitivity at tyr/CB-GCE was calculated to be 24 µA μM^{-1}, which was 11 times higher than at tyr/GP-GCE. The detection limit was 0.004 µM.

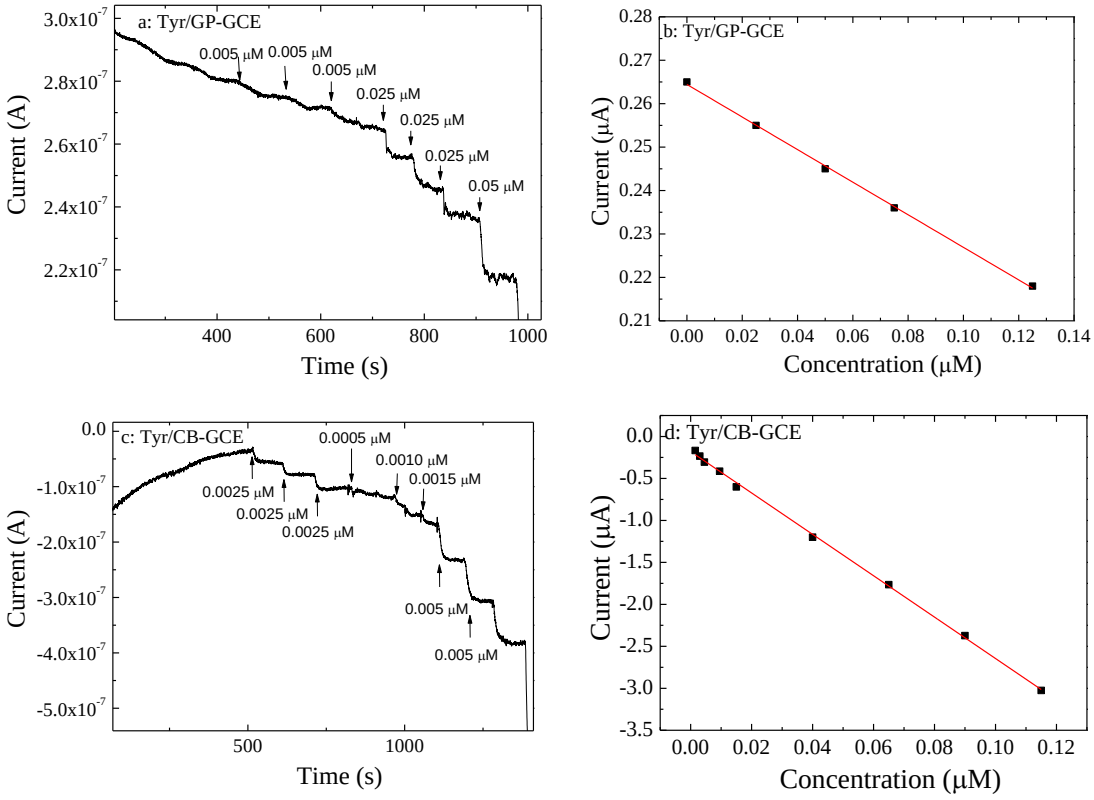

Figure 5.24 Amperometric graph in 0.1 M phosphate buffer with successive addition of phenol at (a) tyr/GP-GCE and (c) tyr/CB-GCE; and (b) and (d) the corresponding plots of current *vs.* concentration of phenol. The applied potential was 0.0 V.

The current-time curves with successive addition of cresol at tyr/GP-GCE and tyr/CB-GCE are displayed in **Figure 5.25**a and c respectively. When adding 0.005 µM cresol,

the current at tyr/GP-GCE was hardly changed while the current drop at tyr/CB-GCE was significant and was about 3 times that of the noise. At tyr/CB-GCE, the current reached equilibrium within 1 s which is quicker than the phenol detection shown in **Figure 5.24**c. **Figure 5.24**b and d shows the plot of current change *vs.* concentration of cresol, from which the sensitivities were calculated to be 1.5 and 12 μA μM^{-1} for tyr/GP-GCE and tyr/CB-GCE respectively. The detection limits were 0.02 and 0.0025 μM correspondingly.

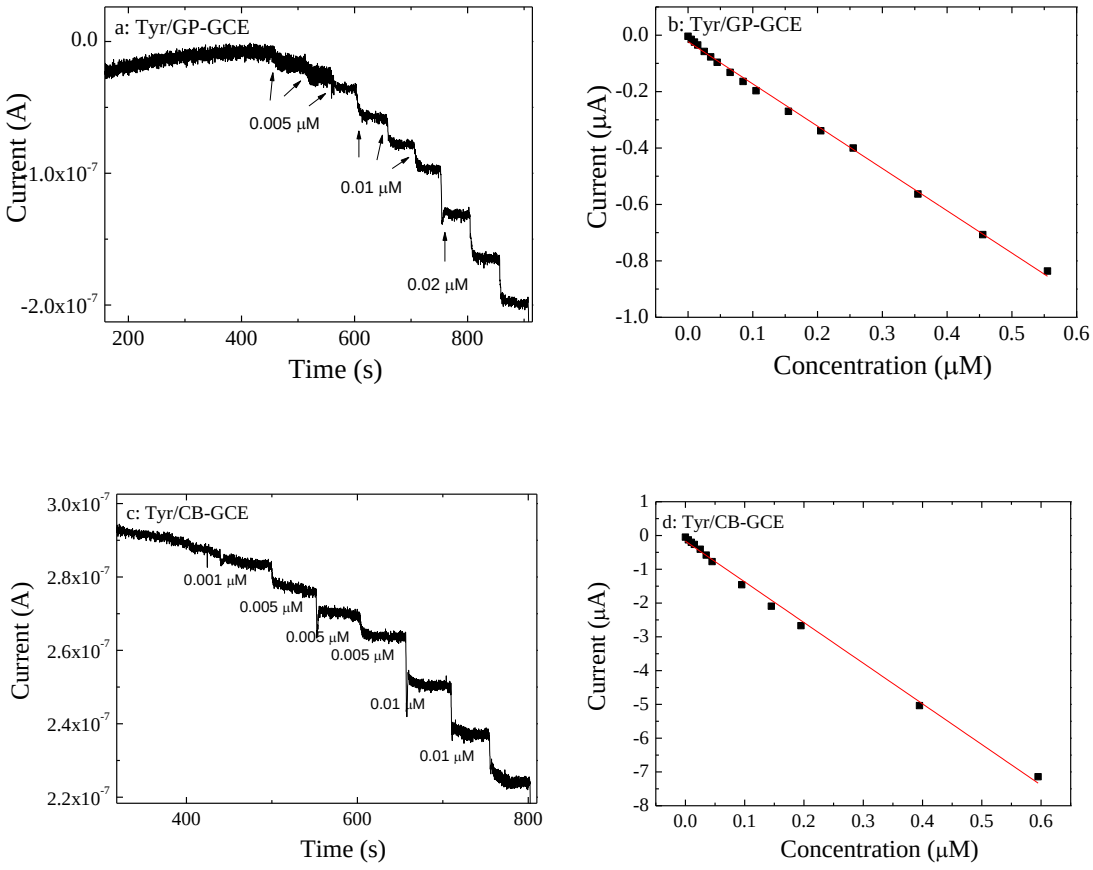

Figure 5.25 Amperometric graph in 0.1 M phosphate buffer and successive addition of phenol at (a) tyr/GP-GCE and (c) tyr/CB-GCE; and the corresponding plots of current against concentration of phenol. The applied potential was 0.0 V.

Both detection limits of phenol, p-cresol at tyr/GP-GCE and tyr/CB-GCE are compared to other sensors from literature in **Table 5.6**. It can be found that the LOD at tyr/GP-

GCE is of the level of 10^{-8} M while the one at tyr/CB-GCE is 10^{-9} M. For most of other bio-sensors, LODs of phenol and p-cresol are around 0.1-5 μM, which are much higher than the value obtained in this work. The most important reason might be the high sensitivity at tyr/CB-GCE (around 10 μA μM^{-1}) in comparison to other sensors (around 0.5 μA μM^{-1}) [3,18,20,21]

Table 5.6 Detection limit (μM) of phenol and p-cresol at various bio-sensors (μM)

Sensors	phenol	p-cresol	Reference
tyr/GP-GCE	0.014	0.02	This work
tyr/CB-GCE	0.004	0.0025	This work
tyr/MWCNTs	1.1	2.0	Hashemnia, S[11]
tyr/Ti	0.13	0.14	Kochana[14]
tyr/Ag-BDDE	0.1	0.2	Zhou, Y[18]
tyr/$CaCO_3$-GCE	0.0062	0.0054	Shan, D[3]
tyr/polymer-BDDE	1.0	0.5	Zhou, Y[15]
HRP-GCE	4.4		Dai, L[21]

5.4 Conclusion

- In this work, bare GCE, ND-GCE, GP-GCE and CB-GCE were investigated to determine phenol compounds, including HQ, DHB, phenol and p-cresol. At bare GCE, ND-GCE and GP-GCE, the redox reaction of phenol compounds were under diffusion control, while it is under adsorption control at CB-GCE surface.

- Both SWV and amperometric methods were used to determine HQ and DHB. The sensitivity was improved by ND-GCE, GP-GCE and CB-GCE in comparison to the bare electrode.
- HQ and DHB were also determined simultaneously at GP-GCE and CB-GCE with little interference with each other by SWV method. In addition, the HQ and DHB were also detected in real samples of tap water, Thames river water and green tea by standard addition method. The recoveries were found to be 97%, 98.8% and 107% respectively.
- Modified by tyrosine, the tyr/GP-GCE and tyr/CB-GCE can be used as sensors to detect phenol and p-cresol.
- The main conclusion is that state-of-the-art or beyond state-of-the-art performance can be obtained using the cheap and simple electrode modifier CB, compared to the expensive or complicated modifiers which are currently in use.

References

(1) Crozier, A.; Jaganath, I. B.; Clifford, M. N. *Nat. Prod. Rep.* **2009**, *26*, 1001.

(2) Ahammad, A. J. S.; Sarker, S.; Rahman, M. A.; Lee, J. J. *Electroanalysis* **2010**, *22*, 694.

(3) Shan, D.; Zhu, M.; Han, E.; Xue, H.; Cosnier, S. *Biosensors & Bioelectronics* **2007**, *23*, 648.

(4) Services, U. S. D. o. H. a. H. *Toxigological Profile for Phenol*, 2008.

(5) Castillo, M.; Domingues, R.; Alpendurada, M. F.; Barcelo, D. *Analytica Chimica Acta* **1997**, *353*, 133.

(6) Maccrehan, W. A.; Brownthomas, J. M. *Analytical Chemistry* **1987**, *59*, 477.

(7) Escarpa, A.; Gonzalez, M. C. *Analytica Chimica Acta* **2001**, *427*, 119.

(8) Tsuchiya, H.; Sato, M.; Kato, H.; Okubo, T.; Juneja, L. R.; Kim, M. *J. Chromatogr. B* **1997**, *703*, 253.

(9) Nagaraja, P.; Vasantha, R. A.; Sunitha, K. R. *Journal of Pharmaceutical and Biomedical Analysis* **2001**, *25*, 417.

(10) Macias-Ruvalcaba, N. A.; Aguilar-Martinez, M.; Perez-Casas, S.; Hernandez, S.; Mejia, E.; Evans, D. H. *Journal of Electroanalytical Chemistry* **2011**, *661*, 130.

(11) Hashemnia, S.; Khayatzadeh, S.; Hashemnia, M. *Journal of Solid State Electrochemistry* **2012**, *16*, 473.

(12) Kong, Y.; Ma, M. J.; Mao, H. H.; Ma, J. Q.; Yao, C. *Analytical Methods* **2012**, *4*, 748.

(13) Fan, L. F.; Wu, X. Q.; Guo, M. D.; Gao, Y. T. *Electrochimica Acta* **2007**, *52*, 3654.

(14) Kochana, J.; Gala, A.; Parczewski, A.; Adamski, J. *Anal. Bioanal. Chem.* **2008**, *391*, 1275.

(15) Zhou, Y. L.; Tian, R. H.; Zhi, J. F. *Biosensors & Bioelectronics* **2007**, *22*, 822.

(16) Mita, D. G.; Attanasio, A.; Arduini, F.; Diano, N.; Grano, V.; Bencivenga, U.; Rossi, S.; Amine, A.; Moscone, D. *Biosensors & Bioelectronics* **2007**, *23*, 60.

(17) Ren, J.; Kang, T.-F.; Xue, R.; Ge, C.-N.; Cheng, S.-Y. *Microchimica Acta* **2011**, *174*, 303.

(18) Zhou, Y.; Zhi, J. *Electrochemistry Communications* **2006**, *8*, 1811.

(19) Ziyatdinova, G.; Gainetdinova, A.; Morozov, M.; Budnikov, H.; Grazhulene, S.; Red'kin, A. *Journal of Solid State Electrochemistry* **2012**, *16*, 127.

(20) Capannesi, C.; Palchetti, I.; Mascini, M.; Parenti, A. *Food Chemistry* **2000**, *71*, 553.

(21) Dai, Z. H.; Xu, X. X.; Wu, L.; Ju, H. X. *Electroanalysis* **2005**, *17*, 1571.

(22) Cao, L.; Sun, H.; Li, J.; Lu, L. *Analytical Methods* **2011**, *3*, 1587.

(23) Lin, H.; Gan, T.; Wu, K. *Food Chemistry* **2009**, *113*, 701.

(24) Yin, H. S.; Zhang, Q. M.; Zhou, Y. L.; Ma, Q. A.; Liu, T.; Zhu, L. S.; Ai, S. Y. *Electrochimica Acta* **2011**, *56*, 2748.

(25) Wang, L.; Zhang, Y.; Du, Y.; Lu, D.; Zhang, Y.; Wang, C. *Journal of Solid State Electrochemistry* **2012**, *16*, 1323.

(26) Tsai, Y.-C.; Chiu, C.-C. *Sensors and Actuators B: Chemical* **2007**, *125*, 10.

(27) Balasubramanian, K.; Burghard, M. *Anal. Bioanal. Chem.* **2006**, *385*, 452.

(28) Wang, J.; Fang, L.; Lopez, D. *Analyst* **1994**, *119*, 455.

(29) Koelmans, A. A.; Jonker, M. T. O.; Cornelissen, G.; Bucheli, T. D.; Van Noort, P. C. M.; Gustafsson, O. *Chemosphere* **2006**, *63*, 365.

(30) Boehm, H. P. *Carbon* **1994**, *32*, 759.

(31) Arduini;, F. *Electroanalysis* **2012**.

(32) Narmadha, M.; Noel, M.; Suryanarayanan, V. *Journal of Electroanalytical Chemistry* **2011**, *655*, 103.

(33) Shahil, K. M. F. *Nano Letters* **2012**, *12*, 861.

(34) Yang, W.; Ratinac, K. R.; Ringer, S. P.; Thordarson, P.; Gooding, J. J.; Braet, F. *Angew. Chem.-Int. Edit.* **2010**, *49*, 2114.

(35) Chung, D. D. L. *Journal of Materials Science* **2004**, *39*, 2645.

(36) De Carvalho, R. M.; Mello, C.; Kubota, L. T. *Analytica Chimica Acta* **2000**, *420*, 109.

(37) Ahammad, A. J. S.; Rahman, M. M.; Xu, G.-R.; Kim, S.; Lee, J.-J. *Electrochimica Acta* **2011**, *56*, 5266.

(38) Li, M.; Ni, F.; Wang, Y.; Xu, S.; Zhang, D.; Chen, S.; Wang, L. *Electroanalysis* **2009**, *21*, 1521.

(39) Qi, H. L.; Zhang, C. X. *Electroanalysis* **2005**, *17*, 832.

(40) Ding, Y. P.; Liu, W. L.; Wu, Q. S.; Wang, X. G. *Journal of Electroanalytical Chemistry* **2005**, *575*, 275.

(41) Zhao, D.-M.; Zhang, X.-H.; Feng, L.-J.; Jia, L.; Wang, S.-F. *Colloids and Surfaces B-Biointerfaces* **2009**, *74*, 317.

(42) Thangaraj, R.; Manjula, N.; Kumar, A. S. *Analytical Methods* **2012**, *4*, 2922.

(43) Ghanem, M. A. *Electrochemistry Communications* **2007**, *9*, 2501.

(44) DuVall, S. H.; McCreery, R. L. *Analytical Chemistry* **1999**, *71*, 4594.

(45) Cabot; http://www.cabot-corp.com/Specialty-Carbon-Blacks/KBase?recOffset=100.

(46) Qi, H.; Zhang, C. *Electroanalysis* **2005**, *17*, 832.

(47) Han, L.; Hang, X. *Electroanalysis* **2009**, *21*, 124.

(48) Feng, J. J.; Zhao, G.; Xu, J. J.; Chen, H. Y. *Analytical Biochemistry* **2005**, *342*, 280.

(49) Dąbrowski, A.; Podkościelny, P.; Hubicki, Z.; Barczak, M. *Chemosphere* **2005**, *58*, 1049.

(50) Gregg, B. A.; Heller, A. *The Journal of Physical Chemistry* **1991**, *95*, 5970.

(51) Zhang, Y.; Zhang, J.; Wu, H.; Guo, S.; Zhang, J. *Journal of Electroanalytical Chemistry* **2012**, *681*, 49.

(52) Palosz, B.; Pantea, C.; Grzanka, E.; Stelmakh, S.; Proffen, T.; Zerda, T.; Palosz, W. *Diamond and Related Materials* **2006**, *15*, 1813.

(53) Holt, K. B. *Philosophical Transactions of the Royal Society A: Mathematical, Physical and Engineering Sciences* **2007**, *365*, 2845.

(54) Laviron, E. *Journal of Electroanalytical Chemistry and Interfacial Electrochemistry* **1979**, *101*, 19.

(55) Laviron, E. *Journal of Electroanalytical Chemistry and Interfacial Electrochemistry* **1974**, *52*, 355.

(56) Senthil Kumar, K.; Natarajan, P. *Materials Chemistry and Physics* **2009**, *117*, 365.

(57) Zhang, Y.; Zheng, J. B. *Electrochimica Acta* **2007**, *52*, 7210.

(58) Peng, J.; Gao, Z.-N. *Anal. Bioanal. Chem.* **2006**, *384*, 1525.

(59) Ayranci, E.; Duman, O. *Journal of Hazardous Materials* **2005**, *124*, 125.

(60) Brett, C.; Brett, A. M. O. *Electroanalysis*; Oxford University Press, 1998.

(61) Singh, N.; Singh, H. *Journal of Solid State Chemistry* **1981**, *38*, 211.

(62) Codling, D. J.; Zheng, G.; Stait-Gardner, T.; Yang, S.; Nilsson, M.; Price, W. S. *The Journal of Physical Chemistry B* **2013**, *117*, 2734.

(63) Huang, K.; Yu, S.; Wang, L.; Gan, T.; Li, M. *Acta Chimica Sinica* **2012**, *70*, 735.

(64) Deng, K.; Li, C.; Li, X.; Xu, G. *Analytical Letters* **2012**, *45*, 883.

(65) Guo, Q. H.; Huang, J. S.; Chen, P. Q.; Liu, Y.; Hou, H. Q.; You, T. Y. *Sensors and Actuators B-Chemical* **2012**, *163*, 179.

(66) Huo, Z.; Zhou, Y.; Liu, Q.; He, X.; Liang, Y.; Xu, M. *Microchimica Acta* **2011**, *173*, 119.

(67) Land, E. J.; Ramsden, C. A.; Riley, P. A. *Accounts Chem. Res.* **2003**, *36*, 300.

(68) Gatellier, P.; Anton, M.; Renerre, M. *Journal of Agricultural and Food Chemistry* **1995**, *43*, 651.

(69) D'Autreaux, B.; Toledano, M. B. *Nat. Rev. Mol. Cell Biol.* **2007**, *8*, 813.

(70) Imabayashi, S. i.; Kong, Y. T.; Watanabe, M. *Electroanalysis* **2001**, *13*, 408.

Chapter 6 BPA Determination at ND-GCE and CB-GCE

6.1 Introduction

2,2-(4,4-dihydroxydiphenyl) propane (Bisphenol A, BPA) is a man-made carbon-based synthetic compound which is widely used in industry for polycarbonate, epoxy resin and wood processing.[1-3] The final products include food and drink storage containers, baby bottles, tableware, water pipes, papers, compact disks, white dental fillings and sealants.[2,4,5] BPA can be released into the environment during manufacturing processes or by leaching from the final products.[5] **Table 6.1** shows the concentration of BPA found in various environments, including river water, waste landfill, milk and canned food, which vary from 0.043 to 43.8 μM. Because of the widespread use of BPA, it has become one of the major water pollutants.[2,6] Increasing evidence shows that BPA could be harmful for human and wildlife because it can mimic or antagonise effects of endogenous hormones, so called endocrine disruptors.[1,7-10] This effect can be related to various diseases, including obesity, low sperm quality, cancers and diverse pleiotropic actions in the brain.[3,4,6,11,12] Considering the ecological hazard for BPA, US EPA establishes a daily reference dose for chronic oral exposure of 0.05 mg kg^{-1} of bady weight and the European Union and Canada have restricted BPA for use in body bottles.[13] Due to the importance of BPA in environmental monitoring, a reliable, accurate and rapid approach to detect BPA in real time is of great interest.

Table 6.1 Concentration of BPA in the environment (μM)

Sample	Concentration (μM)	
River water[14]	0.43	
Leachates from hazardous waste landfill site[14]	43.8	
Water[2]	7.48	Mackay level environmental distribution
Aquatic biota[2]	0.51	Mackay level environmental distribution
Milk/Fruit juice [15]	0.13	PC into food
Olive oil[15]	0.043	PC into food
Canned food[15]	0.16	

The usual techniques for analysing BPA include gas chromatography/mass spectrometry (GC/MS)[5,16], high performance-liquid chromatography (HPLC)[17,18] and liquid chromatography/mass spectrometry (LC/MS)[19]. The detection limits of these methods can be down to the order of nanomolar. However, they normally require expensive equipment, high-skilled operatives and time-consuming pre-treatment.[4] Moreover, the apparatus is normally located far away from the possible polluted sites.[1,3] In this regard, electro-analysis is an alternative because it can be used for on-line monitoring in a flow system, along with advantages of inexpensive equipment, simple operation, and instant result.[20] BPA can be oxidised at an electrode following the process shown in **Figure 6.1**.[14] Because this oxidation process is irreversible, no reduction peak can be observed.[3] The product can be further oxidised into carbon dioxide, which requires a potential over +2.5 V.[14] However, the detection of BPA by anodic oxidation suffers two main problems. One is that the direct oxidation of BPA at traditional bulk electrode is relatively high, such as +0.95 V at BDD and +1.25 V at

Pt.[14,21,22] Another is electrode fouling because the electropolymerised film of BPA is formed at the electrode surface by the reaction between substrate and phenoxy radicals.[23] As a result, the peak intensity of BPA oxidation decreased rapidly in subsequent cyclic voltammetric scans.[13,22]

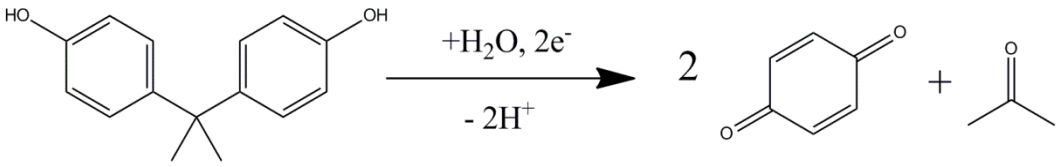

Figure 6.1 Mechanism of BPA oxidation

To tackle these problems, BPA determination is usually performed on electrodes with modification, including metal NPs (Mg–Al layered double hydroxide/GCE[4]), carbon based particles (MWCNT-MAM/GCE[23], MWCNT-GCE[3]), organic compounds (CoPc-CPE[24]), enzymes (tyr-BDD[25]) and their combinations (Au/ssDNA/SWCNT-GCE[26], tyr/MWCNT-GCE[1]). The detection potential at these BPA sensors can be in the region from 0.4 to 0.6 V, and the detection limit can reach the order of micromole, as listed in **Table 6.2**. However, the electrode fouling remains a problem, and moreover, these electrodes often require complicated manufacturing processes which may lead to long fabrication time, low storage stability and poor repeatability.[4]

Table 6.2 Detection limit (μM) and detection range (μM) of BPA at various sensors

Sensors	LOD	Detection Range	Ref.
Tyr/WMCNTs	0.5	0.2-100	Ren, J[27]
Tyr/SWNTs	0.02	0.1-12	Mita, D[1]
Tyr/BDD	1	-	Notsu, H[25]
BDD	0.71	0.44-5.2	Pereira, G[13]
Tyr/Graphite	0.1	0.1-15	Mita, D[1]
LDH/GCE	0.005	0.01-1.05	Yin, H[4]
CoPc-CPE	0.01	0.0875-12.5	Yin, H[24]

In this work, two novel modified sensors were investigated for the detection of BPA in low concentration with minimal fouling at low potential. One is the nano-diamond modified glassy carbon electrode (ND-GCE). It was found that the ND-GCE is less influenced by the electropolymerised film of BPA, as a result of the remarkable chemical resistance.[14,28,29] Also, the noise and background current responses at ND-GCE is small, leading to a large signal/noise ratio and low detection limit.[29] Another BPA sensor is carbon black modified glassy carbon electrode (CB-GCE). The previous chapter has fully demonstrated that CB-GCE is extremely sensitive to quinone, 10 times more than for the bare glassy carbon electrode. Therefore, it is possible to utilise CB-GCE to detect the quinone generated from BPA oxidation that is directly proportional to the concentration of BPA. In this way, the detection potential can be lowered to +0.12 V. Also, the CB-GCE can be disposable because of the low cost of carbon black materials and the simple, efficient and reproducible modification. In this way, the influence of electrode fouling can be eliminated.

6.2 Experimental

The BPA powder was obtained from Sigma-Aldrich of A.C.S. reagent grade, and the solution was prepared by 0.1 M phosphate buffer which had been adjusted to pH 7.4. The procedure to modify BDD electrode was adapted from Chapter 6. Other chemicals and electrochemical equipment in use has been mentioned in previous chapters.

6.3 Result and discussion

6.3.1 BPA determination at ND-GCE: direct oxidation of BPA

6.3.1.1 Cyclic voltammetry of BPA oxidation

Cyclic voltammetry is widely used for the investigation of electrode processes by scanning a chosen region of potential and measuring the current response arising from the electron transfer and the associated reaction that occurs, which is a first step towards developing an electro-analytical procedure.[20] It was employed here to characterise the BPA oxidation process at bare GCE, ND-GCE, GP-GCE and CB-GCE in the absence and presence of 0.2 mM BPA in 0.1 M phosphate buffer. The CVs of the first scan are shown in **Figure 6.2**. The voltammogram in the absence of BPA appears featureless at the bare GCE in the potential region studied. When 0.2 mM BPA is present, an oxidation wave appears at *ca.* +0.54 V without any peak in the reverse scan. This peak is attributed to the irreversible oxidation of BPA, and the possible mechanism has been demonstrated in the literature, as shown in **Figure 6.1**.[4,22] The BPA oxidation peaks are also observed at GP-GCE, ND-GCE and CB-GCE at a similar over-potential (+0.05 V negative shift at CB-GCE). The peak current at these electrodes are higher than the value at bare GCE, and the highest is observed at CB-GCE, consistent with the CVs in other phenolic compounds as mentioned in Chapter 5.

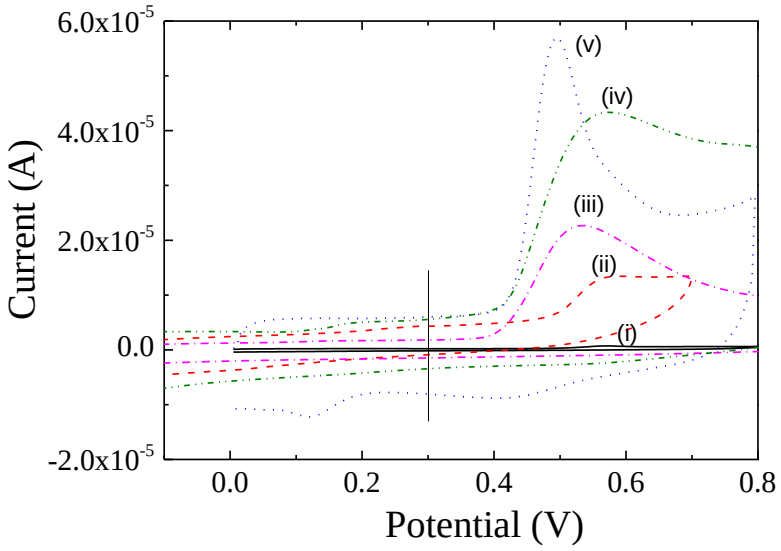

Figure 6.2 Cyclic voltammograms of first scan in the absence (i) and the presence of 0.2 mM BPA in 0.1 M phosphate buffer at (ii) bare GCE, (iii) ND-GCE, (iv) GP-GCE and (v) CB-GCE respectively

Information about double layer capacitance can be obtained from the background current in CVs where non Faradaic response appears. At the potential of +0.3 V (see **Figure 6.2**), the largest current is observed at CB-GCE and lowest at ND-GCE, to which the order of double layer capacitance is directly correlated. The double layer capacitance is attributed to the surface adsorption and surface area. [30-32] ND particles have a non-porous structure and are inert to the chemical adsorption, therefore the double layer capacitance is small and the noise is low. On the other hand, the extremely strong adsorption at CB-GCE results in large capacitance.

6.3.1.2 Electrode fouling

It is extensively reported that the Faradaic response of BPA dropped quickly at the electrode surface with sequential CV scans due to the electrode fouling. The same tendency was also observed at bare GCE, GP-GCE and CB-GCE. Taking the bare GCE as an example, cyclic voltammetry was performed in the presence of 0.2 mM BPA, and

the first two scans are shown in **Figure 6.3**a. There is a clear peak of BPA oxidation on the first scan and the peak current significantly decreases in the second scan, which only 20% of the initial value. In addition, the background current, associated with non-Faradaic response, increases in the second scan, which indicates the enhancement of the double layer capacitance. The reason for this phenomenon is widely accepted to be that after being oxidised, BPA forms an electropolymerised film on electrode surface, resulting in larger double layer capacitance and lower electrode sensitivity.

The CVs in 0.1 M phosphate buffer and 0.2 mM BPA at ND-GCE are displayed in **Figure 6.3**b, with first two scans. Both curves show a clear feature of BPA oxidation. Although the peak current decreases slightly in the second scan, the response remains more than 80% of the initial value and the background current is hardly changed. This implies that the influence of the surface fouling can be minimised at ND-GCE. Such resistance to fouling might be due to weak adsorption of polar functional groups on the nonpolar surface of nano-diamond.[33]

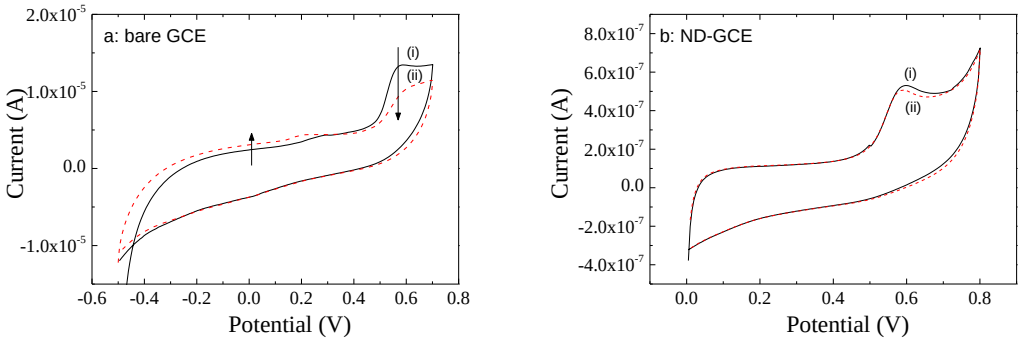

Figure 6.3 Cyclic voltammograms of (i) the first and (ii) the second scans in a solution containing 0.1 M phosphate buffer and 0.2 mM BPA at (a) bare GCE; (b) ND-GCE

6.3.1.3 Peak current *vs.* scan rate: adsorption control

The surface processes of BPA at an electrode have been widely investigated and proved to be adsorption controlled at most BPA sensors.[4,23,24,34] Surface processes at the bare GCE and ND-GCE were also studied by conducting cyclic voltammetry with different scan rates. Because the response to BPA dropped quickly due to electrode fouling in sequential CV scans as demonstrated above, the bare GCE was polished to obtain a fresh surface for each scan rate. Newly prepared ND-GCE was also used each time for a better comparison. The voltammograms of different scan rate at both electrodes in 0.1 M phosphate buffer and 0.2 mM BPA are displayed in **Figure 6.4**. At bare GCE (**Figure 6.4**a), the background current rises with an increase in scan rate. The peaks of BPA oxidation at high scan rate are ill-defined and hard to be measured. Well resolved waves are observed at ND-GCE (**Figure 6.4**b), where the peak current is enhanced with increasing scan rates. The insert graph displays the resulting plot of peak height *vs.* scan rate, which gives a linear response between 20 to 140 mV s^{-1}. This result suggested that the BPA oxidation at ND-GCE is adsorption controlled.

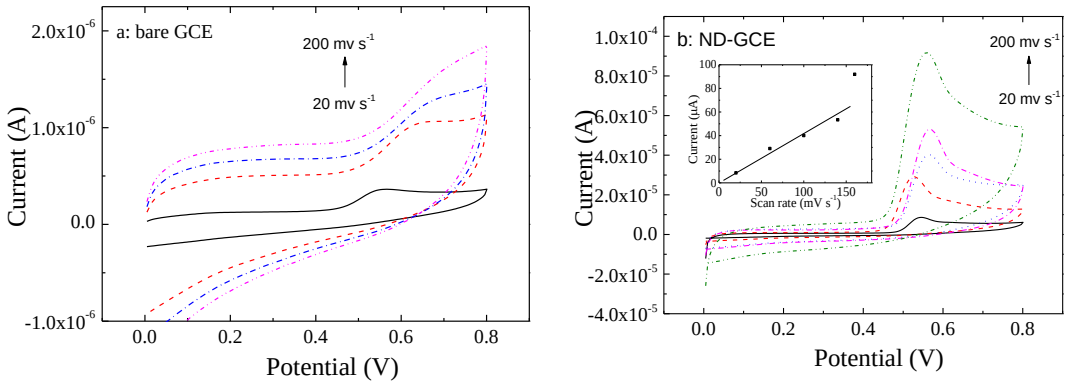

Figure 6.4 Cyclic voltammograms in a solution containing 0.1 M phosphate buffer and 0.2 mM BPA at (a) bare GCE with scan rates of 20, 100, 150 and 200 mV s^{-1} and (b) ND-GCE with scan rates of 20, 60, 100, 140 200 mV s^{-1}; Inset: peak current *vs.* scan rate at ND-GCE

6.3.1.4 Direct BPA determination at ND-GCE by SWV

SWV is a common technique to improve signal-to-noise ratio, by subtracting the background signal contributions to the measured voltammogram.[35] SWV was conducted to determine BPA in the potential window from +0 to +0.8 V with continuous addition of BPA with resulting concentration from 0 to 10 μM in 0.1 M phosphate buffer without changing electrode. **Figure 6.5** displays the voltammograms and the resulting plots of peak height *vs.* concentration of BPA at bare GCE (a and b), CB-GCE (c and d) and ND-GCE (e and f). The initial voltammogram in the absence of BPA appears featureless at all the electrodes. At bare GCE the addition of 2 μM BPA results in a clear oxidation peak at *ca.* +0.53 V. As more BPA is added, the peak height increases correspondingly first, up to 5 μM BPA, and then drops. The reason for the decrease is likely due to the electrode fouling as discussed above. A similar tendency is also observed at CB-GCE that the peak current of BPA oxidation increased first then followed by a decrease when more BPA was added. A linearity of peak height *vs.* BPA concentration is obtained between 0 to 4 μM. The voltammograms at ND-GCE are shown in **Figure 6.5**e with increasing concentration of BPA, where a well resolved wave of BPA oxidation is observed and continually enhanced with increasing BPA concentration. **Figure 6.5**f plots the resulting peak height *vs.* concentration calibration points for the data displayed in **Figure 6.5**e. A good linear response is obtained (R^2>0.99) in the concentration range between 0.1 to 50 μM. The detection limit, noise, sensitivity and detection range at bare GCE, CB-GCE and ND-GCE are shown in **Table 6.3**. The detection limit was calculated by 3 times noise (fluctuation of non-faradaic current in the absence of BPA) divided by sensitivity (slope of current against concentration). The noise at ND-GCE is the smallest and CB-GCE is more sensitive

than the other two. To sum up, the lowest detection limit was obtained at ND-GCE as well as the widest detection range.

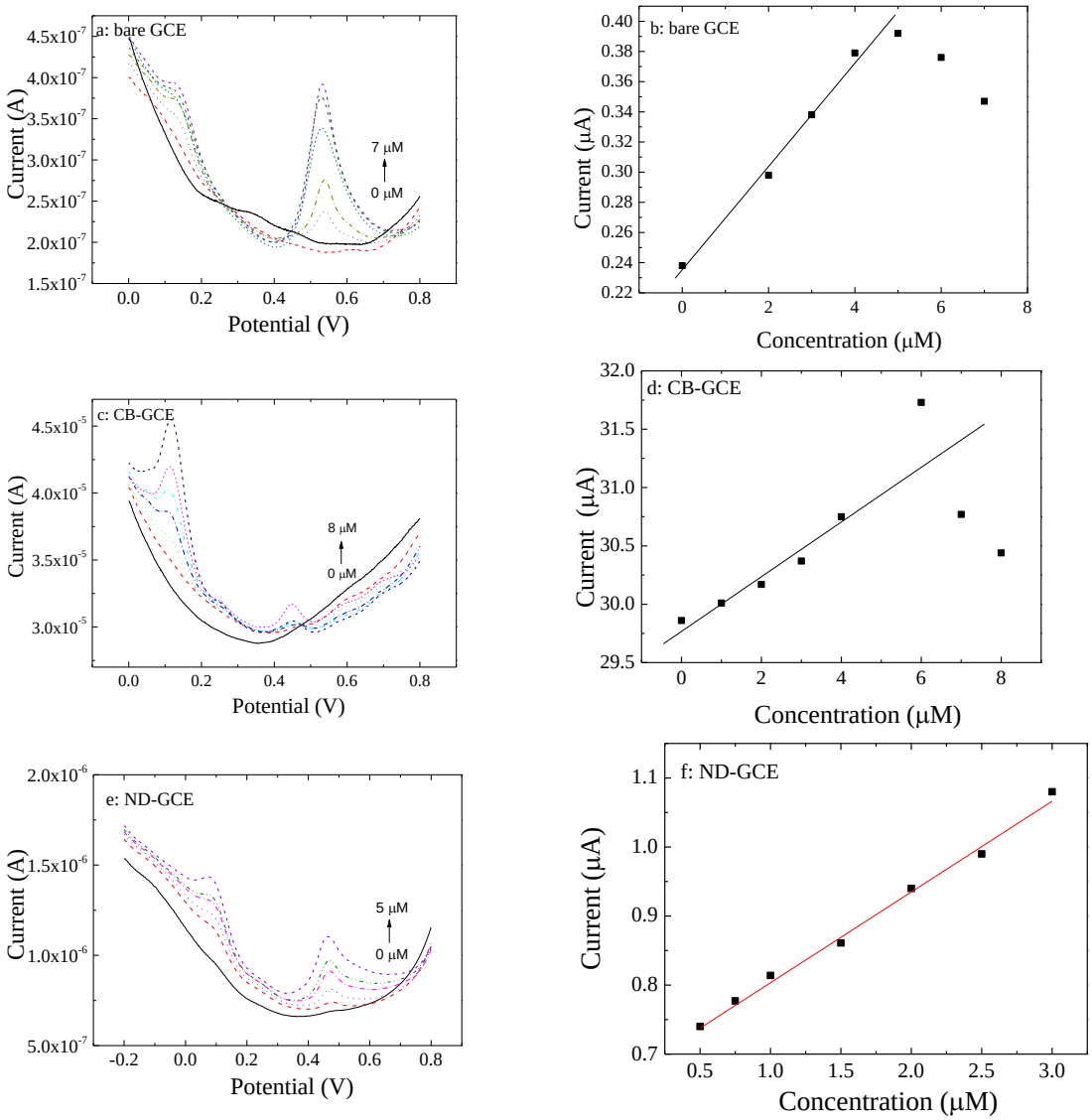

Figure 6.5 Square wave voltammograms of increasing BPA in steps of 1 μM in 0.1 M phosphate buffer at (a) bare GCE, (c) CB-GCE and (e) ND-GCE; and (b), (d), (f) the resulting plots of peak current *vs.* BPA concentration

Table 6.3 Detection limit (μM), detection range (μM) and sensitivity (μA μM^{-1}) of BPA detection at bare GCE, CB-GCE and ND-GCE by SWV method

Sensors	Noise (A)	Sensitivity	LOD	Detection range
Bare GCE	1.0×10^{-9}	0.03	0.10	1-5
CB-GCE	2.4×10^{-9}	0.30	0.024	0.5-3
ND-GCE	2.1×10^{-10}	0.05	0.013	0.1-50

6.3.2 BPA determination at CB-GCE: redox of quinone

6.3.2.1 Direct detect BPA oxidation at CB-GCE

The main problem for CB-GCE to detect BPA continually is due to the strong electrode fouling. One of the solutions is to use fresh electrode for each experiment to obtain more accurate data, which is possible for CB-GCE because of the low cost and simple modification. Another solution is to detect BPA via DHI which will be discussed in subsequent work. The SWV was performed in 0.1 M phosphate buffer and various concentrations of BPA from 1 to 50 μM at CB-GCEs from 0 to +0.8 V. Some representative voltammograms are displayed in **Figure 6.6**a. A clear feature of BPA oxidation is observed and an increase in peak height is seen with an increase in BPA concentration raises at all concentrations, in contrast to what is seen in **Figure 6.5**b. The resulting points of peak current *vs.* BPA concentration, up to 100 μM, are plotted in **Figure 6.6**b, yielding a linear response between 0 to 30 μM. The detection limit can be calculated to be 0.054 μM with sensitivity of 0.849 μA μM^{-1} and noise of 0.016 μA. Although the linearity between the CV responses and BPA concentration is relatively poor because of the individual differences between freshly CB-GCEs, this method significantly improves the signal and avoids the electrode fouling at CB-GCE in comparison to the results of SWV at continuous addition of BPA at the same electrode

(shown in **Figure 6.5**c). The LODs obtained from both continuous CB-GCE and fresh CB-GCE are in the same order since the sensitivity and noise are similar.

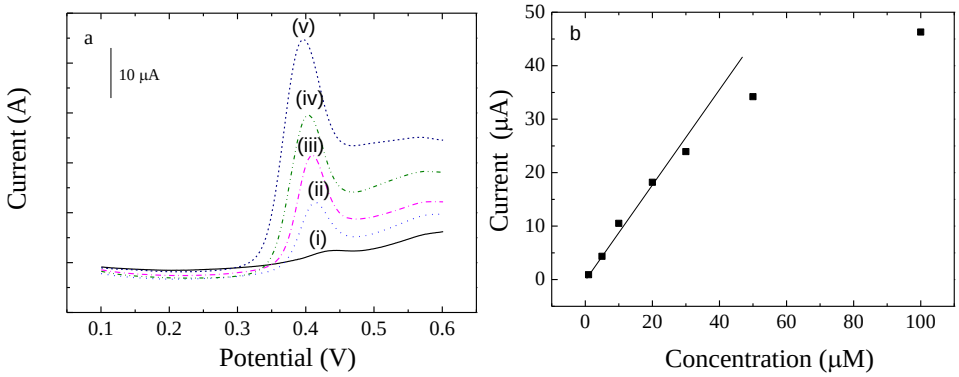

Figure 6.6 (a) Square wave voltammograms at freshly prepared CB-GCE in 0.1 M phosphate buffer and 1, 10, 20, 30 and 50 µM BPA respectively and (d) plot of peak current *vs.* BPA concentration

6.3.2.2 Cyclic voltammetry of quinone redox reaction

6.3.2.2.1 Cyclic voltammerty

Another approach to determine BPA at CB-GCE is by detecting the quinone form to determine the BPA concentration. As mentioned above, the oxidation of BPA will generate quinone as a by-product. The oxidation and reduction of quinone results in a pair of peaks in CVs as shown in **Figure 6.2** at a potential of about +0.1 V Due to the strong adsorption at carbon black, these peaks of quinone are much more significant at CB-GCE than at the bare GCE and ND-GCE. The redox properties of the quinone generated by BPA oxidation at CB-GCE were therefore studied in order to determine BPA in solution. **Figure 6.7**a shows CVs of three sweep cycles at CB-GCE in a solution containing 0.1 M phosphate buffer and 0.2 mM BPA. A clear oxidation peak can be observed in the first scan with no reverse wave, corresponding to an irreversible oxidation process of BPA. This peak current dropped significantly in the second and third scans, in agreement with previous results at bare GCE. However, from the second

scan, a pair of redox peaks appears at about +0.15 V, and is enhanced in consecutive scans. This pair of peaks corresponds to the quinone/hydroquinone reaction.[22] The plots of peak current of BPA oxidation and quinone redox reaction against scan cycles are shown in **Figure 6.7**b and **Figure 6.7**c respectively, from the data obtained from **Figure 6.7**a. It can be seen from **Figure 6.7**b that the CV response to BPA oxidation dropped quickly in the first 3 cycles and then decreased linearly as more voltammetric scans were carried out. On the other hand, the peak current of the quinone redox reaction increases gradually, and reaches a plateau eventually. It appears the electrode rapidly loses the ability to efficiently oxidise BPA due to fouling, but retains the ability to respond to quinones which develop in the solution even when fouled.

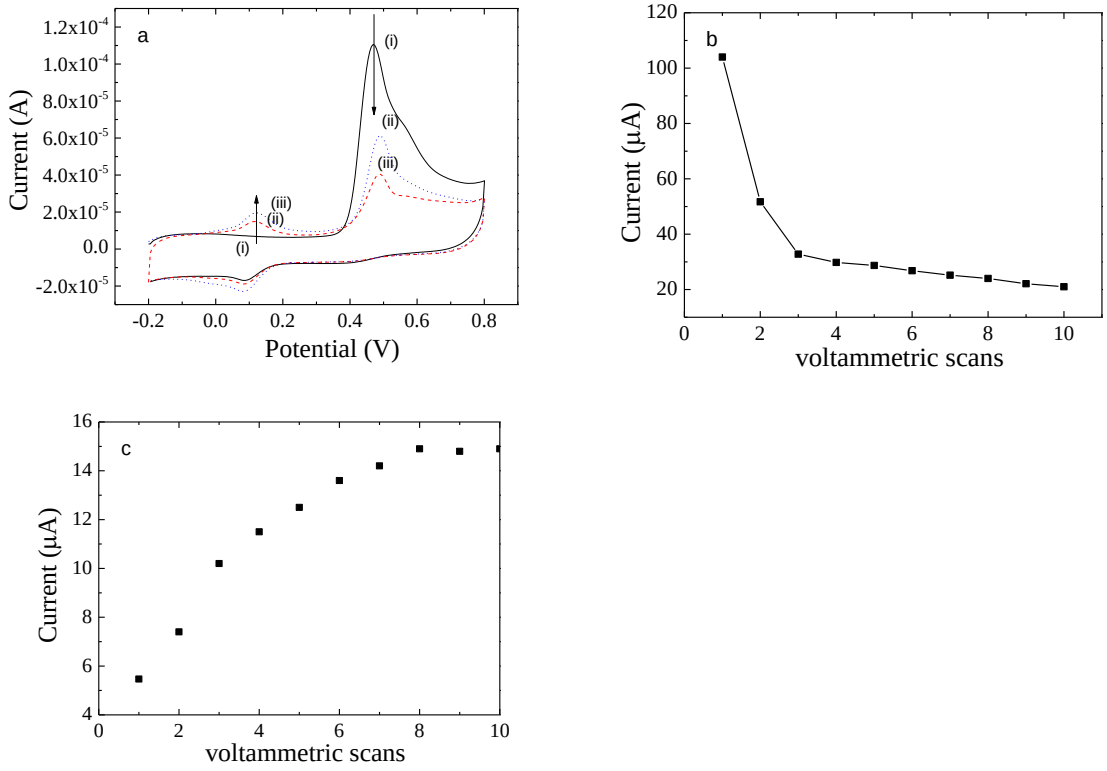

Figure 6.7 (a) Cyclic voltammograms of consecutive scans, (i) first, (ii) second and (iii) third, in a solution containing 0.2 mM BPA and 0.1 M phosphate buffer at CB-GCE; (b) plot of peak current of BPA *vs.* cyclic voltammetric scans; (d) plot of peak current of quinone reduction *vs.* cyclic voltammetric scans.

Figure 6.8 displays CVs at CB-GCE in 0.1 M phosphate buffer with the continuous addition of BPA with resulting concentration from 0 to 200 μM into 0.1 M phosphate buffer, and the resulting plots of peak current *vs.* BPA concentration. All the experiments were performed at the same CB-GCE. The peaks corresponding to BPA oxidation and qunione/hydroquinone redox are observed. As the concentration of BPA increases the peak currents are all enhanced. Due to the electrode fouling, the peak current of BPA increases nonlinearly with the concentration, as shown in **Figure 6.8**b. However, for quinone, the peak current shows a linear increase with BPA from a low to high concentration. The points of peak current against BPA concentration are displayed in **Figure 6.8**c, where both results of oxidation and reduction are of good accuracy. This result indicates that the peaks of quinone are dependent on the concentration of BPA, and are less influenced by the electrode surface fouling.

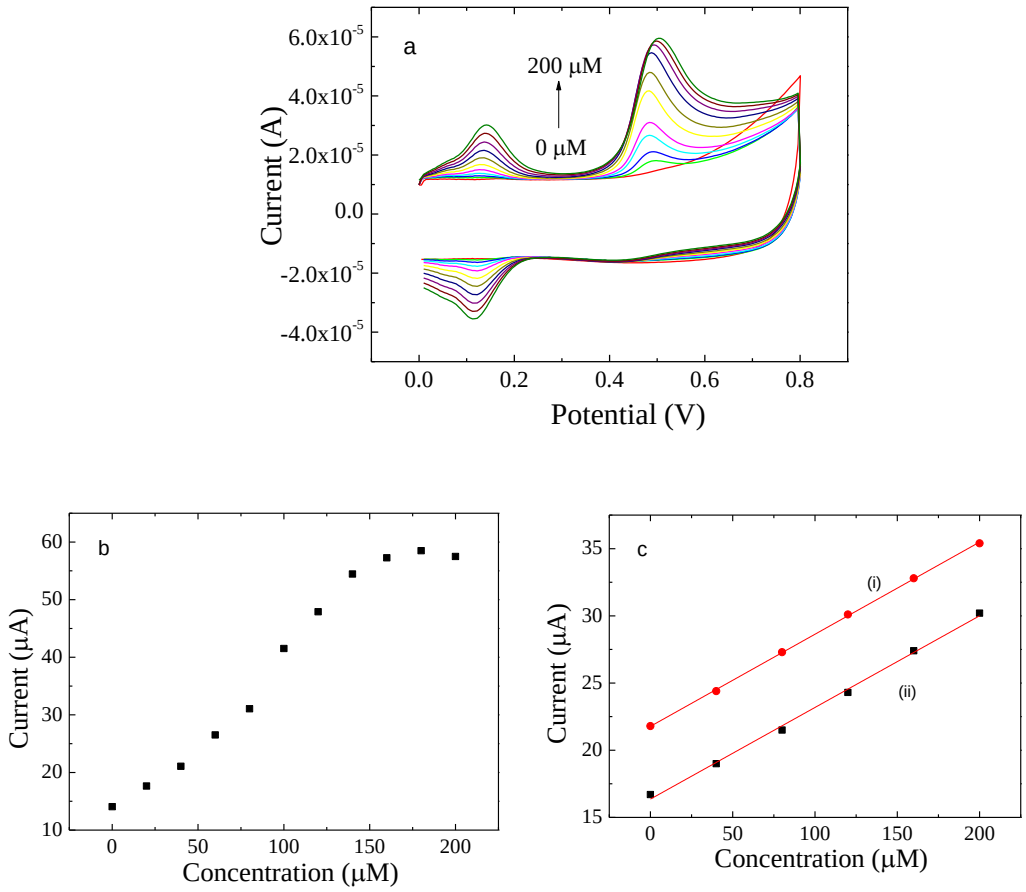

Figure 6.8 (a) Cyclic voltammograms at CB-GCE in 0.1 M phosphate buffer with the continuous addition of BPA from 0 to 200 µM in steps of 20 µM; (b) plot of peak current of BPA oxidation *vs.* BPA concentration and (c) plot of (i) reduction and (ii) oxidation peak current of quinone *vs.* BPA concentration

6.3.2.2.2 Peak current vs. scan rate: adsorption control

The surface processes of both BPA oxidation and the quinone redox reaction at CB were studied by cyclic voltammetry carried out in a solution containing 0.2 mM BPA and 0.1 M phosphate buffer with different scan rate. **Figure 6.9** displays the CVs of the first scan at fresh CB-GCE as a function of scan rates. The feature of BPA oxidation can be clearly observed and the peak current is enhanced as the scan rates increased from 20 to 200 mV s^{-1}. Also enhanced is the background current because at higher scan rate the double layer capacitance is increased. The plot of peak current against scan rate is shown in **Figure 6.9**b. It is apparent that the peak current is linearly dependent on the

scan rate, not square root of scan rate (shown in Inset), showing that the process of BPA oxidation is under adsorption control at the CB-GCE surface.

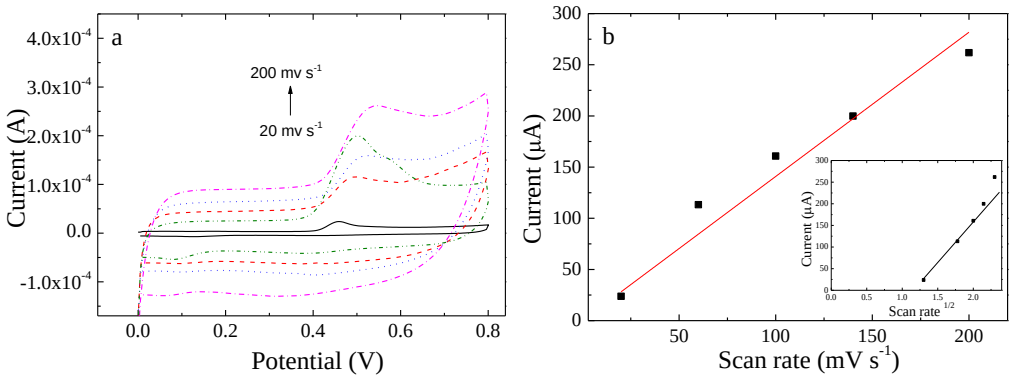

Figure 6.9 (a) Cyclic voltammograms in a solution containing 0.1 M phosphate buffer and 0.2 mM BPA with different scan rate of 20, 60, 100, 140 and 200 mV s^{-1} at CB-GCE which was freshly prepared each time; (b) resulting plot of peak current *vs.* scan rate; Insets: resulting plot of peak current *vs.* square root of scan rate

The CVs shown in **Figure 6.10**a were carried out in 0.1 M phosphate buffer and 0.2 mM BPA at CB-GCE with increasing scan rate from 20 to 200 mV s^{-1}. Before the experiment, the electrode was scanned for 10 cycles in the same solution with scan rate of 50 mV s^{-1} in order to allow the quinone to reach equilibrium at carbon black surface and obtain a stable voltammetric response of quinone. It can be observed that the peak height for BPA oxidation does not change significantly but those responses to quinone redox reaction are enhanced according to the increasing scan rate. An excellent linear response is obtained (R^2>0.999) between peak current and scan rate as shown in **Figure 6.10**b, which indicates that the redox reaction of quinone is under adsorption control at CB-GCE surface and agrees with previously results showing that the reaction of phenol, cresol, HQ and DHB are all under adsorption controlled at CB-GCE.

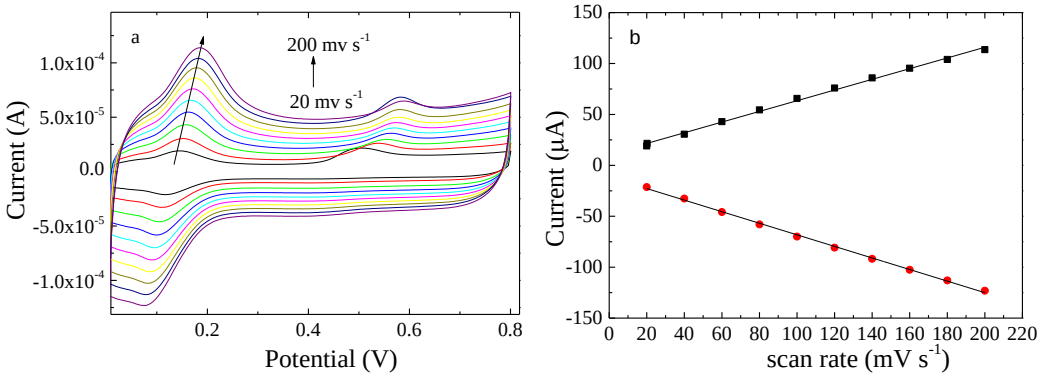

Figure 6.10 (a) Cyclic voltammograms in the solution containing 0.2 mM BPA and 0.1 M phosphate buffer at scan rate from 20 to 200 mV s^{-1} in steps of 20 mV s^{-1}, at CB-GCE; (b) plot of peak current *vs.* scan rate

6.3.2.2.3 Square wave voltammetry

As seen above (**Figure 6.8**), the voltammetric response of the quinone redox reaction at CB-GCE is proportional to the BPA concentration present in solution and therefore can be potentially utilised to determine BPA indirectly. The process was demonstrated as follows. A fixed potential of +0.6 V was applied for 60 s after addition of BPA solution into 0.1 M phosphate buffer in order to oxidise BPA and produce quinone. Then SWV was performed from 0 to +0.3 V. The preconditioning potential of +0.6 V is chosen because BPA oxidation occurs at about +0.5 V as suggested from CV, therefore +0.6 V is sufficient to drive the reaction and allow quinone to be generated and accumulated at electrode surface. The preconditioning time of 60 s was also optimised as follows. **Figure 6.11** displays the SWV profiles as a function of preconditioning time from 10 s to 90 s in 0.1 M phosphate buffer and 10 µM BPA at CB-GCE. A well resolved wave of quinine oxidation can be observed at *ca.* +0.13 V, and increased with longer preconditioning time. However, after 60 s, the increase is not significant; therefore, the pre-treatment was performed for 60 s in the following experiments.

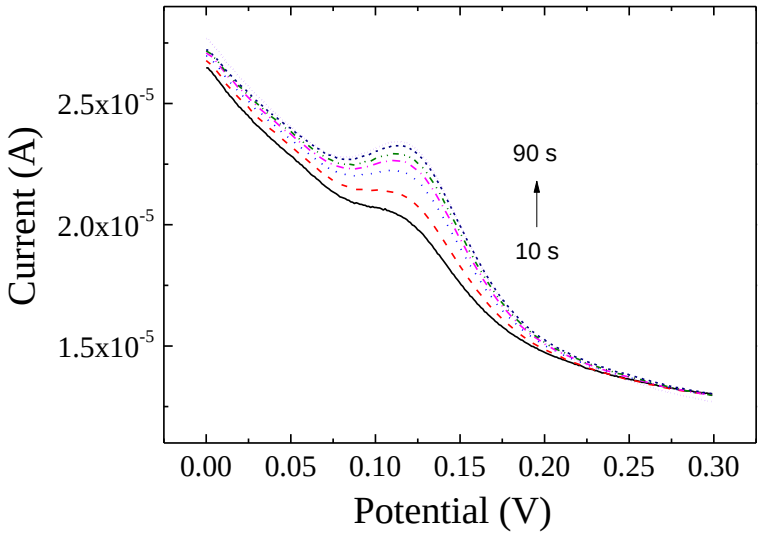

Figure 6.11 Square wave voltammograms at CB-GCE in a solution containing 0.1 M phosphate buffer and 10 μM BPA after applying a fixed potential of +0.6 V for 10, 20, 30, 40, 50, 60 and 90 s respectively.

The optimised procedure was conducted to determine BPA. The voltammagrams with continuous addition of BPA into 0.1 M phosphate buffer at bare GCE, ND-GCE and CB-GCE are shown in **Figure 6.12**a-c, without changing electrodes. A wave of quinone oxidation can be observed at bare GCE and ND-GCE at around +0.15 V. However, it is broad and ill-feature. At CB-GCE, a well-defined peak appears at *ca.* +0.12 V, and is enhanced with increasing BPA. The plot of peak current against BPA concentration is present in **Figure 6.12**e (square points) in the range of 0 to 10 μM. The Inset shows a wider range of BPA from 0 to 160 μM. A good linear response was obtained between 0 to 80 μM (R^2>0.99). This linearity is significantly improved compared with those obtained from the direct detection of BPA oxidisation shown in **Figure 6.5**d and **Figure 6.6**b. The accuracy and precision are also improved. The detection limit can be calculated to be 0.062 μM with the sensitivity of 1.159 μA μM^{-1} and a noise of 2.4×10^{-9} A.

Because the detection of BPA discussed above was carried out at the same CB-GCE, the electrode fouling to CB-GCE surface should be taken into consideration. SWV were also carried out at newly prepared CB-GCEs (preconditioning at +0.6 V for 60 s) in various BPA concentrations. The voltammograms are shown in **Figure 6.12**d, and the resulting plot of peak current *vs.* BPA concentration can be found in **Figure 6.12**e (triangle points). These points are in good agreement to the plots obtained from **Figure 6.12**c. In other words, the performance at a single CB-GCE for various BPA concentrations is similar to those using fresh CB-GCE for each BPA concentration. It implies that the fouling does not influence the electrochemical response of quinone at CB-GCE by this method.

Also, ten CB-GCE sensors were kept in a dry box for various times from two hours to one month, and tested by SWV (preconditioning at +0.6 V for 60 s) in 0.1 M phosphate buffer and 10 μM BPA. The RSD was about 95%, which indicated CB-GCE sensor is stable and reproducible.

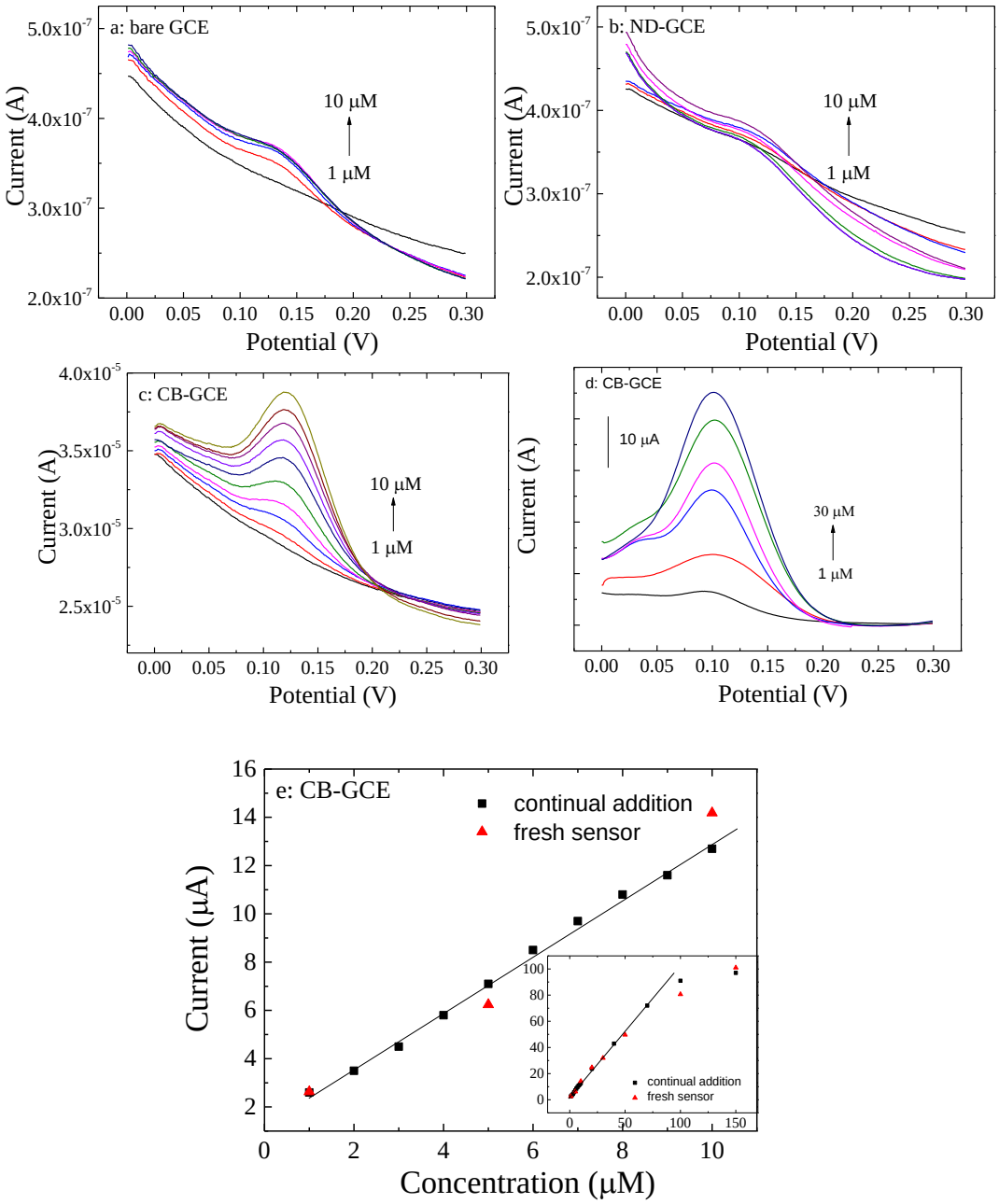

Figure 6.12 Square wave voltammograms in a solution containing 0.1 M phosphate buffer with continuous addition of BPA from 1 to 10 μM in steps of 1 μM (preconditioning at +0.6 V for 60 s) at (a) bare GCE, (b) ND-GCE and (c) CB-GCE; (d) the SWV performed at fresh CB-GCE in the presence of 1, 5, 10, 20 and 30 μM BPA respectively and (e) plot of peak current *vs.* BPA concentration from the data displayed in (c) and (d)

6.3.2.2.4 Interference

Since the BPA determination at CB-GCE was via the redox reaction of quinone, the interference from other phenolic compounds (HQ and DHB) which can co-exist in the

environment should be taken into account. It was studied by standard addition method as mentioned in Chapter 5. A linear line of peak current *vs*. BPA concentration was obtained first (see **Figure 6.12**e) by the procedure described above. Then the same SWV was performed in a solution of 0.1 M phosphate buffer, 10 μM HQ and 10 μM DHB, in the presence and absence of 5 μM BPA. The difference in peak height corresponds to the concentration in the linear graph obtained above, so called found concentration of BPA. The ratio of found concentration to the addition concentration (5 μM) is called recovery, which can imply the accuracy of BPA detection in the presence of quinone in solution. The average recovery of 5 samples was found to be 100.8%. This result shows that the presence of HQ and DHB does not significantly affect the determination of BPA by this method.

6.3.3 Comparison: ND-GCE, CB-GCE and other BPA sensors

Here we compare two methods to detect BPA in this work, *i.e.* direct determination at ND-GCE and indirect determination at CB-GCE via quinone redox, with other BPA sensors in the literature in terms of detection limit, detection range, interference and other aspects, in order to meet requirements of BPA monitoring in environment. As displayed in **Table 6.1**, the BPA concentration found in environment normally vary from 0.043 to 43.8 μM. However, although some modified electrodes, like LDH/GCE[4], were reported to provide a very low detection limit of 5 nM, the detection limit of many BPA sensors are of the order of 10^{-7} M as shown in **Table 6.2**. What is more important is that the detection range is always below 20 μM, which is lower than the concentration in some environmental samples like those from waste landfill site[14]. In this work, the detection limit of the order of 10^{-8} M can be obtained at both ND-GCE and CB-GCE, and the detection range is up to 50 μM at ND-GCE and 80 μM at CB-GCE. The low

detection limit and wide detection range can satisfy the requirement for BPA determination in environmental monitoring.

As mentioned above, another problem for environmental monitoring is the interference arising from the high detection potential (from +0.4 to +1.2 V depending on electrodes) where other electro-chemical reactions might occur, considering the complex composition in environmental samples. The detection potential at ND-GCE is *ca.* +0.5 V, which is relatively low compared with other sensors, such as CNT/GCE (+0.59 V), BDD (+0.95 V) and Pt (+1.25 V). And the inertness of ND-GCE can minimise the interference. The CB-GCE method can determine BPA at +0.12 V, which is the lowest amongst all the BPA sensors as we know. It can be a suitable choice for those samples which is sensitive to high detection potential.

6.3.4 Simultaneous detection of HQ, DHB and BPA

The simultaneous detection of HQ, DHB and BPA was also studied in this work. SWV was performed in a solution containing 0.1 M phosphate buffer, 10 μM HQ, 10 μM DHB with the continuous addition of BPA. The voltammograms at bare GCE, ND-GCE and CB-GCE are shown in **Figure 6.13**. Two oxidation peaks can be observed at bare GCE and ND-GCE (**Figure 6.13**a and b). One peak at around +0.5 V is attributed to BPA oxidation and another around +0.15 V is assigned to HQ & DHB. The overlap of the electro-response of HQ and DHB at bare GCE and ND-GCE has been demonstrated in previous work. With the addition of BPA, this peak value of HQ & DHB remains almost the same while the peak for BPA oxidation increase gradually. The sensitivity of BPA determination at ND-GCE was calculated to be 0.047 μA μM^{-1} which was close to the result of 0.05 μA μM^{-1} when HQ and DHB was absent. On the other hand, observed from **Figure 6.13** c are the voltammograms at CB-GCE, where three clear oxidation

features appear corresponding to HQ, DHB and BPA oxidation from low to high potential respectively. However, with the addition of BPA, all three peak heights increased. This enhancement may be a result of the quinone generated from BPA oxidation. To sum up, the simultaneous detection of HQ, DHB and BPA remains a target to be resolved because of the overlap of electro-chemical response of HQ and DHB, and the interference to HQ and DHB signal from BPA oxidation.

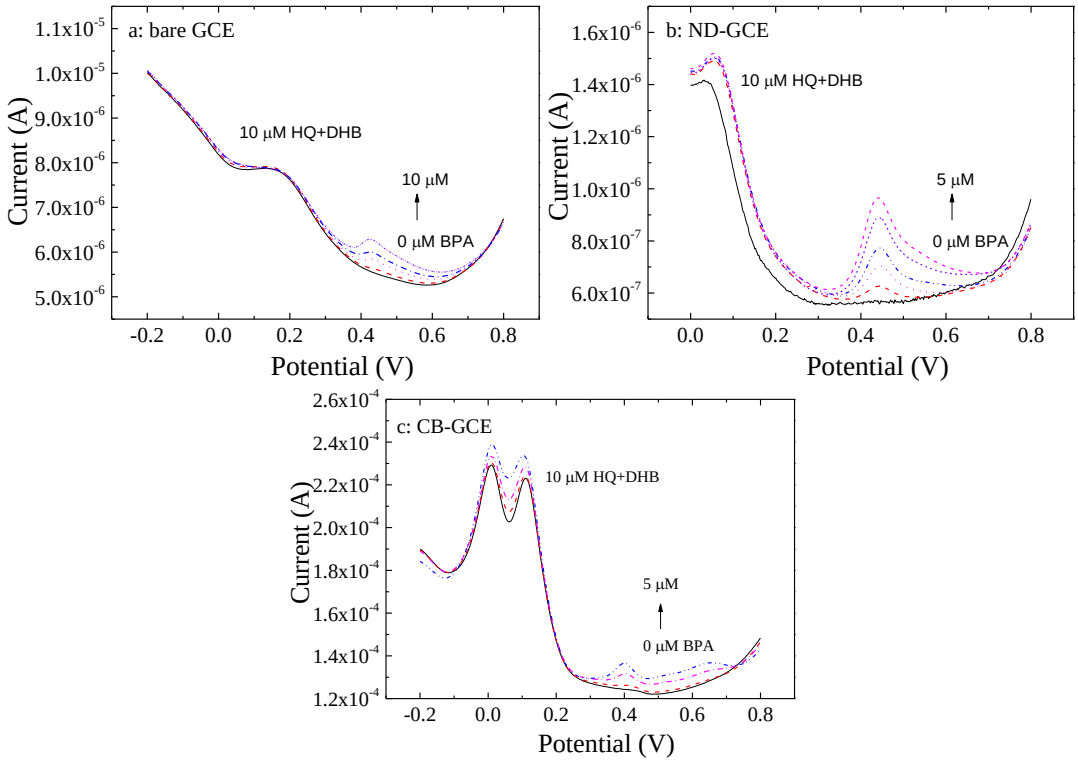

Figure 6.13 Square wave voltammograms in a solution containing 0.1 M phosphate buffer, 10 μM HQ and DHB and increasing concentration of BPA from 0 to 5 μM in steps of 1 μM at (a) bare GCE, (b) ND-GCE and (c) CB-GCE

6.4 Conclusion

The difficulties for BPA detection in many sensors include electrode fouling, high detection potential and limited detection range. In this work, two BPA sensors were developed to tackle these problems.

- The cyclic voltammetry results showed that BPA can be oxidised directly at bare GCE, ND-GCE and CB-GCE at about 0.5 V. CB-GCE shows higher peak current and ND-GCE exhibited the lower double layer capacitance and smaller noise. Subsequent studies of peak current against scan rate shows that BPA oxidation is under adsorption control at bare GCE, ND-GCE and CB-GCE.
- During the oxidation of BPA, electropolymerised films were formed and thus fouling the electrode surface, resulting in a decrease of BPA peak current at both bare GCE and CB-GCE. However, at ND-GCE, the decrease was insignificant. The reason may be that the non-polar surface of ND-GCE can resist the formation of oxidative polymerisation of BPA, thereby being free from the electrode fouling.
- SWV was performed in the potential range of 0 to +0.8 V to detect BPA by BPA oxidation at bare GCE, ND-GCE and CB-GCE directly. The performance at ND-GCE is a significant improvement over those afforded by bare GCE and CB-GCE, giving a linear response in the range from 0.1 to 50 μM and a calculated detection limit of 0.013 μM.
- To eliminate the influence of electrode fouling, fresh CB-GCE was used for each experiment to determinate BPA. The detection limit can be calculated to be 0.054 μM with sensitivity of 0.849 μA μM^{-1} and noise of 0.016 μA.

- It is observed that after oxidation of BPA, a pair of redox peak appeared at *ca.* +0.12 V. It is attributed to the quinone which is generated from BPA oxidation. The CV of quinone shows that the peak currents of quinone reactions are proportional to BPA concentration at CB-GCE. The oxidation and reduction of quinone are proved to be adsorption controlled.
- BPA was determined at CB-GCE by SWV scanning from 0 to +0.3 V, with preconditioning at +0.6 V for 60 s. The precondition is to oxidise BPA and generate quinone. An excellent linear response between peak current and BPA concentration can be obtained up to 80 μM, with a detection limit of 0.062 μM.
- SWV was also performed at fresh CB-GCE each time, and the values obtained are close to those carried out at a single CB-GCE. It proves that the influence of electrode fouling is small in this method, and the CB-GCE sensor is stable and reproducible.
- The presence of HQ and DHB, which may co-exist with BPA in environment, did not influence BPA detection at ND-GCE and CB-GCE significantly. However, these three species cannot be simultaneously detected at these sensors.

References

(1) Mita, D. G.; Attanasio, A.; Arduini, F.; Diano, N.; Grano, V.; Bencivenga, U.; Rossi, S.; Amine, A.; Moscone, D. *Biosensors & Bioelectronics* **2007**, *23*, 60.

(2) Staples, C. A.; Dorn, P. B.; Klecka, G. M.; O'Block, S. T.; Harris, L. R. *Chemosphere* **1998**, *36*, 2149.

(3) Li, J.; Kuang, D.; Feng, Y.; Zhang, F.; Liu, M. *Microchimica Acta* **2011**, *172*, 379.

(4) Yin, H. S.; Cui, L.; Ai, S. Y.; Fan, H.; Zhu, L. S. *Electrochimica Acta* **2010**, *55*, 603.

(5) Calafat, A. M.; Kuklenyik, Z.; Reidy, J. A.; Caudill, S. P.; Ekong, J.; Needham, L. L. *Environmental Health Perspectives* **2005**, *113*, 391.

(6) Lang, I. A.; Galloway, T. S.; Scarlett, A.; Henley, W. E.; Depledge, M.; Wallace, R. B.; Melzer, D. *JAMA: the journal of the American Medical Association* **2008**, *300*, 1303.

(7) Welshons, W. V.; Nagel, S. C.; vom Saal, F. S. *Endocrinology* **2006**, *147*, s56.

(8) Kang, J.-H.; Kondo, F.; Katayama, Y. *Toxicology* **2006**, *226*, 79.

(9) Galloway, T.; Cipelli, R.; Guralnik, J.; Ferrucci, L.; Bandinelli, S.; Corsi, A. M.; Money, C.; McCormack, P.; Melzer, D. *Environmental Health Perspectives* **2010**, *118*, 1603.

(10) Vandenberg, L. N.; Maffini, M. V.; Sonnenschein, C.; Rubin, B. S.; Soto, A. M. *Endocrine Reviews* **2009**, *30*, 75.

(11) Melzer, D.; Rice, N. E.; Lewis, C.; Henley, W. E.; Galloway, T. S. *PloS one* **2010**, *5*, e8673.

(12) vom Saal, F. S.; Myers, J. P. *JAMA: the journal of the American Medical Association* **2008**, *300*, 1353.

(13) Pereira, G. F.; Andrade, L. S.; Rocha-Filho, R. C.; Bocchi, N.; Biaggio, S. R. *Electrochimica Acta* **2012**, *82*, 3.

(14) Murugananthan, M.; Yoshihara, S.; Rakuma, T.; Shirakashi, T. *Journal of Hazardous Materials* **2008**, *154*, 213.

(15) Bailey, D. A. B.; Hoekstra, D. E. J. *Background Paper on Sources and Occurrence of Bisphenol A Relevant for Exposure of Consumers*, World Health Organization, 2010.

(16) Zafra, A.; del Olmo, M.; Suárez, B.; Hontoria, E.; Navalón, A.; Vílchez, J. L. s. *Water Res.* **2003**, *37*, 735.

(17) Inoue, K.; Kato, K.; Yoshimura, Y.; Makino, T.; Nakazawa, H. *Journal of Chromatography B: Biomedical Sciences and Applications* **2000**, *749*, 17.

(18) Sajiki, J.; Takahashi, K.; Yonekubo, J. *Journal of Chromatography B-Analytical Technologies in the Biomedical and Life Sciences* **1999**, *736*, 255.

(19) Horie, M.; Yoshida, T.; Ishii, R.; Kobayashi, S.; Nakazawa, H. *Bunseki Kagaku* **1999**, *48*, 579.

(20) M.A.Brett, C.; Brett, A. M. O. *Electroanalysis*; Oxford University Press: Oxford, 1998.

(21) Ngundi, M. M.; Sadik, O. A.; Yamaguchi, T.; Suye, S. *Electrochemistry Communications* **2003**, *5*, 61.

(22) Kuramitz, H.; Matsushita, M.; Tanaka, S. *Water Res.* **2004**, *38*, 2331.

(23) Li, Y.; Gao, Y.; Cao, Y.; Li, H. *Sensors and Actuators B: Chemical* **2012**, *171*, 726.

(24) Yin, H.-s.; Zhou, Y.-l.; Ai, S.-y. *Journal of Electroanalytical Chemistry* **2009**, *626*, 80.

(25) Notsu, H.; Tatsuma, T.; Fujishima, A. *Journal of Electroanalytical Chemistry* **2002**, *523*, 86.

(26) Moraes, F. C.; Silva, T. A.; Cesarino, I.; Machado, S. A. *Sensors and Actuators B: Chemical* **2012**.

(27) Ren, J.; Kang, T.-F.; Xue, R.; Ge, C.-N.; Cheng, S.-Y. *Microchimica Acta* **2011**, *174*, 303.

(28) Hu, J.; Holt, K. B.; Foord, J. S. *Analytical Chemistry* **2009**, *81*, 5663.

(29) Compton, R. G.; Foord, J. S.; Marken, F. *Electroanalysis* **2003**, *15*, 1349.

(30) Arduini, F. *Electroanalysis* **2012**.

(31) Boehm, H. P. *Carbon* **1994**, *32*, 759.

(32) Lonergan, M. C.; Severin, E. J.; Doleman, B. J.; Beaber, S. A.; Grubb, R. H.; Lewis, N. S. *Chemistry of Materials* **1996**, *8*, 2298.

(33) Nekrassova, O.; Lawrence, N. S.; Compton, R. G. *Analyst* **2004**, *129*, 804.

(34) Wang, Q.; Wang, Y.; Liu, S.; Wang, L.; Gao, F.; Gao, F.; Sun, W. *Thin Solid Films* **2012**, *520*, 4459.

(35) Lo, T. W.; Aldous, L.; Compton, R. G. *Sensors and Actuators B: Chemical* **2012**, *162*, 361.

Chapter 7 Carbon Black Modified Electrode for Dopamine Detection

7.1 Introduction

Dopamine (DA) is one of the most important excitatory chemical neurotransmitters in mammalian central nervous, cardiovascular, renal and hormonal systems.[1] DA imbalance is also associated with several important diseases like Parkinson and Schizophrenia.[2] Since DA can be easily oxidised at a low potential, electro-analysis offers a simple, quick, sensitive approach for DA detection, and the mechanism has been fully demonstrated as shown in **Figure 7.1**.[2-4] However, this method is highly restricted by the interference of ascorbic acid (AA) and uric acid (UA) which always co-existed with DA in environment because the oxidation potential of AA and UA are highly overlapped with DA. In addition, the DA that have been oxidised would be reduced by AA and re-oxidised again at electrode surface, which influence the accuracy and precision of the electrochemical response of DA.[5]

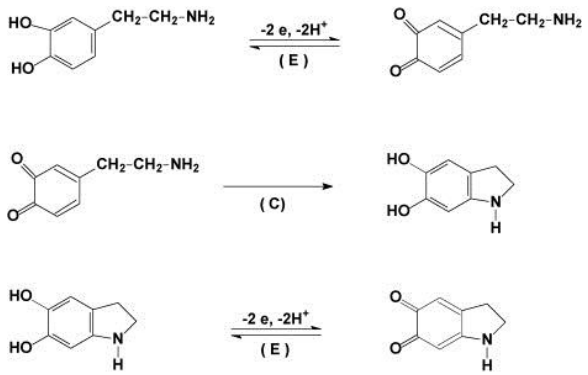

Figure 7.1 The mechanism of DA redox reactions [6]

To minimise the interference, two strategies are widely applied. One is shifting the oxidation potential of AA or DA by electrode modification with nanomaterials (Pd/CNFs[7], carbon nanotube[8], gold nanoparticles[9], Fc-SWCNT[10], $La(OH)_3$[11]) or polymers (neural red[12], EBT[5,13], Evans Blue[14]), in order to oxidise AA at a more negative potential than DA and separate their peaks. The range of these modified electrode are truly huge and highly diverse.[15] Since AA is negatively charged in aqueous environments but DA is not, the other method is coating the electrode surface by a negative charged film[16], such as Nafion[10], SDS[17] and PBV[18], AA is then repelled from the surface and only the oxidation peak of DA can be observed. The recovery of DA in the presence of AA can be achieved at about 95% by surface modification and 97% by the negative change film coating. However, considering the concentration of AA can be 100 times higher than DA[7], the interference is still significant. Some literature reported another pair of peaks around -0.3/-0.5 V in cyclic voltammograms of DA at MWCNT-poly (DBA) electrode, f-MWCNTs-poly films electrode and carbon nanotubes-ionic liquid gel modified electrode.[6,8,12,19] This pair of peaks is attributed to the 5,6-dihydroxyindole (DHI) which is generated from the cyclisation, oxidation and rearrangement of dopamine-quinone. The mechanism is explained in **Figure 7.1**. It is also reported that the redox peaks of 5,6-dihydroxyindole are strongly affect by pH. It can only appear at a high pH and is relatively ill-defined and weak in a neutral solution. Detecting DHI provides a possible approach to determine DA because the DHI concentration is proportional to the DA concentration in the solution, and the low detection potential can avoid the interference from AA and UA. However, only a few papers are concerned about the redox reaction of DHI, and to date, no sensor has been reported to determine DA via DHI. The reason may be that the peak current of DHI decayed quickly in continuous voltammetric scans, and most in situ DA determinations

have to take place in a neutral solution where the electrochemical response of DHI is weak.

Carbon black stands out as a good candidate to solve these problems. The strong adsorption on CB can enhance the electrochemical response to a great extent. As observed previously, the peak currents of phenolic compounds were one order of magnitude higher at CB-GCE than at bare GCE. Also, the experiments showed that the redox reaction of DHI at CB-GCE occurred in a much wider pH range. Therefore the detection in a neutral solution is possible. In addition, the similar process of indirect determination via by-product has been studied at CB-GCE, to determine BPA via quinone. Together with other advantages like low cost and simple modification procedure, carbon black becomes a promising alterative to other modified sensors. In this work, DA was determined at CB-GCE by two methods. One is direct oxidising DA at CB-GCE at *ca.* +0.15 V, and a simultaneous determination of AA, UA and DA was carried out. The other one is to detect DA via the determination of DHI at about -0.3 V. Both methods exhibit sound sensitivity, detection limit and good selectivity.

7.2 Experimental

AA, DA and UA of A.C.S. reagent grade were purchased from Sigma Aldrich of A.C.S. reagent grade. The structure of DA, AA and UA are shown in **Figure 7.2**. All the solutions were prepared in 0.1 M phosphate buffer which had been adjusted to pH 7.4. The procedure to modify BDD electrode by carbon black was adopted from the previous chapter. Other chemicals and regular electrochemical methods have been described in previous chapters.

(a) (b) (c)

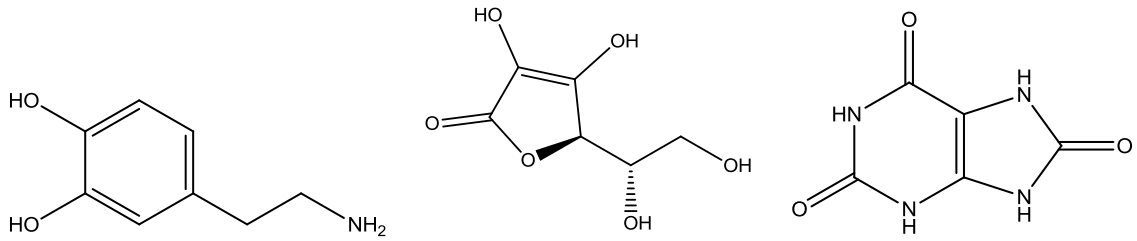

Figure 7.2 The structures of (a) dopamine, (b) ascorbic acid and (c) uric acid

7.3 Results and discussion

7.3.1 DA oxidation at CB-GCE

7.3.1.1 Cyclic voltammetry of AA, UA and DA at bare GCE and CB-GCE

Cyclic voltammetry of AA, DA and UA was conducted respectively at CB-GCE from -0.4 to +0.4 V in 0.1 M phosphate buffer, as shown in **Figure 7.3**. The CVs at bare GCE (line i) are also displayed for comparision. It can be seen that the background current at CB-GCE is much higher than that at bare GCE, indicating a larger double layer capacitance as discussed in the previous chapter. In the presence of 100 μM AA (**Figure 7.3**a), an irreversible oxidation peak appears at *ca.* +0.22 V without a reduction wave in the reverse scan at bare GCE, whilst both oxidation and reduction features are observed at CB-GCE at *ca.* -0.07/-0.22 V. Similarly, **Figure 7.3**b shows one irreversible oxidation peak for 10 μM UA at +0.29 V at bare GCE and one pair of peaks at +0.26/+0.25 V at CB-GCE. The oxidation of DA occurs at +0.16 V at bare GCE and +0.14/+0.13 V at CB-GCE, as shown in **Figure 7.3**c. Another pair of peaks is also observed at CB-GCE at -0.30/-0.31, which can be attributed to the redox reaction of DHI.[6,8,12,19] Comparing the oxidation potential of AA, UA and DA at both electrodes, they all negatively shift at CB-GCE (0.29 V for AA, 0.03 V for UA and DA) and the

shift of AA is the most significant. Also the currents are all enhanced at CB-GCE and the reversed reduction peak can be observed although weaker than the oxidation one. The DHI can also be detected at CB-GCE, but not at bare GCE.

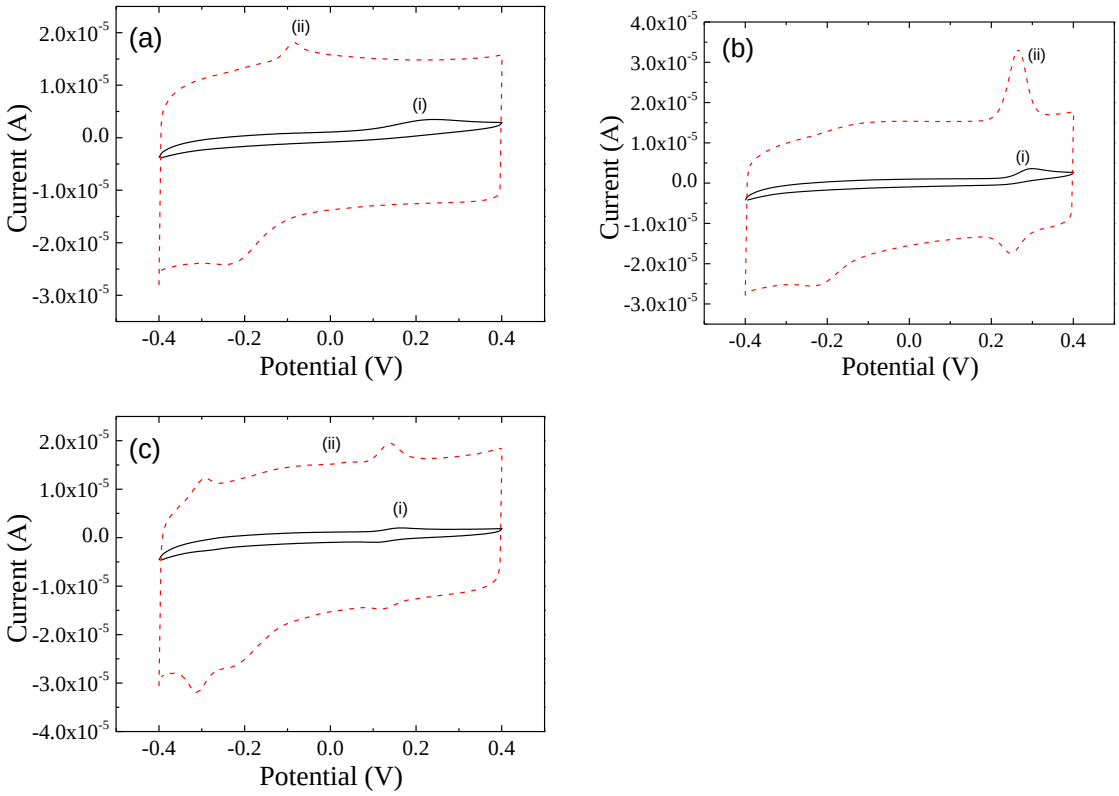

Figure 7.3 Cyclic voltammograms of (a) 100 µM AA, (b) 10 µM UA and (c) 10 µM DA at (i) bare GCE and (ii) CB-GCE in 0.1 M phosphate buffer

The cyclic voltammetry was also conducted to detect AA, UA and DA simultaneously. **Figure 7.4** shows the second redox voltammatric cycle in a solution containing 0.1 M phosphate buffer, 2 mM AA, 0.1 mM UA and 0.1 mM DA at bare GCE and CB-GCE. The concentration of AA is about 20 times higher than DA and UA, associated with the ratio in blood plasma.[20] At bare GCE, only one broad oxidation peak is observed in the potential range from +0.1 to +0.3 V, implying a severe overlap of the oxidation peaks of AA, DA and UA. However, at CB-GCE, four pairs of peak are well identified. Comparing to **Figure 7.3**, three pairs of redox peaks at *ca.* -0.29/-0.31 V, +0.03/-0.1 V and +0.20/+0.15 V are attributed to DHI, AA and DA respectively. The oxidation peak

of UA is found at +0.31 V and a broad and ill-featured reduction wave of UA can be observed at +0.3 V. It demonstrates that the electrochemical responses of redox reactions of AA, DA and UA were well separated at CB-GCE.

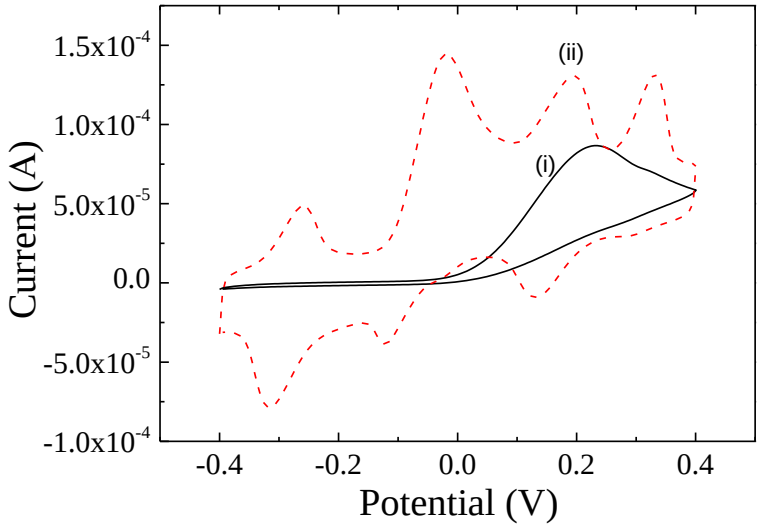

Figure 7.4 Cyclic voltammograms at (i) bare GCE and (ii) CB-GCE in the solution containing 0.1 M phosphate buffer, 2 mM AA, 0.1 mM UA and 0.1 mM DA

7.3.1.2 DHI at CB-GCE

To further investigate the electrochemical response of DA at CB-GCE, repeated cyclic voltammetric scans were carried out in a solution containing 0.1 M phosphate buffer and 0.1 mM DA from -0.6 V to +0.6 V. The first two CV scans are shown in **Figure 7.5**. In first cycle, only one oxidation peak of DA appears at about +0.2 V and in the reverse direction, the corresponding reduction peak appears at +0.2 V first, followed by another reduction peak at about -0.3 V. Upon the second cycle, another oxidation peak begins to emerge before the peak of DA oxidation. It is compatible with the mechanism shown in **Figure 7.1** that the oxidation of DA generates DHI which can be reduced and oxidised at the electrode surface.

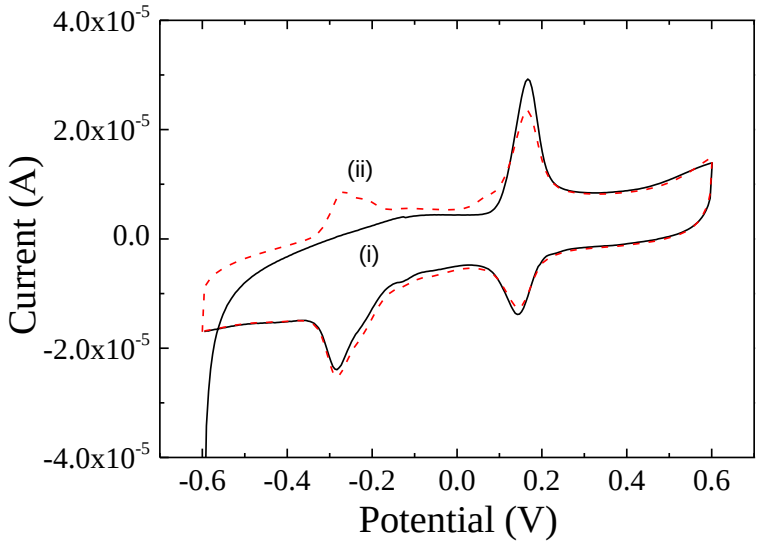

Figure 7.5 (i) First and (ii) second scan of cyclic voltammogram of 0.1 mM DA at CB-GCE in 0.1 M phosphate buffer.

To further investigate the relationship between DA and DHI, cyclic voltammetry with DA concentration increasing from 0 to 50 μM was further conducted at CB-GCE from -0.4 to 0 V, in 0.1 M phosphate buffer. In this potential range, DA is hardly oxidised, therefore only the response of DHI can be detected. The CVs are shown in **Figure 7.6**a. In the presence and absence of DA, the electrochemical curves are all featureless and no significant peak can be observed. Then the cyclic voltammetry was carried out under the analogous conditions but before scanning, a fixed potential of +0.4 V was applied for 10 s as a precondition, at which potential DA was oxidised. The resulting profiles are shown in **Figure 7.6**b, where a pair of peaks is clearly observed to grow with an increase in DA. It comes to the conclusion that the oxidation of DA is necessary to generate DHI.

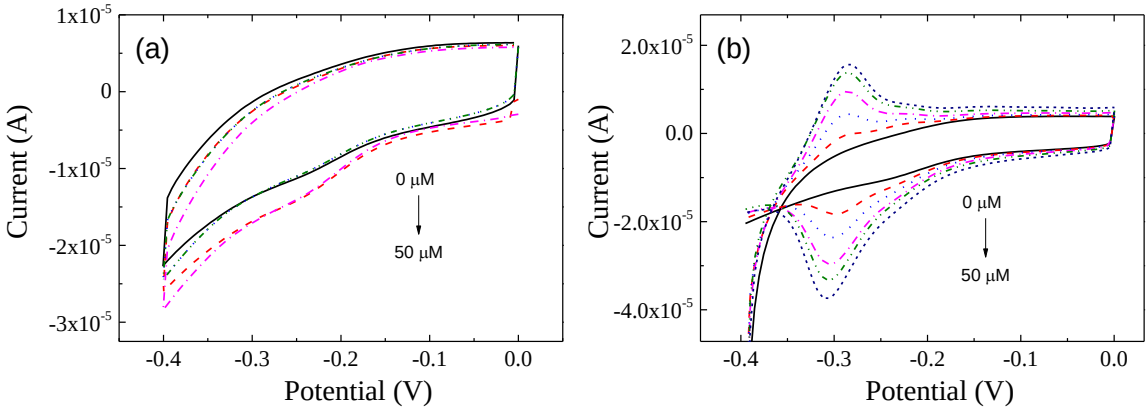

Figure 7.6 Cyclic voltammograms at CB-GCE in 0.1 M phosphate buffer and continuous addition of DA from 0 to 50 μM in steps of 10 μM (a) scanning from 0 to -0.4 V; (b) preconditioning of +0.4 V for 10 s each time, then scanning from 0 to -0.4 V

7.3.1.3 Peak current *vs.* scan rate: adsorption control for DA and DHI at CB-GCE

The surface processes of DA and DHI at CB-GCE were investigated in a scan rate study. Cyclic voltammetry was carried out at CB-GCE in a solution containing 0.1 M phosphate buffer and 100 μM DA with increasing scan rate. The voltammograms from 20 to 200 mV s^{-1} are shown in **Figure 7.7**a. Two pairs of redox peaks are observed at all CVs for DA (+0.1 V) and DHI (-0.3 V) respectively. For the oxiation and reduction of DA, it is apparent that the peak currents are enhanced in magnitude along with scan rate. Both anodic and cathodic currents are plotted as a function of scan rate in **Figure 7.7**b, yielding a linear response from 20 to 200 mV s^{-1}. The proportional relationship of peak current to scan rate at CB-GCE represents a diagnostic of electrode reaction of adsorbed species. Also seen from **Figure 7.7**a, the redox peak potentials shift apart at higher scan rates. The data of the peak potential corresponding to scan rate from 20 to 1000 mV s^{-1} are displayed in **Figure 7.7**c, with the logarithm of scan rate as X axis. The *Laviron equation* can be applied to calculate the heterogeneous electron transfer rate constant, as demonstrated in Equation 5.1. The graph of E_p=f (log ν) was shown in **Figure 7.7**c. The transfer rate constant k_s, transfer coefficient α and electron n were calculated as 2.12 cm

s^{-1}, 0.56 and 2.3. The value of k_s, α and n of DA oxidation at some other electrodes are listed in **Table 7.1**. α was claimed to be around 0.5 at most of electrodes, except one at MWCNT-polymer (0.98), and the electron number n was reported to be 2 approximately. The results achieved in this work are in agreement with those reports. The electron transfer rate constant obtained in this work (2.12 cm s^{-1}) is relatively higher than others, where are 1.66 cm s^{-1} at Ni/Al-CILE and 1.42 cm s^{-1} at MWCNT-polymer.

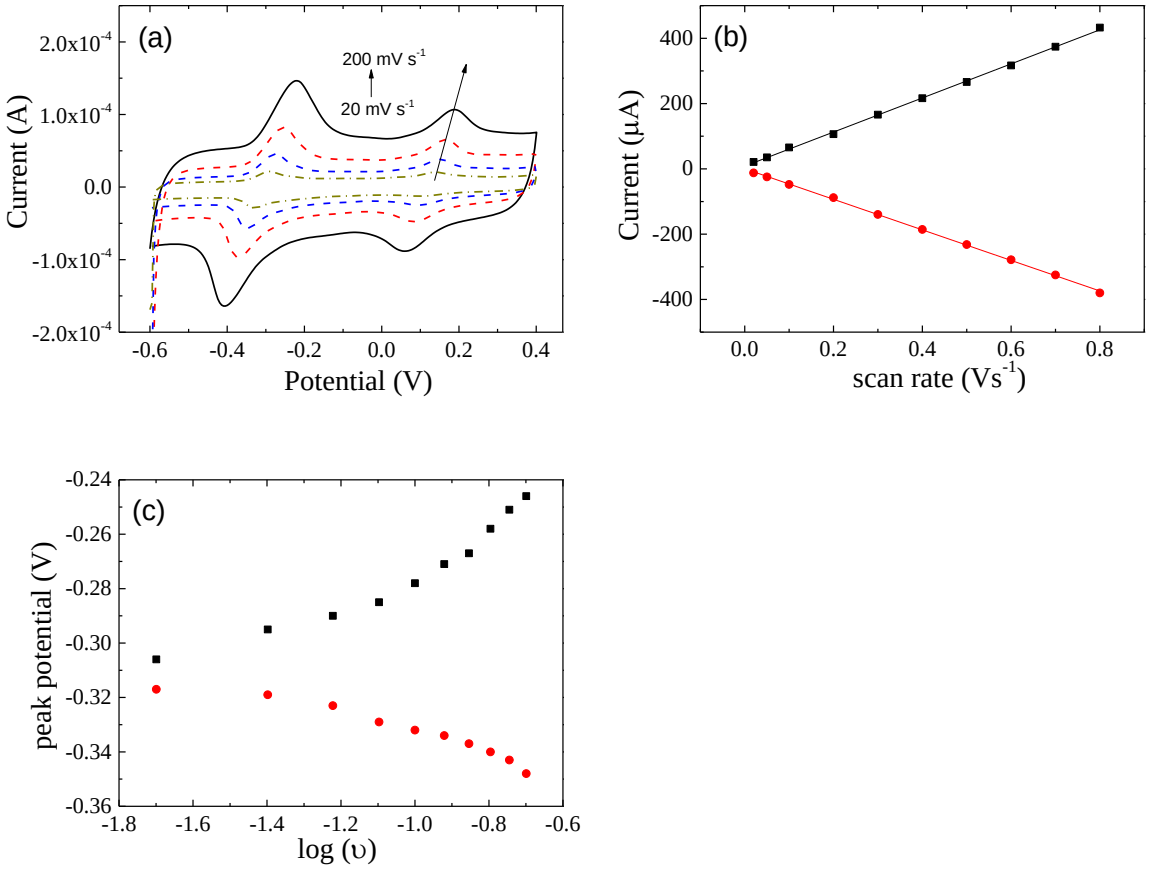

Figure 7.7 (a) Representative cyclic voltammograms of 0.1 mM DA in 0.1 M phosphate buffer at CB-GCE with scan rate of 20, 50, 100 and 200 mV s^{-1}; (b) the plot of current of redox peaks at *ca.* +0.14 V *vs.* scan rate and (c) their potential *vs.* logarithm of scan rate

Table 7.1 Kinetic parameters for redox of DA, where α is diffusion coefficient, n is the number of electron transferred, H is the number of proton and k_s is the heterogeneous electron transfer rate constant

Electrodes	α	n	κ_s(cm s^{-1})	H	Reference
CB-GCE	0.56	2.3	2.12	2.3	This work
Ni/Al-CILE	0.426	2.25	1.66	2	Zhu, Z.[2]
MWCNT-poly (DBA)	0.98	2	1.42	2	Zhou, X[8]

As shown in **Figure 7.7**a, a further redox reaction also occurs at CB-GCE in the potential range between -0.2 to -0.4 V, which is attributed to DHI. The peak current is also proportional to the scan rate, suggesting that the redox reaction of DHI at CB-GCE is also controlled by the adsorption of species on electrode surface. In order to eliminate the influence of DA redox in the DHI reaction, the cyclic voltammetry was carried out from 0 to -0.4 V where only peaks of DHI can be observed. Before experiment, a potential of +0.4 V was applied for 10 s to oxidise DA and generate DHI. CVs with increasing scan rate from 20 to 200 mV s^{-1} are depicted in **Figure 7.8**a, and also shown are the resulting plot of peak current *vs.* scan rate (**Figure 7.8**b) and peak potential *vs.* logarithm of scan rate (**Figure 7.8**c). The dependence of peak current on scan rate suggests that the reaction of DHI is adsorption controlled at CB-GCE. Using the *Laviron equation*, k_s, α and n are calculated as 1.69, 0.336 and 2. However, there are few reported reviews of these parameters in the literature.

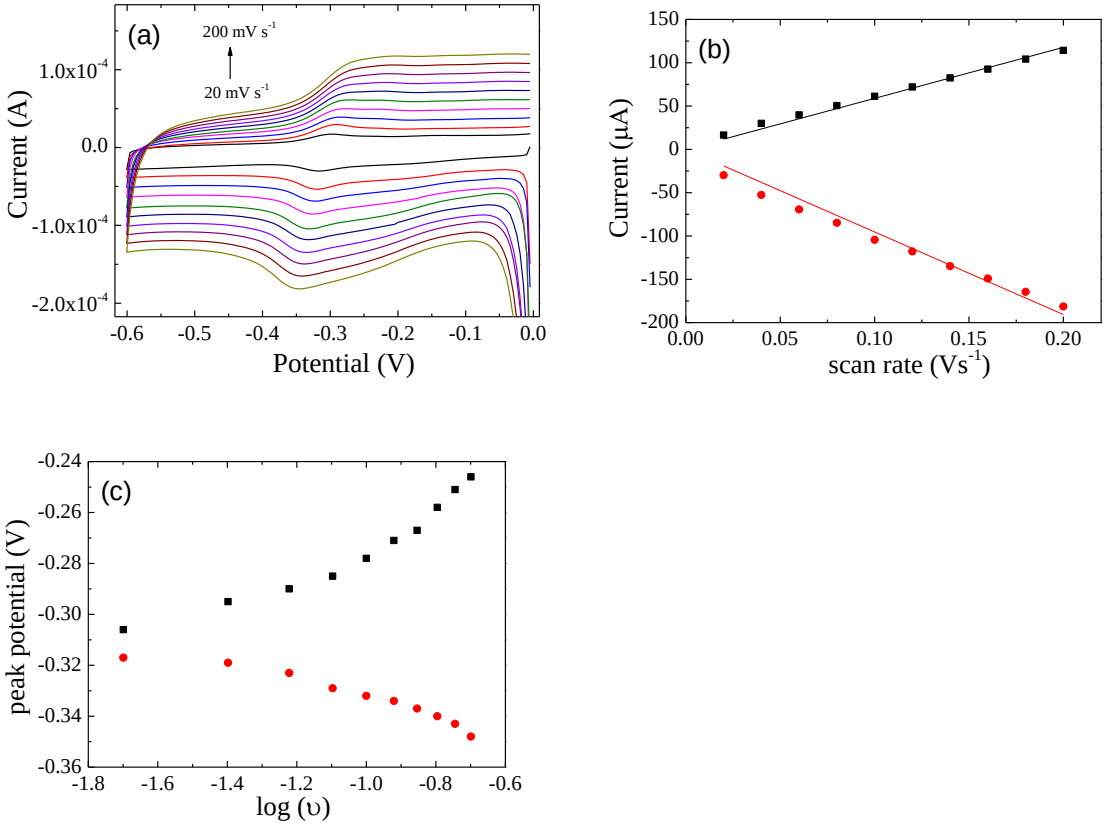

Figure 7.8 Cyclic voltammograms in 0.1 M phosphate buffer and 100 µM DA at CB-GCE from 0 to -0.6 V with increasing scan rate from 20 to 200 mV s^{-1} in steps of 20 mV s^{-1} preconditioning at +0.4 V for 10 s; (b) the resulting plot of current of redox peaks *vs.* scan rate and (c) plot of potential *vs.* logarithm of scan rate

In order to further study the adsorption of DA and DHI at CB-GCE, the CB-GCE was immersed into a solution containing 0.1 M phosphate buffer and 1 mM DA, and then was scanned from -0.4 to +0.4 V in 0.1 M phosphate buffer after being carefully rinsed. The second scan of various immersing time from 0 to 30 s are shown in **Figure 7.9**, to observe of both DA and DHI peaks. The peak current is enhanced quickly at the beginning and the current remains relatively the same value after 10 second. It indicates that the adsorption of DA may be saturated at the CB-GCE surface.

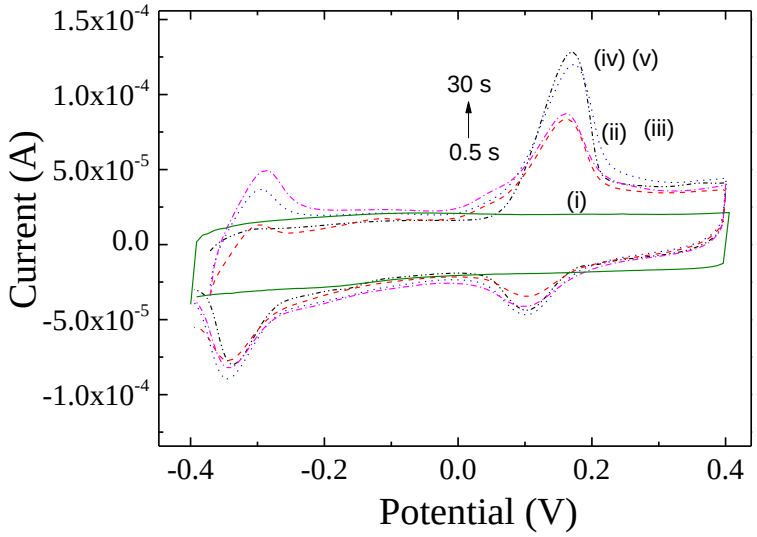

Figure 7.9 Cyclic voltammograms in 0.1 M phosphate buffer at CB-GCE, after immersing CB-GCE into 1 mM DA for time lengths of (i) 0, (ii) 0.5, (iii) 1, (iv) 10 and (v) 30 s

7.3.1.4 Influence of pH

The influence of the pH was investigated by conducting cyclic voltammetry in a solution containing 0.1 M PBS and 0.1 mM DA where the pH was justified from 1 to 11 by NaOH and H_3PO_4 solution. The CVs at bare GCE are shown in **Figure 7.10**a. It can be seen that the oxidation potential of DA shifted from +0.5 V at pH 1 to 0 V at pH 10, and correspondingly the reduction potential shifted from +0.4 V at pH 1 to +0.1 V at pH 8. The peak potential is linearly dependent on the pH, with a slope of around -0.062 V per pH unit, compatible with a 2e, 2H+ redox step. This pH dependence was also reported in other papers.[12,19] Another pair of peaks is found appearing at pH 9, and shifting negatively at pH 10. S. Chen and his colleagues[21] observed that at lower pH value, the CVs of DA in the potential range of -0.4 to +0.8 V showed a single redox couple and a second redox couple appears at higher pH values (pH >8).

At CB-GCE, of which CVs are shown in **Figure 7.10**b, both pairs of peaks of DA and DHI are observed from pH 1 to pH 11. Similar to the result at bare GCE, those peaks

also negatively shift as pH increases. The plot of peak potential of DA redox reaction against pH is shown in **Figure 7.10**b and the one of DHI are plotted in **Figure 7.10**c. The peak potential of DA exhibits an excellent linear dependence on pH in the range investigated, giving a fitting line E = 0.127-0.059 pH. The slope of 0.059 indicates that the number of proton in the redox reaction should be equal to the number of electron, *i.e.* the proton should be 2. This result is in accordance with other literature, which data are shown in **Table 7.1**. The peak potential of DHI also linear correlated to the pH from 1 to 8 with a slope of 0.060, close to 0.059. Both reactions of DA and DHI are compatible with the 2e, 2H+ redox step as proposed. In high pH range, the slope of DHI reaction potential was getting smaller, which indicates that fewer protons may be involved in the reaction.

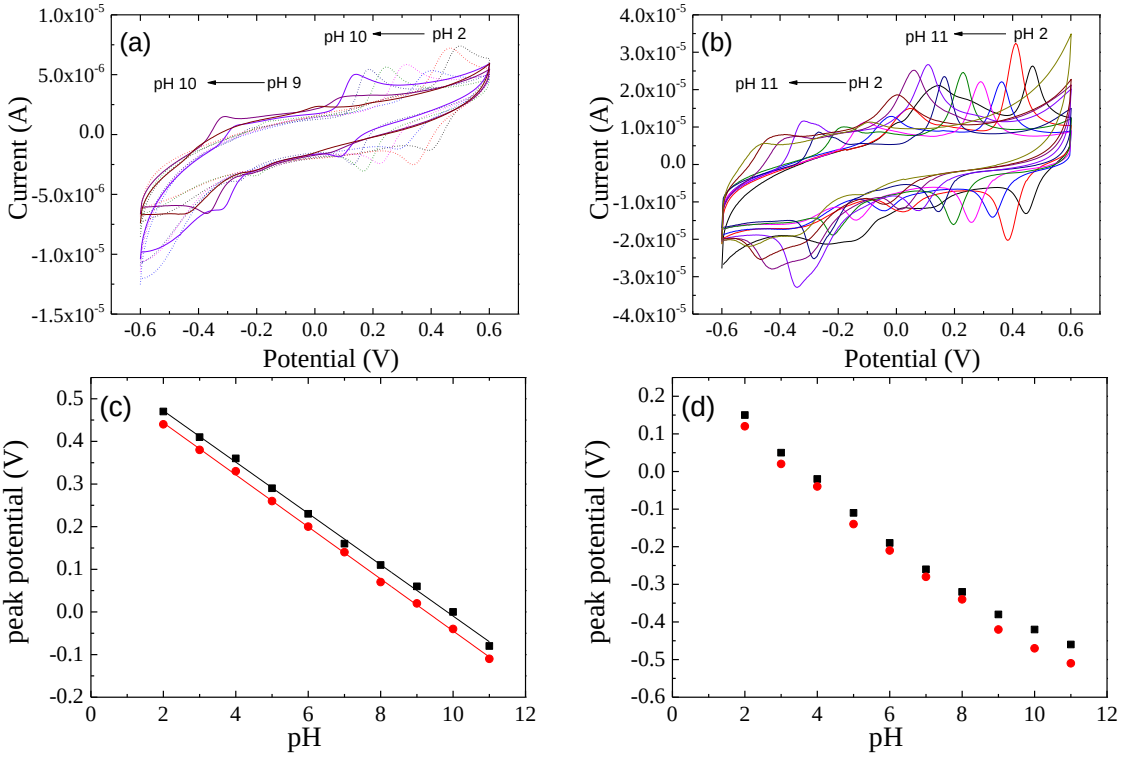

Figure 7.10 Cyclic voltammograms of 0.1 mM DA at (a) bare GCE and (b) CB-GCE in the potential range from -0.6 to +0.6 V in 0.1 M phosphate buffer with pH from 1 to 12 in steps of 1; the resulting plot of the peak potential at CB-GCE of (c) DA and (d) DHI *vs.* solution pH

7.3.1.5 Influence of CB loading

In this work, the glassy carbon substrate was modified by dropping 2 mg mL^{-1} carbon black suspensions (in Mill-Q water) onto the surface and then dried in the fume hood for 2 hours. The quantity of carbon materials in the surface affects the strength of electrochemical response and background current, therefore need to be optimised. The carbon black suspension of 2, 5, 10, 20 and 40 μL, corresponding to 0.028, 0.071, 0.14, 0.28 and 0.56 μg cm^{-2}, were dropped onto different GCE substrates, dried in the open aire, and then rinsed carefully by water. Then cyclic voltammetry was carried out at these CB-GCEs in a solution containing 0.1 M phosphate buffer and 0.1 mM DA. The CVs of the second scan are shown in **Figure 7.11**a. Two pairs of redox peaks can be clearly observed in all profiles. It is apparent that the absolute value of peak current rises with increasing amount of carbon black on the surface. The background current, associated with the double layer capacitance is also found to be enhanced, as greater carbon black loadings allow stronger adsorption. The points of peak current against the volume of carbon black suspension are plotted in **Figure 7.11**b. Number 1-4 present the oxidation of DHI, oxidation of DA, reduction of DA and reduction of DHI respectively, corresponding to the number in **Figure 7.11**a. For the redox reaction of DA (2 and 3), the peak current rises with the increase in CB from 2 to 10 μL, before reaching a plateau as even larger amount of CB amount is loaded. Similarly, the electrochemical response of DHI also increases with more modifiers initially before getting also reaching a plateau, as shown in **Figure 7.11**b 1 and 4. Note that, the background current grows all along with the increasing amount of CB materials although the peak current remains the same. The reason could be that more carbon black materials can bring more active sites on the electrode surface, until all the possible GCE surfaces are occupied. At the same time, more CB always results in larger double layer capacitance, leading to a larger

background current. In the subsequent experiments, 10 μL (0.14 μg cm^{-2}) carbon black materials were used to modify electrode for the detection of DA.

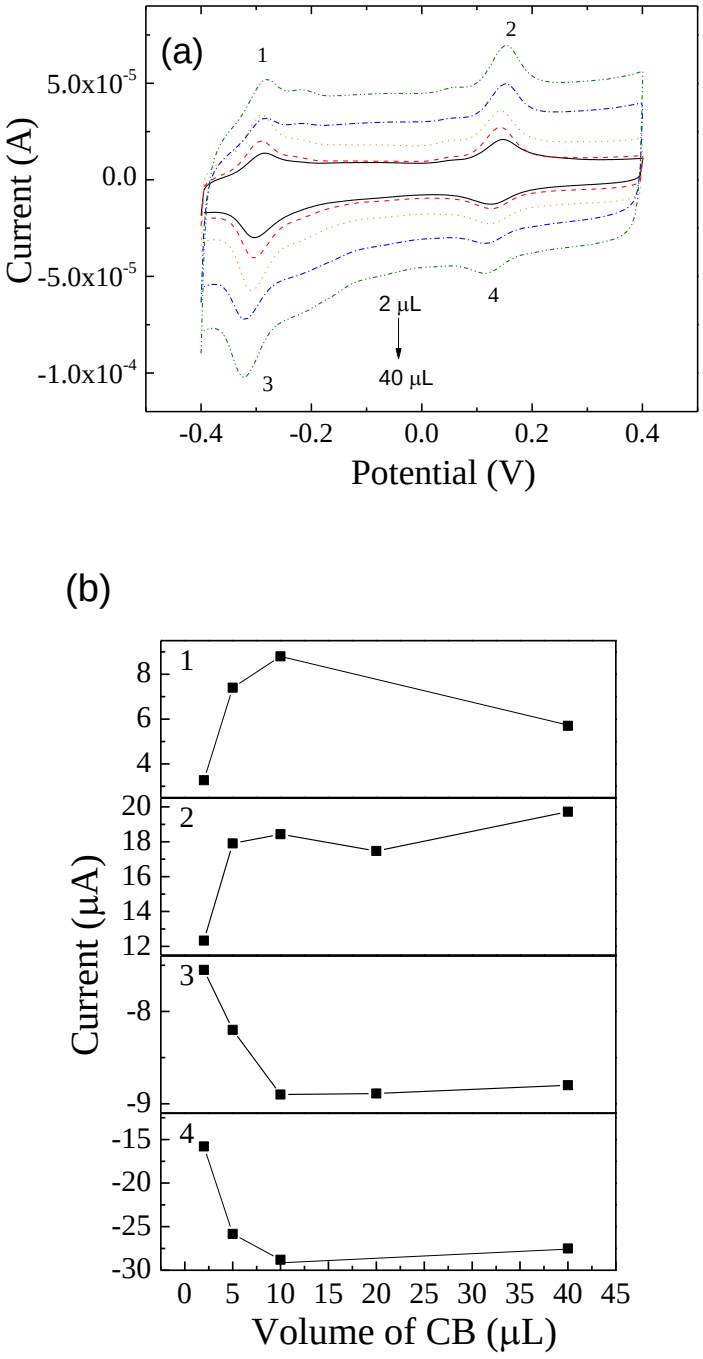

Figure 7.11 (a) Cyclic voltammograms in 0.1 M phosphate buffer and 0.1 mM DA at CB-GCEs which are modified by 2, 5, 10, 20 and 40 μL 2 mg L^{-1} carbon black suspension respectively; (b) the current of each peaks in (a) *vs.* the volume of carbon black.

7.3.2 DA determination at CB-GCE

7.3.2.1 SWV by DA oxidation

SWV was used to determine DA at CB-GCE by both the direct oxidation method and the indirect method via detecting DHI. The direct determination will discussed first and the indirect approach will be discussed subsequently. The experiments were performed in 0.1 M phosphate buffer at CB-GCE with progressive additions of 1 μM DA, resulting concentration from 1 to 10 μM, scanning from 0 to +0.4 V. In this potential range, only the oxidation of DA was driven. The CVs are displayed in **Figure 7.12**. In the absence of DA, a featureless wave is observed and when DA was added, a well-resolved peak assigned to DA oxidation starts to emerge at *ca.* +0.15 V and increases with increasing with higher DA concentration. The resulting plot of peak current against the DA concentration is shown in the inset. A linear line is obtained (R^2> 0.999) with the slope of 0.13 μA μM^{-1}, where the detection limit can be achieved as 0.06 μM (S/N=3).

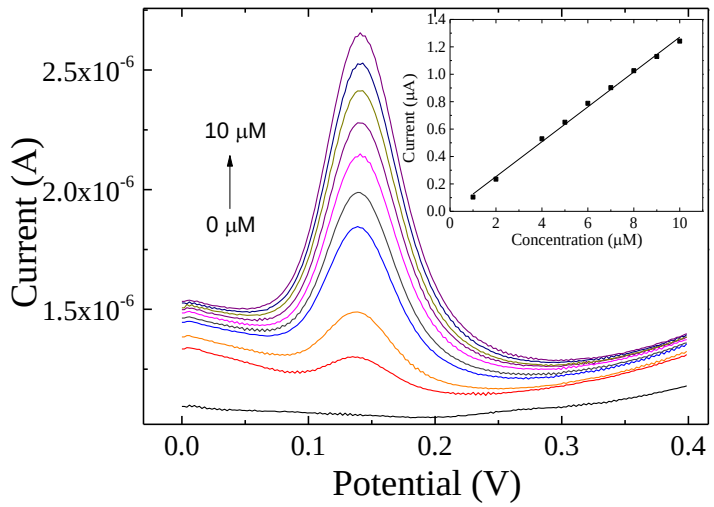

Figure 7.12 Square wave voltammograms at CB-GCE in a solution containing 0.1 M phosphate buffer with continuous addition of DA from 0 to 10 μM in steps of 1 μM. Inset: plot of peak current *vs.* the concentration of DA

7.3.2.2 SWV via DHI reduction

Another method to determine DA is via DHI reduction by SWV from 0 to -0.6 V after preconditioning by applying +0.6 V for 10 s. The CVs of DA from 0 to 8 μM at CB-GCE in 0.1 M phosphate buffer are shown in **Figure 7.13**. In the absence of DA, the curve is featureless and when DA was added, one peak at about -0.3 V appears. The points of peak current against DA concentration are plotted in the inset, yielding a linear line with slope of 0.61 μA μM^{-1}. The detection limit was calculated to be 0.013 μM (S/N=3) in the range from 0.1 to 40 μM. In comparison to the method of direct oxidation above, this approach is superior in terms of sensitivity and LOD. Further comparison of both methods and other DA sensor will be discussed subsequently.

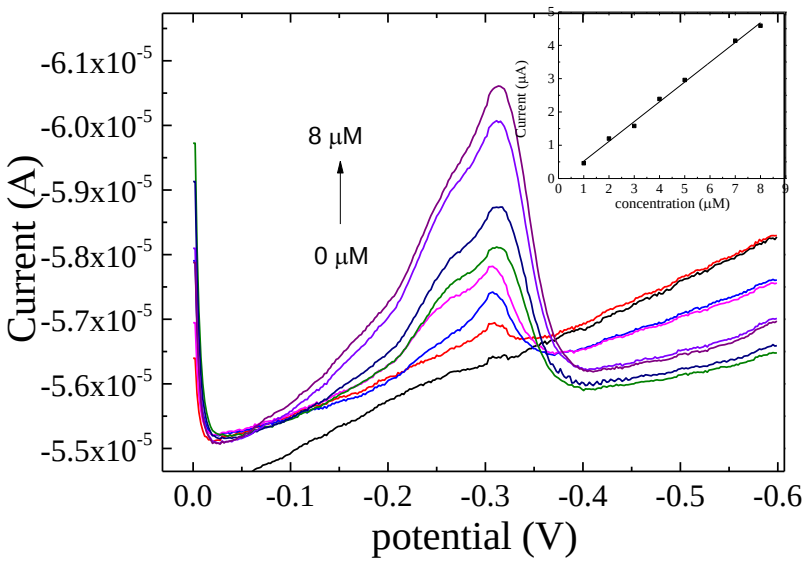

Figure 7.13 Square wave voltammograms in 0.1 M phosphate buffer with continuous addition of DA from 0 to 8 μM in steps of 1 μM (preconditioning at +0.6 V for 10 s) at CB-GCE. Inset: plot of peak current *vs.* DA concentration

7.3.2.3 Interference of AA and UA

The detection of DA suffers from the interference of AA to a great extent, since the concentration of AA is generally much higher (20–100 times in human body, up to 1000 times in some environmental samples) than that of DA.[7,22,23] Because UA always co-exists with AA and DA, it might also influence the detection in monitoring although UA usually has the same concentration level as DA. The interference of AA and UA in both methods was studied based on their concentration ratio in human body. The direct oxidation method is considered first. SWV was conducted at CB-GCE in a solution containing 0.1 M phosphate buffer, 2 mM AA and 0.1 mM UA, with continuous addition of DA from 0 to 0.1 mM. The voltammograms are displayed in **Figure 7.14**. It can be seen that along with the higher DA concentration, the peak assigned to AA almost remains the same value while the one of UA is slightly decreased. The peak of DA is enhanced gradually without overlap with AA and UA. The interference was also studied by spike and recovery method which has been detailed in section 5.3.1.4. In this method, 0.05 mM DA was detected in 0.05 mM UA, 1mM and 10 mM AA respectively. The average recovery data are shown in **Table 7.2**. The recovery of DA by direct detection method is 96.3 % in UA, and 108.6 % in 1 mM AA. It indicates that the detection of DA by this method is relatively free from the interference of UA and 20 times AA. However, the recovery of 0.05 mM DA in 10 mM AA is 113.5%, showing that in the presence of large excess AA, the influence is still significant.

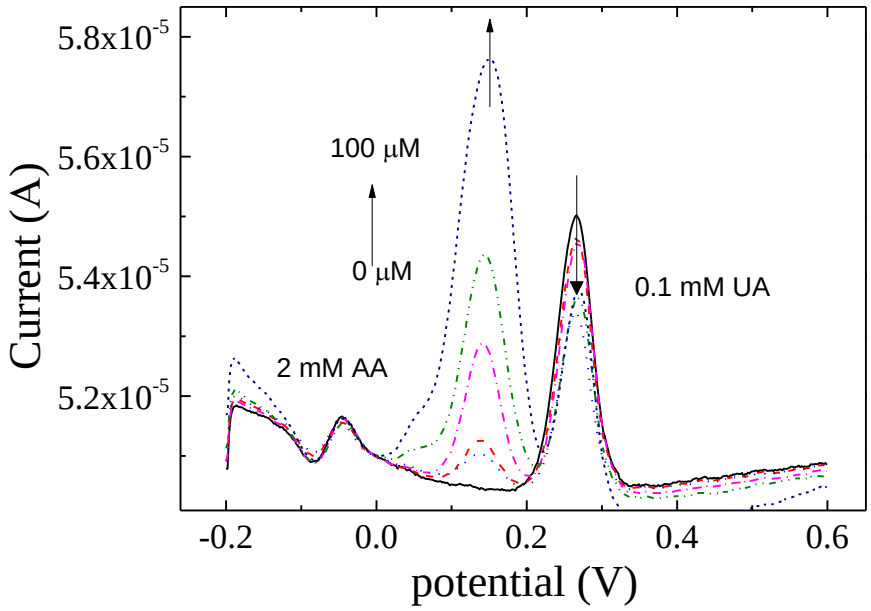

Figure 7.14 Square wave voltammograms from -0.2 to +0.6 V at CB-GCE in a solution containing 0.1 M phosphate buffer, 2 mM AA, 0.1 mM UA and 0, 5, 10 40, 60 and 100.μM DA respectively

In order to observe the influence of AA in the redox reaction of DHI, cyclic voltammetry was conducted from -0.4 to 0 V after preconditioning of +0.6 V for 10 s, in a solution containing 0.1 M phosphate buffer, 0.05 mM DA and continuous addition of AA from 0 to 10 mM. The CVs are shown in **Figure 7.15**. A pair of peaks assigned to DA is observed at about -0.3 V and hardly affected by the large excess of AA. The recovery experiment was also performed and the data are shown in **Table 7.2**. Apparently, the found DA concentration by the indirect method via DHI is closer to the real concentration in the solution than that obtained by the direct oxidation. It indicates that the indirect approach is more accurate in the presence of AA and UA, and suffers less interference.

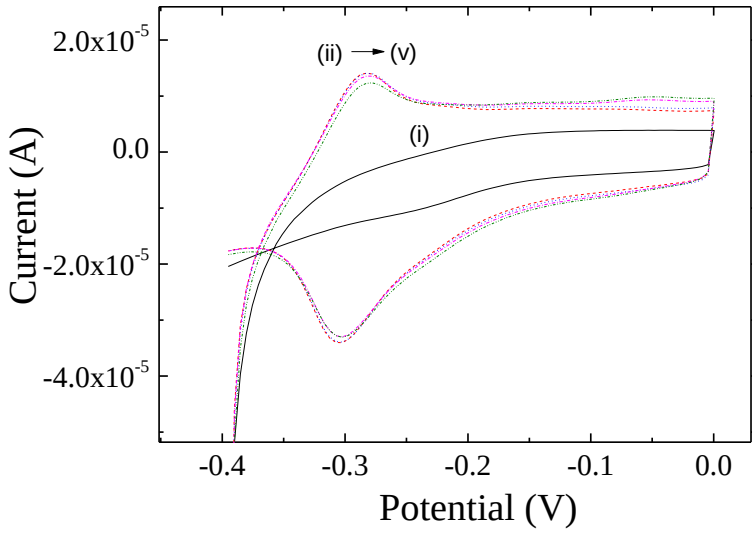

Figure 7.15 Cyclic voltammograms at CB-GCE (preconditioning at +0.6 V for 10 s) in 0.1 M phosphate buffer (i) in the absence and presence of 50 μM DA and (ii) 0, (iii) 0.05, (iv) 1 and (v) 10 mM AA respectively

Table 7.2 The recovery of DA at CB-GCE electrode in 0.1 M phosphate buffer by direct and indirect determination

	Add DA	Direct oxidised		Indirect via DHI	
		Found (μM)	Recovery	Found(μM)	Recovery
0.05 mM UA	0.05 mM	0.048	96.3%	0.050	99.2%
1 mM AA	0.05 mM	0.054	108.6%	0.051	102.7%
10 mM AA	0.05 mM	0.056	113.5%	0.050	100.1%

7.3.2.4 Comparison with other DA sensors

Table 7.3 lists the detection limit, sensitivity and the detection range of the DA determination at CB-GCE in this work and some other successful DA sensors reported in the literature. The sensitivity of CB-GCE (0.61 μA μM^{-1}) is consistently higher than other electrodes (0.03-0.23 μA μM^{-1}), consistent with previous work on the

determination of phenol, p-cresol, BPA, HQ and DHB in chapter 5. This seems attributed to the strong adsorption properties and high surface area of carbon black. As a result, the detection limit achieved at CB-GCE (0.013 μM) is very competitive in comparison to others such as PtAu-GCE and WMNTs (0.2-5 μM). And this detection limit can also meet the requirement in most real sample, such as in human plasma (0.23 μM)[20] and brain (0.02-0.2 μM)[24]. In addition, the recovery of DA in the presence of AA was reported as in the range of 90-110% at various electrodes, such as 96.73-104.79 % at LP-CPE[4], 98-102% at poly(9-aminoacridine)-modified electrode[25] and 94-110% at SDS-CPE[17]. In this work, the recovery achieved from indirect detection method (via DHI) is only about 100% to 102%, showing that this method is less affected by AA than most of other methods. The reason might be that this method can alleviate the interaction between AA and DA to a great extent. Although the detection range is relatively narrow at CB-GCE, it satisfied most requirement of DA monitoring since the DA concentration in being is normally lower than 10 μM due to the rapid and efficient metabolism.

Table 7.3 Sensitivity (μA μM^{-1}), detection range (μM) and detection limit (μM) at various DA sensors

Sensors	Sensitivity	Detection range	Detection limit	Reference
CB-GCE	0.127	0.1-20	0.06	This work (direct)
CB-GCE	0.61	0.1-40	0.013	This work (via DHI)
CNTs-$La(OH)_3$		0.5-35.4	1.67	Zhang, Y[11]
MWNTs-$OMIMPF_6$	0.23	1-100	0.1	Zhao, Y[19]
Fc@DWNTs/GCE	0.03	0.5-20	0.3	Cheng, H[10]
Ni/Al-LDH	0.08	10-700	5.0	Zhu, Z[2]
P_3MT/Au NPs		1.0-32	0.24	Huang, X[26]
TPY/PFE	0.062	1-250	0.2	Domenech, A[27]
Au NPs	0.04	Up to 40	0.22	Raj, C[9]
CILE	-	2-150	1.0	Safavi, A[28]
DA-film/Au	0.06	1-60	0.2	Luczak, T.[6]

7.4 Conclusion

In this work, CB-GCE was used to determine DA by two methods, *i.e.* direct oxidation and indirect via DHI.

- In comparison to bare GCE, the redox potential of AA is largely shifted at CB-GCE, therefore avoiding the overlap of oxidation peaks of AA and DA, which

enable the simultaneous detection of AA, DA and UA. At the same time, the sensitivity is enhanced significantly at CB-GCE.

- The redox peaks of DHI are observed at about -0.3 V at CB-GCE. And these peaks can only be observed after the oxidation of DA.
- The peak potentials of both DA redox and DHI redox are all linearly correlated to the scan rate at CB-GCE, showing that these reactions are under adsorption control at CB-GCE. The k_s, α and n were calculated as 2.12 cm s^{-1}, 0.56 and 2.3 for DA redox, and 1.69 cm s^{-1}, 0.336 and 2 for DHI respectively.
- These peaks are significantly influenced by solution pH. The peak potential is more negative in higher pH, yielding a linear relationship with a slope of 0.059 for DA and 0.060 for DHI. Therefore, the number of proton involved in the reactions equals to the number of electron, *i.e.* 2, which is in agreement with the mechanism reported by literature.
- The amount of CB on the electrode surface also affects the response of DA and DHI, in terms of both peak current and non-faradaic background current.
- DA was determined by SWV at CB-GCE from 0 to +0.6 V, where the direct oxidation occurred. A linear line is obtained (R^2 > 0.999) with a slope of 0.13 μA $μM^{-1}$, where detection limit of 0.06 μM are obtained.
- Another method to determine DA is via DHI reduction by SWV from 0 to -0.6 V after the preconditioning of applying +0.6 V for 10 s. The precondition is to oxidise the DA and generate DHI at the electrode surface. The detection limit was 0.013 μM.
- The interference of AA and UA was studied. The recovery of DA in the presence of AA and UA was improved to 99%~101% by the indirect detection

method (via DHI), which proves that the interference of AA and UA was eliminated to a great extent with this method.

References

(1) Zhang, H. M.; Li, N. Q.; Zhu, Z. W. *Microchem J.* **2000**, *64*, 277.

(2) Zhu, Z.; Qu, L.; Guo, Y.; Zeng, Y.; Sun, W.; Huang, X. *Sensors and Actuators B-Chemical* **2010**, *151*, 146.

(3) Zhu, L. J.; Lu, Y. L.; Wang, Y. Q.; Zhang, L. Q.; Wang, W. C. *Applied Surface Science* **2012**, *258*, 5387.

(4) Sun, W.; Yang, M.; Jiao, K. *Anal. Bioanal. Chem.* **2007**, *389*, 1283.

(5) Gilbert, O.; Swamy, B. E. K.; Chandra, U.; Sherigara, B. S. *International Journal of Electrochemical Science* **2009**, *4*, 582.

(6) Luczak, T. *Electrochimica Acta* **2008**, *53*, 5725.

(7) Huang, J.; Liu, Y.; Hou, H.; You, T. *Biosensors & Bioelectronics* **2008**, *24*, 632.

(8) Zhou, X.; Zheng, N.; Hou, S. R.; Li, X. J.; Yuan, Z. B. *Journal of Electroanalytical Chemistry* **2010**, *642*, 30.

(9) Raj, C. R.; Okajima, T.; Ohsaka, T. *Journal of Electroanalytical Chemistry* **2003**, *543*, 127.

(10) Cheng, H. M.; Qiu, H. X.; Zhu, Z. W.; Li, M. X.; Shi, Z. J. *Electrochimica Acta* **2012**, *63*, 83.

(11) Zhang, Y.; Yuan, R.; Chai, Y. Q.; Zhong, X.; Zhong, H. A. *Colloids and Surfaces B-Biointerfaces* **2012**, *100*, 185.

(12) Yogeswaran, U.; Chen, S.-M. *Electrochimica Acta* **2007**, *52*, 5985.

(13) Yao, H.; Sun, Y. Y.; Lin, X. H.; Tang, Y. H.; Huang, L. Y. *Electrochimica Acta* **2007**, *52*, 6165.

(14) Lin, L.; Chen, J.; Yao, H.; Chen, Y.; Zheng, Y.; Lin, X. *Bioelectrochemistry* **2008**, *73*, 11.

(15) Henstridge, M. C.; Dickinson, E. J. F.; Aslanoglu, M.; Batchelor-McAuley, C.; Compton, R. G. *Sensors and Actuators B-Chemical* **2010**, *145*, 417.

(16) Roy, P. R.; Okajima, T.; Ohsaka, T. *Bioelectrochemistry* **2003**, *59*, 11.

(17) Patrascu, D. G.; David, V.; Balan, I.; Ciobanu, A.; David, I. G.; Lazar, P.; Ciurea, I.; Stamatin, I.; Ciucu, A. A. *Analytical Letters* **2010**, *43*, 1100.

(18) Hsu, C.-Y.; Vasantha, V. S.; Chen, P.-Y.; Ho, K.-C. *Sensors and Actuators B-Chemical* **2009**, *137*, 313.

(19) Zhao, Y. F.; Gao, Y. Q.; Zhan, D. P.; Liu, H.; Zhao, Q.; Kou, Y.; Shao, Y. H.; Li, M. X.; Zhuang, Q. K.; Zhu, Z. W. *Talanta* **2005**, *66*, 51.

(20) Reymond, M. J.; Speciale, S. G.; Porter, J. C. *Endocrinology* **1983**, *112*, 1958.

(21) Chen, S. M.; Peng, K. T. *Journal of Electroanalytical Chemistry* **2003**, *547*, 179.

(22) Oreopoulos, D. G.; Lindeman, R. D.; Vanderjagt, D. J.; Tzamaloukas, A. H.; Bhagavan, H. N.; Garry, P. J. *J. Am. Coll. Nutr.* **1993**, *12*, 537.

(23) Rumsey, S. C.; Levine, M. *J. Nutr. Biochem.* **1998**, *9*, 116.

(24) Wightman, R. M.; May, L. J.; Michael, A. C. *Analytical Chemistry* **1988**, *60*, 769A.

(25) Fang, B.; Liu, H.; Wang, G.; Zhou, Y.; Jiao, S.; Gao, X. *Journal of Applied Polymer Science* **2007**, *104*, 3864.

(26) Huang, X.; Li, Y.; Wang, P.; Wang, L. *Anal Sci* **2008**, *24*, 1563.

(27) Domenech, A.; Garcia, H.; Domenech-Carbo, M.; Galletero, M. *Analytical Chemistry* **2002**, *74*, 562.

(28) Safavi, A.; Maleki, N.; Moradlou, O.; Tajabadi, F. *Analytical Biochemistry* **2006**, *359*, 224.